AD-A286 407

**WL-TR-94-3123**

# Nonlinear Dynamics of the Planar Pitch Attitude Motion for a Gravity-Gradient Satellite

Harry A. Karasopoulos
WL/FIMH

August 1994

Final Report for the Period June 1990 - June 1994

*Approved for Public Release; Distribution is Unlimited*

FLIGHT DYNAMICS DIRECTORATE
WRIGHT LABORATORY
AIR FORCE MATERIEL COMMAND

WRIGHT-PATTERSON AIR FORCE BASE, OH 45433-7913

94-35786

'94 1 1 21 006

## Notice

When Government drawings, specifications, or other data are used for any purpose other than in connection with a definitely Government-related procurement, the United States Government incurs no responsibility or any obligation whatsoever. The fact that the government may have formulated or in any way supplied the said drawings, specifications, or other data, is not to be regarded by implication, or otherwise in any manner construed, as licensing the holder, or any other person or corporation; or as conveying any rights or permission to manufacture, use, or sell any patented invention that may in any way be related thereto.

This report is releasable to the National Technical Information Service (NTIS). At NTIS, it will be available to the general public, including foreign nations.
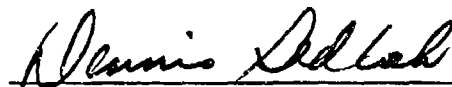
This technical report has been reviewed and is approved for publication.


Harry Karasopoulos, Aerospace Engineer
Flight Mechanics Research Section

Valentine Dahlem, Chief
Aerothermodynamics and Flight
Mechanics Research Branch


Dennis Sedlock, Acting Chief
Aeromechanics Division


If your address has changed, if you wish to be removed from our mailing list, or if the addressee is no longer employed by your organization please notify WL/FIMH, Bldg 450, 2645 Fifth St, Ste 7, WPAFB, OH 45433-7913 to help us maintain a current mailing list.

Copies of this report should not be returned unless return is required by security considerations, contractual obligations, or notice on a specific document.

# DISCLAIMER NOTICE
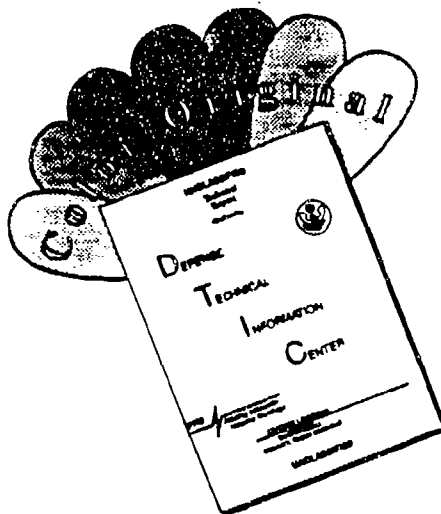
THIS DOCUMENT IS BEST
QUALITY AVAILABLE. THE COPY
FURNISHED TO DTIC CONTAINED
A SIGNIFICANT NUMBER OF
COLOR PAGES WHICH DO NOT
REPRODUCE LEGIBLY ON BLACK
AND WHITE MICROFICHE.

| 1. AGENCY USE ONLY (leave blank) | 2. REPORT DATE<br>August 1994 | 3. REPORT TYPE AND DATES COVERED<br>Final    June 1990 to June 1994 | |
|---|---|---|---|

| 4. TITLE AND SUBTITLE<br>Nonlinear Dynamics of the Planar Pitch Attitude Motion for a<br>Gravity-Gradient Satellite | 5. FUNDING NUMBERS<br><br>PE:  62201F<br>PR:  2404 |
|---|---|
| 6. AUTHOR(S)<br>Harry A. Karasopoulos | TA:  07<br>WU:  XB |

| 7. PERFORMING ORGANIZATION NAME(S) AND ADDRESS(ES)<br>Flight Dynamics Directorate<br>Wright Laboratory<br>Air Force Materiel Command<br>Wright Patterson AFB, OH 45433-7562 | 8. PERFORMING ORGANIZATION<br>REPORT NUMBER |
|---|---|

| 9. SPONSORING / MONITORING AGENCY NAME(S) AND ADDRESS(ES)<br>Flight Dynamics Directorate<br>Wright Laboratory<br>Air Force Materiel Command<br>Wright Patterson AFB, OH 45433-7562 | 10. SPONSORING / MONITORING<br>AGENCY REPORT NUMBER<br><br>WL-TR-94-3123 |
|---|---|

**11. SUPPLEMENTARY NOTES**

| 12a. DISTRIBUTION / AVAILABILITY STATEMENT<br><br>Approved for public release; distribution is unlimited. | 12b. DISTRIBUTION CODE |
|---|---|

**13. ABSTRACT** *(Maximum 200 words)*

The nonlinear dynamics of the planar pitch attitude motion for a gravity-gradient satellite in an elliptical orbit about a central body are investigated using phase diagrams, Poincare' maps, bifurcation plots, spectral density plots, Lyapunov exponents, and chaos diagrams. The satellite is assumed to be a rigid body influenced only by torques from an inverse-square gravitational field, and its major axis is assumed to be normal to the orbit plane. The resultant planar pitching motion is either periodic, quasiperiodic, or chaotic, depending upon the values of the system parameters, eccentricity and satellite inertia ratio. The relationships of the system parameters to the nonlinearity of the system are explored with chaos diagrams, which incorporate the results of the Lyapunov exponent calculations into a useful tool for predicting the onset of chaotic motion in parameter space. The border between regular and chaotic motion in the chaos diagrams is shown to be fractal. The dynamics of the basic problem supplemented by the addition of damping terms and an oblate, axially symmetric central body are also investigated. Strange attractors are found and the validity of Melnikov's method to predict the border between chaos and regular motion is examined.

| 14. SUBJECT TERMS<br>nonlinear dynamics, satellite, chaos, Melnikov, gravity-gradient,<br>strange attractor, fractal | 15. NUMBER OF PAGES<br>227 |
|---|---|
| | 16. PRICE CODE |

| 17. SECURITY CLASSIFICATION<br>OF REPORT<br>UNCLASSIFIED | 18. SECURITY CLASSIFICATION<br>OF THIS PAGE<br>UNCLASSIFIED | 19. SECURITY CLASSIFICATION<br>OF ABSTRACT<br>UNCLASSIFIED | 20. LIMITATION OF<br>ABSTRACT<br>UNLIMITED |
|---|---|---|---|

# Foreword and Acknowledgments

The research documented in this report was performed during the period of June 1990 through June 1994, under the in-house work unit (240407XB) "Orbit Boost, Reentry, and Perturbation Analysis." This study is an extension of research initiated during the summer of 1990 at the University of Cincinnati, and it has been carried out under the guidance of Professor David L. Richardson of the Department of Aerospace Engineering and Engineering Mechanics. The analyses and report were completed at the Aerothermodynamics and Flight Mechanics Research Branch, Aeromechanics Division, Flight Dynamics Directorate of the Wright Laboratory at Wright-Patterson Air Force Base, Ohio. This technical report is being concurrently published as a University of Cincinnati Ph.D. dissertation.

The author would like to express his gratitude and utmost appreciation to his dissertation advisor Dr. David L. Richardson, for his guidance and constant encouragement throughout this endeavor. Thanks are also due to dissertation committee members, Dr. Trevor Williams and Dr. Paul Orkwis, for their interest and advice, to Val Dahlem and the Aeromechanics Division for providing the time to complete this effort, and to friends and family for their invaluable support. Especially to Natalie and other friends not here to see this. They taught me much about love, life, and perspective.

# Contents

# List of Figures

xiii

xix

# List of Symbols

| | |
|---|---|
| $a$ | Orbit semimajor axis |
| $a_r$ | Radial perturbative acceleration due to the oblateness of the central body |
| $a_t$ | Transverse perturbative acceleration due to the oblateness of the central body |
| $c_{ij}$ | Direction cosines |
| $C$ | Constant of integration |
| $C_D$ | Damping coefficient |
| $C_{D_*}$ | Damping coefficient multiplied by $h^3/\mu^2$ |
| $\mathcal{C}$ | Direction cosine matrix of the $c_{ij}$ |
| $d_{ij}$ | Direction cosines |
| $\mathcal{D}$ | Direction cosine matrix of the $d_{ij}$ |
| $e$ | Orbit eccentricity |
| $f$ | Orbit true anomaly |
| $\mathcal{F}(k, \psi)$ | Elliptic integral of the first kind |
| $h$ | Angular momentum per unit mass |
| $I$ | Orbit inclination angle |
| $I_x$ | Moment of inertia about the yaw axis |
| $I_y$ | Moment of inertia about the roll axis |
| $I_z$ | Moment of inertia about the pitch axis |
| $J_2$ | Oblateness spherical harmonic term in the Earth's gravitational potential |
| $k$ | Modulous of the elliptic integral of the first kind |
| $K$ | Satellite moment of inertia ratio |
| $\mathcal{K}(k)$ | Complete elliptic integral of the first kind |
| $\mathcal{L}$ | Effective Lagrangian function |
| $m$ | Number of pitch angle revolutions (tumbling case) or oscillations (libration case) |
| $m$ | Satellite mass |
| $M$ | Central body mass |
| $N$ | Number of orbits |
| $p$ | Orbit parameter (semilatus rectum) |
| $p_*$ | Scaled orbit parameter |
| $P$ | Integration step size constant |
| $P$ | Winding number or resonant period |
| $r$ | Radial distance |

| | |
|---|---|
| $r_c$ | Distance from the center of mass of the central body to the center of mass of the orbiting body |
| $R_e$ | Central body's mean equatorial radius |
| $t$ | Time |
| $T_f$ | Orbital period |
| $\mathcal{T}$ | Effective kinetic energy |
| $T_\psi$ | Pitching period |
| $\mathcal{V}$ | Effective potential energy |
| | |
| $\alpha_i$ | Constituents of the potential function |
| $\Delta\tau$ | Integration step size |
| $\theta$ | Argument of latitude |
| $\vartheta$ | Satellite roll angle |
| $\lambda$ | Constant of integration |
| $\mu$ | Central body's gravitational constant |
| $\rho$ | Distance from satellite's center of mass to differential mass $dm$ |
| $\sigma_1$ | First Lyapunov exponent |
| $\sigma_2$ | Second Lyapunov exponent |
| $\Sigma$ | Constituents of the potential function |
| $\phi$ | Transformation variable |
| $\phi$ | Satellite yaw angle |
| $\psi$ | Satellite pitch angle measured from the local vertical |
| $\psi'$ | Derivative of the pitch angle with respect to the true anomaly or the argument of latitude |
| $\psi''$ | Second derivative of the pitch angle with respect to the true anomaly or the argument of latitude |
| $\omega$ | Angular velocity |
| $\omega$ | Argument of periapsis |
| $\omega_c$ | Constant angular velocity for a circular orbit |
| $\Omega$ | Longitude of the ascending node |

# 1    Introduction

## 1.1    Nonlinear Dynamics and Chaos

The modern study of nonlinear dynamics, which includes chaos, bifurcation, and
other subjects, has caused a revolution in many scientific and engineering fields. In
the last few years startling marriages have taken place between the field of nonlinear
dynamics and multitudes of other diverse disciplines, ranging from meteorology to
economics, and physiology to sociology. There are so many new applications and
research opportunities emerging from nonlinear systems analysis that a large staff
would be required just to keep current with the literature. Why is this occurring?
Because modern nonlinear analysis is a tool that can be used to finally make sense
out of data that was previously thought to be nonsense. It allows the analyist to find
hidden order in systems that appeared to be completely random; it makes possible
the engineering analysis of systems that could not be effectively analyzed only a few
years ago.

Classical mechanics, born with Newton, has proven to be an invaluable tool to
the scientist and engineer. This tool has worked so well that engineers and scientists
have long viewed nature as an orderly, clock-like machine of great predictability. We
usually work with deterministic systems, that is systems with known, non-random
initial conditions, parameters, and equations of motion, and we typically assume that
our calculated solutions are unique and determinable. Nevertheless it is a mistake
to assume that the response of a deterministic system is always predictable – that
it can be calculated for all time by merely integrating the appropriate equations of
motion. Reality shows that the response of most deterministic systems is not always,
in a sense, deterministic but can be chaotic over some range of initial conditions and
system parameters.

If one had a large enough computer and enough knowledge, many believe, the
future of every particle in the world could be determined by integrating enough
equations. This stretch of the deterministic view is at odds with chaos. Chaotic
motion for a conservative system is stochastic or random motion (with a hidden
structure) that makes anything other than very short-term predictability of an
object's state impossible. Whether for a conservative or dissipative system, chaos is an
exponential divergence of any two initially close trajectories, and hence is an extreme

1

sensitivity to very small changes in initial conditions. Because of these characteristics, it is impossible for any computer to predict the exact behavior of the simplest chaotic system for more than short integration times.

Most scientists and engineers have traditionally been trained to avoid nonlinear analyses. We have been taught over and over to linearize a system's equations, to avoid the small but nasty terms that make analysis so difficult – the same terms that may lead to chaotic behavior for most systems over some range of initial conditions and system parameters. Usually we are rewarded for making these simplifying assumptions by producing analyses that work well in the physical world. The failure of the Tacoma-Narrows bridge, for example, was the exception, not the rule. Nevertheless, ignoring the nonlinear terms in some problems can be dangerous. The price of this ignorance may range from the inclusion of small, ignorable errors into the solution to non-optimal design, or even system catastrophic behavior.

Consider one of the simplest and most commonly applied dynamical system example used in college dynamics courses, the dynamics of the classical frictionless pendulum. Almost every engineer and scientist has studied this problem in elementary physics or elementary engineering mechanics courses. Invariably, linearization is preached; few students have ever seen its exact nonlinear solution and would recognize the Jacobi (elliptic) integrals in the solution. Although chaotic motion does not appear in this simple problem, the difference between the exact and the linearized solutions of the pendulum's period can be greater than fifteen percent. Moreover, merely placing the support of the pendulum in a steady circular motion in the vertical plane creates a chaotic system [1]. This example is not exceptional. Most dynamical system mathematical models with nonlinear terms will exhibit chaotic behavior for some range of values of the systems parameters and for some initial conditions. All we need is a minimum of a two degree-of-freedom, autonomous nonlinear system, or its dynamic equivalent, a one degree-of-freedom, nonautonomous nonlinear system. Obviously most engineering system mathematical models satisfy this requirement.

While the application of modern nonlinear analysis to aeromechanics and astrodynamics is still in its infancy, some particularly innovative efforts have laid the foundation for decades of research. Wisdom [2] explained the presence of the 3/1 Kirkwood gap in the distribution of the asteroid belt between Mars and Jupiter by nonlinear analysis and very clever long-term integration techniques, a problem that had baffled scientists for over one hundred years. He showed that chaotic (and many quasiperiodic) astroid trajectories near the 3/1 Kirkwood gap had, over millions of years, occasional spikes in eccentricity that caused either collisions with Mars or close enough passages for the astroid to be removed from the gap. In March of 1990 researchers at the University of Maryland published a paper suggesting that chaotic

2

systems may be controlled by using only small perturbations of a system parameter [3]. By the end of that year a research team at the Naval Surface Warfare Center controlled a real, physical, chaotic system for the first time [4,5,6]. Around this time an independent research team at the Naval Research Laboratory published their results on driving systems with chaotic signals and demonstrated synchronization of two chaotic systems, another first in chaos theory [7,8]. The implications of these feats are awesome. Some chaotic, or apparently random, motions may now be controlled. Furthermore, the nonlinear regimes that we have been trained to avoid in many systems may now be explored. As an example, Grummen Corporation is currently working on applying the results of this research on control of chaotic systems to build adaptive wings from smart materials that use twist instead of flaps and ailerons [9]. This, instead of applying aeroelastic theory to predict and avoid the flight regimes that could produce structural catastrophic failure.

Almost every Air Force scientist and engineer currently working in research and development would benefit from a fundamental knowledge of chaos theory. Unfortunately, few are familiar with this field although the Air Force Office of Scientific Research (AFOSR) is funding research in related areas. In past AFOSR sponsored research, chaotic motion has been shown to exist in wind tunnel tested aerosurfaces with structural nonlinearities [10]. AFOSR also funded compressor stall research utilizing bifurcation and other nonlinear dynamic analysis tools at the University of Maryland, and buffeting suppression at the University of Colorado. Active control of complex nonlinear dynamic systems are the goals of many of these efforts, including control of deformable lifting surfaces and flutter suppression. While this is a grand step in the right direction, emphasis should also be placed on research of the fundamentals of chaos and nonlinear analysis. In a 1991 article, Langreth [6] wrote in *Science* that

> ...it's no coincidence that most of the pioneering work is done in Navy Laboratories: Since 1983 the Office of Naval Research has been the only government agency with a funding program specifically for chaos studies.

As is the case for many research organizations in the 1990s, the USAF is past due to make an attitude change, and to invest in learning about a critically important field which affects all aspects of aerospace research and development and is vital towards the systems engineering approach.

## 1.2 Pitch Attitude Motion for Gravity-Gradient Satellites

### 1.2.1 Past Work

Large attitude perturbations due to gravity-gradient torques on artificial satellites are well known phenomena. Today, these and other perturbations must be carefully considered and accounted for in the design process. Pitch angle perturbations are often of special interest to the designer because of the central-body pointing requirements of many Earth orbiting satellites. They also must be considered when examining space station orientations and experiment requirements for the Space Shuttle and other trans-atmospheric spacecraft. For these reasons, the planar pitch-attitude dynamics of a gravity-gradient satellite has received a great deal of attention.

A number of studies have utilized nonlinear analysis tools such as Poincaré maps to study the planar pitch dynamics for an eccentric orbit [11,12,13,14,15,16]. Zlatoustov et al. [11] (also in Beletskii [12]) studied families of periodic solutions and found that stable periodic solutions exist for every value of eccentricity. Modi and Brereton [13] applied the method of harmonic balance to obtain families of periodic solutions and found that at the maximum eccentricity for stable motion, the solution must be periodic. In more recent work, modern analytical and numerical nonlinear analysis methods have been applied to the uncontrolled gravity-gradient pitch motion problem. The emphasis of much of this research has been on the application of Melnikov's analytical method [17] to examine criteria for the onset of chaos near the separatrices of nearly-integrable systems. Koch and Bruhn [18] utilized the Melnikov method to analyze this problem, taking into account additional terms due to a non-spherical gravitational field and magnetic dipole-dipole interaction between the satellite and the central body. Seisl and Steindl [19] also applied the Melnikov method, supplementing the basic problem with an aerodynamic drag term. Both of these analyses are valid for only small values of eccentricity due to assumptions required by the Melnikov method.

Tong and Rimrott [20] also examined the basic problem but with more emphasis upon numerical investigation, presenting two sequences of Poincaré maps of varying values of eccentricity while holding the inertia ratio constant. Using a combination of branching theory, Floquet theory, high-precision numerical integration, and other methods, Gulyaev et al. [21] found that at least one of the routes to chaos for this problem occurs through period-doubling bifurcations. Tong and Rimrott [22] also found period doubling bifurcations leading to chaos for the basic problem

4

supplemented with a damping term.

There is an increasing amount of interest in the basic problem supplemented with controls. Cole and Calico [23] examined the nonlinear dynamics of a spinning symmetric satellite in an elliptic orbit subject to control torques about two of the spacecraft axes. Gray and Stabb [24] applied Melnikov's method to produce analytical criteria for the onset of chaos in the controlled pitch motion for a gravity-gradient satellite.

## 1.2.2  Objectives of This Work

The main objective of this research is to examine the nonlinear dynamics of the pitch equation of motion for a gravity-gradient satellite in an elliptical orbit about a central body. Another goal is to provide an informal introduction to some of the modern nonlinear analysis techniques with an example application. To accomplish these objectives, periodic, quasiperiodic, and chaotic motion are discussed through presentations of phase diagrams, Poincaré maps, bifurcation plots, spectral density plots, Lyapunov exponents, and chaos diagrams. The closed-form solutions to the circular orbit case are also examined for comparison purposes. It is shown that the pitch angle may exhibit either chaotic or regular motion, depending upon the values of the system parameters and initial states.

This report extends the numerical investigation of the nonlinear dynamics of the planar pitching motion for a gravity-gradient satellite in an elliptical orbit about a central body with an inverse-square gravitational field. Various nonlinear analysis tools are applied to further the numerical exploration of the pitch motion for arbitrary values of eccentricity and satellite inertia ratio. Emphasis is placed on numerical prediction of transition from regular to chaotic motion through the use of Lyapunov exponents. The relationships of the system parameters to the nonlinearity of the system are explored with chaos diagrams, which incorporate the results of the Lyapunov exponent calculations into a valuable, innovative tool for predicting the onset of chaotic motion. Although chaos diagrams have appeared in a few previous works, they tend to be coarsely gridded (see [1] for example) making definition of the boundary between chaotic and regular motion difficult to discern. In this report finely gridded chaos diagrams are constructed in color, allowing the boundary to be easily seen and revealing its fractal properties.

The dynamics of a real satellite are not as simple as the models employed in this study. An actual spacecraft is subjected to a variety of internal and external torques that may contribute linear and nonlinear damping forces. Thus, another objective of

this work is to provide a precursory examination of the pitch dynamics of the basic system with a few modifications – the effect of an oblate central body for an eccentric, polar orbit, and the effect of the addition of two separate damping terms. One finds that inclusion of the oblateness effects can significantly alter the pitch dynamics of the gravity-gradient satellite. Eccentricity (assumed constant in previous nonlinear analyses of planar gravity-gradient pitch dynamics) is shown to vary almost 15% in one example. With this more elaborate model, chaos is detected in areas of the phase space where previous investigations found only regular motion.

The first damping term investigated is simple linear damping, previously briefly studied by Tong and Rimrott [22]. The work presented here builds upon that foundation. The second damping term investigated here is nonlinear damping proportional to the square of the velocity. To the author's knowledge, the nonlinear damping case has not been previously examined except for a study presenting the derivation of the Melnikov function by Seisl and Steindl [19]. The validity of Melnikov's method in the prediction of the border between chaos and regular motion is also investigated for the two damping cases. This method has been applied a number of times in the past but with a minimum of emphasis upon its accuracy. Many references present very impressive analytical derivations of the Melnikov chaos criteria but make little or, in a few cases, no mention of the accuracy of the prediction. In fact, Tortorelli and Vakakis [25] investigated the accuracy of experimental and analytical chaos prediction techniques for a forced Duffing oscillator and found the Melnikov criteria to have approximately an order of magnitude error. The Melnikov chaos criteria for the nonlinear damping case was previously derived (as noted above) but the criteria for the linear damping case does not appear in the literature.

Specifically, the unique (to the best of the author's knowledge) and most important contributions of this work are:

- Detailed examination using modern numerical nonlinear analysis tools of the planar pitch dynamics of a gravity-gradient satellite in an eccentric orbit about a spherical central body.

- Numerical examination using nonlinear analysis tools of the oblate central body case and of the case with a nonlinear damping term proportional to the square of the velocity.

- High resolution chaos diagrams and use of color in them to portray the relative magnitudes of the Lyapunov exponents.

- Numerical discovery of a fractal border between regular and chaotic motion in

6

parameter space, and examination of the structure of the parameter space with respect to the location of periodic solutions.

- One of the first analyses of the pitching dynamics of a gravity-gradient satellite not to be limited to either small values of eccentricity or to fixed inertia ratios, hence demonstrating that chaos is a function of both of these parameters instead of only eccentricity.

- Important reminder that meeting the Melnikov chaos criteria does not necessarily mean that the motion is truly chaotic, but instead may indicate transient chaos and regular steady state motion.

In Section 2 the equation of motion for the planar pitching motion of a satellite in an elliptical orbit about a spherical central body is presented with the underlying assumptions involved in its derivation. Analytical and numerical nonlinear analysis tools used in this study are briefly described in Section 3. The pitching motion for a gravity-gradient satellite in a circular orbit is investigated in Section 4 and Section 5 presents the examination of the nonlinear dynamics of the elliptical orbit case. The particular case of an eccentric polar orbit about an oblate central body is briefly examined in Section 6 and the results are compared to those obtained from the spherical central body model of Section 5. [1] Section 7 presents an initial look at the eccentric orbit case with the separate damping terms and examines the validity of the Melnikov chaos prediction criteria. Conclusions and recommendations for further study are given in Section 8. More detailed derivations of some of the equations used in this research are presented in the Appendix.

---

[1]Interim reports of this work appear in the form of three papers by Karasopoulos and Richardson [26,27,28]. The first [26] contains an overview of the content of Section 4 of this report as well as a portion of Section 5. The second paper [27] contains much of the remainder of Section 5. Documentation of the oblate central body case of Section 6 can be found in [28].

# 2 Equations of Motion

The satellite is assumed to be a rigid body influenced only by torques from an inverse-square gravitational field. Satellite energy dissipation and other torques, such as aerodynamic, magnetic, thermal bending, or solar radiation pressure, are ignored. Other assumptions used in the derivation of the equation of motion are:

- The satellite's major axis is normal to the orbit plane.

- Satellite roll and yaw angles and their rates are zero. For zero pitch angle, the minor and intermediate axes point in the radial and transverse directions, respectively.

- The satellite's largest dimension is very small compared to the orbit radius.

- The satellite's mass is negligible with respect to the mass of the central body.

The resulting pitch equation of motion for a gravity-gradient satellite in an elliptical orbit about a central body is[1]

$$\frac{d^2\psi}{dt^2} + \frac{d^2f}{dt^2} + \frac{3\mu}{2r^3}K\sin 2\psi = 0. \tag{2.1}$$

The center of mass of the satellite follows a Keplerian orbit and thus obeys the relations,

$$\frac{df}{dt} = \frac{h}{r^2}, \tag{2.2}$$

$$\frac{dr}{dt} = \frac{\mu}{h}e\sin f, \tag{2.3}$$

$$r = \frac{h^2}{\mu(1 + e\cos f)}, \tag{2.4}$$

and

$$\frac{d^2f}{dt^2} = -\frac{2\mu e\sin f}{r^3}, \tag{2.5}$$

where $e$ is the orbital eccentricity, $f$ is the true anomaly, $r$ is the orbit radius, $\mu$ is the Earth's gravitational constant, and $\psi$ is the pitch angle measured with respect

---

[1]Although a detailed derivation of this equation is not explicitly given in this report, it can be easily derived from the more complicated equations for a satellite in an eccentric polar orbit about an oblate central body presented in Section 6 and in the Appendix.
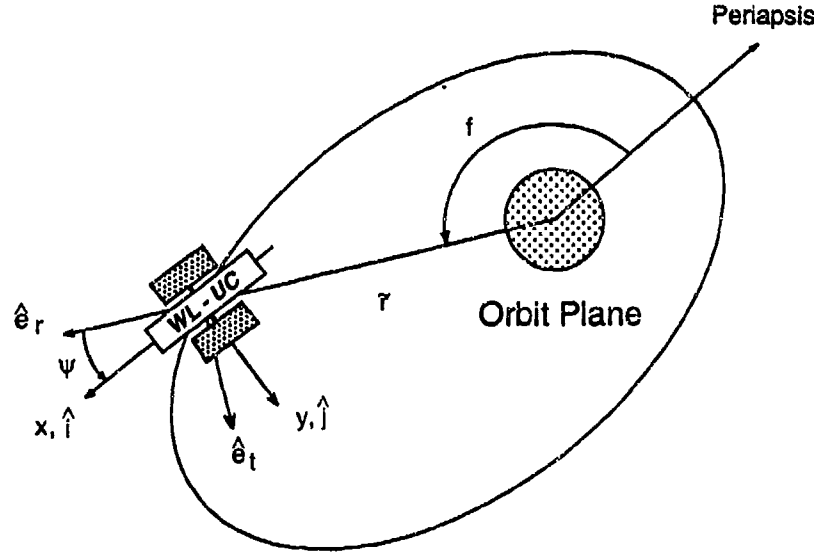
Figure 2.1: Orbit and Attitude Geometry.

to the radial direction, as seen in Figure 2.1. The satellite inertia ratio, $K$, is a non-dimensional function of the principal moments of inertia of the satellite, defined as

$$K = \frac{I_y - I_x}{I_x} = \frac{I_{roll} - I_{yaw}}{I_{pitch}}. \tag{2.6}$$

It is assumed $I_z > I_y > I_x$, which are sufficient conditions for stable three-axis rotations of a satellite in circular orbit about a spherical central body. For pitch oscillations about the radial direction, the inertia ratio has the range $0.0 \leq K \leq 1.0$. The upper limit corresponds to the inertia properties of a dumbbell satellite and the lower limit to an axially symmetric satellite.[2]

Substitution of the Equations 2.4 and 2.5 into Equation 2.1 gives the equation of motion with the true anomaly, $f$, as the independent variable in place of time,

$$\frac{d^2\psi}{df^2}(1 + e \cos f) - 2e\left(\frac{d\psi}{df} + 1\right)\sin f + \frac{3}{2}K\sin 2\psi = 0. \tag{2.7}$$

---

[2] Negative values of the inertia ratio are physically possible but correspond to defining the pitch angle from the transverse direction instead of the local vertical.

9

The dynamics of the pitching motion as described by this equation forms the basis of this report. Modifications to this equation, such as adding central body oblateness effects or damping terms, are discussed in later sections.

# 3  Nonlinear Analysis Tools

A variety of analysis tools and techniques exist that may be utilized to study nonlinear systems. Brief introductions to these methods are presented in the following paragraphs, and some examples are also incorporated. Specifically, the construction and application of phase diagrams, Poincaré maps, bifurcation diagrams, Fast Fourier Transforms (FFTs), Lyapunov exponents, and chaos diagrams are included. Numerical error and its propagation in chaotic systems is also discussed.

## 3.1  Phase Diagrams

The equation of motion for the pitching of a gravity-gradient satellite in an elliptical orbit about a central body, discussed in the previous section, has one degree of freedom and is non-autonomous. Written with true anomaly as the independent variable, it has a three-dimensional solution space, $(\psi, \psi', f)$, and a two-dimensional phase space, $(\psi, \psi')$. The solution to this equation of motion is generally found by numerical integration and its trajectory is represented by a three dimensional curve lying in the solution space. A phase diagram, or phase plane diagram, is simply formed by collecting the phase space solutions at each value of true anomaly during the integration and plotting them on one plane (Figure 3.1).

Periodic oscillations appear as closed curves on a phase plane plot. Subharmonic periodic oscillations appear as closed curves that cross themselves; an example is presented in Figure 3.2. This phase diagram represents a period 7 solution, that is, one pitch oscillation occurs exactly every seven orbits about the central body. Close examination of this plot reveals seven cycles about the $\psi = 0$ line. Quasiperiodic trajectories, however, appear as unclosed curves on a phase diagram. Figure 3.3 depicts an example phase diagram for 30 orbits of a quasiperiodic trajectory. Note the trajectory falls within a heart-like shape that would eventually be completely filled if enough orbits were integrated.

Chaotic trajectories will also eventually completely fill the phase space if the equation of motion was integrated through enough orbits. The phase plane diagram for a chaotic trajectory will differ from those depicting regular motion in that the

11

Constructing a Phase Plane Diagram
from the Solution Space ($\psi$, $\psi'$, f )

$S_T = \Sigma S_n$

$\Delta f \to 0$

Phase Plane Diagram
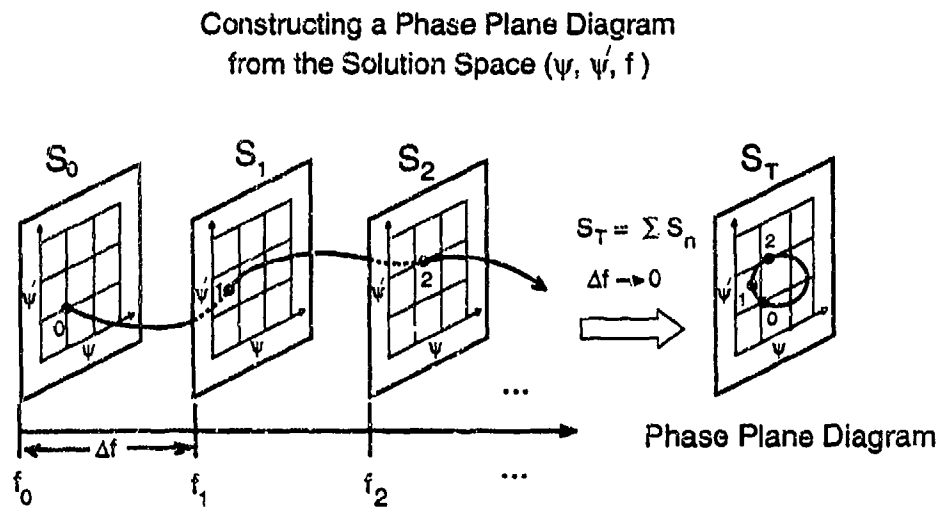
Figure 3.1: Constructing a Phase Plane Diagram from the Solution Space $(\psi, \psi', f)$.



Example Phase Diagram for a Period 7/1 Trajectory*
K=1.0, e=0.313, (0.,0.)

*1 Oscillation in 7 Orbits

Pitch Angle Rate, $\psi'$, (rad/rad)

Pitch Angle, $\psi/\pi$, (rad/rad)
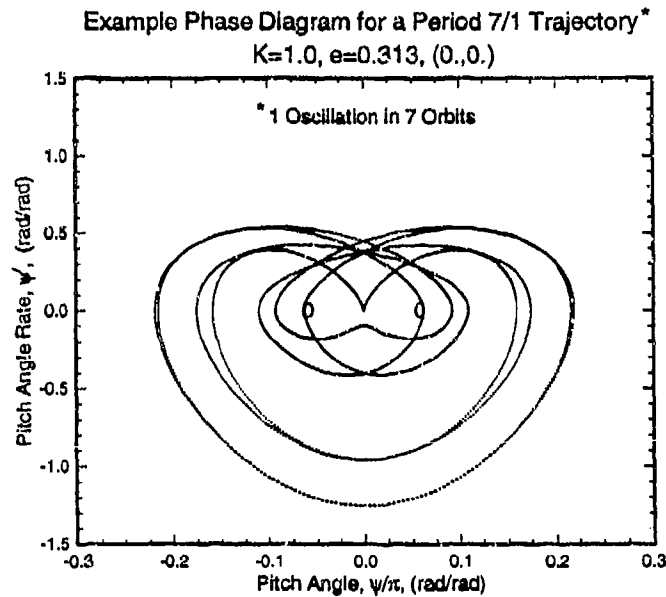
Figure 3.2: Example Phase Plane Diagram for a Period 7 Trajectory for $K = 1.0$, $e = .313$, and $(0., 0.)$.

12

Example Phase Diagram for a Quasiperiodic Trajectory
K=1.0, e=0.311, (0.,0.)
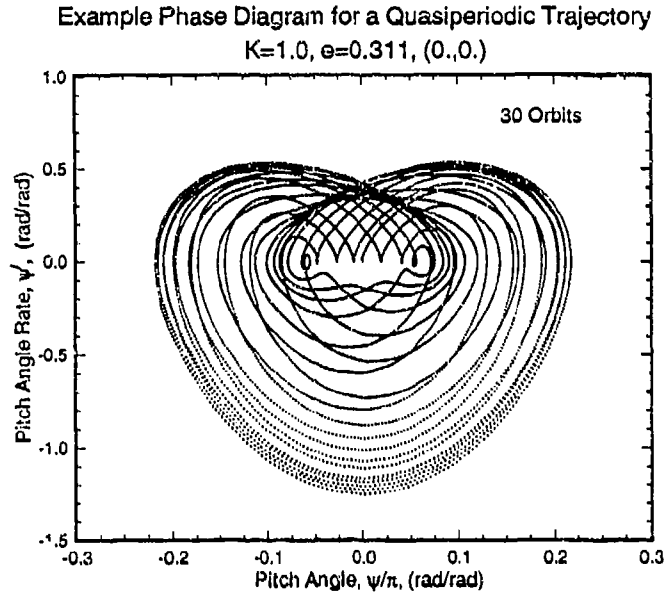


Figure 3.3: Example Phase Plane Diagram for a Quasiperiodic Trajectory for $K = 1.0$, $e = .311$, and $(0., 0.)$.

trajectory roams across large portions of the phase space. In the example phase diagram for a chaotic trajectory of Figure 3.4, the trajectory randomly leaves and enters the central phase space area in which the quasiperiodic trajectory was confined. This central area represents pitch libration and the outer portion of the phase space depicts pitch tumbling. This example plot shows the case where chaotic pitching motion randomly alternates between libration and tumbling. Neither chaotic (aperiodic) nor quasiperiodic trajectories will ever repeat or close in the phase plane and thus may sometimes be difficult to differentiate. Poincaré maps, a particular mapping or sub-space of a phase diagram, are discussed in the next section and are often much more useful.

Numerical calculations made extensive use of an optimized coefficients version of a Runge-Kutta integration algorithm. This routine has excellent stability characteristics and a local truncation error of the integration step-size raised to the 6th power. Typical integration step-sizes for the true anomaly ranged from $2\pi/250$ to $2\pi/150$.

Example Phase Diagram for a Chaotic Trajectory
K=1.0, e=0.33, (0.,0.)
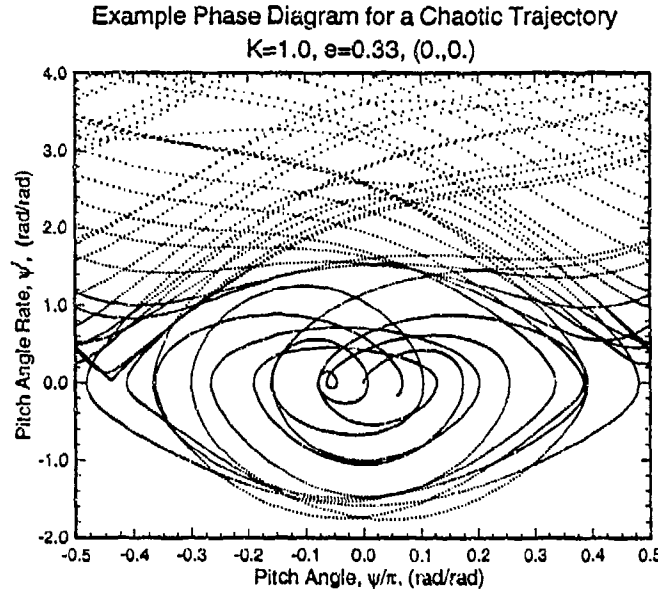


Figure 3.4: Example Phase Plane Diagram for a Chaotic Trajectory for $K = 1.0$, $e = .33$, and $(0., 0.)$.

## 3.2 Poincaré Maps

The purpose of a Poincaré map, or surface of section, is to facilitate the study of a system's phase space by eliminating a system variable. A Poincaré map is made by plotting a discrete collection of points created from integrating the equation of motion and periodically sampling the generated values of states at a particular point in the trajectory. Thus, a Poincaré plot provides a sort of "stroboscopic" view of the phase space. In this study the continuous three-space of $(\psi, \psi', f)$[1] is mapped into the discrete two-space of $(\psi_n, \psi_n')$ by collecting and plotting $N$ values of

$$\psi_n \equiv \psi(f_n) \quad (\text{modulo } \pi), \quad \text{and} \quad \psi_n' \equiv \psi'(f_n), \tag{3.1}$$

where

$$f_n = 2n\pi + f_0, \quad n = 0, 1, 2, \dots N. \tag{3.2}$$

The concept of constructing a Poincaré map from the system's solution space is demonstrated in Figure 3.5. Instead of combining the pitch angle and pitch rate values at every value of true anomaly as for a phase diagram, to create a Poincaré map these values are collected at only one particular value of true anomaly for each orbit, $f_*$. In

---

[1]The prime ( ′ ) denotes differentiation with respect to true anomaly, $f$.

14

Constructing a Poincaré Map from Solution Space ( $\psi$, $\psi'$, f )

$f_* \rightarrow f_* + 2\pi n$   n=0,1,2,...

Multiple Passes Through $S_*$
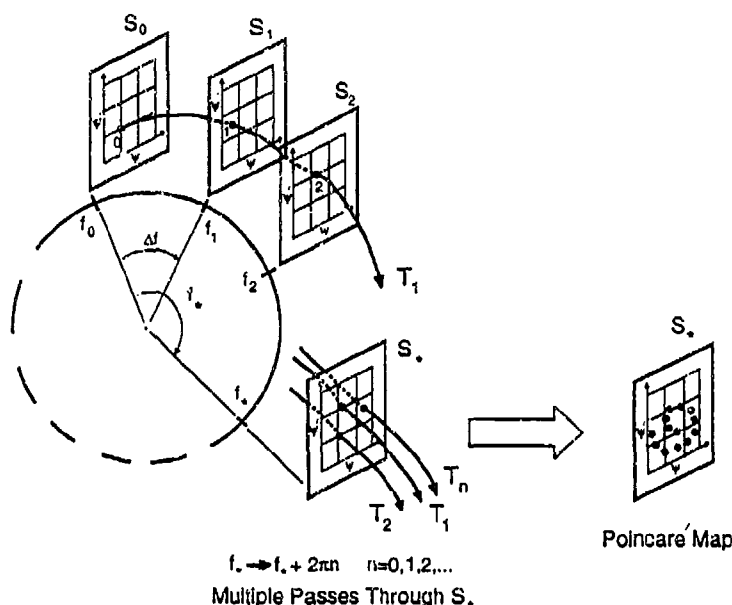
Figure 3.5: Constructing a Poincaré Map from the Solution Space $(\psi, \psi', f)$.

this problem, periapsis was chosen arbitrarily to be $f_*$; thus, solutions to the equations of motion are sampled once each orbit as the satellite passed through periapsis. At least 20 orbits are integrated before data is plotted to allow the trajectories to settle.

Both regular and chaotic motion may be observed in the Poincaré maps. Periodic motion is characterized as one or more fixed points. Quasiperiodic motion produces a closed contour on the surface of section when a sufficient number of trajectory samples are mapped. Chaotic motion appears on a Poincaré map as a non-ordered scattering of points which, if $N$ were large enough, would completely fill an area of the surface of section.

An example Poincaré map is presented in Figure 3.6.[2] This map displays a collection of data from seven trajectories, created from integrating the equations of motion with seven different initial conditions, to form a combination Poincaré map. Pitch angle is given in this example plot for values ranging from $-\frac{\pi}{2}$ to $\frac{\pi}{2}$ since its solution is $\pi$ periodic for this system. Even with this periodicity, a number of Poincaré maps are presented in later sections for pitch angles ranging from $-\pi$ to $\pi$ for increased clarity of the mapping characteristics. Chaotic motion is clearly visible in this example plot as well as an assortment of quasiperiodic and periodic solutions.

---

[2]Note the "n" subscript has been dropped from $\psi$ and $\psi'$ in this particular Poincaré map and in all of the others presented in the following sections.

15
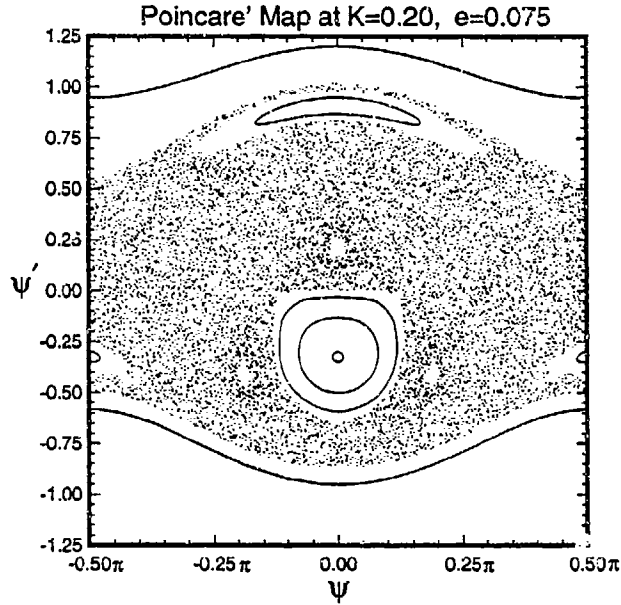
Figure 3.6: Example Poincaré Map ($K = 0.2$ and $e = .075$).

## 3.3  Bifurcation Plots

An often applied technique for examining the effects of parameter variations on a dynamical system is the bifurcation diagram. A bifurcation, or branching, can be thought of as a sudden, qualitative change in the motion or state of a system as a system parameter is varied. The transition from a stationary state to regular motion and the transition from regular to chaotic motion as a system parameter is varied are examples of bifurcations. Bifurcation diagrams can often show at a quick glance what type of motion occurs for ranges of a system parameter for specific initial conditions; they often aid in the determination of what transition form from regular to chaotic motion, or "route to chaos", is favored by the system.

To make a bifurcation diagram, a system state or some other measure of the motion is periodically sampled in the same manner as for the Poincaré map, and then plotted as a function of a system parameter. Numerous options exist for bifurcation diagrams for our problem since we have two elements in the system state space $(\psi, \psi')$, two system parameters, $e$ and $K$, and an infinite number of initial conditions.

An example bifurcation diagram of pitch angle versus eccentricity is given in Figure 3.7 for the initial state $(0., 0.)$ and an inertia ratio of $K = 1.0$. This plot, showing 50 passes through periapsis for each value of eccentricity, displays all three

16

## Example Bifurcation Diagram for K=1.0 and (0.,0.)
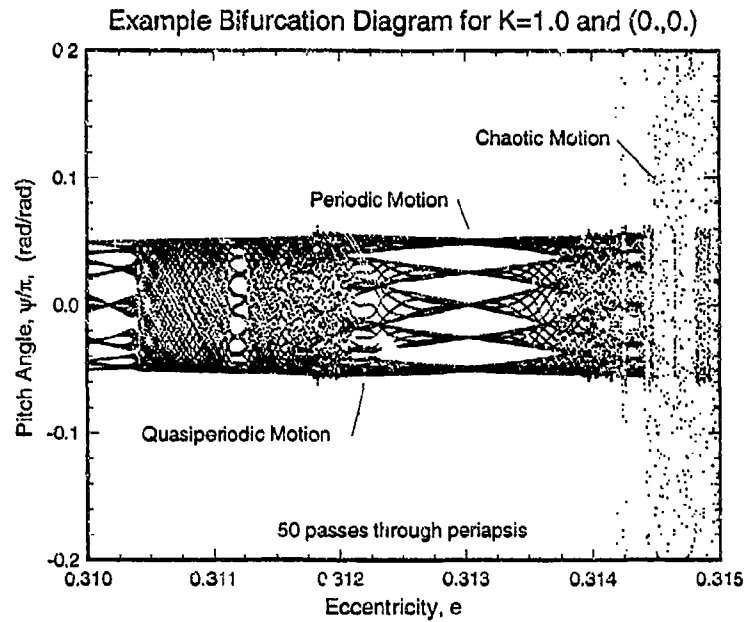


Figure 3.7: Example Bifurcation Diagram for $K = 1.0$ and $(0., 0.)$.

types of motion. Chaotic motion, represented by the stochastic regions of the diagram, occurs for a number of values of eccentricity, especially for large $e$. Periodic motion occurs at a few select eccentricities, such as near $e = .313$ and close to $e = .3102$. Quasiperiodic motion is represented by the darkened areas away from the chaotic regions.[3] Because of coupling, if $\psi$ is chaotic $\psi'$ will also be chaotic and bifurcation diagrams of only one of these system states is necessary to deduce the system's motion. It should be emphasized that although the example bifurcation plot above depicts 50 periapsis passes for each value of eccentricity, we are not guaranteed that motion that appears to be quasiperiodic in this diagram will not become chaotic (or at least display its true chaotic nature) until the 51st or 52nd or even the 50,000th pass through periapsis.

## 3.4 Power Spectra: FFT Plots

One of the most used methods to detect chaotic motion and to investigate transition is to examine the power spectra of the trajectories. The Fast Fourier Transform (FFT) technique was applied in this study to create these power spectra. For many systems,

---

[3]Some caution must be taken when attempting to distinguish between quasiperiodic and chaotic motion. Often a Poincaré map or other tool may be necessary to make this distinction.

17

especially those with only a few degrees of freedom, chaos is indicated when spectral analysis results in a broad spectrum of frequencies. When experiencing regular motion, such systems typically have only one or perhaps a few dominant frequencies present in the power spectra, $\omega_0, \omega_1, \ldots$ Often a sign of impending transition is the appearance of subharmonics $\omega_0/n$, $n = 1, 2, 3, \ldots$, in the spectra. In particular, frequency halving spikes may occur at $m\omega_0/2$, $m = 1, 3, 5, \ldots$, corresponding to the much celebrated period doubling route to chaos. Periodic motion will typically have the simplest spectra and FFT plots of quasiperiodic motion will have an additional fundamental frequency, incommensurate with the first. Harmonics (or "superharmonics") often occur for this latter type of motion, producing frequencies $n\omega_i$, $n = 1, 2, 3, \ldots$ If more than one dominant frequency exists then there may also be present linear combinations of the two or more fundamental frequencies.

Three example FFT plots are presented in Figures 3.8 - 3.10. Figure 3.8 depicts the pitch angle power spectra for a period one (one pitch oscillation per orbit) trajectory. One fundamental frequency appears as a peak at a scaled frequency of 1.0, and the other peaks represent its harmonics. Figure 3.9 presents a pitch angle FFT plot for a quasiperiodic trajectory. For this case, two fundamental frequencies are present, one at a scaled frequency of about 1.0 and the other at about 1.62. The amplitude spikes at 2.0, 3.0, and 4.0 are superharmonics of the first fundamental frequency, and the spikes near 2.62 and 3.62 are superharmonics of the second fundamental frequency. The very small, lower frequency spikes are likely linear combinations of the fundamentals or are subharmonics. Figure 3.10 presents an example FFT plot for chaotic motion, clearly demonstrating the characteristic broad spectrum of frequencies.

## 3.5 Lyapunov Exponents and Chaos Diagrams

The Lyapunov exponents for a particular trajectory are a measure of the mean exponential rate of divergence of initially neighboring trajectories. A positive Lyapunov exponent indicates the trajectory is chaotic, and hence the predictability of its future states quickly vanishes with time. The time (or true anomaly) scale in which this predictability vanishes is a function of the magnitude of the largest Lyapunov exponent, $\sigma_1$, called the "first" Lyapunov exponent. Because Equation (2.1) represents a perturbed one degree-of-freedom, nonautonomous Hamiltonian system, two Lyapunov exponents of equal magnitude but opposite sign exist for each

18

Example Fast Fourier Transform of Pitch Angle for
Periodic (1/1) Motion: K=1.0, e=.3, (0.,0.153420)

Orbits 100-110
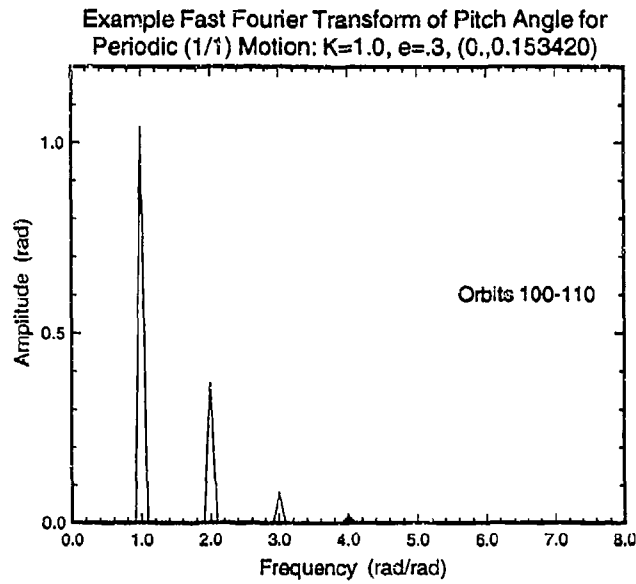
Figure 3.8: Example Fast Fourier Transform of Pitch Angle for Periodic (1/1) Motion: $K = 1.0$, e=.3, $(0., 0.153420)$.

Example Fast Fourier Transform of Pitch Angle for
Quasiperiodic Motion: K=1.0, e=.3, (0.,0.3)

Orbits 100-110
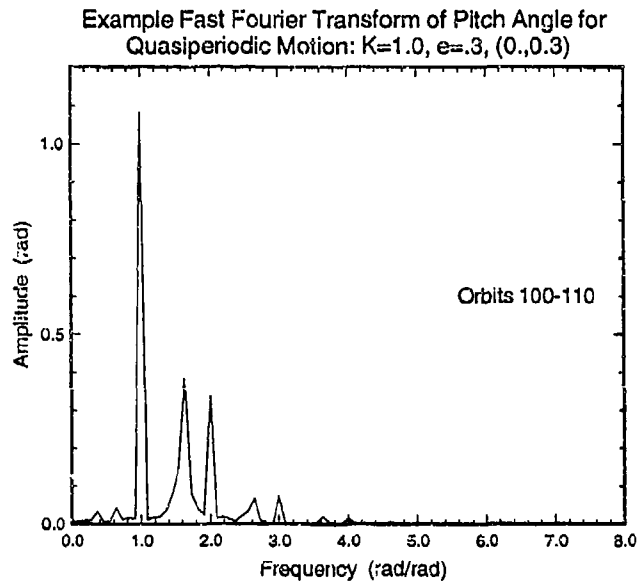
Figure 3.9: Example Fast Fourier Transform of Pitch Angle for Quasiperiodic Motion: $K = 1.0$, e=.3, $(0., 0.3)$.

19

Example Fast Fourier Transform of Pitch Angle for
Chaotic Motion: K=1.0, e=.33, (0.,0.)
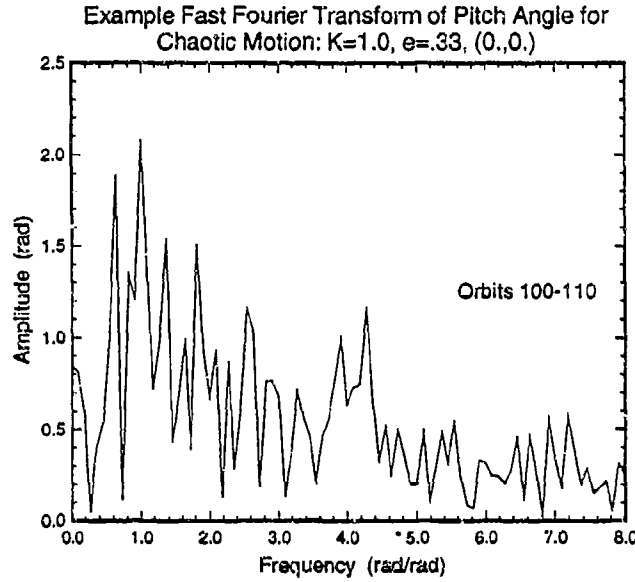
Figure 3.10: Example Fast Fourier Transform of Pitch Angle for Chaotic Motion: $K = 1.0$, e=.33, $(0., 0.)$.

trajectory.[4] These exponents are zero for regular motion, and non-zero for chaotic motion. For the latter case, the greater the value of $\sigma_1$, the greater the trajectory's sensitivity to initial conditions, and the more "chaotic" the trajectory. Because of the absence of strange attractors for a perturbed Hamiltonian system, a chaotic trajectory tends to fill the phase space uniformly. As a result, Lyapunov exponents for such systems tend toward a constant value as the number of orbits integrated, $N$, tends to infinity, regardless of the initial value of the state vector.

In the calculation of Lyapunov exponents one examines the change in dimension of a small circle of initial conditions of radius $\delta_0$ in the phase space over N orbits, or iterations of the Poincaré map. Through stretching and contraction of the phase space, the circle is transformed after a small $\Delta f$ into an approximate ellipse having semimajor and semiminor axes, $\delta_1$ and $\delta_2$, where

$$\delta_1(\Delta f) = \delta_0 2^{\sigma_1 \Delta f} \quad \text{and} \quad \delta_2(\Delta f) = \delta_0 2^{\sigma_2 \Delta f}. \tag{3.3}$$

---

[4]In other words, phase space is conserved for mappings of Hamiltonian systems. This is not the case for dissipative systems where the phase area shrinks as the number of mappings increases, and the magnitude of the first Lyapunov exponent (which measures the stretching in one direction) is less than that of the second Lyapunov exponent (which measures the contraction in another direction.)

20

The first Lyapunov exponent for a discrete system is

$$\sigma_1 = \lim_{N \to \infty} \frac{1}{f_N - f_0} \sum_{p=1}^{N} \log_2 \frac{\delta(f_p)}{\delta(f_{p-1})}. \tag{3.4}$$

A number of techniques for the calculation of Lyapunov exponents appear in the literature. In this study, Lyapunov exponents were computed using a modified version of a code given in Appendix A of Wolf, et al. [29].

Chaos diagrams plot the magnitude of the first Lyapunov exponent as a function of the system parameters, and thus indicate the occurrence and relative magnitude of chaotic motion for specified initial states. In this study chaos diagrams were numerically calculated for a full range of eccentricity and inertia ratio values, $0 \le e \le 1$ and $0 \le K \le 1$. Lyapunov exponents were calculated in 400x500 and 320x400 point grids. A color scale was assigned to the positive exponents to distinguish between relative magnitudes of the chaotic motion, a relative measurement of how quickly initially neighboring trajectories exponentially diverge. Example chaos diagrams and a discussion of their applications will be presented in a later section.

Theoretically, a sufficient criteria for determining the existence of chaotic motion for a particular set of initial conditions and system parameters is to calculate the first Lyapunov exponent using Equation (3.4) over an infinite number of orbits and check if $\sigma_1$ is greater than zero. In reality, one is restricted to $N \ll \infty$ and one finds that the value of $\sigma_1$ is generally dependent upon $N$. This dependence was mild and had little influence on results over the vast majority of the range of eccentricity and satellite inertia ratio investigated. Very close to transition from regular to chaotic motion, however, the plot of the Lyapunov exponents versus N often had low amplitude oscillations about zero. The Lyapunov exponents for regular motion very close to transition especially took a great number of orbits to settle down to zero. The results presented in Figure 3.11 illustrate these trends. The Lyapunov exponents calculated for $e = .01$, regular motion far from transition, hugged the $\sigma_1 = 0$ line after only a few orbits. In contrast, the $\sigma_1$ curve representing regular motion close to transition ($e = .075$) had relatively large oscillations about zero, even after the Lyapunov exponents had been calculated and averaged over a number of orbits. Likewise, the Lyapunov exponents for $e = .076$, chaotic motion close to transition, required more $N$ to settle down to its $\sigma_\infty$ value than for $e = .2$, chaotic motion far from transition.

Because of these trends, a small, positive constant, $c$, was used instead of zero as the threshold to determine if the motion was regular or chaotic in the chaos diagrams. The criteria for chaotic motion in the chaos diagrams therefore was $\sigma_1 > c$. Practical

21

**First Lyapunov Exponent vs N**
**for K=0.2 and (0.0,0.0)**
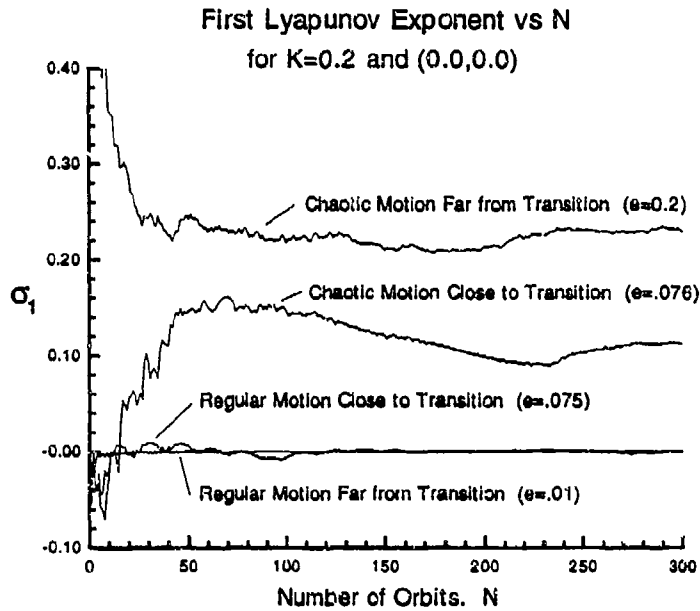
Figure 3.11: Example Lyapunov Exponents for $K = 0.2$ and Initial Conditions $(0.0, 0.0)$.

limitations on computer time restricted $N$ to a value of 50.[5] Coarsely gridded but more accurate (large $N$) computations showed that both the relative magnitudes of the exponents and the border between chaotic and regular motion were reasonably robust with $N=50$.

## 3.6 Error Considerations

Along with any presentation of Lyapunov exponent calculations should be some discussion of numerical error. It is important to understand the value of the results derived from the numerical integration of the equations of motion for a system that exhibits both regular and chaotic motion. One might ponder, for example, how integration results could be valid in the chaotic regime when considering that every integration algorithm has some inherent error and that two initially close trajectories diverge exponentially, causing the integration errors to enlarge exponentially. The answer to this question is fairly simple. Only certain analysis results obtained by numerical integration are valid. Numerical integration can accurately determine the

---

[5]Run-times of nearly a week were required to generate these diagrams using a Convex 3440 computer.

22

long term evolution of the pitch angle (in terms of predicting specific state variable values) for a gravity-gradient satellite *only* if the motion is regular. Long-term, steady-state values of the pitch angle can not be determined with any accuracy for a chaotic trajectory. However, certain useful information may still be gleaned from long-term integration of chaotic trajectories. Specifically, one can accurately calculate Lyapunov exponents and Poincaré maps. Usually state variable prediction accuracy is seriously degraded after only a small integration period for chaotic motion.

Error, $E$, grows approximately with the expression

$$E(t) \approx \epsilon \exp \sigma_1 t \tag{3.5}$$

or, in this case,

$$E(\Delta f) \approx \epsilon \exp \sigma_1 \Delta f \tag{3.6}$$

where $\sigma_1$ is the largest Lyapunov exponent and $\epsilon$ is the error for each integration step. For regular motion this error is linear since $\sigma_1 = 0$, but for chaotic motion $\sigma_1 > 0$ and the error grows exponentially. Rewriting this equation for $\Delta f$ gives

$$\Delta f \approx \frac{\ln E/\epsilon}{\sigma_1} \tag{3.7}$$

The error for each integration step, $\epsilon$, is composed of the sum of round-off and truncation errors. Round-off integration error depends on the number and kind of mathematical operations executed during each step. Hence, it is dependent on the precision of the computer [6] and independent of the integration step size. In contrast, truncation integration error, error incurred by using a finite approximation to an infinite series, is dependent only on the integration algorithm. The dominant error source in this study was the truncation error.

These local integration errors can cause the solution to "jump" from the true trajectory to a close lying (in phase space) false trajectory. Successive hops can quickly result in a trajectory that is very different than the true one for a highly nonlinear system. A conservative estimate of per-step integration error can be made by consideration of only the truncation error of the employed integration routine. The integration routine used in this study was an optimized coefficients version of a Runge-Kutta integration algorithm with a local truncation error of the integration step size raised to the 6th power. Typical integration step sizes applied in the numerical analyses were $\Delta \tau \approx \frac{2\pi}{150}$ giving a local truncation error of $\epsilon \approx 5.4 \times 10^{-9}$ radians.

As an example of error propagation in chaotic systems, note that the value of the first Lyapunov exponent for the case where $K=1.0$, $e=0.3$, and initial conditions

---

[6] The Silicon Graphics Iris computers used in this study carry 64 bits in double precision.

(0.0, $.0$) is approximately $\sigma = 0.34$ rad$^{-1}$. Using $\epsilon = 5.4 \times 10^{-9}$ radians, one finds that the error has increased by a factor of 1000 after less than $3\frac{1}{2}$ orbits. By the 10th and 20th orbits, integration error in pitch angle has swelled to 10.2, and $19.4 \times 10^9$ radians, respectively.

Even though it is impossible to accurately perform long-term numerical integration of a chaotic system, Parker et al. [30] points out that long-term integration for the calculation of Poincaré maps and Lyapunov exponents is legitimate. Chaotic attractors attract chaotic trajectories and for Hamiltonian systems, phase space is conserved over mappings – stretching in one direction is exactly countered by contraction in another. Thus, although divergence in one direction occurs, there is a convergence in another direction into the attractor. The exact location of the $n$th trajectory within a particular attractor will generally not be known with any accuracy. However, the fact that particular trajectory lies somewhere within the attractor is accurate, as will be the shape of the attractor in phase space as seen in a Poincaré map. Using numerical integration to calculate a chaotic system's Lyapunov exponents is also valid regardless of the integration error. This can be seen by noting the Lyapunov exponent is defined as an *average* exponent over all time, or in this particular case, over in infinite range of true anomaly. Thus, a Lyapunov exponent is averaged over every point on an attractor and is largely independent of the integration accuracy for a large enough $\Delta f$.

Studies [31,32,33] have shown that spurious solutions are possible due entirely to the discretization of a continuous differential equation, even for integration increments below the linearized stability limit of the integration method. In a similar study, Lorenz [34] showed "computational chaos" may occur in turns with quasiperiodic motion for a range of step sizes before the differencing scheme finally blows up. The message is obvious: care is required in the selection of the integration step size. As an example, the application of an integration stepsize of only $2\pi/50$ for $K$=1.0, $e$=0.3, and a large initial pitch rate (0.,2.50) created the "false" Poincaré map of Figure 3.12. This surface of section displays chaotic motion instead of the quasiperiodic tumbling of the "true" Poincaré map presented in Figure 3.13.

False Poincaré Plot at K=1.0, e=0.3, (0.,2.5), and Integration Stepsize $2\pi/50$
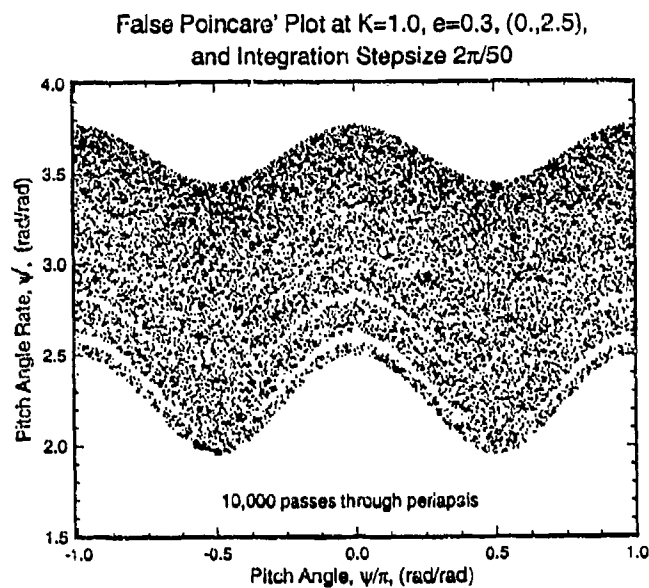
Figure 3.12: False Poincaré Plot at $K = 1.0$, $e = 0.3$, $(0., 2.5)$ and Integration Stepsize $2\pi/50$.



True Poincaré Plot at K=1.0, e=0.3, (0.,2.5), and Integration Stepsize $2\pi/150$
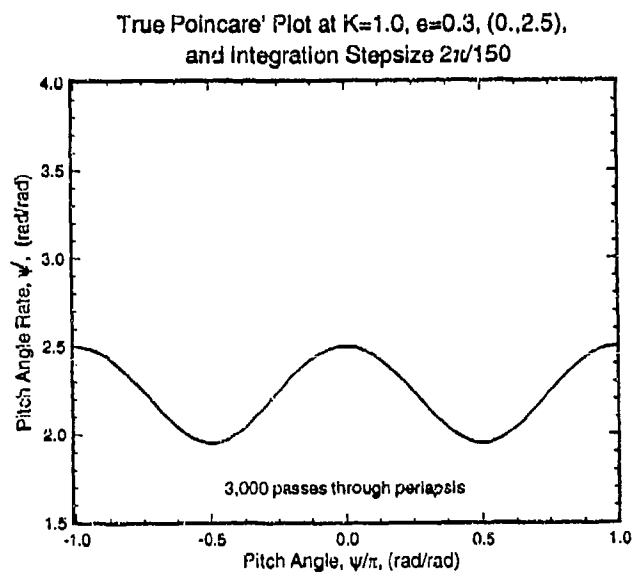
Figure 3.13: True Poincaré Plot at $K = 1.0$, $e = 0.3$, $(0., 2.5)$ and Integration Stepsize $2\pi/150$.

# 4 Circular Orbit Case

The circular orbit pitching problem is an important special case of the more general elliptical orbit problem, providing the form of the solutions in the limit as $e \rightarrow 0$. The solution to the circular orbit case can be found analytically and is well known ([13,35,36] for example) yet few solutions appear in the literature for both tumbling and libration, and especially for periodic motions. In addition, many of the earlier studies such as [35] were accomplished for a fixed inertia ratio of a dumbbell satellite, $K = 1.0$. To provide a more complete examination of this problem, and to gain insight to the application of the numerical nonlinear analysis techniques introduced in the preceding section, the circular motion pitching problem is analyzed in some detail for arbitrary values of inertia ratio in the sections below. The problem is first attacked analytically – solutions to the tumbling and libration types of motion are derived and presented. Some of these solutions are then numerically examined using nonlinear analysis methods, with emphasis upon their interpretation.

## 4.1 Analytical Analysis

The pitch equation of motion for a circular orbit, Equation 2.7, reduces to

$$\frac{d^2\psi}{df^2} + 3K \sin\psi \cos\psi = 0. \tag{4.1}$$

This equation has a form essentially similar to the equation for a simple, conservative pendulum; its phase plane has identical features and differs in that the pendulum's phase space repeats every $2\pi$ radians whereas the phase space for Equation 4.1 repeats every $\pi$ radians. Like the conservative pendulum, the phase surface for this case of the gravity-gradient satellite pitch problem is actually a cylinder. This cylinder can be represented with a plane (Figure 4.1) by recognizing that all points on the plane at an arbitrary $(\psi, \psi')$ correspond to $(\psi + k\pi, \psi')$ where $k = 0, \pm 1, \pm 2, \ldots$ Phase plane plots and Poincaré maps in this study therefore have the pitch angle range of at least $-\frac{\pi}{2} \leq \psi \leq +\frac{\pi}{2}$; for clarity, often a range of $-\pi \leq \psi \leq +\pi$ is presented.

The representative phase plane diagram for the circular orbit case presented in Figure 4.1 shows the two major types of motion that may occur for this problem – pitch angle libration (oscillation) and pitch angle tumbling (continuous rotation).

26
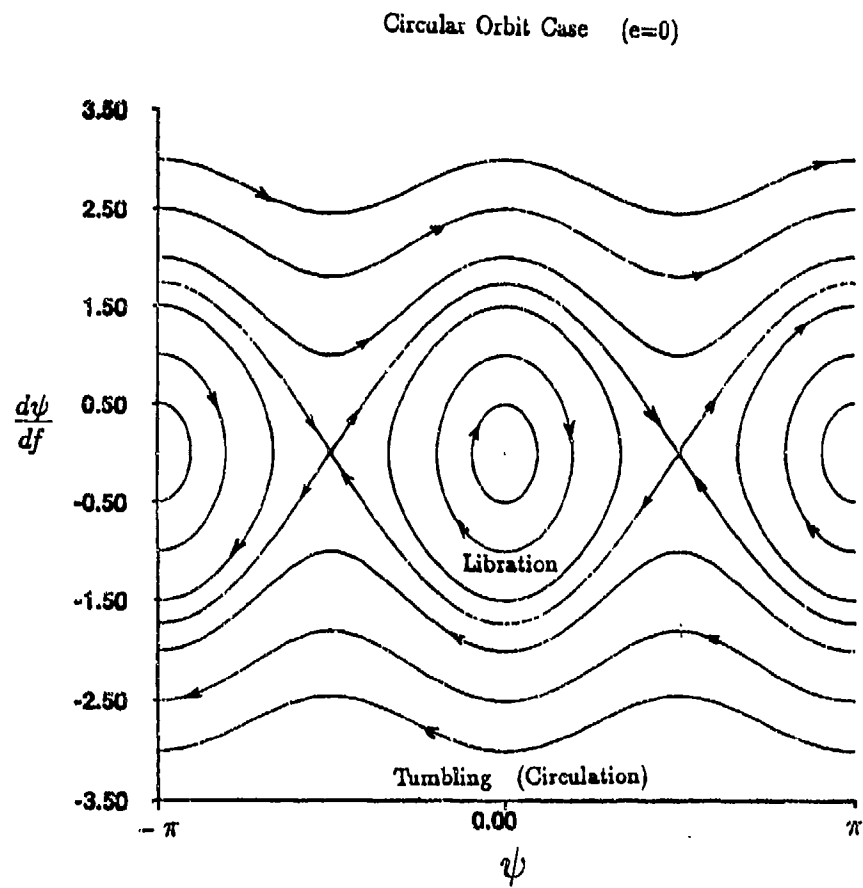
Figure 4.1: Representative Phase Plane for a Circular Orbit at $K = 1.0$.
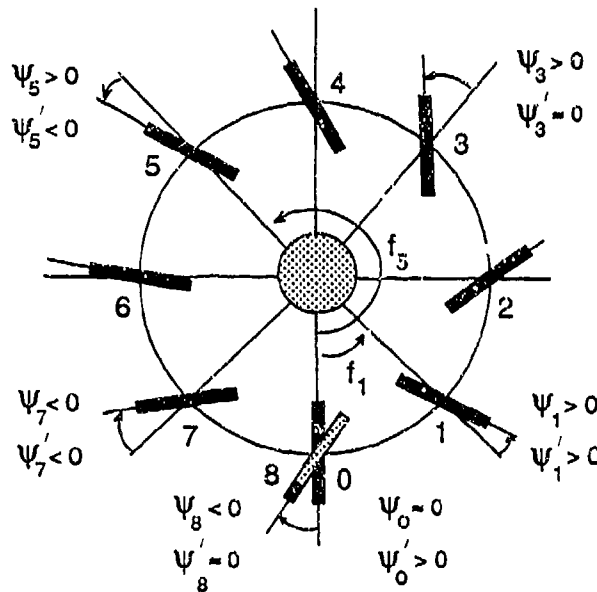
Figure 4.2: Example of Pitch Libration.

Libration occurs for the portion of the phase space where the curves are closed, and tumbling occurs along the sinusoidal-like curves; these two types of motion are separated in the phase plane by separatrices[1] in which the period of the motion is infinite. Separatrices connect the two saddle points in this figure and enclose the centers. The progression of pitch angle and pitch angle rate values follows the direction of the arrows on the diagram's curves. Figures 4.2 and 4.3 present caricatures of these two types of motion for a bar-like satellite[2] in a circular orbit.

The stable equilibrium point at $(0.0, 0.0)$ in the phase diagram corresponds to the synchronous state where the satellite always points towards the Earth (Figure 4.4). For this case the satellite never rotates relative to the Earth, and its minor moment of inertia is exactly aligned with the local vertical. The unstable equilibria (at $\pm\frac{\pi}{2}$ in the phase diagram) correspond to the alignment of the satellite's minor moment of inertia with the local horizontal (Figure 4.5). Other unstable equilibria are also possible, and will be discussed in more detail later. The equation of motion precludes the true "inertially" stablized case as depicted in Figure 4.6 except in the limit as $K \to 0$ because of the requirement for $d\psi = -df$. Small oscillations about this attitude are possible, however, and this nearly inertial case has been studied in

---

[1]An appropriately named feature. Separatrices separate different areas of the phase plane and hence separate different types of motion.

[2]Although the shape of the satellite in these figures is arbitrary, its inertia properties are not – see the assumptions in Section 2.
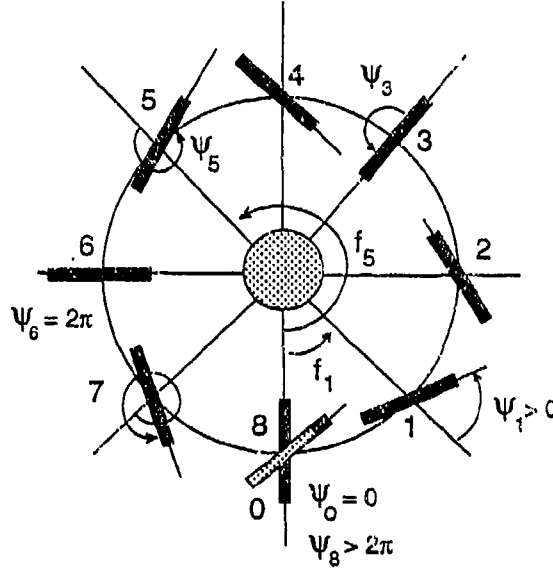
Figure 4.3: Example of Pitch Tumbling.

the past by Elrod [37].

The derivative of the true anomaly with respect to time is constant for a circular orbit,

$$\dot{f} = \omega_c = \sqrt{\frac{\mu}{r_c{}^3}}, \tag{4.2}$$

where $\omega_c$ is a constant dependent on the circular orbital radius, $r_c$, and the planet gravitational constant, $\mu$. Thus,

$$\ddot{\psi} + 3K\omega_c{}^2 \sin\psi \cos\psi = 0, \tag{4.3}$$

and integrating once gives

$$\dot{\psi}^2 + 3K\omega_c{}^2 \sin^2\psi = C^2, \tag{4.4}$$

where $C^2$ is the constant of integration. It is advantageous to define another constant, $\lambda$, such that

$$C^2 \equiv 3K\omega_c{}^2\lambda^2. \tag{4.5}$$

This allows the equation of motion to written as

$$\dot{\psi}^2 = C^2(1 - \frac{1}{\lambda^2}\sin^2\psi). \tag{4.6}$$

29

$$\psi(f) = \psi'(f) = 0$$
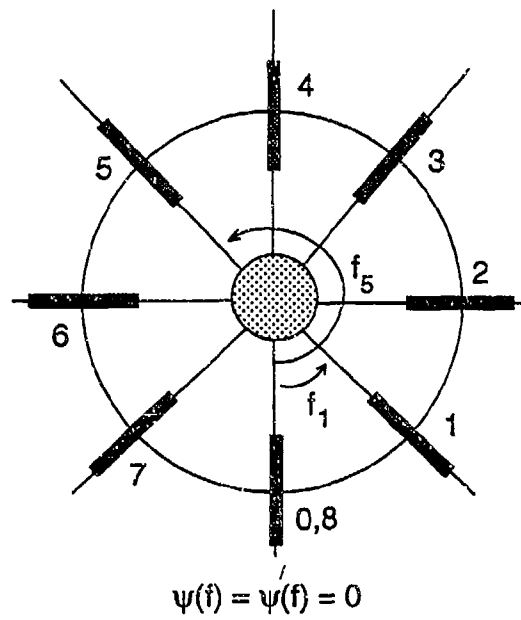
Figure 4.4: Stable Equilibrium: Synchronous Orbit.



$$\psi(f) = .5\pi \quad \psi'(f) = 0$$
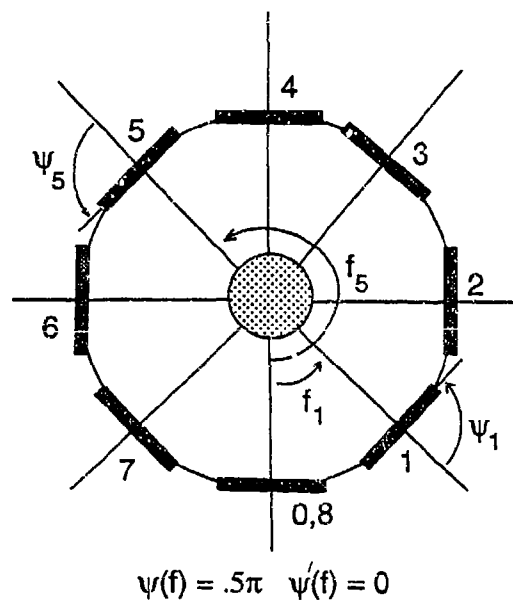
Figure 4.5: Unstable Equilibrium.

30
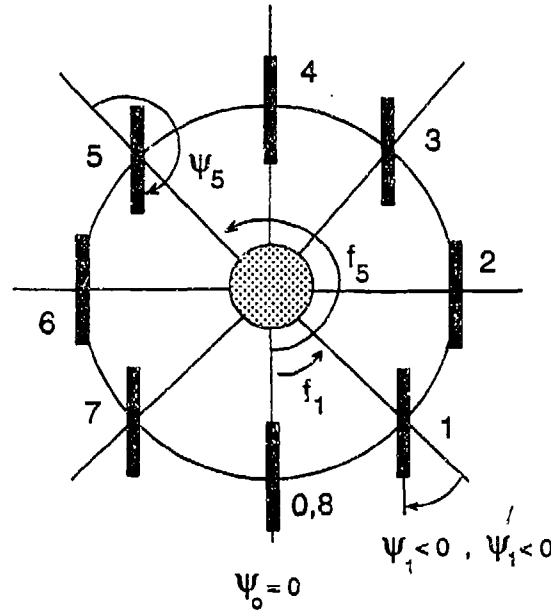
Figure 4.6: Ideal "Inertially" Stablized Case.

Like the simple pendulum, the pitching motion of a gravity-gradient satellite in a circular orbit may either be a libration about the local vertical ($\lambda > 1$) or a tumbling motion ($\lambda < 1$). Either type of motion may have periodic or quasiperiodic solutions. Motion along a separatrix would occur in the limit as $\lambda \to 1$ but this type of motion would require an infinite period and is physically impossible. Chaotic motion cannot occur in this simplified one degree-of-freedom problem.[3]

### 4.1.1 Tumbling

The equation of motion for the tumbling case ($\lambda > 1$) may be written as

$$\int C \, dt = \int \frac{d\psi}{\sqrt{1 - \frac{1}{\lambda^2}\sin^2\psi}}. \tag{4.7}$$

Choosing initial time, $t_0$ such that $\psi(t_0) = 0$ gives $\dot{\psi}(t_0) = \pm C = \pm\dot{\psi}_{max}$ and $\psi(t) = \psi_f$. Integrating with these conditions produces

$$C(t - t_0) = \int_0^{\psi_f} \frac{d\psi}{\sqrt{1 - k^2\sin^2\psi}}. \tag{4.8}$$

---

[3]Indeed, chaotic motion can only occur in autonomous systems of higher order than 1 DOF.

31

This is an elliptic integral of the first kind and it is represented by $\mathcal{F}(k, \psi_f)$. This integral is a function of the final pitch angle and the modulus, $k$, where

$$k^2 \equiv \frac{1}{\lambda^2} \qquad (4.9)$$

and

$$\lambda = \frac{\dot{\psi}_{max}}{\omega_c\sqrt{3K}}. \qquad (4.10)$$

The solution to this integral is given by the equations

$$C(t - t_0) = \mathcal{F}(k, \psi_f) = \sqrt{3K}\lambda\omega_c(t - t_0) \qquad (4.11)$$

and

$$\sin\psi_f = sn(\mathcal{F}, k). \qquad (4.12)$$

$sn(\mathcal{F}, k)$ is the elliptic sine function whose value may be calculated by an approximation to the infinite series

$$sn(\mathcal{F}, k) = \mathcal{F} - (1 + k^2)\frac{\mathcal{F}^3}{3!} + (1 + 14k^2 + k^4)\frac{\mathcal{F}^5}{5!} - $$
$$(1 + 135k^2 + 135k^4 + k^6)\frac{\mathcal{F}^7}{7!} + \dots \qquad (4.13)$$

The general solution for the pitch angle of a tumbling satellite in a circular orbit is given by

$$\psi = \sin^{-1}\left[ sn\left( \sqrt{3K}\lambda\omega_c\left(t - t_0\right), \frac{1}{\lambda}\right)\right] \qquad (4.14)$$

and

$$\dot{\psi} = \sqrt{3K}\omega_c\sqrt{\lambda^2 - \sin^2\psi}. \qquad (4.15)$$

Both of these equations are functions of $K$, $\lambda$, and $\Delta t$ (or equivalently, $\Delta f$.) Increasing $\lambda$ or inertia ratio increases both pitch angle and its rate for the tumbling case. These solutions are suitable for analysis over a portion of the satellite's orbit but a somewhat tidier form may be found by evaluation over complete orbits.

The complete elliptic integral of the first kind, $\mathcal{K}(k)$, is a function of only the modulus and is defined as the elliptic integral of the first kind evaluated at $\frac{\pi}{2}$,

$$\mathcal{K}(k) \equiv \mathcal{F}\left(k, \frac{\pi}{2}\right) = \int_0^{\pi/2} \frac{d\phi}{\sqrt{1 - k^2\sin^2\phi}}. \qquad (4.16)$$

Over $m$ complete revolutions of the pitch angle

$$\mathcal{F}(k, \psi + m\pi) = 2m\mathcal{K}(k) + \mathcal{F}(k, \psi). \qquad (4.17)$$

32

Hence

$$CT_\psi = \mathcal{F}(k, 2\pi) = 4\mathcal{K}(k) \tag{4.18}$$

for one complete pitch angle revolution of period $T_\psi$. Because the orbital period of the satellite in a circular orbit is simply

$$T_f = \frac{2\pi}{\omega_c}, \tag{4.19}$$

the periodic portion of the tumbling motion is equal to the orbital period when

$$T_f = T_\psi \tag{4.20}$$

or

$$CT_\psi = 4\mathcal{K}(k). \tag{4.21}$$

Substitution gives

$$\sqrt{3\overline{K}}\omega_c\lambda \cdot \frac{2\pi}{\omega_c} = 4\mathcal{K}(k), \tag{4.22}$$

which produces the rel tionship

$$\mathcal{K}\left(\frac{1}{\lambda}\right) = \frac{\pi}{2}\lambda\sqrt{3\overline{K}}. \tag{4.23}$$

This expression, a function only of the satellite's inertia ratio and $\lambda$, may be recursively solved to find $P = 1/1$ (one pitch revolution per orbit) solutions using the relationship

$$\mathcal{K}(k) = \frac{\pi}{2}\left[1 + \left(\frac{1}{2}\right)^2 k^2 + \left(\frac{3}{2\cdot4}\right)^2 k^4 + \left(\frac{3\cdot5}{2\cdot4\cdot6}\right)^2 k^6 + \ldots\right] \tag{4.24}$$

By inspection, a form of this equation may be written that lends itself to numerical approximations of the complete elliptic integral of the first kind,

$$\mathcal{K}(k) = \frac{\pi}{2}\left[1 + \sum_{p=1}^{q}\left[\left(\prod_{j=1}^{p}\frac{2j-1}{2j}\right)^2 \cdot k^{2p}\right]\right]. \tag{4.25}$$

The number of terms in addition to $\frac{\pi}{2}$ in the approximation is given by $q$ in this equation.

To determine the appropriate conditions required for periodic motion of the tumbling pitch angle commensurate with respect to the true anomaly, define the winding number, $P$, as the frequency ratio (and inverse of the period)

$$P \equiv \frac{m \text{ pitch angle revolutions}}{n \text{ orbits}}. \tag{4.26}$$

33

The relationship

$$mT_\psi = nT_f \tag{4.27}$$

therefore leads to the expression

$$P = \frac{T_f}{T_\psi} = \frac{m}{n} = \frac{\lambda \pi \sqrt{3K}}{2\mathcal{K}(\frac{1}{\lambda})}. \tag{4.28}$$

Using Equation 4.28, one can recursively solve for $\lambda$ and hence the initial conditions

$$\vec{\psi}(t_0) = \begin{bmatrix} \psi(t_0) \\ \dot{\psi}(t_0) \end{bmatrix} = \begin{bmatrix} 0 \\ \omega_c \lambda \sqrt{3K} \end{bmatrix} \tag{4.29}$$

required for the vehicle to have a specified resonant periodic orbit. Denoting the differentiation with respect to true anomaly by the superscript " ′ ", one can also write Equation 4.29 as

$$\vec{\psi}(f_0) = \begin{bmatrix} \psi(f_0) \\ \psi'(t_0) \end{bmatrix} = \begin{bmatrix} 0 \\ \lambda \sqrt{3K} \end{bmatrix} \tag{4.30}$$

dropping $\omega_c$ and thus making the initial conditions independent of orbital radius.

## 4.1.2   Libration

The equation of motion for the pitch angle libration of a gravity-gradient satellite in a circular orbit about a central body is

$$\dot{\psi}^2 = C^2(1 - \frac{1}{\lambda^2}\sin^2\psi). \tag{4.31}$$

Using the same initial conditions as for the tumbling case, $\psi(t_0) = 0$ , again gives $\dot{\psi}(t_0) = \dot{\psi}_{max}$, and $C = \pm\dot{\psi}_{max} = \pm\omega_c\lambda\sqrt{3K}$. Alternatively, one may choose $t_0$ such that $\dot{\psi}(t_0) = 0$ and $\psi(t_0) = \psi_{max} = \sin^{-1}\lambda$ by beginning the integration at the point in the phase diagram where the trajectory crosses the abscissa. Hence, given $\lambda$, the initial conditions are either

$$\vec{\psi}_1(t_0) = \begin{bmatrix} 0 \\ \omega_c\lambda\sqrt{3K} \end{bmatrix} \quad \text{or} \quad \vec{\psi}_2(t_0) = \begin{bmatrix} \sin^{-1}\lambda \\ 0 \end{bmatrix}, \tag{4.32}$$

and the equation of motion may be written as

$$\frac{\dot{\psi}^2}{3K\omega_c^2} = \sin^2(\psi_{max}) - \sin^2\psi. \tag{4.33}$$

The solution to the libration case (as for the tumbling case) is

$$C(t - t_0) = \int_{\psi_0}^{\psi_f} \frac{d\psi}{\sqrt{1 - \frac{1}{\lambda^2}\sin^2\psi}}. \tag{4.34}$$

This integral is not in the form of an elliptic integral of the first kind because $\frac{1}{\lambda^2}$ is greater than 1. A variable change is used to obtain this form, requiring the definition of a transformation variable, $\phi$:

$$\sin\phi \equiv \frac{\sin\psi}{\sin(\psi_{max})}. \tag{4.35}$$

As $\psi$ varies from 0 to $\psi_{max}$, $\phi$ may range from 0 to $\phi_{max}$. Taking the derivative of this equation,

$$\dot{\phi}^2 = \frac{\dot{\psi}^2\cos^2\psi}{\sin^2(\psi_{max}) \cdot \cos^2\phi}, \tag{4.36}$$

and noting that

$$\cos^2\phi = 1 - \sin^2\phi = 1 - \frac{\sin^2\psi}{\sin^2(\psi_{max})}, \tag{4.37}$$

one can write

$$\dot{\phi}^2 = \frac{\dot{\psi}^2\cos^2\psi}{\left(\sin^2(\psi_{max}) - \sin^2\psi\right)} = \frac{\dot{\psi}^2\cos^2\psi}{\left(\dot{\psi}^2/3K\omega_c^2\right)} = 3K\omega_c^2\left(1 - \sin^2(\psi_{max}) \cdot \sin^2\phi\right). \tag{4.38}$$

This leads to

$$\omega_c\sqrt{3K}(t - t_0) = \sqrt{3K}(f - f_0) = \int_0^{\phi_f} \frac{d\phi}{\sqrt{1 - k^2\sin^2\phi}}, \tag{4.39}$$

where

$$k = \sin\psi_{max} = \lambda, \quad \lambda^2 < 1. \tag{4.40}$$

This integral (Equation 4.39) is now in the form of the elliptic integral of the first kind. General solutions to the pitch libration problem may therefore be derived in the same manner as for the tumbling case,

$$C(t - t_0) = \mathcal{F}(k, \phi_f) = \sqrt{3K}\lambda(f - f_0) \tag{4.41}$$

and

$$\sin\phi_f = sn(\mathcal{F}, k) = \frac{\sin\psi_f}{\sin(\psi_{max})}. \tag{4.42}$$

The general solution for the pitch angle libration is given by

$$\psi = \sin^{-1}\left[\lambda\, sn\left(\lambda, \sqrt{3K}\lambda\omega_c(t - t_0)\right)\right] \tag{4.43}$$

35

and

$$\dot{\psi} = \sqrt{3K}\omega_c\sqrt{\lambda^2 - \sin^2\psi}. \tag{4.44}$$

Both of these equations are functions of $K$, $\lambda$, and $\Delta t$. Decreasing $\lambda$ or the inertia ratio decreases both the pitch angle and its rate. Integrating over one quarter of the closed ellipse in phase space, for one complete libration

$$(t - t_0) = \frac{T_\psi}{4}, \tag{4.45}$$

$$\psi_{max} = \phi_{max} = \frac{\pi}{2}, \tag{4.46}$$

and

$$\omega_c\sqrt{3K}T_\psi = 4\int_0^{\frac{\pi}{2}} \frac{d\phi}{\sqrt{1 - \lambda^2\sin^2\phi}}. \tag{4.47}$$

This integral is now a complete elliptic integral of the first kind, dependent only upon $\lambda$ and hence,

$$T_\psi = \frac{4}{\sqrt{3K}}\mathcal{K}(\lambda). \tag{4.48}$$

The period is dependent only on $\lambda$, the sine of the maximum pitch angle attained during an orbit, and $K$, the inertia ratio for the satellite.

To determine the appropriate conditions required for periodic motion of the librating pitch angle commensurate with respect to the true anomaly, recall that for $m$ libration oscillations in $n$ orbits

$$mT_\psi = nT_f, \tag{4.49}$$

leading to the expression

$$P = \frac{T_f}{T_\psi} = \frac{m}{n} = \frac{\pi\sqrt{3K}}{2\mathcal{K}(\lambda)}. \tag{4.50}$$

Using Equations 4.50 and 4.25, one can recursively solve for $\lambda$ and hence for either set of initial conditions

$$\vec{\psi}_1(f_0) = \begin{bmatrix} 0 \\ \lambda\sqrt{3K} \end{bmatrix} \quad \text{or} \quad \vec{\psi}_2(f_0) = \begin{bmatrix} \sin^{-1}\lambda \\ 0 \end{bmatrix} \tag{4.51}$$

required for the vehicle to have a specified periodic libration.

### 4.1.3  Solutions

In the last subsections, periodic solutions to the tumbling and libration cases satisfied the equations

$$P_{tumble} = \frac{m}{n} = \frac{\lambda\pi\sqrt{3K}}{2\mathcal{K}(\frac{1}{\lambda})}, \quad \lambda > 1 \tag{4.52}$$

36

$$P_{libration} = \frac{m}{n} = \frac{\pi\sqrt{3K}}{2\mathcal{K}(\lambda)}, \quad \lambda < 1 . \tag{4.53}$$

Since

$$\lim_{k \to 0} \mathcal{K}(k) = \lim_{k \to 0} \left\{ \frac{\pi}{2} \left[ 1 + \left(\frac{1}{2}\right)^2 k^2 + \left(\frac{3}{2 \cdot 4}\right)^2 k^4 + \ldots \right] \right\} = \frac{\pi}{2}, \tag{4.54}$$

the maximum possible values for the libration and tumbling periods are

$$P_{libration_{max}} = \lim_{\lambda \to 0} P_{libration} = \sqrt{3K} \tag{4.55}$$

and

$$P_{rotation_{max}} = \lim_{\lambda \to \infty} P_{rotation} = \infty. \tag{4.56}$$

These results are intuitive. The more energy put into a tumbling trajectory, the greater the tumbling frequency without limit. On the other hand, if enough energy is put into a librational trajectory, a limit will be reached where additional energy will cause the satellite's trajectory to transition from oscillation to rotation. This maximum periodic libration limit is plotted in Figure 4.7 as a function of inertia ratio. According to this plot, no harmonics are possible (we cannot have two oscillations in one orbit, for example) in a librational trajectory. In fact, the largest librational frequency allowed is for the case of a dumbbell satellite ($K = 1.0$) where $m/n$ is approximately 17/10. Subharmonic librational motion can occur but is also limited for values of inertia ratio of less than approximately 1/3. For example, period 2 ($m/n$=1/2) libration cannot be realized by satellites with inertia ratios less than about 1/12. In the limit, as $K \to 0$, $P_{libration} \to 0$. This result is obvious when one considers that the pitch angle solution to the circular orbit equation of motion for $K = 0$ (the case of an axially symmetric satellite) is linear, $\psi(f) = C_1 f + C_2$.

Figure 4.8 presents the values of $K$ and $\lambda$ required for various periodic solutions of pitch angle libration and tumbling. While there exists a broad range of inertia ratio and $\lambda$ combinations that produce tumbling motion, the range of combinations for libration motion are often more limited, especially for higher period motion. For example, satellite tumbling with a periodic motion component of frequency 3/2 may occur for almost any value of $K$, whereas frequency 3/2 libration can only exist for satellites having inertia ratios between about 0.75 and 1.0.

Figure 4.9 presents the maximum pitch angle attained for various periodic solutions for the circular orbit libration case. Careful selection of a satellite's inertia properties and/or selection of the initial state vector is necessary to attain a small maximum pitch libration angle. This figure demonstrates that the lower a satellite's
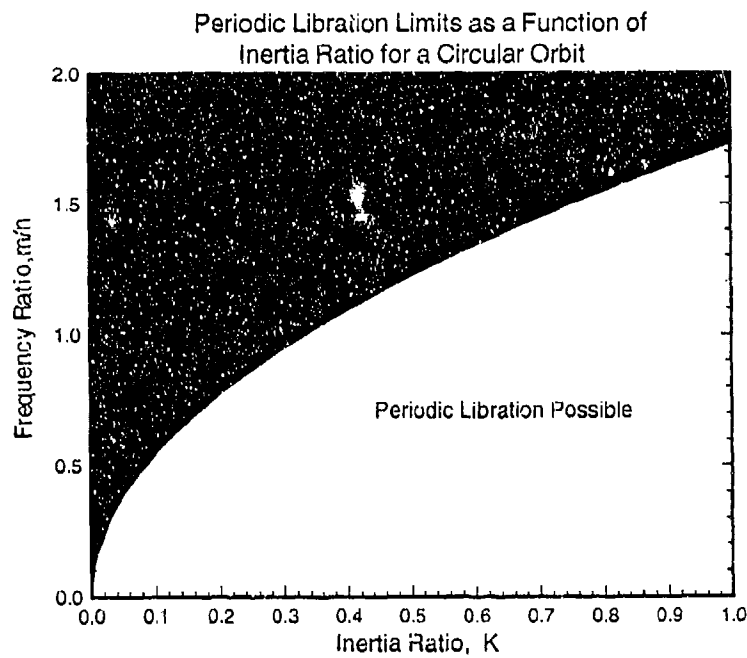
Figure 4.7: Periodic Libration Limits as a Function of Inertia Ratio for a Circular Orbit.
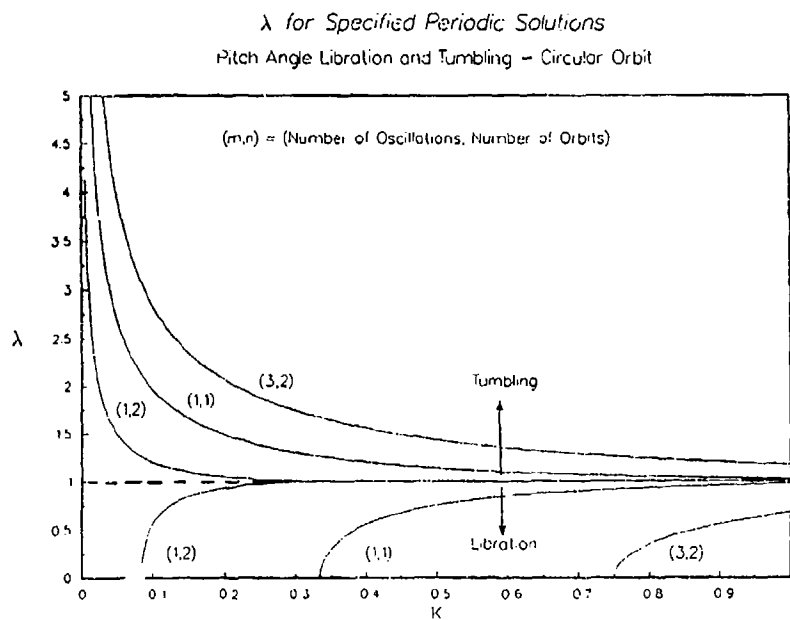


Figure 4.8: Values of $\lambda$ for Periodic Libration and Tumbling.

Figure 4.9: Maximum Pitch Angle for Periodic Libration Solutions.

inertia ratio, the larger the pointing error for a specified variance in $K$. In other words, the required knowledge of the accuracy of $K$ in order to keep $\psi_{max}$ within specified limits increases with decreasing inertia ratio. For example, with a $P = 3/2$ orbit, $K = 0.75$ will give pitch oscillations of less than one degree of magnitude. An error in $K$ of .01 can give maximum pitch angles of about 10 degrees. For $P = 1/2$ orbits, however, a value of $K$ of about .08334 gives less than one degree of pitch whereas an error in $K$ of .01 gives a maximum pitch angle of about 27 degrees.

The maximum value of $\psi'$ attained for various periodic solutions for the circular orbit libration case is given in Figure 4.10. Note that for any periodic libration solutions, the magnitude of the maximum $\psi'$ remains less than 2. In fact, the limiting values for $\psi'$ and $\psi$ for pitch angle libration occur as $\lambda \rightarrow 1$ and they depend only on $K$ (Figure 4.11). These curves are the separatrices of the phase diagram (representing quasiperiodic solutions with an infinite period) and this plot therefore depicts the change in the form of the separatrices as a function of the satellite's inertia ratio.

For the tumbling case where

$$sn(\mathcal{F}, k) = \mathcal{F} - (1 + \frac{1}{\lambda^2})\frac{\mathcal{F}^3}{3!} + (1 + 14\frac{1}{\lambda^2} + \frac{1}{\lambda^4})\frac{\mathcal{F}^5}{5!} - \ldots, \qquad (4.57)$$

39
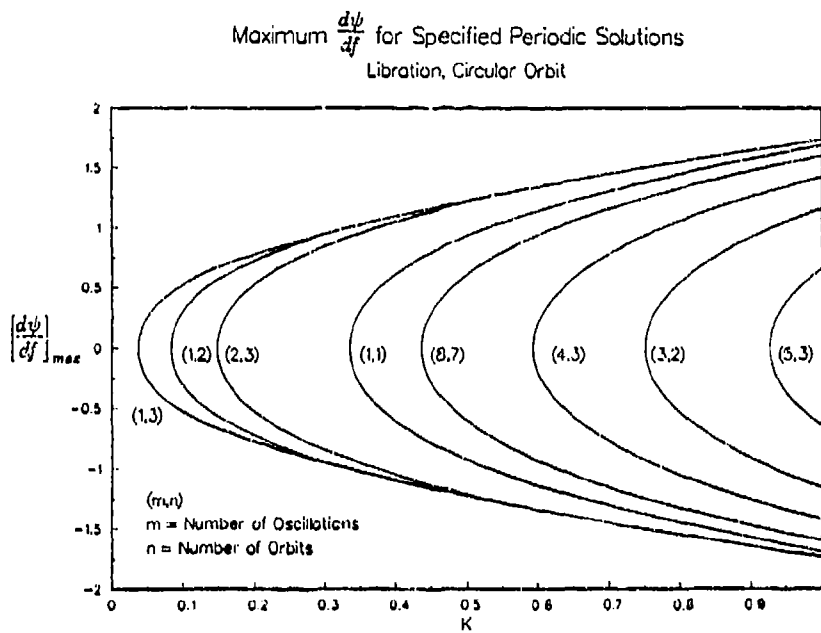
Figure 4.10: Maximum $\psi'$ for Periodic Libration Solutions.
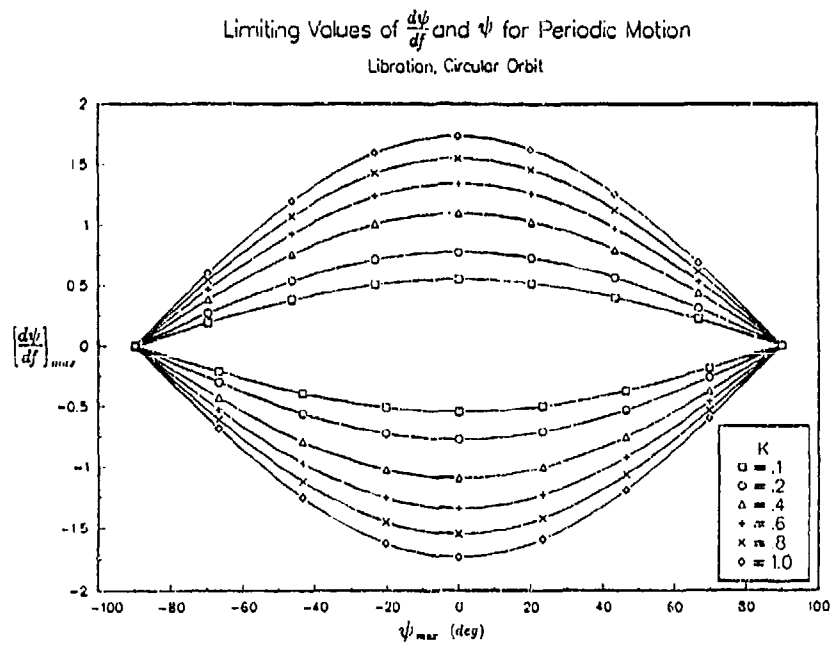


Figure 4.11: Limiting Values of $\psi'$ and $\psi$ for Libration Solutions.

40

$$\lim_{\lambda \to \infty} sn(\mathcal{F}, \frac{1}{\lambda}) = \sin(\mathcal{F}). \qquad (4.58)$$

Because

$$\sin(\mathcal{F}) = \sin(\psi) = \sin[C(t - t_0)], \qquad (4.59)$$

then

$$\lim_{\lambda \to \infty} \psi = \sqrt{3K} \lambda (f - f_0). \qquad (4.60)$$

Likewise,

$$\lim_{\lambda \to \infty} \psi' = \sqrt{3K} \lambda. \qquad (4.61)$$

Thus, as $\lambda$ becomes large, the tumbling $\psi$ linearly increases with elapsed time ($\Delta f$) and both $\psi$ and $\psi'$ increase with increasing $K$.

As $\lambda$ approaches 0 for the case of libration,

$$sn(\mathcal{F}, k) = \mathcal{F} - (1 + \lambda^2)\frac{\mathcal{F}^3}{3!} + (1 + 14\lambda^2 + \lambda^4)\frac{\mathcal{F}^5}{5!} - \ldots, \qquad (4.62)$$

$$\lim_{\lambda \to 0} sn(\mathcal{F}, \lambda) = \sin \mathcal{F} = \sin[C(t - t_0)] = \sin \phi = \frac{\sin \psi}{\lambda}, \qquad (4.63)$$

and

$$\lim_{\lambda \to 0} \psi = \lambda \sin\left[\sqrt{3K}\omega_c\lambda(t - t_0)\right]. \qquad (4.64)$$

This indicates that as $\lambda$ approaches zero, pitch angle libration magnitude also approaches zero. These results may be viewed in Figures 4.12 - 4.17, which present periodic pitch angle and pitch angle rate solutions for inertia ratios of 1.0, 0.5, and 0.1, respectively. In Figure 4.12 the 4/1 tumbling solution ($\lambda = 2.41$) has almost a linear slope whereas the 3/2 libration solution ($\lambda = 0.67$) has the smallest pitch angle amplitude of the curves shown. As inertia ratio decreases to $K=0.1$ in Figure 4.16 and Figure 4.17, the frequency or winding number[4] of the libration and tumbling motion pitch angle solutions increases for a given value of $\lambda$.

## 4.2  Numerical Analysis

In order to help gain insight to the application of the numerical nonlinear analysis techniques introduced in Section 3, a few different solutions to the equations of motion

---

[4]This is also called the rotation number in some sources.
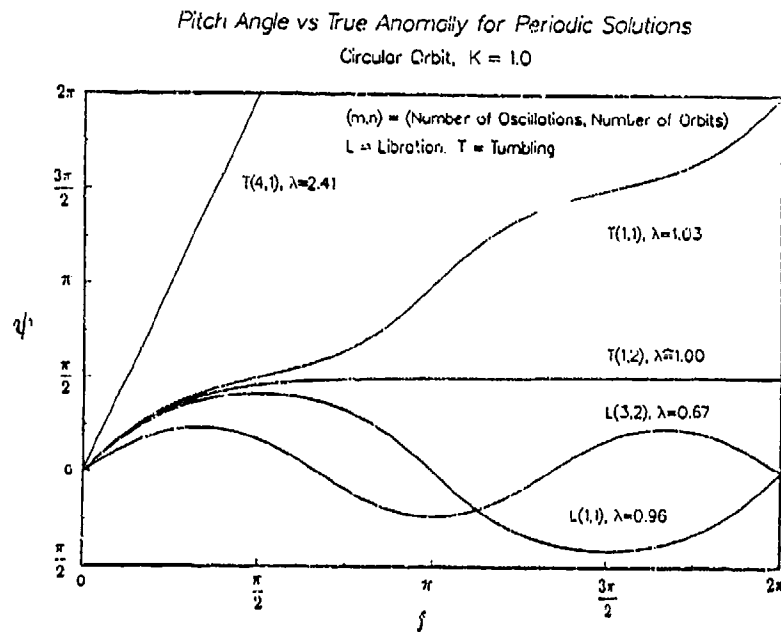
Figure 4.12: Pitch Angle Periodic Solutions at $K=1.0$ for Libration and Tumbling.
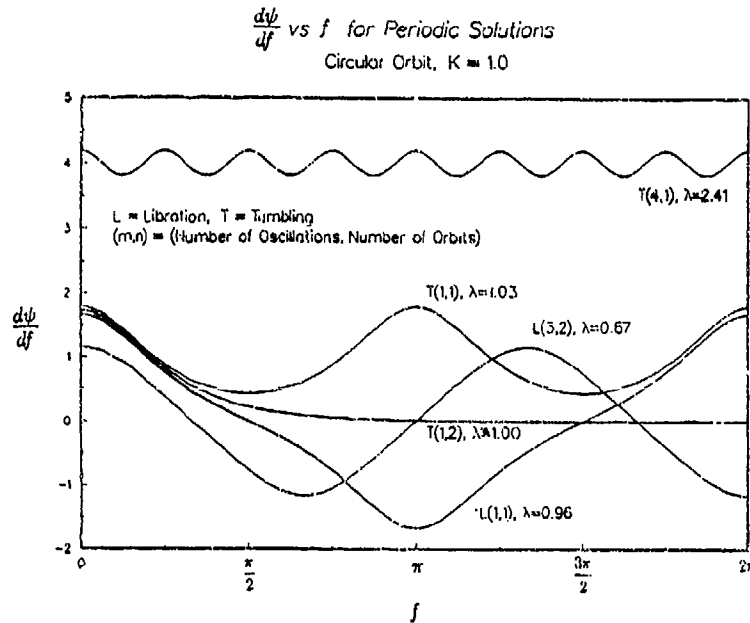


Figure 4.13: Pitch Angle Rate Periodic Solutions at $K=1.0$ for Libration and Tumbling.
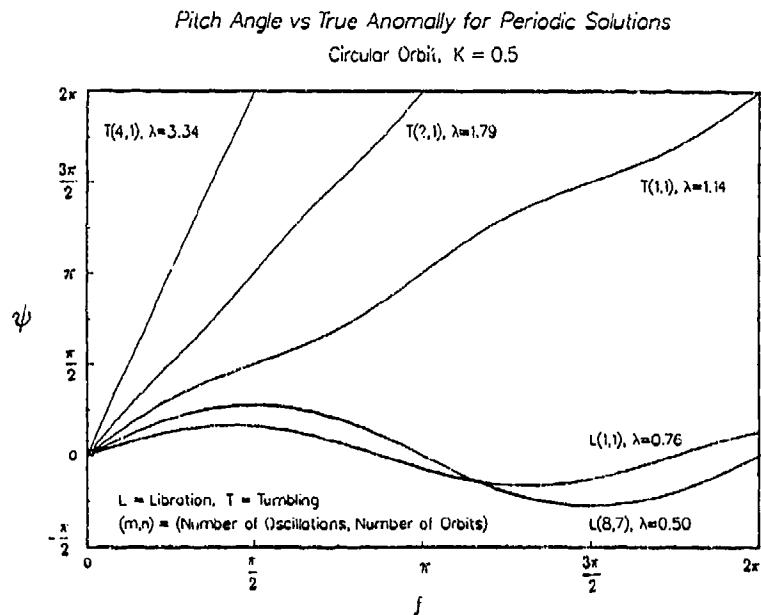
Figure 4.14: Pitch Angle Periodic Solutions at $K=0.5$ for Libration and Tumbling.
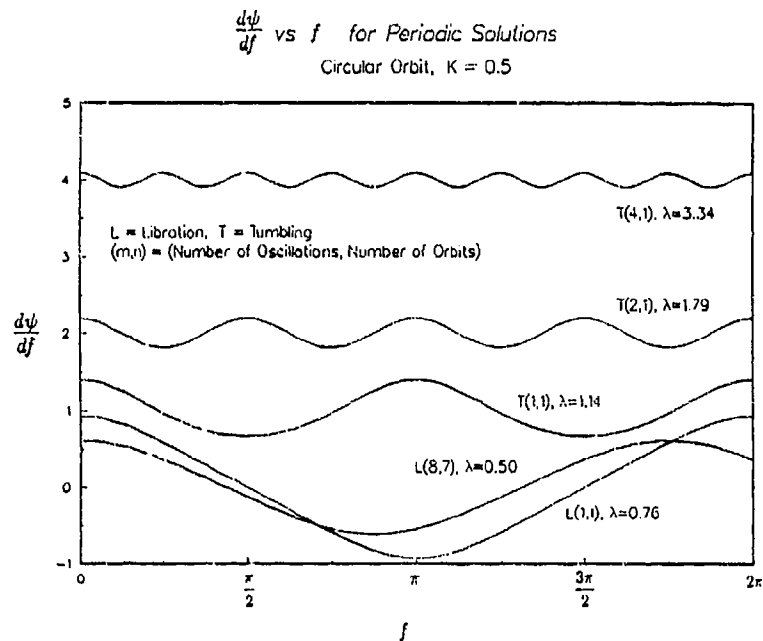


Figure 4.15: Pitch Angle Rate Periodic Solutions at $K=0.5$ for Libration and Tumbling.
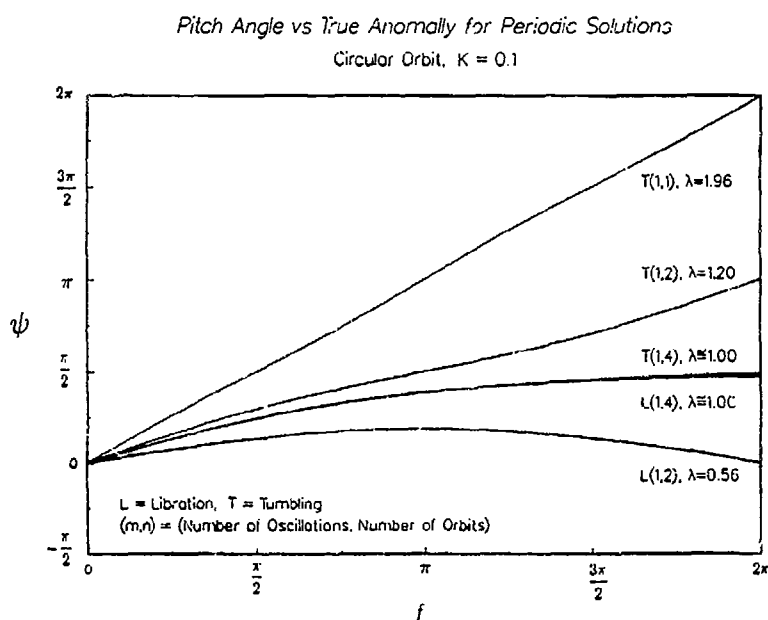
Figure 4.16: Pitch Angle Periodic Solutions at $K=0.1$ for Libration and Tumbling.
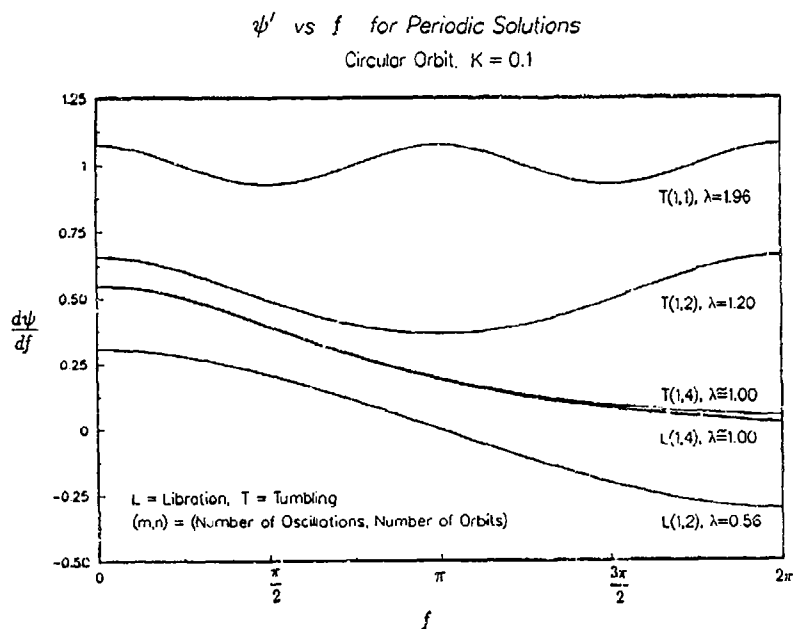


Figure 4.17: Pitch Angle Rate Periodic Solutions at $K=0.1$ for Libration and Tumbling.

Phase Space Plot for K=0.5, e=0., and
Various Initial States
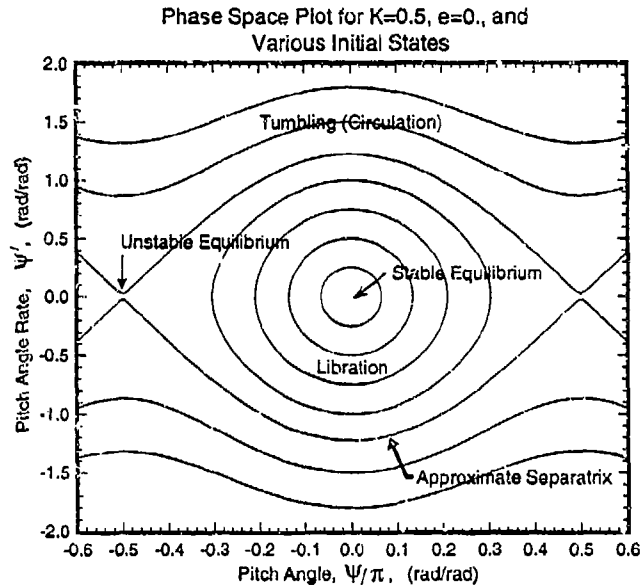


Figure 4.18: Phase Space Plot for $K$=0.5, $e = 0.$, and Various Initial States.

of the circular orbit problem are presented below in the form of series of plots of the state variable responses, solution space, Poincaré maps, and phase diagrams. Almost all of these example solutions are for an arbitrarily shaped satellite in a circular orbit having an inertia ratio of $K = 0.5$, and differ only in the initial state variable values. The first series depicts a representative quasiperiodic libration solution for the initial state $(0.0, 0.5)$, and the second shows a representative quasiperiodic tumbling solution for the initial condition $(0., 1.5)$. These two series are followed by examples of various periodic rotation and libration solutions.

The phase space for this problem[5] appears in Figure 4.18. As in the phase space plot of Figure 4.1, two distinct types of motion appear – pitch angle libration (oscillation) and pitch angle tumbling (continuous rotation). Libration occurs for the portion of the phase space enclosed by the separatrices and tumbling occurs in the phase space outside the separatrices. For a zero initial pitch angle, a satellite in a circular orbit with $K = 0.5$ would have to have an initial pitch rate approximately between $-1.2$ and $+1.2$ in order to oscillate about the local vertical; any other initial value of pitch rate would result in tumbling motion. Thus the type of motion produced for an arbitrary initial state can be predicted by merely examining this phase plot: an initial state of $(0.0, 0.5)$ has to produce libration, for example, and an initial state of $(0.0, 1.5)$ has to produce tumbling, at least for the given inertia ratio.

---

[5]Remember, the phase space is merely a plot of $\psi'(f)$ versus $\psi(f)$ for a change in $f$ and for a sampling of initial states.

45

Pitch Angle Response for K=0.5, e=0., and
Initial State (0.,0.5) for Orbits #100 - 105
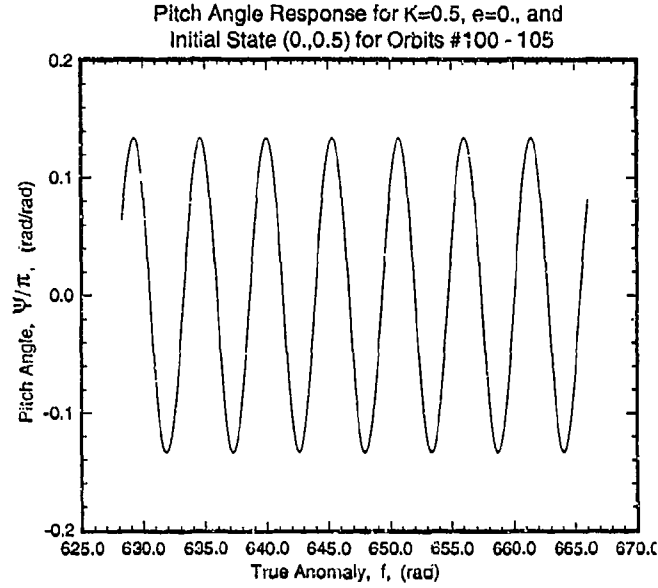


Figure 4.19: Pitch Angle Response for an Example Quasiperiodic Libration Trajectory: $K = 0.5$, $e = 0.$, and $(0., 0.5)$ for Orbits #100-105.

## 4.2.1 Example Quasiperiodic Libration Solution: $\vec{\psi}_o = (0.0, 0.5)$

The first example series depicts a representative libration solution for the initial state $(0.0, 0.5)$. Figure 4.19 and Figure 4.20 present the simple sinusoidal responses of the pitch angle and its rate versus true anomaly over six orbits (arbitrarily chosen to be orbits #100-105). The pitch and pitch rate frequency is incommensurate with the orbit frequency, causing the motion to be quasiperiodic.

Figure 4.21 shows the solution space for this problem; this is merely a three dimensional plot of pitch angle versus pitch rate versus true anomaly. The phase space of this solution, Figure 4.22, is found by ignoring true anomaly values – one simply views the solution space plot from one end. A Poincaré map showing 2000 orbits is presented for this solution in Figure 4.23. If this solution had been periodic instead of quasiperiodic, this map would have consisted of one or a few points instead of a distinct curve.

46
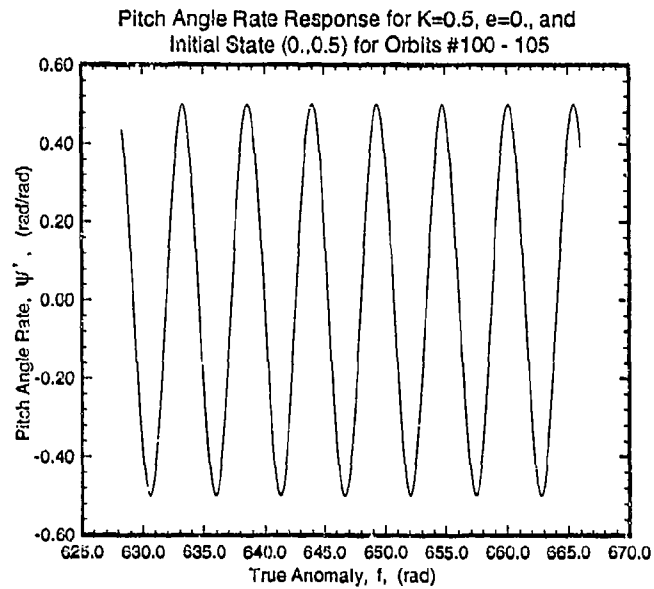
Figure 4.20: Pitch Angle Rate Response for an Example Quasiperiodic Libration Trajectory: $K = 0.5$, $e = 0.$, and $(0., 0.5)$ for Orbits #100-105.
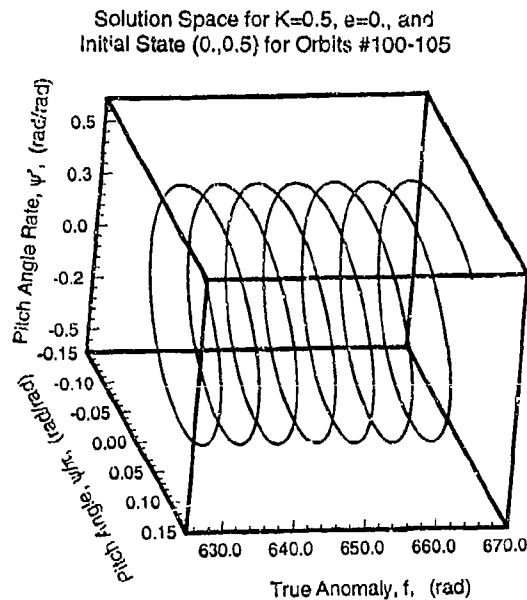


Figure 4.21: Solution Space Plot for an Example Quasiperiodic Libration Trajectory: $K = 0.5$, $e = 0.$, and $(0., 0.5)$ for Orbits #100-105.

Phase Space Plot for K=0.5, e=0., and
Initial State (0.,0.5) for Orbits #100 - 105
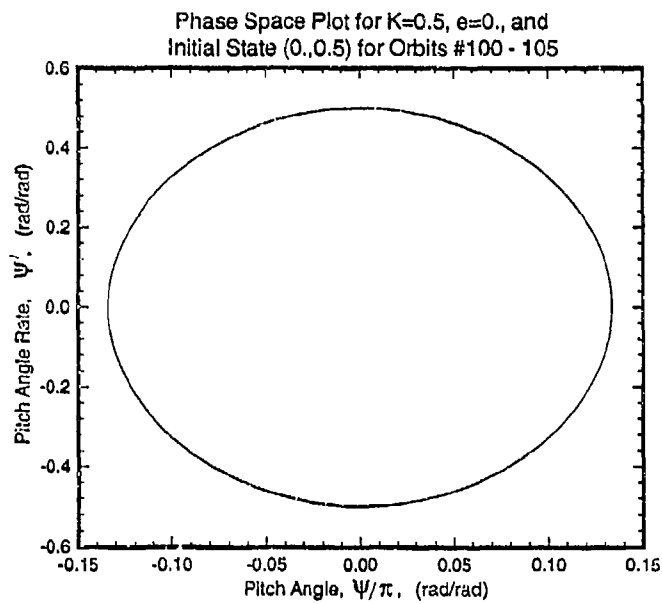
Figure 4.22: Phase Space Plot for an Example Quasiperiodic Libration Trajectory: $K = 0.5$, $e = 0.$, and $(0., 0.5)$ for Orbits #100-105.



Poincare' Plot of 2000 Orbits for K=0.5, e=0.,
and Initial State (0.,0.5)
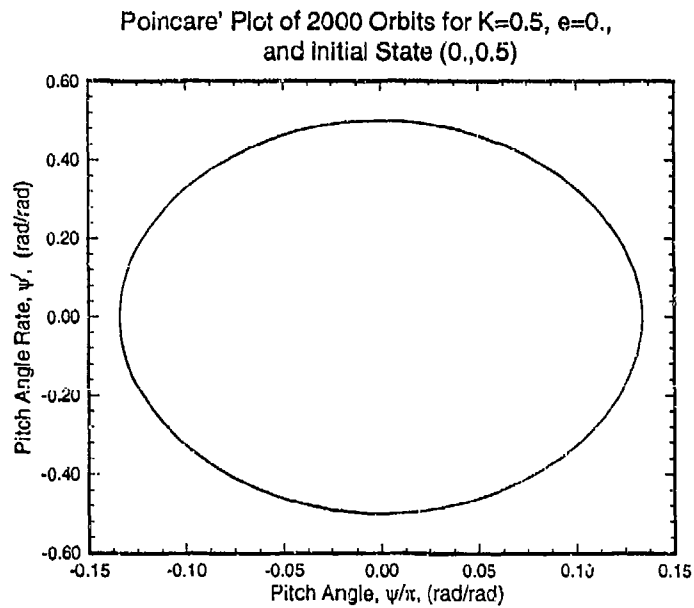
Figure 4.23: Poincaré Map of 2000 Orbits for an Example Quasiperiodic Libration Trajectory: $K = 0.05$, $e = 0.$, and $(0., 0.5)$.

48
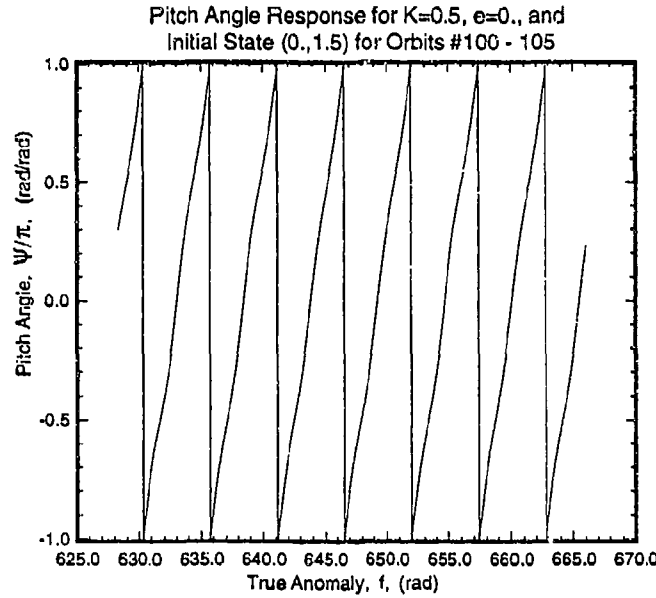
Figure 4.24: Pitch Angle Response for an Example Quasiperiodic Tumbling Trajectory: $K = 0.5$, $e = 0.$, and $(0., 1.5)$ for Orbits #100-105.

## 4.2.2 Example Quasiperiodic Tumbling Solution: $\vec{\psi}_o = (0.0, 1.5)$

This example series depicts a representative quasiperiodic tumbling solution for the initial state $(0.0, 1.5)$. Figures 4.24 and Figure 4.25 present the responses of the pitch angle and its rate versus true anomaly over six orbits. Pitch angle actually increases monotonically as a result of the tumbling motion, although for convenience, $\psi$ is calculated modulo $\pi$ for Figure 4.24. As in the last example, the frequencies of the periodic portion of the tumbling motion and the orbital motion are incommensurate, causing the tumbling motion to be quasiperiodic.

The phase space of this particular solution is given by Figure 4.26. The integration began at the initial state $(0., 1.5)$ and the progression of the integration curve is from left to right in this plot. A Poincaré map of a large number of orbits would look identical to this phase space plot, although it is important to recognize the fundamental differences between these two types of plots. Remember that the phase space map is formed from state vector values collected and plotted at every integration step in at least part of an orbit, whereas a Poincaré map includes only one state vector value for each orbit; in this case this value is collected at each periapsis

49
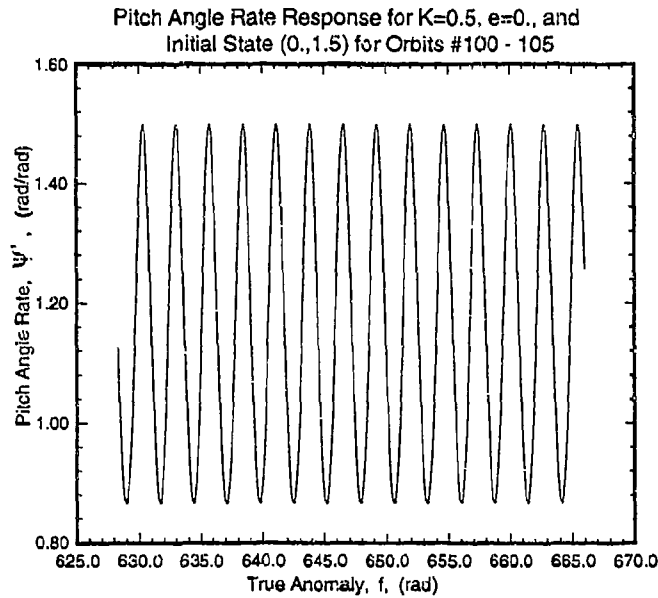
Figure 4.25: Pitch Angle Rate Response for an Example Quasiperiodic Tumbling Trajectory: $K = 0.5$, $e = 0.$, and $(0., 1.5)$ for Orbits #100-105.

passage. If enough orbits are integrated, these two types of plots will be identical for quasiperiodic motion in a circular orbit, but not for periodic motion. Figure 4.27 shows a Poincaré map for this solution for only 10 data points, or 10 consecutive periapsis passages. The order of these points (actually collected after a number of orbits were integrated to allow the solutions to settle) are given by the numbers in this figure. Figure 4.28 shows the Poincaré map for this example trajectory for 2000 orbits.
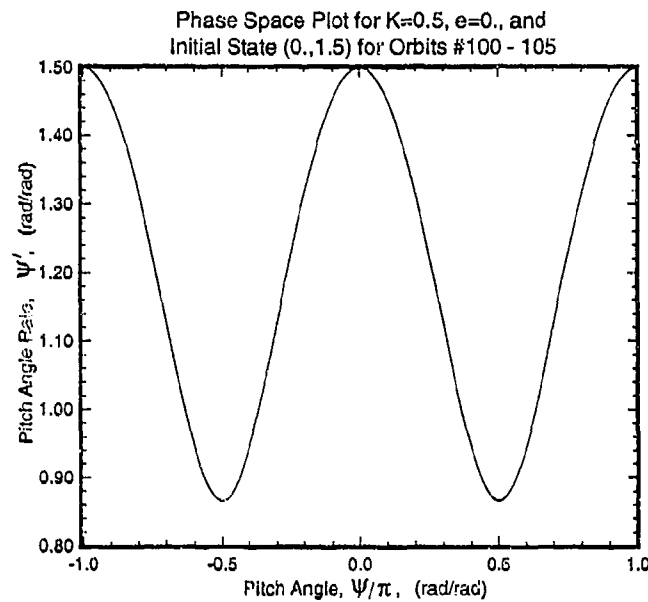
Figure 4.26: Phase Space Plot for an Example Quasiperiodic Tumbling Trajectory: $K = 0.5$, $e = 0.$, and $(0., 1.5)$ for Orbits #100-105.
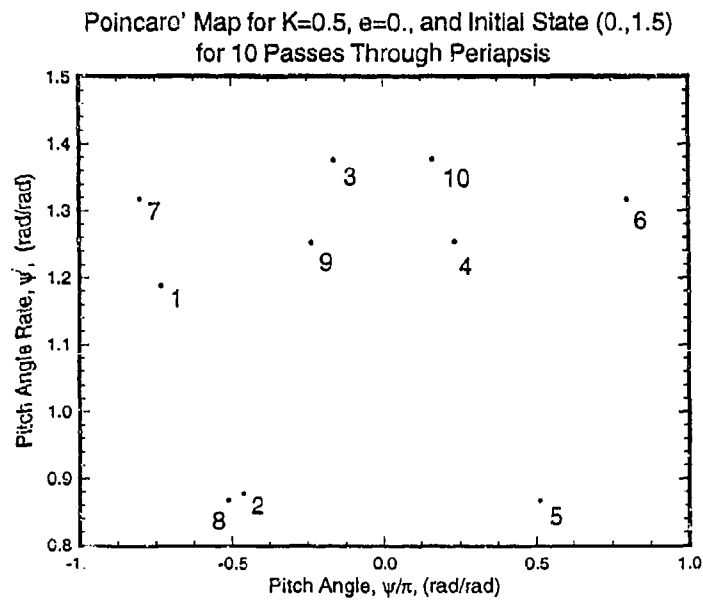


Figure 4.27: Poincaré Map for an Example Quasiperiodic Tumbling Trajectory: $K = 0.5$, $e = 0.$, and $(0., 1.5)$ for 10 Passes Through Periapsis.
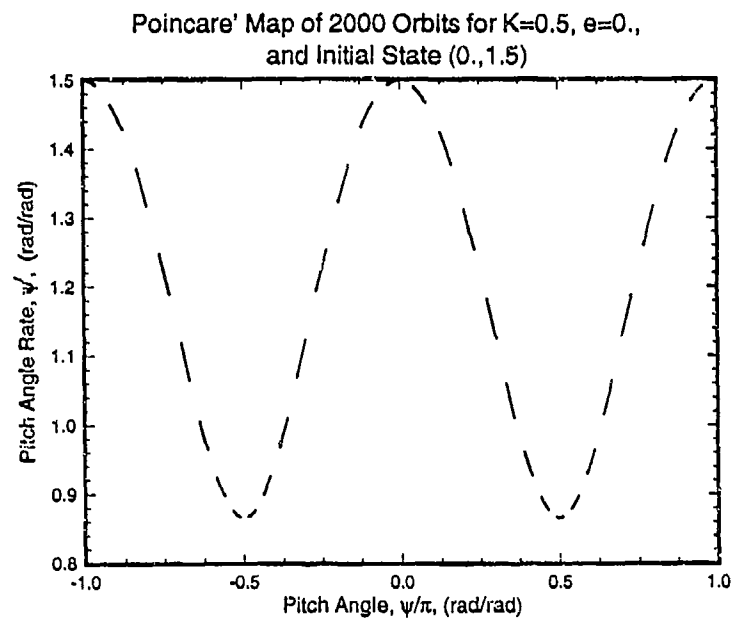
Figure 4.28: Poincaré Map of 2000 Orbits for an Example Quasiperiodic Tumbling Trajectory: $K = 0.5$, $e = 0.$, and $(0., 1.5)$.

### 4.2.3   Periodic Pitch Tumbling Examples

Using the analytical methods developed in Section 4.1, we can find the initial conditions required to produce periodic solutions for both the tumbling and libration cases. In practice, one is generally more interested in pitch libration than in tumbling because pointing requirements generally make the former type of motion more desirable. Hence, only two example periodic pitch tumbling trajectory plots are included here, and more space is devoted later to periodic libration.

The first example of a periodic pitch tumbling trajectory is given by Figure 4.29, the pitch angle response for a $P = 4/1$ harmonic solution, with $K = 1.0$ and the initial state $(0., 4.1895926)$. After only two orbits, the satellite has tumbled through about 50.27 radians, making eight complete rotations. In contrast, Figure 4.30 presents the pitch angle response for a $P = 1/2$ subharmonic trajectory, with $K = 0.1$ and the initial state $(0., 0.6576532)$. The satellite makes one complete rotation for every two orbit revolutions. In addition, the oscillatory component of this pitch angle response is significantly greater than that for the $P = 4/1$ trajectory, which was almost linear.
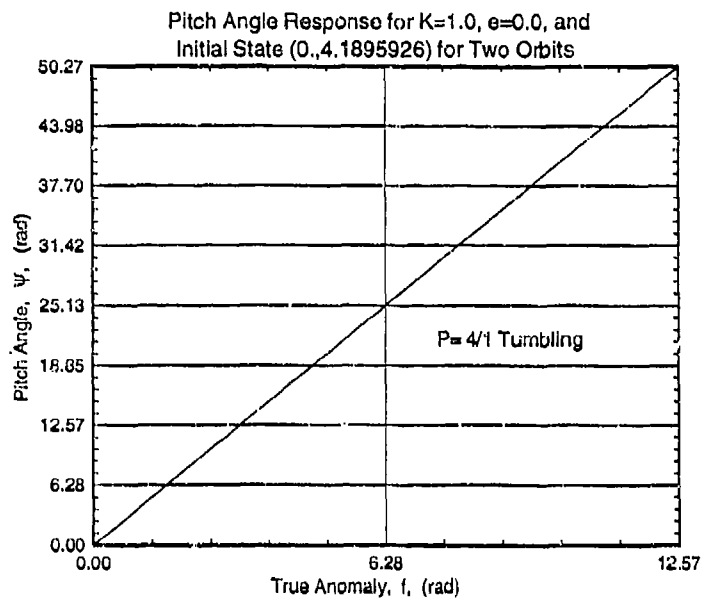
Figure 4.29: Pitch Angle Response for $P = 4/1$ Tumbling: $K = 1.0$, $e = 0.0$, and $(0., 4.1895926)$ for Two Orbits.
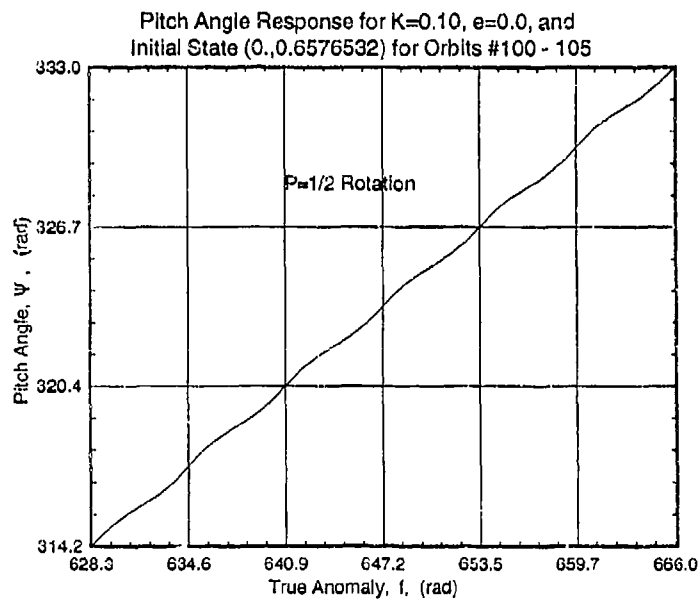


Figure 4.30: Pitch Angle Response for $P = 1/2$ Rotation: $K = 0.1$, $e = 0.0$, and $(0., 0.6576532)$ for Two Orbits.
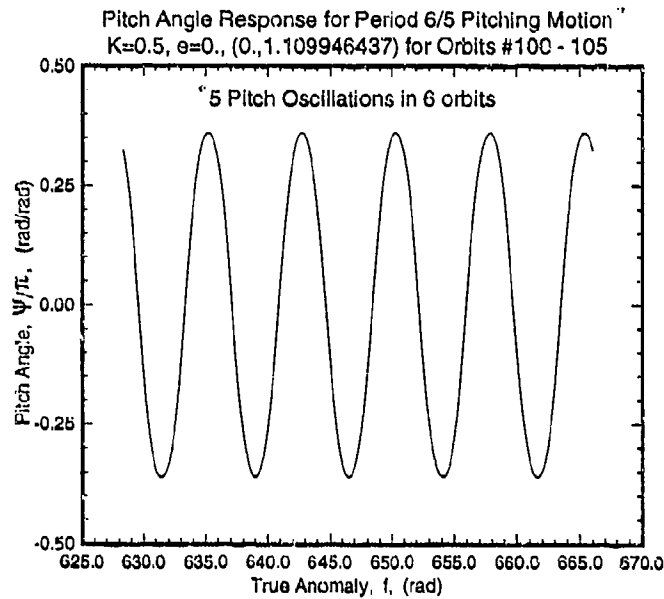
Figure 4.31: Pitch Angle Response for $P = 5/6$ Libration: $K = 0.5$, $e = 0.$, and $(0., 1.109946437)$ for Orbits #100-105.

## 4.2.4 Periodic Pitch Libration Examples

Figures 4.31 - 4.35 are a series of plots depicting a stable frequency 5/6 (or period 6/5 or $P = 5/6$ – i.e. five pitch oscillations in six orbits) libration that occurs for the initial state $(0., 1.109946437)$. Figures 4.31 and 4.32 present the state variables as a function of true anomaly for orbit numbers 100 through 105. Five complete pitch oscillations occur during this $12\pi$ period of true anomaly.

Figure 4.33 depicts the three-dimensional solution space for this example trajectory, and its phase space diagram is shown in Figure 4.34. At a glance both of these figures indicate the solution is periodic. A Poincaré map of this trajectory is given in Figure 4.35. Note that this mapping will consist of only six fixed points (their size was exaggerated in this figure for clarity) for any number of orbits more than six that are integrated.

An infinite number of unstable periodic libration trajectories are possible; a few examples are given in a representative Poincaré map in Figure 4.36. The square
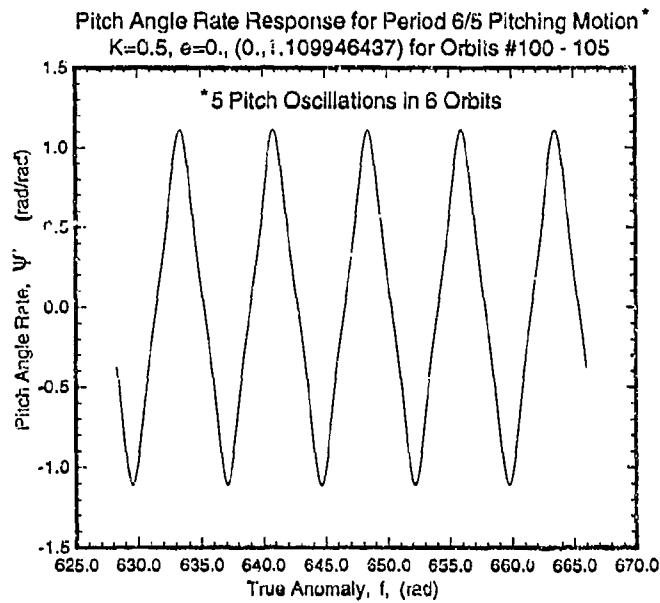
Figure 4.32: Pitch Angle Rate Response for $P = 5/6$ Libration: $K = 0.5$, $e = 0.$, and $(0., 1.109946437)$ for Orbits #100-105.
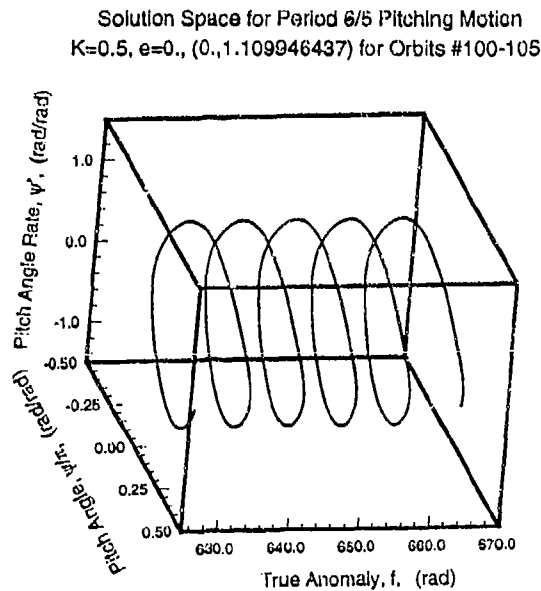


Figure 4.33: Solution Space Plot for $P = 5/6$ Libration: $K = 0.5$, $e = 0.$, and $(0., 1.109946437)$ for Orbits #100-105.

**Phase Space Plot for Period 6/5 Pitching Motion***
K=0.5, e=0., (0 , 1.109946437) for Orbits #100 - 105

*5 Pitch Oscillations in 6 Orbits
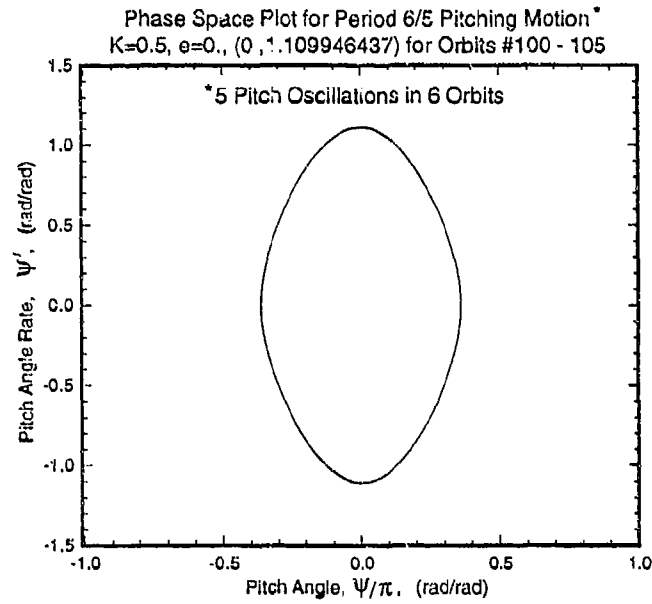
Figure 4.34: Phase Space Plot for $P = 5/6$ Libration: $K = 0.5$, $e = 0.$, and $(0., 1.109946437)$.



**Poincare' Plot for Period 6/5 Pitching Motion***
K=0.5, e=0., (0.,1.109946437)

* 5 Oscillations in 6 Orbits
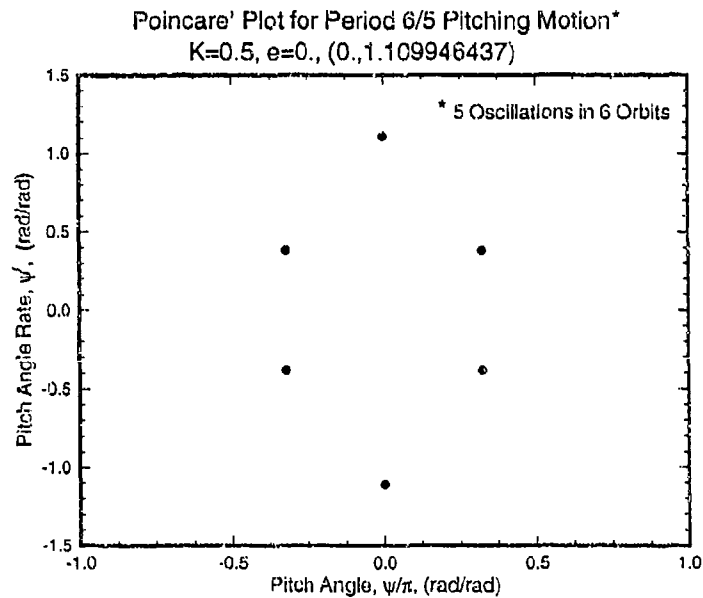
Figure 4.35 Poincaré Plot for $P = 5/6$ Libration: $K = 0.5$, $e = 0.$, and $(0., 1.109946437)$.
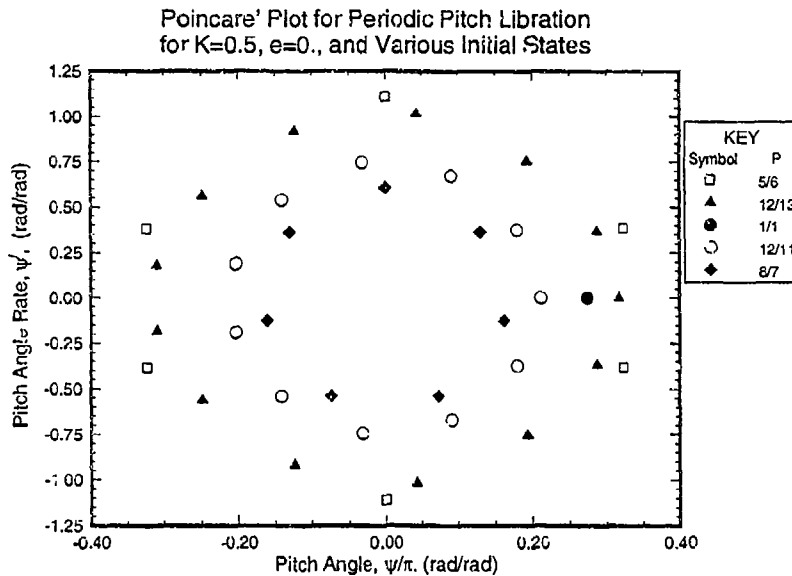
Figure 4.36:  Representative Poincaré Plot for Unstable Periodic Libration for $K = 0.5$, $e = 0.$, and Various Initial States.

symbols in this plot indicate the fixed points of the $P = 5/6$ solution that was shown in more detail in the preceding plots. The other symbols represent the fixed points of the other periodic librations as seen in the key for this plot. Note that as the winding number (frequency) increases from $5/6$ to $8/7$, the fixed points move closer to the origin. The unstable $1/1$ solution shown in this figure is different from the stable and unstable $P = 1/1$ solutions displayed in Figures 4.4 and 4.5, for which $\psi$ is constant and $\psi'$ is zero for all $f$. For the unstable $1/1$ libration case of Figure 4.36, the state vector is not constant for all $f$, but it is for every periapsis passage. In other words, $\psi(f_o) = \psi(f_o + 2n\pi) \approx 49.3$ deg, and $\psi'(f_o) = \psi'(f_o + 2n\pi) = 0$ where $n = 1, 2, 3, \ldots$ An orbit-attitude caricature of this particular trajectory is presented in Figure 4.37.

Because phase plots and Poincaré maps are constructed from a limited sampling of initial conditions, they only depict a few of the infinite number of possible curves. Figure 4.38 presents a combination of some of the possible quasiperiodic and periodic solutions previously shown in one Poincaré mapping.

## 4.2.5  Summary

In this section the pitching motion for a gravity-gradient satellite in a circular orbit about a central body has been shown to either be tumbling or libration and either

$\Psi_4 = -49.3$ deg
$\Psi_4' = 0$

$\Psi_5 = -36.2$ deg
$\Psi_5' = +.58$

4

$\Psi_3 = -36.2$ deg
$\Psi_3' = -.58$

5

3

$\Psi_6 = 0$ deg
$\Psi_6' = .93$

$\Psi_2 = 0$ deg
$\Psi_2' = -.93$

6

2

$f_1$

$\Psi_7 = 36.2$ deg
$\Psi_7' = .58$

7

1

$\Psi_1 = 36.2$ deg
$\Psi_1' = -.58$

0, 8

periapsis

$\Psi_0 = \Psi_8 = 49.3$ deg
$\Psi_0' = \Psi_8' = 0$
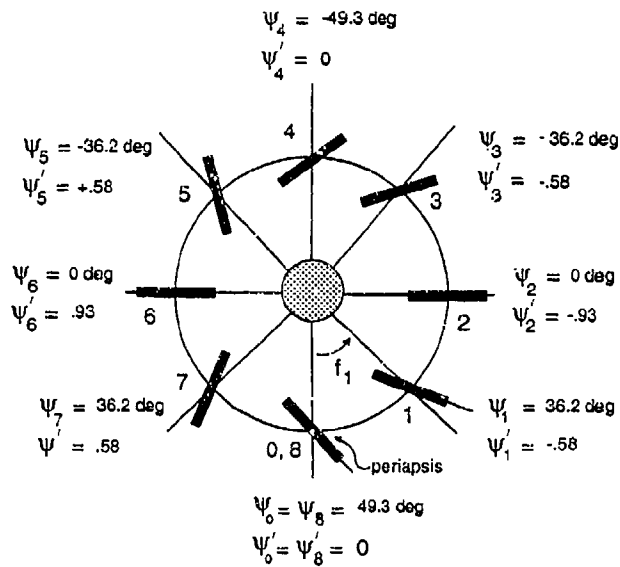
Example Unstable Period 1/1 Trajectory: K=0.5, e=0.

Figure 4.37: Example Unstable $P = 1/1$ Libration Trajectory: $K = 0.5$, $e = 0.$, and (49.33573 deg, 0.).

Poincare' Map for K=0.5, e=0.0, and
Various Initial States

Tumbling (Circulation)

P=1/1 Solutions

Unstable P=1/1

P=5/6

Libration

P=8/7

Approximate Separatrix

Pitch Angle Rate, $\Psi'$, (rad/rad)

Pitch Angle, $\Psi/\pi$, (rad/rad)
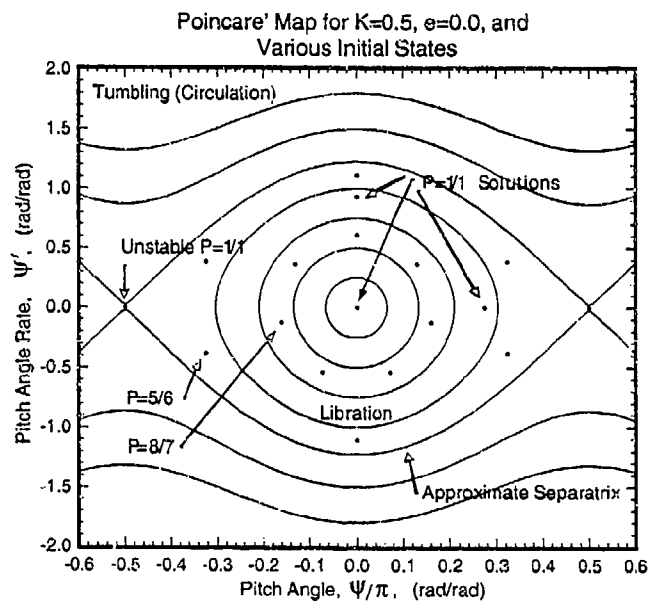
Figure 4.38: Poincaré Map for $K = 0.5$, $e = 0.$, and Various Initial States.

59

periodic or quasiperiodic. Analytical solutions were developed to describe each of these types of motion and example solutions were presented. Numerically obtained example trajectories were also presented for each type of motion, and many were accompanied by example Poincaré maps, phase diagrams, and solution space plots. The contribution of this work for the circular orbit problem lies mainly in providing a more complete examination of this problem for arbitrary values of inertia ratio.

# 5　Eccentric Orbit Case

## 5.1　Introduction

From Section 2, the pitch equation of motion for a gravity-gradient satellite in an elliptical orbit about a central body is

$$\frac{d^2\psi}{df^2}\left(1 + e\cos f\right) - 2e\left(\frac{d\psi}{df} + 1\right)\sin f + \frac{3}{2}K\sin 2\psi = 0. \tag{5.1}$$

This is a nonlinear equation with both system parameters acting as coefficients to nonlinear terms. Thus, one expects both $e$ and $K$ to affect the nonlinearity of the system, particularly if the common limiting assumption of small values of pitch angle is not made and the $\sin 2\psi$ term is not replaced with $2\psi$.

The objective of this section is to examine the nonlinear pitching motion of a satellite that the above equation models. This is accomplished through the examination of the different types of motion possible for this system, namely periodic, quasiperiodic, and chaotic trajectories. Sequences of bifurcation diagrams, Poincaré maps, Lyapunov exponents, and chaos diagrams are presented to help describe these types of motions and to investigate the location and fractal form of the boundary between chaotic and regular motion in parameter and phase space. The structure of the chaos diagrams is also examined. Analytical periodic pitch solutions for an axially symmetric satellite are presented and periodic formations in the bays of regular motion in the chaos diagrams for non-zero values of inertia ratio are observed.

### 5.1.1　Definition of Terms

Before getting underway, it is useful to briefly define some of the terms used in this and in later sections. [1]

The term "separatrix" was briefly discussed in the last section. Separatrices are simply trajectories in phase space that separate the phase space into regions where different types of motion occur, connecting saddle points and enclosing centers. A

---

[1] The language of this relatively new field is still transient and can be confusing. Often two or three different names for the same phenomenon or phase space structure appear in the literature.

Poincaré map is a subspace of the phase space and the sequential mapping of a trajectory into this subspace can form structures similar to that found in the phase space. Thus, the literature often uses the term "separatrix" or "heteroclinic orbit" for the equivalent appearing structure in a Poincaré map. A separatrix or heteroclinic orbit in a surface of section, however, connects two "hyperbolic fixed points" instead of saddle points.

A hyperbolic fixed point in the Poincaré map represents an unstable steady state or periodic orbit. Similarly, an "elliptic fixed point" represents a stable steady state or periodic orbit. These points are types of "critical points" which lie on, or are connected by, "manifolds." A manifold is simply a continuous curve composed of a collection of points in a Poincaré map. More technically, a manifold or "invariant curve" is a subspace of phase space where a trajectory with initial conditions in the manifold remains in the manifold for all time under the action of the equations of motion. Stable ($W^s$) and unstable ($W^u$) manifolds are merely the invariant curves that approach and recede (exponentially slowly) from a hyperbolic fixed point, and are thus parts of the heteroclinic orbit.

An attractor is a point, or set of points (a subspace of phase space,) that a trajectory approaches after the transients die out. Attractors are the structures in phase space that the trajectories are eventually drawn to, such as a limit cycle, an equilibrium point, a sink, or a strange attractor. A conservative system really has no attractors since there is no dissipation and hence no real transients, although some references nonetheless call stochastic regions attractors.

In this report the terms stochastic and chaotic have been (and will be) used interchangably for Hamiltonian systems. This is typical in most references although some caution is due. Stochastic means random, which is precisely the behavior of a chaotic trajectory of a Hamiltonian system *after some initial increment of time.* It takes a finite amount of time or, for this problem, a finite change in true anomaly before the motion of a chaotic trajectory is truly stochastic or random. In other words, the long-term behavior of a chaotic trajectory is stochastic although the transient behavior need not be.

## 5.1.2   Hamiltonian Chaos

The planar pitching problem examined here is a Hamiltonian system -- that is a system with no dissipation and in which all forces can be derived from a potential. For zero eccentricity, the solution to the equation of motion is well understood and chaos cannot occur. The Hamiltonian for the circular orbit case is integrable and the

62

phase space trajectories are confined to a two-dimensional torus manifold. The values of the two frequencies (pitch and true anomaly) determine the motion. An irrational winding number produces quasiperiodic motion, appearing as a closed curve on a surface of section. On the torus manifold, however, quasiperiodic motion means that a single orbit will ultimately uniformly cover the torus. Integer combinations of the frequencies produces periodic motion: closed orbits on the torus, and points on the Poincaré map.

For non-zero values of eccentricity, however, Equation (5.1) describes a perturbed Hamiltonian system (by $e$) that is non-integrable. Nonlinear theory[2] points out that stochastic, or apparently random, motion (chaos) will always occur in such a system for any non-zero value of the perturbation parameter. Heteroclinic tangles form around the separatrices of harmonic and subharmonic solutions (the heteroclinic orbits), giving birth to layers of chaos in the vicinity of the separatrices. These areas of chaos are bounded by invariant curves. Trajectories cannot cross these boundaries and a trajectory that is initially chaotic (regular), remains chaotic (regular) for all time.[3] Hence, the pitch angle can experience either regular or chaotic motion for various initial states and values of the system parameters, $e$ and $K$. Both types of motion may occur at a very close proximity to each other in phase space, and the transition between the two types of behavior can be complex. Although these regions of chaos exist for any non-zero value of eccentricity, their area of the phase space tends towards zero as $e \rightarrow 0$.

Figure 5.1 illustrates some of this nomenclature as well as providing a little insight into the formation of chaotic regions in the Poincaré map for the eccentric orbit case. For an unperturbed system such as for the circular orbit case, the Poincaré map is very simple. Separatrices or heteroclinic orbits connect the hyperbolic points and only regular motion can exist. The two incoming trajectories to each hyperbolic point are the stable manifolds and the outgoing trajectories are the unstable manifolds. The unstable manifold emanating from one hyperbolic point joins smoothly with the stable manifold entering another hyperbolic point. When subjected to a perturbation such as the eccentric orbit terms, however, the stable and unstable manifolds intersect transversely forming a "heteroclinic point". Topologically, if a single intersection exists, an infinite number of other intersections must also exist, leading to a infinitely many heteroclinic points. This forms a "heteroclinic tangle"[4], a small portion of

---

[2]Percival [38] and Chernikov et al. [39] provide excellent overviews of Hamiltonian chaos theory. More detailed approaches can be found in [40], [41], and [42].

[3]This is only true for non-dissipative systems. Damping destroys the invariant curves allowing transient chaos to occur and, possibly, strange attractors to exist. Dissipative system chaos is discussed in more detail in Section 7.

[4]Heteroclinic orbits, points, and tangles would be called "homoclinic" if the stable and unstable
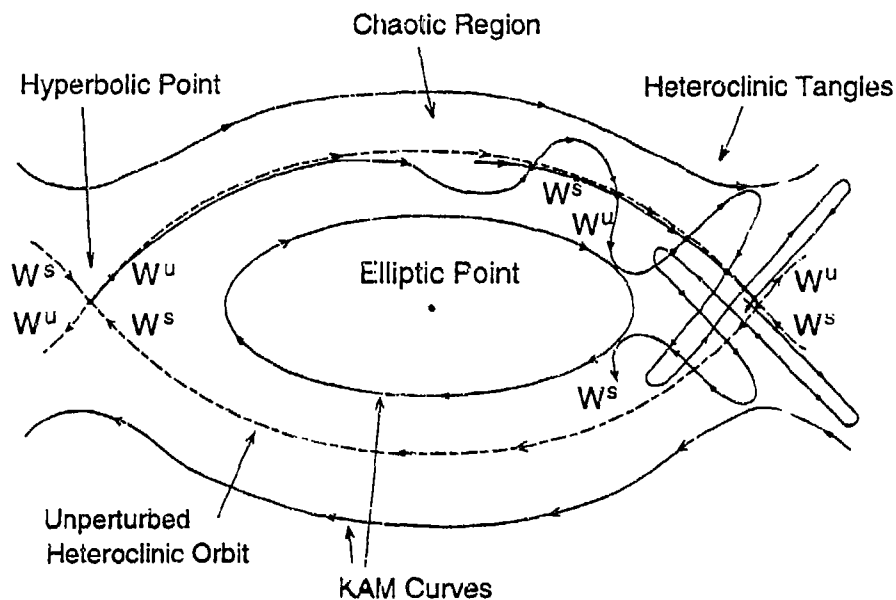
Figure 5.1: Nomenclature an ... : Formation of Heteroclinic Tangles in the Poincaré Map

which is shown on the right side of Figure 5.1. A heteroclinic tangle gives us chaotic or stoch...:ic motion in the vicinity of the unperturbed heteroclinic orbit.

The areas of chaos in a Poincaré map are also known as "resonance layers". They are bounded by invariant curves called KAM curves (after the highly acclaimed works of Kolmogorov, Arnold, and M ser), which are closed paths on the Poincaré map representing quasipe ...lic motion, and they increase in size as the perturbation increases. KAM the ry 1 r nonli ear H. iltonian systems states that for an integrable Hamiltonian syste u perturbe ich that it becomes non-integrable, invariant surfaces continu to exist for most ... .i conditions. This means that although the motion about the separatrices is s icu..:tic. it is constrained by KAM curves, ie. regular motion still exists for small perturbations.

In most past exaiiinations of chaos, eccentricity is viewed as a small parameter and the above theory works well. For moderate and large values of eccentricity, however, $e$ is no longer a small perturbation and the appearance of chaos in this system depends also on the other system parameter, $K$.

---

manifolds entered and left the same hyperbolic fixed point.

## 5.1.3 Transition Between Regular and Chaotic Motion

Because chaos is usually highly localized for a perturbed Hamiltonian system, it is often difficult to define a precise criteria for the onset of "global" chaos over a large range of system parameters and initial states. This transition is often subjectively defined as the point where most of the phase space becomes covered by stochastic regions, and it is occasionally more qualitatively defined in terms of a particular percentage of the phase space where chaos occurs.

Numerous techniques exist for predicting the transition from regular to chaotic motion and from local to global chaos. Chirikov's resonance overlap method [43] is an analytical method which provides an estimate for the transition to global chaotic motion as a function of the perturbation parameter. It was applied to this problem by Tong and Rimrott [20] for $K = 1$ and under-predicted their numerically determined value of eccentricity for the onset of global chaos by roughly 50%. Melnikov's method (a useful analytical tool for predicting the transition to local chaotic motion in terms of the system parameters) cannot be applied to Equation (5.1) because the eccentricity perturbation is not dissipative. It has, however, been applied to the gravity-gradient problem supplemented with additional terms (see [18], [19], and [24], for example) although limited to only small values of $e$.[5]

A number of numerical transition prediction techniques also exist. Fourier spectra of trajectories can give particularly useful information about the transition process itself. Sensitivity analysis of a system on its initial conditions may deliver reasonable estimates for the onset of chaos, as shown by Tortorelli and Vakakis [25]. Sequences of Poincaré maps can provide estimates for the onset of both local and global chaos over a large range of initial states for a particular set of system parameters. Lyapunov exponents typically provide an accurate, if computationally expensive, determination of whether a trajectory is regular (periodic or quasiperiodic) or chaotic. When grids of Lyapunov exponents are computed and formed into chaos diagrams, one obtains a useful method for determining the onset of chaos over large ranges of the system parameters for particular initial states.

---

[5]The Melnikov method is discussed in more detail and is applied to two damping cases in Section 7.
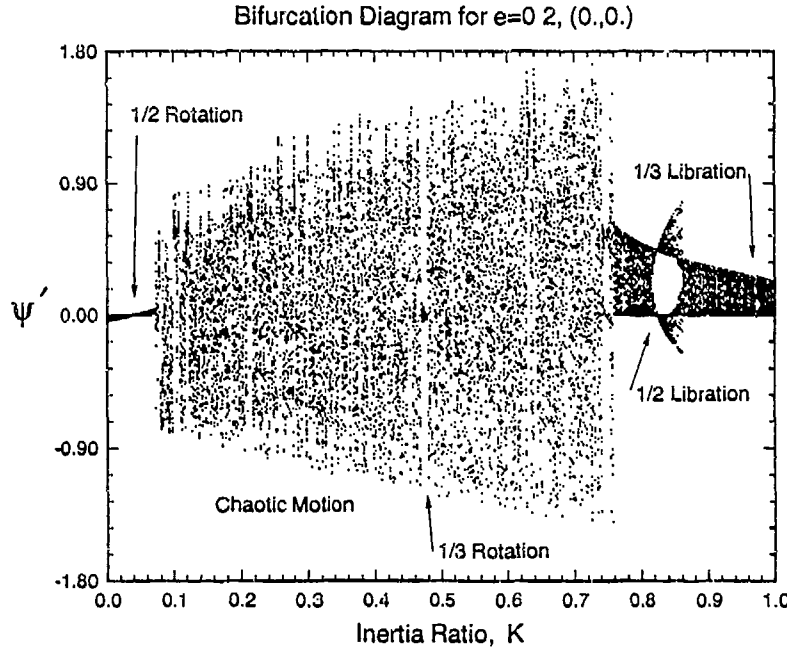
Figure 5.2: Bifurcation Diagram for $\epsilon = 0.20$, $(0., 0.)$.

## 5.2  Types of Motion

Figure 5.2 presents an example bifurcation diagram of pitch rate with inertia ratio as the bifurcation parameter and for $\epsilon = 0.2$. A complicated mixture of chaotic and regular motion occurs for different values of $K$. The regular motion is primarily quasiperiodic but a number of periodic solutions also exist of which a few are labeled in this plot. As for the circular orbit case, the regular motion may be classified as either periodic or quasiperiodic and either librational or rotational. It will be shown later that although the pitching motion for the circular orbit case is restricted to either libration or tumbling, the eccentric case allows for a seemingly random combination of these two types of motion in a chaotic trajectory.

Closer examination of this bifurcation diagram and accompanying phase diagrams reveals an interesting feature. Only rotational motion occurs in the regular motion band for small values of inertia ratio and in the tiny band close to $K = 0.48$, whereas the region of regular motion for large $K$ is inhabited only by librational trajectories. This bifurcation diagram serves as a source of example trajectories to briefly study.
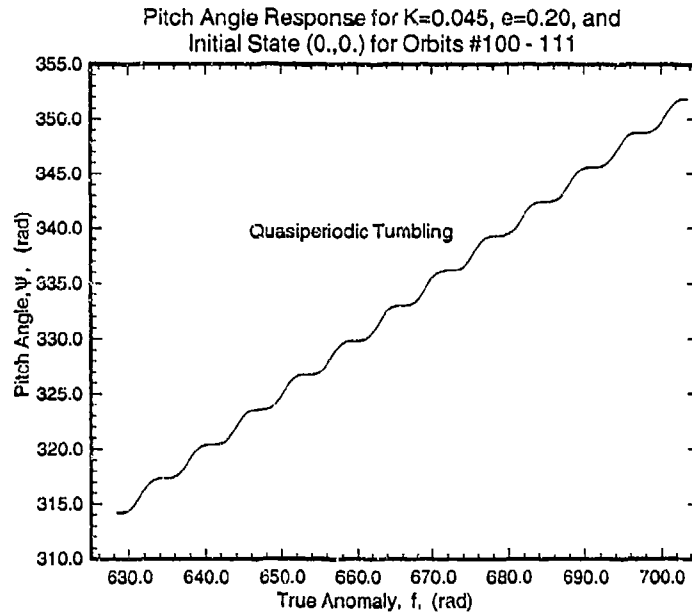
Figure 5.3: Pitch Angle Response for a Quasiperiodic Rotational Trajectory: $K = 0.045$, $e = 0.20$, $(0., 0.)$ for Orbits #100-111.

## 5.2.1 Tumbling (or Rotational) Motion

The first example trajectory is quasiperiodic tumbling at $K = 0.045$ near the $P = 1/2$ rotation solution depicted in Figure 5.2. Pitch angle versus true anomaly is presented in Figure 5.3 for 12 orbits. This orbit is nearly periodic with a frequency ratio or winding number of close to $1/2$; about 56 tumbling revolutions occur over the first 112 orbits. Pitch angle increases monotomically due to a continuously non-negative pitch rate (Figure 5.4).

The phase diagram for this trajectory, calculated by integrating the equation of motion over twelve orbits, is presented in Figure 5.5. The phase space pattern would be a solid band if enough orbits were integrated and a simple curve if the rotational trajectory had an exact winding number of $1/2$. The Poincaré map for this trajectory is given in Figure 5.6.

Already significant differences can be found between the circular and elliptical orbit cases. The phase diagrams and their corresponding Poincaré maps for the circular orbit case were identical (compare Figures 4.18 and 4.38) since the phase space remained constant with true anomaly. Adding eccentricity to the problem
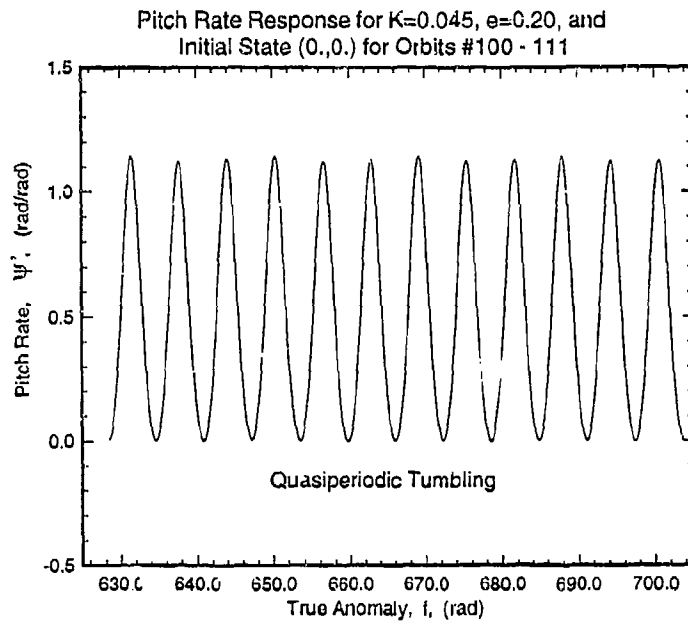
Figure 5.4: Pitch Rate Response for a Quasiperiodic Rotational Trajectory: $K = 0.045$, $e = 0.20$, $(0., 0.)$ for Orbits #100-111.
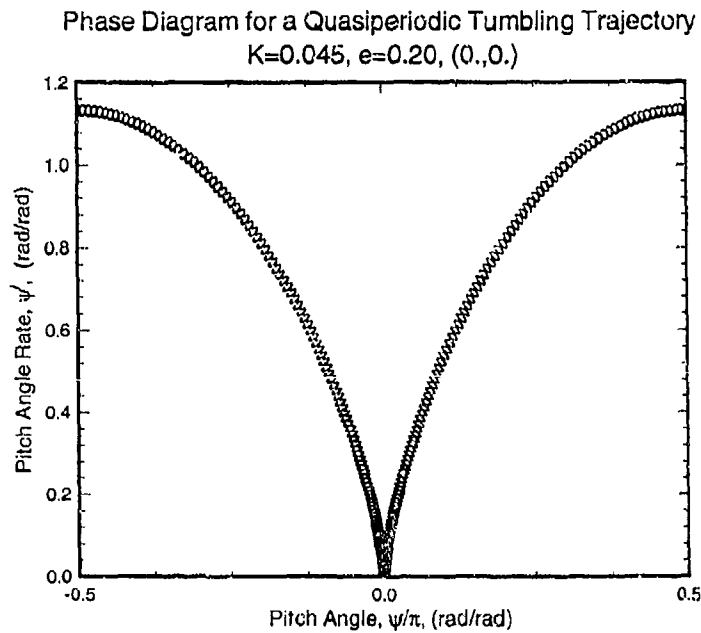


Figure 5.5: Phase Diagram for a Quasiperiodic Rotational Trajectory: $K = 0.045$, $e = 0.20$, $(0., 0.)$.
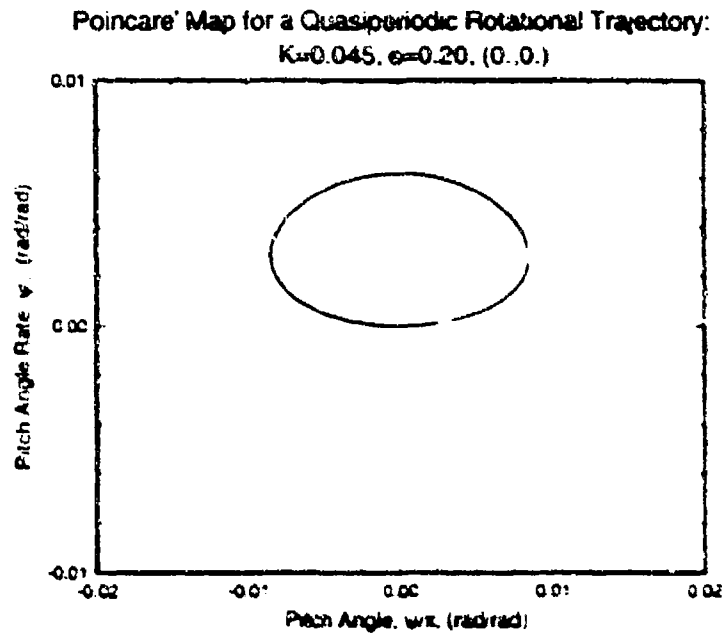
**Figure 5.6:** Poincaré Map for a Quasiperiodic Rotational Trajectory: $K = 0.045$. $e = 0.20$, $(0..0.)$.

complicates the analysis, in effect adding another dimension to the problem. The pitch dynamics now vary as true anomaly varies and the Poincaré map collects only a portion (only the data at periapsis) of the data viewed in its corresponding phase space diagram.

A second example tumbling trajectory, this one with a frequency ratio of $P = 1/3$, is described by Figures 5.7 - 5.9. The first plot presents the pitch angle response over 30 orbits for the $P = 1/3$ tumbling trajectory, depicted in Figure 5.2 between the two large regions of chaotic motion. The periodic oscillatory component of the tumbling motion produces 10 oscillations for this 30 orbit period of true anomaly.

In general, tumbling motion is actually a combination of pure rotation and pure libration. This can be seen in the plot of pitch rate versus true anomaly in Figure 5.8. Here pitch rate can be viewed as having two components, a rotational part composed of the non-negative portion of the large spike, and a libration part comprised of the remaining portion of the oscillation. The phase diagram for this example trajectory appears in Figure 5.9, and further emphasizes the duality of the tumbling motion.

69
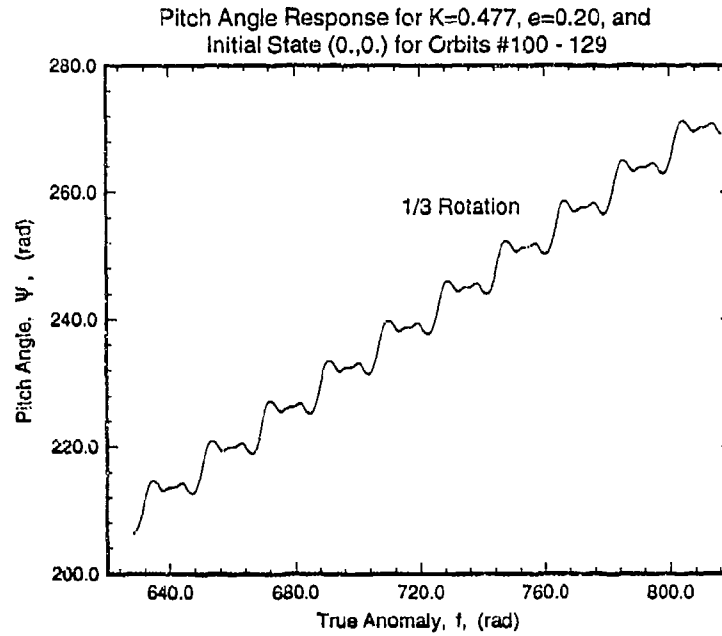
Figure 5.7: Pitch Angle Response for a $P = 1/3$ Rotational Trajectory: $K = 0.477$, $e = 0.20$, $(0., 0.)$ for Orbits #100-129.
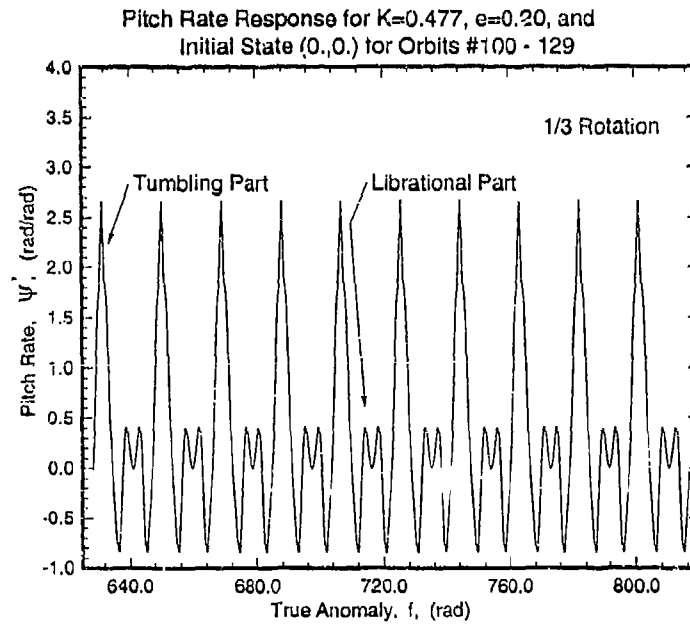


Figure 5.8: Pitch Rate Response for a $P = 1/3$ Rotational Trajectory: $K = 0.477$, $e = 0.20$, $(0., 0.)$ for Orbits #100-129.

70
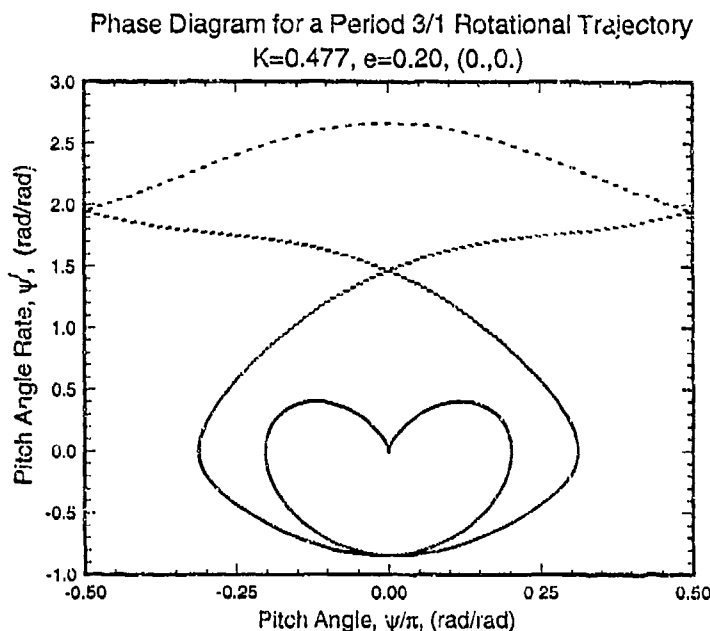
Figure 5.9: Phase Diagram for a $P = 1/3$ Rotational Trajectory: $K = 0.477$, $e = 0.20$, $(0., 0.)$.

## 5.2.2 Librational Motion

Figures 5.10 and 5.11 present an example of quasiperiodic libration for a value of $K = 0.8$ from the right side of Figure 5.2. In general, a very convenient feature of phase diagrams is that they provide information about the limits of the state variables for the complete range of $f$ that they were integrated over. For example, Figure 5.11 depicts the phase diagram for this case over 30 orbits, and shows that pitch angle is constrained to be less than about $\pm.16$ radians (approximately 9.2 degrees) for the *entire range* of true anomaly over these 30 orbits. In contrast, the Poincaré maps show the state limits only at the values of true anomaly corresponding to periapsis.

Recall that a limited portion of the phase diagram for a quasiperiodic trajectory (either librational or rotational) would be completely filled if enough orbits were integrated. Figure 5.12 emphasizes this notion; it is identical to Figure 5.11 except that it displays the phase diagram over 90 orbits instead of 30. The Poincaré map for this trajectory (Figure 5.13) does not show these limits but it does reveal the trajectory to be quasiperiodic at a quick glance.

Figures 5.14 and 5.15 display subharmonic libration of frequency 1/3 for the

71
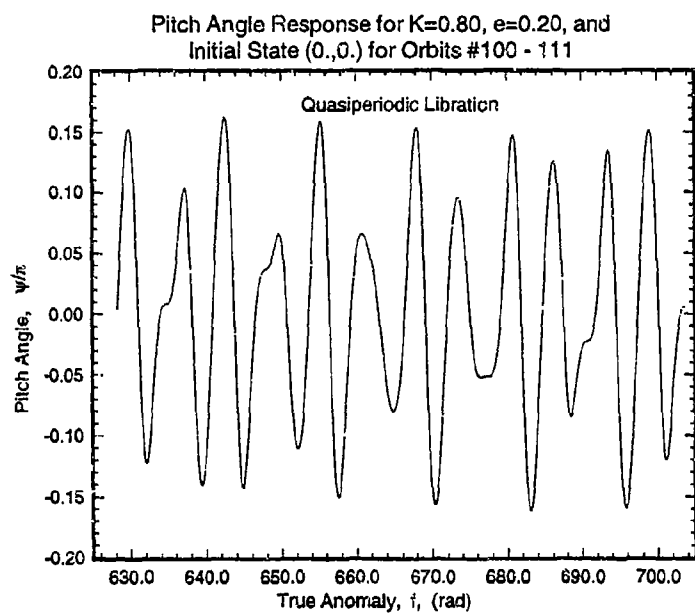
Figure 5.10: Pitch Angle Response for a Quasiperiodic Librational Trajectory: $K = 0.80$, $e = 0.20$, $(0., 0.)$ for Orbits #100-111.
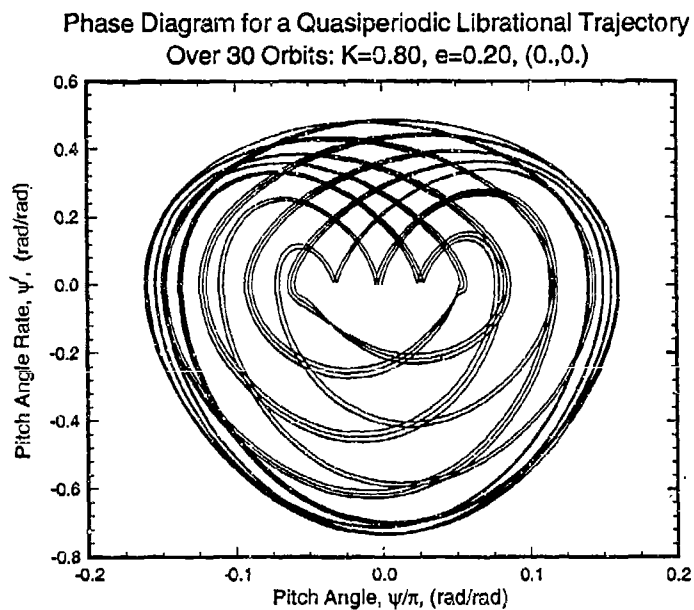


Figure 5.11: Phase Diagram for a Quasiperiodic Librational Trajectory Over 30 Orbits: $K = 0.80$, $e = 0.20$, $(0., 0.)$.

72
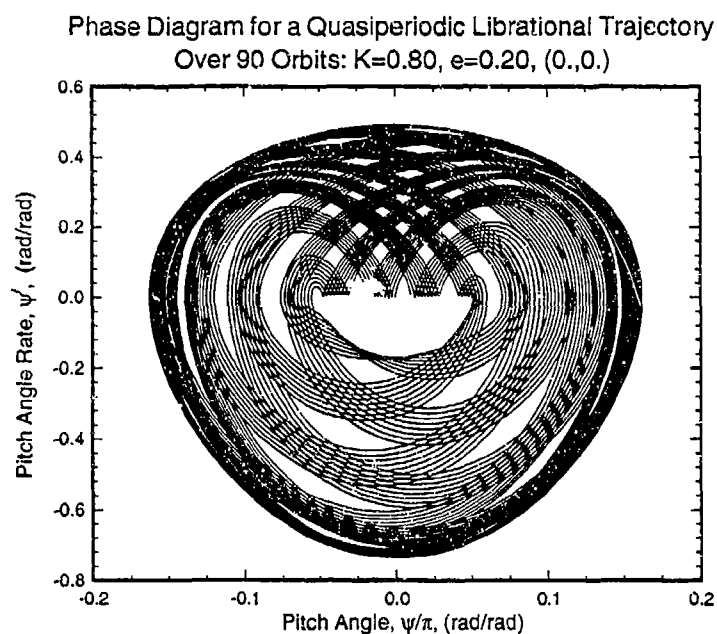
Figure 5.12: Phase Diagram for a Quasiperiodic Librational Trajectory Over 90 Orbits: $K = 0.80$, $e = 0.20$, $(0., 0.)$.
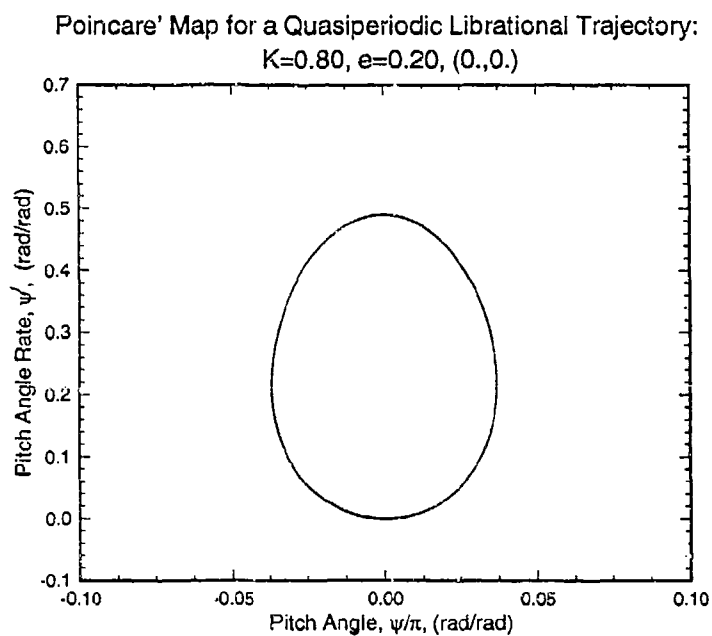


Figure 5.13: Poincaré Map for a Quasiperiodic Librational Trajectory: $K = 0.80$, $e = 0.20$, $(0., 0.)$.
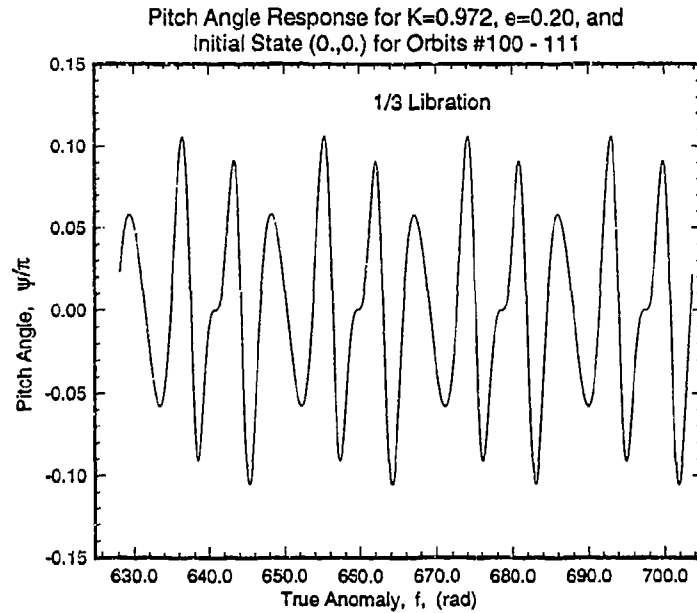
Figure 5.14: Pitch Angle Response for a $P = 1/3$ Librational Trajectory: $K = 0.972$, $e = 0.20$, $(0., 0.)$ for Orbits #100-111.

trajectory labeled in Figure 5.2 at $K = 0.972$. Four complete pitch oscillations are clearly visible over the 12 orbits displayed in Figure 5.14, and the periodicity of the trajectory is obvious from the phase diagram of Figure 5.15. Unlike the quasiperiodic case discussed above, the phase diagram for this trajectory is fixed regardless if the trajectory is calculated over one orbit or a thousand.

## 5.2.3 Chaotic Motion

The above results have shown that quasiperiodic and periodic librational and tumbling trajectories for an eccentric orbit look similar to their circular orbit counterparts. Chaotic motion becomes possible for the system with the addition of the orbit eccentricity to the problem. Two example chaotic trajectories are presented below. The first is chaotic tumbling with relatively small oscillatory components over most of the 30 orbits. This trajectory, for an inertia ratio of $K = 0.2$, is in the chaotic region of the bifurcation diagram of Figure 5.2 sandwiched by two regions of regular rotational motion. As such, it exhibits primarily rotational motion as displayed in the pitch angle versus true anomaly plot of Figure 5.16 and in its phase diagram of Figure 5.17. Only one libration-like path can be seen in the bottom of the phase diagram (compare to the phase diagrams for tumbling and libration in Figures 5.11 and 5.5,

Phase Diagram for a Period 3/1 Librational Trajectory
K=0.972, e=0.20, (0.,0.)
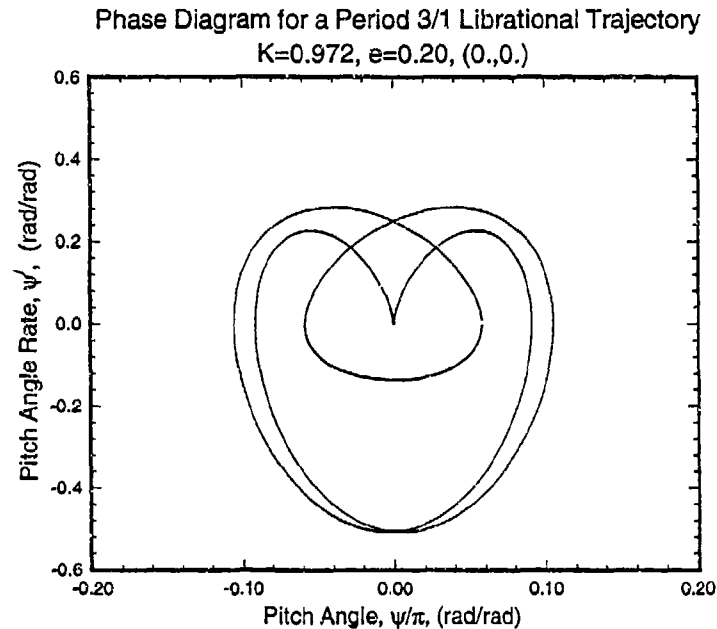


Figure 5.15: Phase Diagram for a $P = 1/3$ Librational Trajectory: $K = 0.972$, $e = 0.20$, $(0., 0.)$.

for example) over the 30 integrated orbits.

The second example chaotic trajectory, from the chaotic region at $K = 0.60$ close to the librational portion of the bifurcation diagram of Figure 5.2, not surprisingly displays a great deal more of oscillatory-like motion than the previous example. Figures 5.18 and 5.19 both show this trajectory to be a mixture of rotation and oscillation.

The phase diagrams for these two chaotic example trajectories cover an extremely large portion of the phase space in comparison to the phase diagrams depicting regular motion. Remember that due to exponential divergence of neighboring chaotic trajectories, all accuracy is lost during the integration of the equation of motion after only a small number of integration steps. Hence, one will typically have no idea what the state of the satellite will be at an arbitrary $f$ -- it could be anywhere within the bounds set by the phase diagrams. This contrasts sharply with the case of regular motion.

The Poincaré maps for these two example chaotic trajectories are presented in Figures 5.20 and 5.21 with the same scale for ease of comparison.
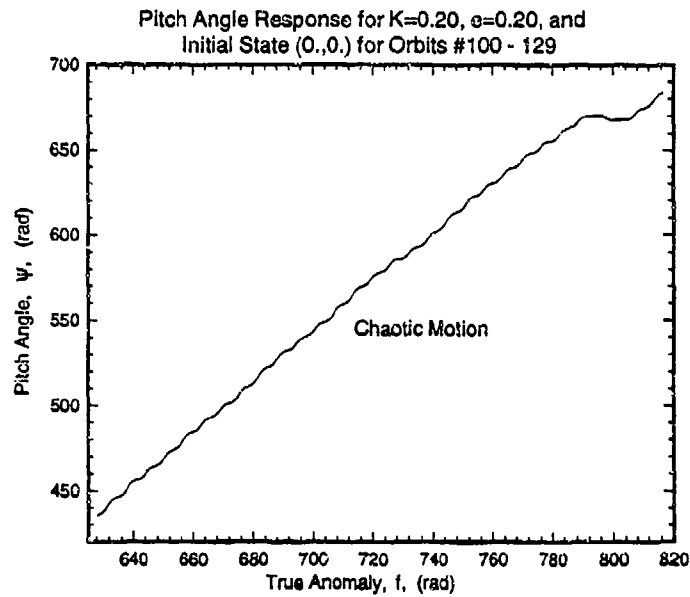
Figure 5.16: Pitch Angle Response for a Chaotic Trajectory for 30 Orbits: $K = 0.20$, $e = 0.20$, $(0., 0.)$ for Orbits #100-129.
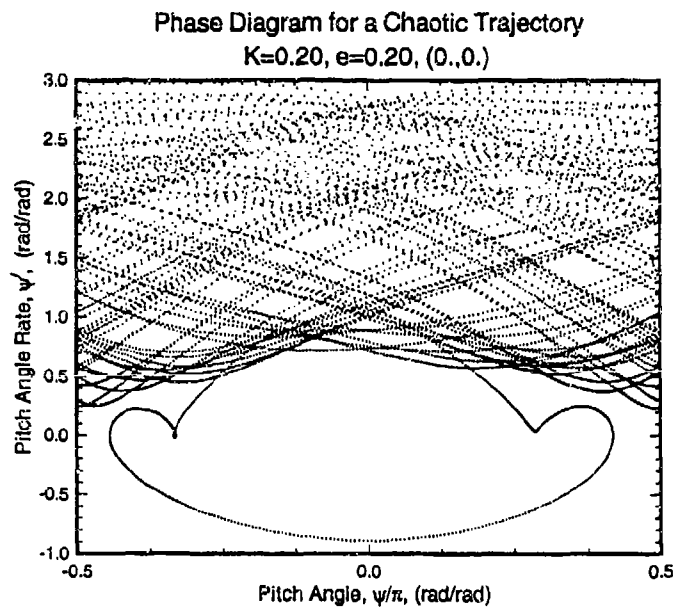


Figure 5.17: Phase Diagram for a Chaotic Trajectory for 30 Orbits: $K = 0.20$, $e = 0.20$, $(0., 0.)$ for Orbits #100-129.
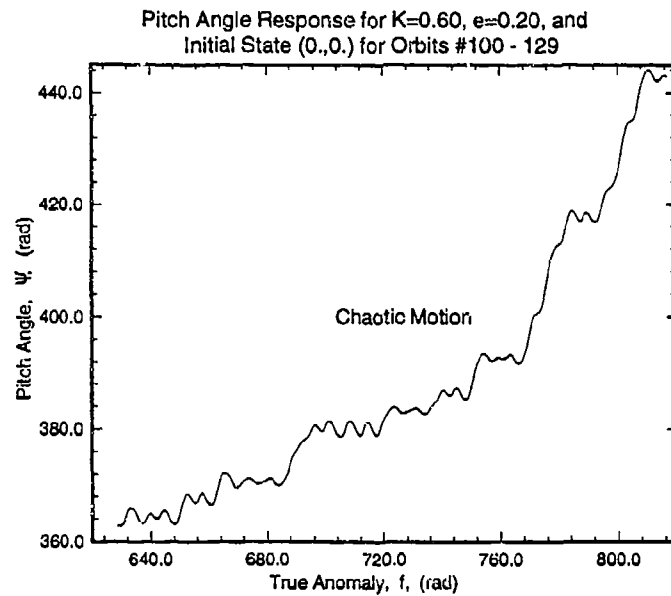
Figure 5.18: Pitch Angle Response for a Chaotic Trajectory for 30 Orbits: $K = 0.60$, $e = 0.20$, (0., 0.) for Orbits #100-129.
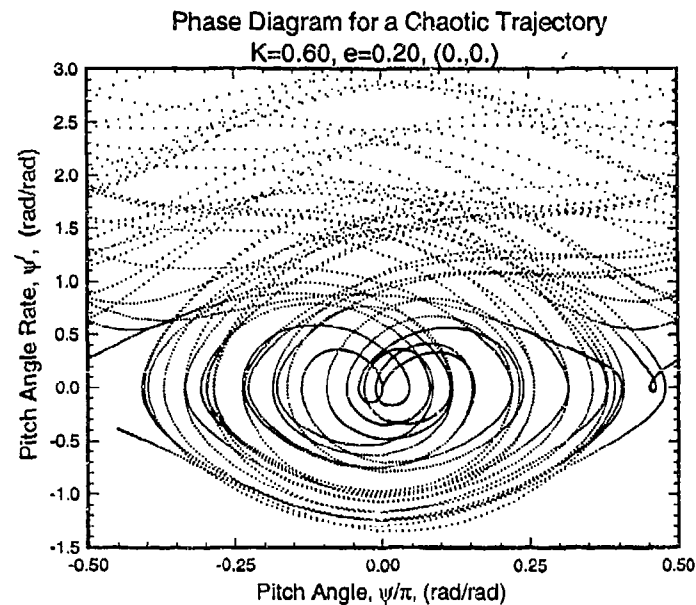


Figure 5.19: Phase Diagram for a Chaotic Trajectory for 30 Orbits: $K = 0.60$, $e = 0.20$, (0., 0.) for Orbits #100-129.
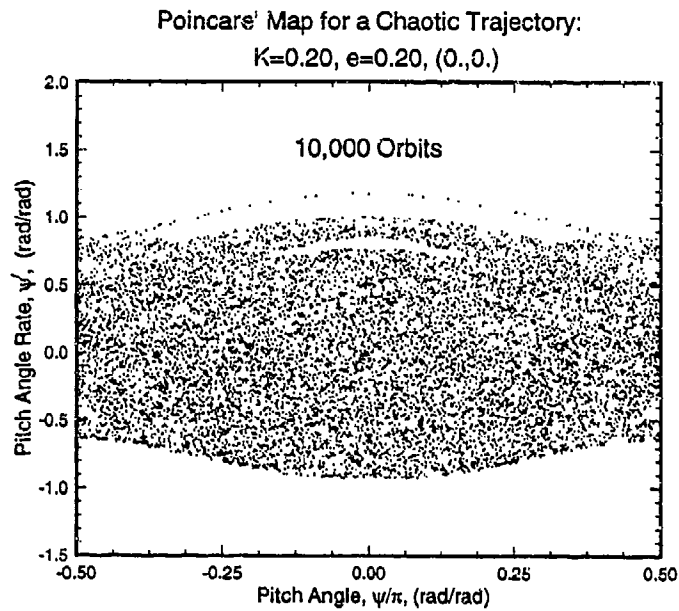
Figure 5.20: Poincaré Map for a Chaotic Trajectory for 10,000 Orbits: $K = 0.20$, $e = 0.20$, $(0., 0.)$.
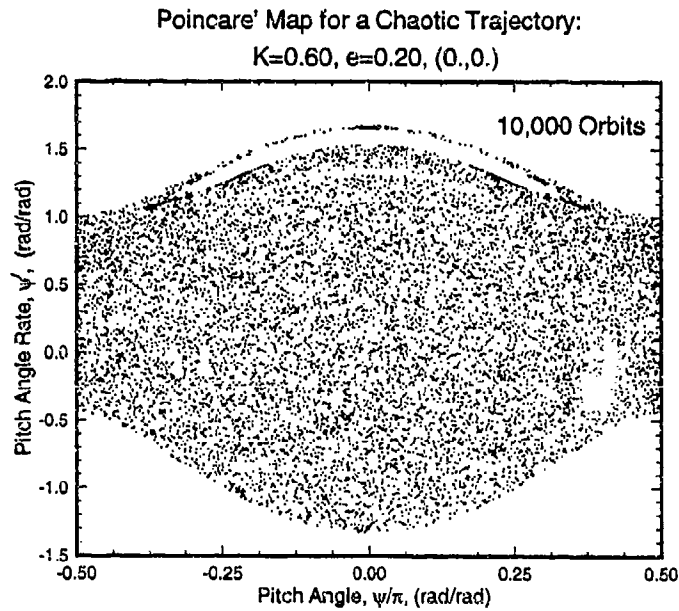


Figure 5.21: Poincaré Map for a Chaotic Trajectory for 10,000 Orbits: $K = 0.60$, $e = 0.20$, $(0., 0.)$.

The chaotic surfaces of section at periapsis for these two trajectories differ significantly in the amount of area covered by chaotic motion. The trajectory for the satellite with the smaller inertia ratio is constrained to a smaller area on the Poincaré map. Both plots demonstrate the stochastic or random qualities of Hamiltonian chaos; the chaotic regions in each of the Poincaré maps appear to be uniformly visited by the sole trajectory integrated over numerous orbits.[6]

## 5.3  Determining the Nature of the Motion

### 5.3.1  Determining the Motion via Poincaré Maps

Figures 5.22 - 5.25 present four Poincaré maps for eccentricities of $e = 0.0, .01, .075$, and 0.2, respectively, and for constant satellite inertia ratio, $K = 0.20$. The surface of section for the circular orbit case (Figure 5.22) displays the types of regular motion that exist for the unperturbed problem. Periodic motion may be observed in the stable $P = 1/1$ solution at the origin, which corresponds to the synchronous state where the satellite always points towards the central body. The unstable periodic equilibria at $(\pm\frac{\pi}{2}, 0.)$ correspond to the alignment of the satellite's minor moment of inertia with the local horizontal. The separatrices or heteroclinic orbits connect these unstable equilibria and separate the motion into two types: pitch tumbling, or circulation, which occurs outside the separatrices, and pitch libration, which occurs inside. Quasiperiodic orbits appear in this figure as islands about the origin. It is emphasized that Figure 5.22 depicts only a few of the infinite number of actual periodic and quasiperiodic solutions. $P = 3/4$ (3 pitch oscillations in 4 orbits) and 2/3 solutions occur, for example, for the initial conditions (0., .2705812) and (0., .527911), respectively. These and other resonances all have their own separatrices that may produce regions of chaos for some $e > 0$.

In agreement with nonlinear dynamics theory, the general trend of this sequence of Poincaré maps (and others – see Karasopoulos and Richardson [26]) is that an increase in eccentricity causes the area of phase space where chaotic motion occurs to enlarge while the area of regular motion decreases. More detailed information about the pitch motion may also be gleaned from these plots. Figure 5.23 indicates

---

[6]Chaos in a dissipative system generally is not stochastic. Instead of a seemingly random wandering over phase space, a chaotic trajectory for a dissipative system moves into some form of an attractor which is often fractal. More on this matter will be discussed in Section 7.
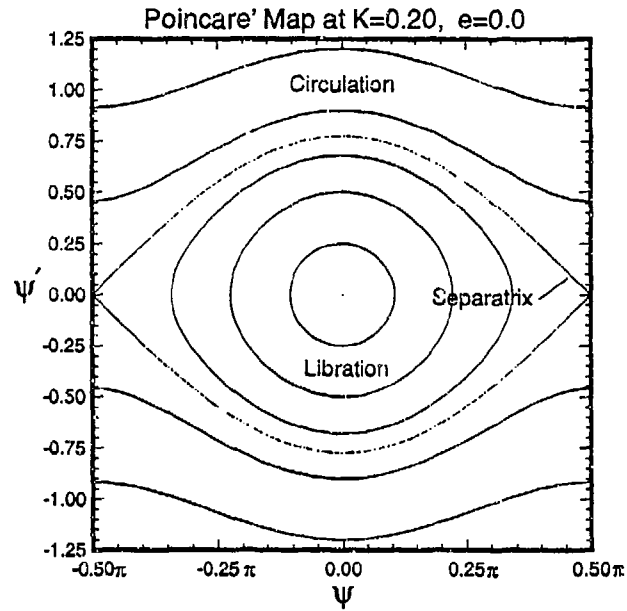
Figure 5.22: Poincaré Map for $K = 0.2$ and $e = 0.0$.
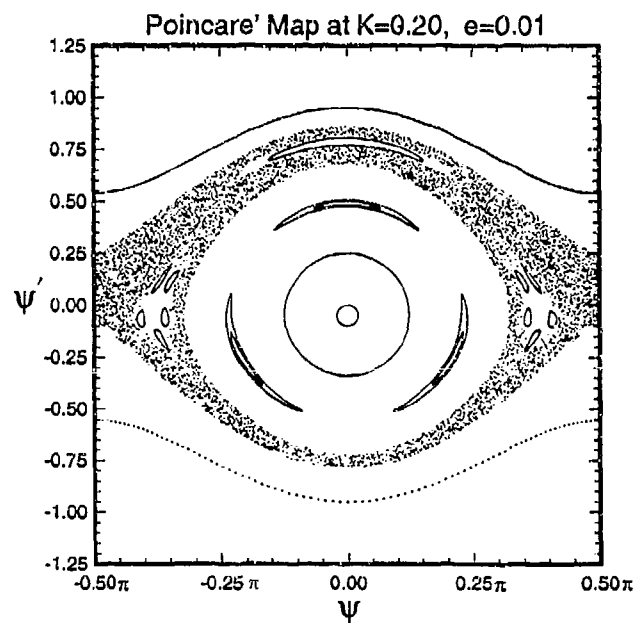


Figure 5.23: Poincaré Map for $K = 0.2$ and $e = .01$.
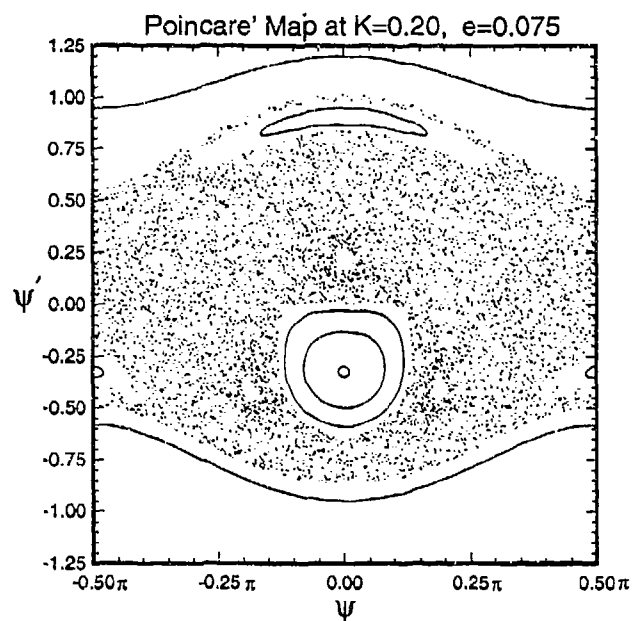
Figure 5.24: Poincaré Map for $K = 0.2$ and $e = .075$.
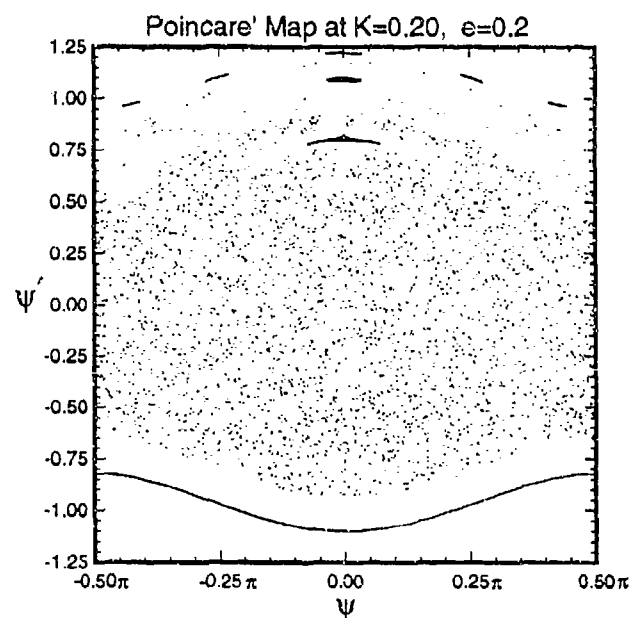


Figure 5.25: Poincaré Map for $K = 0.2$ and $e = .20$.

that necessary but insufficient approximate conditions for pitch libration to occur for $K = 0.20$ and $e = .01$ are $-.70 < \psi_o' < .80$, and for pitch tumbling to be possible, $\psi_o' > .85$ or $\psi_o' < -.75$. These bands of initial states where periodic or quasiperiodic pitch libration can occur are significantly reduced when eccentricity is increased to .075 (Figure 5.24), and almost non-existent at $e = 0.2$ in Figure 5.25. The Poincaré map of Figure 5.23 illustrates local chaos; the onset of global chaos occurs for some value of eccentricity between $e = .075$ (Figure 5.24) and $e = .2$ (Figure 5.25).

One may also use Poincaré maps to track the type of motion for a particular initial state over a variation in one of the system parameters. For example, consider the trajectory with the initial state $(\psi_o, \psi_o') = (0., 0.)$ and $K = 0.2$ in Figures 5.22 - 5.25. The trajectory with this initial condition is quasiperiodic but very close to a $P = 1/1$ solution for $e = .01$ (Figure 5.23), at the border between quasiperiodic and chaotic motion for $e = .075$ (Figure 5.24), and chaotic for $e = 0.2$ (Figure 5.25). Thus, one can examine sequences of Poincaré maps and obtain reasonable estimates for the onset of chaos. One advantage of using Poincaré maps for this purpose is that the type of motion may be determined very quickly for an entire area of initial states. One may deduce from Figure 5.24, for example, that not only does the particular initial state $(0., -.3)$ produce nearly periodic motion, but $(0., -.2)$ would as well. A disadvantage, however, is that two $(K$ and $e)$[7] detailed and lengthy sequences would generally have to be constructed to obtain accurate estimates of the parameter values at which the transition to chaotic motion occurs for a particular initial state. In contrast, chaos diagrams provide this information in only one plot.

Figures 5.26 - 5.29 display another example sequence of Poincaré maps for a fixed value of inertia ratio ($K = 0.10$) and varying eccentricity. Again the subset area of phase space of regular motion shrinks with increasing $e$, replaced with regions of chaotic motion. Islands of regular motion shrink with increasing $e$ and often change form.

Such sequences can also be constructed holding eccentricity constant and varying inertia ratio in an attempt to learn the general influence of $K$ on the system. Figures 5.30 - 5.33 present an example sequence for $e = 0.20$. Generally, as for the varying eccentricity sequences, increasing inertia ratio values cause the chaotic regions to increase in size. Regular motion trajectories appear and disappear in a seemingly random fashion as $K$ is varied, however, unlike the case for the variable eccentricity sequences discussed above.

---

[7]Previously reported work from this study (Karasopoulos and Richardson [26]) demonstrated transition to be a function of satellite inertia ratio, $K$, as well as eccentricity.

Poincare' Map for Numerous Trajectories:
K=0.10, e=0.01
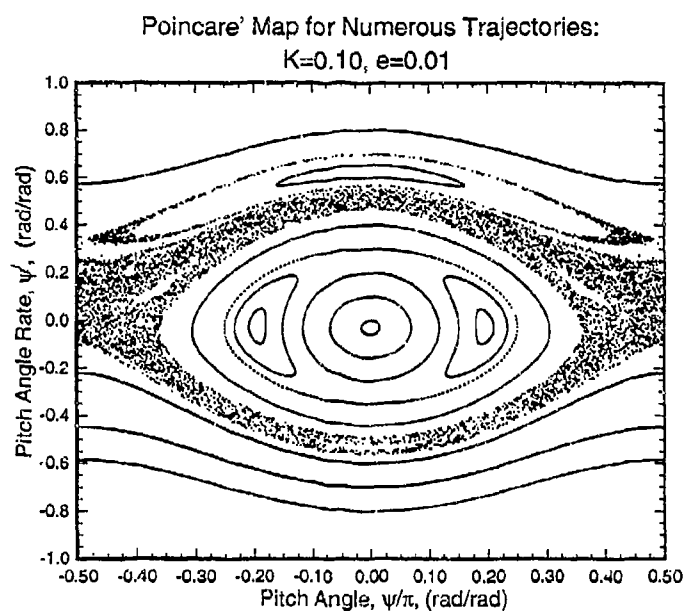


Figure 5.26: Poincaré Map for $K = 0.1$ and $e = .01$.

Poincare' Map for Numerous Trajectories:
K=0.10, e=0.05
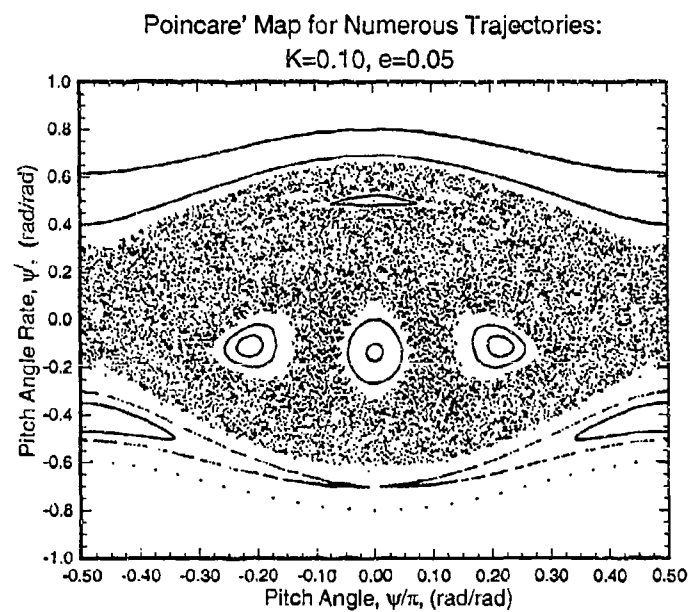


Figure 5.27: Poincaré Map for $K = 0.1$ and $e = .05$.

Poincare' Map for Numerous Trajectories:
K=0.10, e=0.10
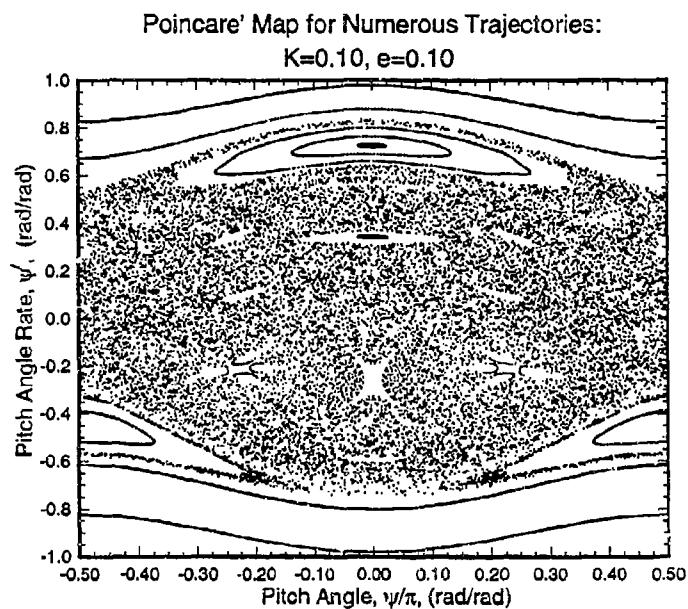


Figure 5.28: Poincaré Map for $K = 0.1$ and $e = .10$.

Poincare' Map for Numerous Trajectories:
K=0.10, e=0.30
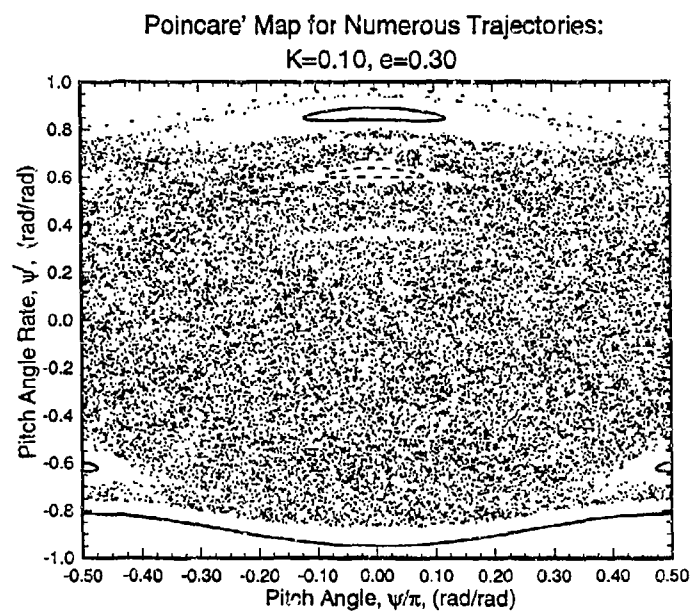


Figure 5.29: Poincaré Map for $K = 0.1$ and $e = .30$.

Poincare' Map for Numerous Trajectories:
K=0.10, e=0.20
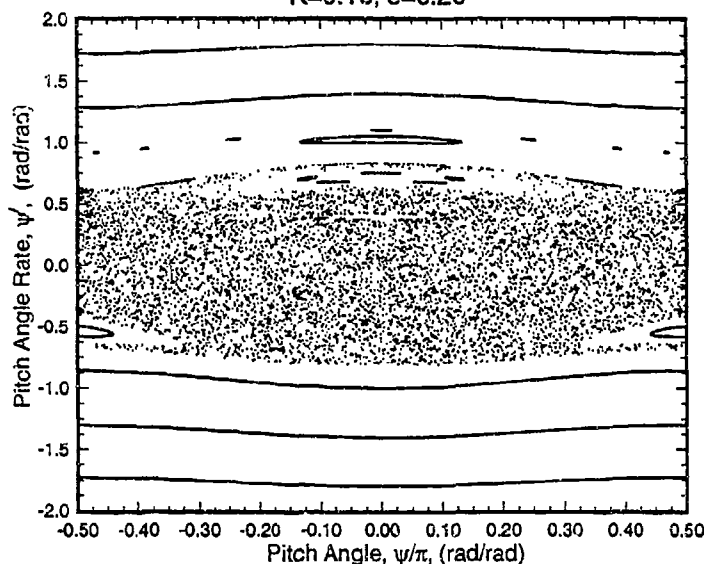


Figure 5.30: Poincaré Map for $K = 0.1$ and $e = .20$.

## 5.3.2 Determining the Motion via Bifurcation Diagrams

Bifurcation diagrams, whose formulation was discussed in Section 3, can provide significant insight into the motion of the satellite. Figures 5.34 and 5.35 present bifurcation diagrams of $\psi$ and $\psi'$, respectively, with eccentricity as the bifurcation parameter, an inertia ratio of $K = 1.0$, and the initial state $\vec{\psi}_o = (0., 0.)$. Both[8] plots show obvious regions of regular and chaotic motion and a quick glance indicates that the onset of chaos occurs close to $e = 0.3$ on this scale. Magnification of this transition area[9] reveals a complex mixture of chaotic and regular motion (Figures 5.36 and 5.37). A periodic solution exists near $e = 0.313$, and a localized chaotic region surrounded by a region of regular trajectories occurs near $e = 0.312$.

Figure 5.38 presents a bifurcation diagram for pitch angle in the area near $e = 0.312$. Regions of chaotic motion, quasiperiodic motion, and even periodic motion appear and then disappear as $e$ increases, apparently until a global onset of chaos is reached, somewhere about $e = 0.3145$. This structure is repeated again and again in

---

[8]Because pitch angle rate must be chaotic if the pitch angle itself is chaotic (and vice versa), one needs only to examine either one of this set of bifurcation diagrams to determine if the motion at a particular value of eccentricity is regular or chaotic.

[9]More accurately, this is a re-calculation of the bifurcation diagrams for a smaller range of $e$ near transition.

Poincare' Map for Numerous Trajectories:
K=0.25, e=0.20
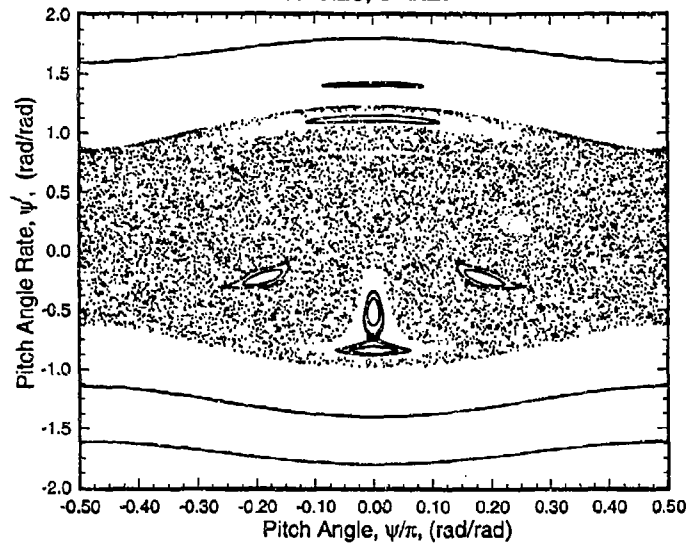


Figure 5.31: Poincaré Map for $K = 0.25$ and $e = .20$.

Poincare' Map for Numerous Trajectories:
K=0.75, e=0.20
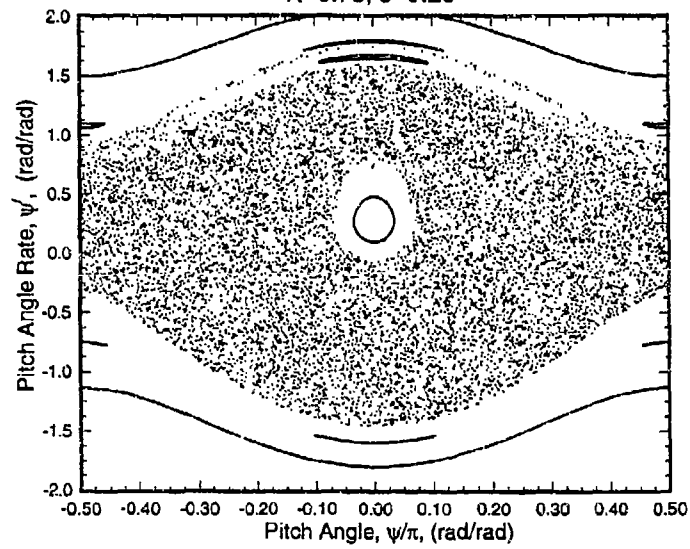


Figure 5.32: Poincaré Map for $K = 0.75$ and $e = .20$.

Poincare' Map for Numerous Trajectories:
K=1.0, e=0.20
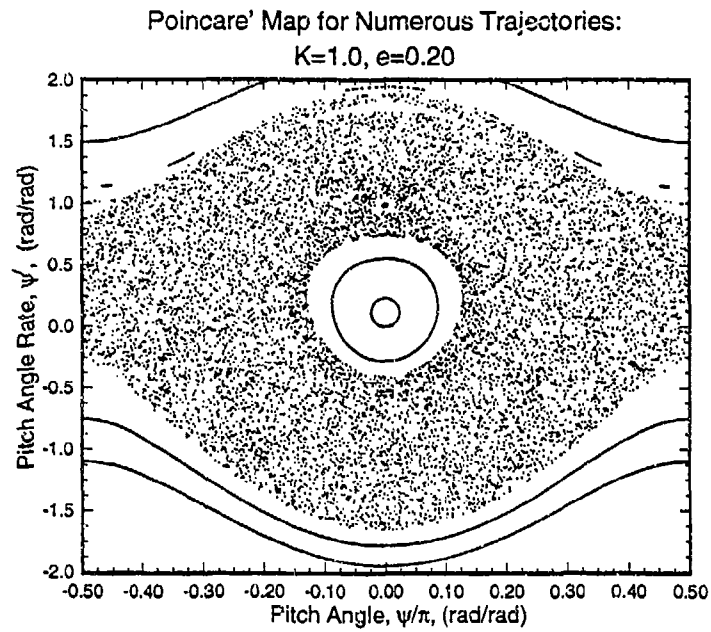


Figure 5.33: Poincaré Map for $K = 1.0$ and $e = .20$.

Bifurcation Diagram for K=1.0, (0.,0.)
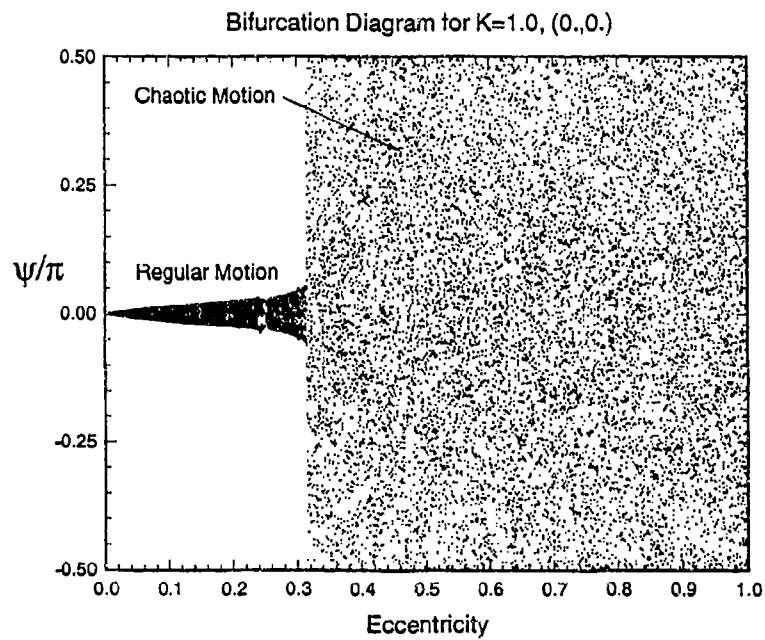


Figure 5.34: Pitch Angle Bifurcation Diagram for $K = 1.0, (0., 0.)$.
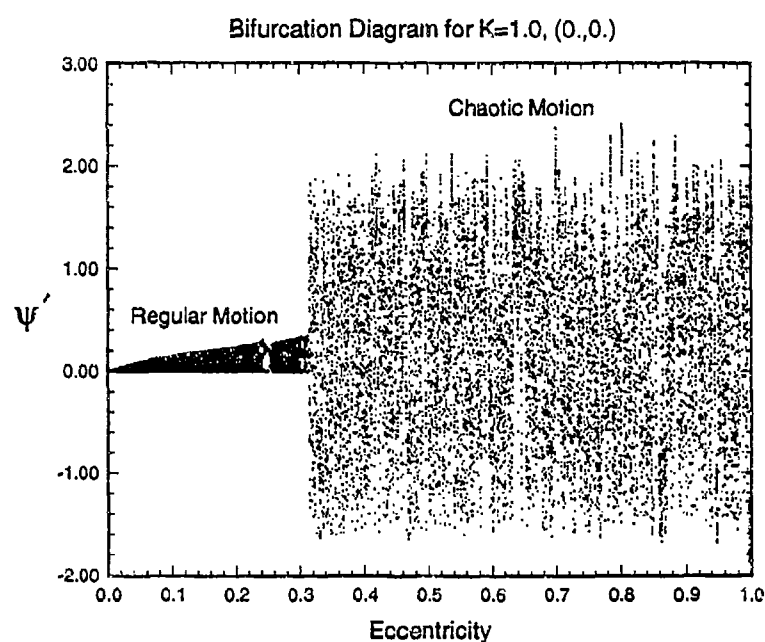
Figure 5.35: Pitch Rate Bifurcation Diagram for $K = 1.0, (0., 0.)$.
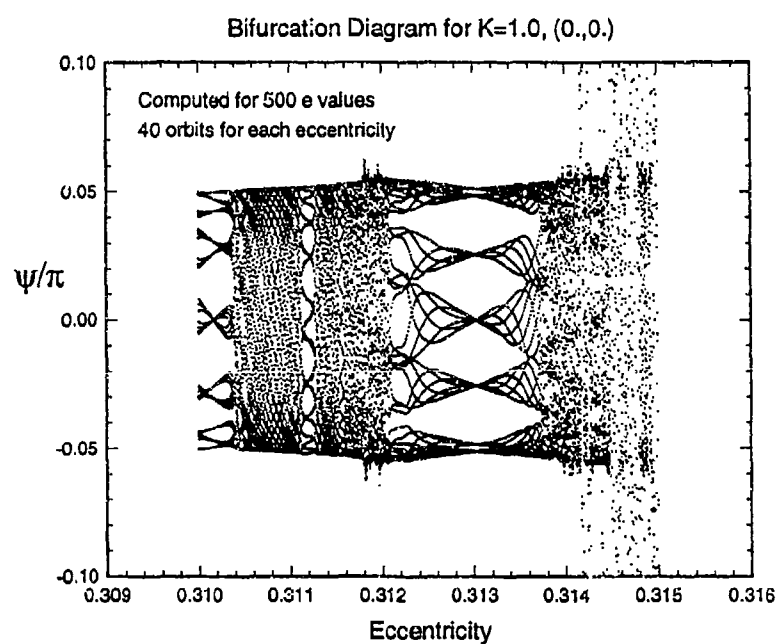


Figure 5.36: Pitch Angle Bifurcation Diagram near Transition for $K = 1.0, (0., 0.)$.
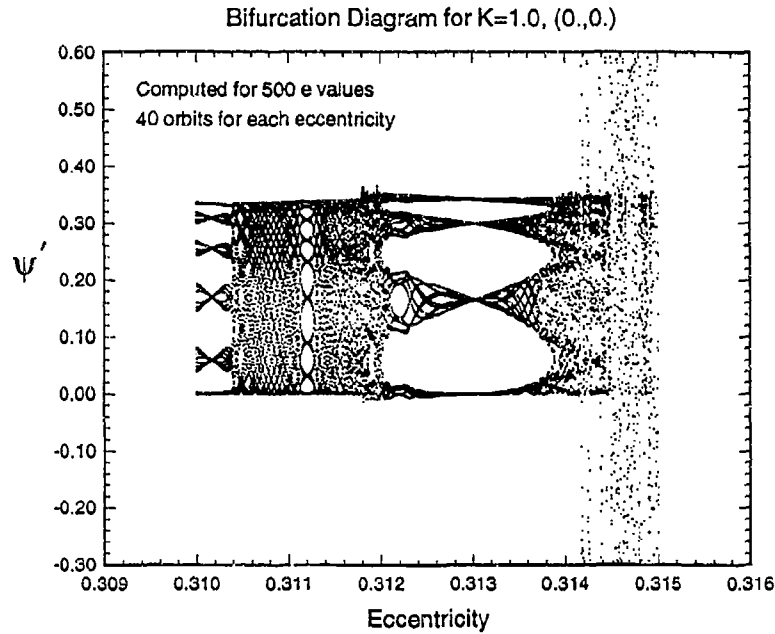
Figure 5.37: Pitch Rate Bifurcation Diagram near Transition for $K = 1.0$, (0.,0.).

further magnifications of the area near the onset of global chaos. These and other similar magnification sequences of bifurcation diagrams for other values of inertia ratio and initial states displayed no signs of simple period doubling bifurcations near transition as a function of eccentricity only, as found in the work of Tong and Rimrott [22] and here (Section 7) for this problem with the addition of a damping term.

Three dimensional bifurcation plots displaying both $\psi$ and $\psi'$ solutions versus eccentricity are useful for determining the winding number of subharmonic trajectories. For example, the $\psi$ bifurcation diagram of Figure 5.39 shows a periodic solution that skips between five pitch angle values for $e = .3041$, $K = 1.0$ and (0.,0.), whereas the same trajectory alternates between only three $\psi'$ values as depicted in Figure 5.40. The three dimensional bifurcation diagram for this case (Figure 5.41) shows this solution to be a subharmonic libration with a winding number of 1/5. Plots of this particular trajectory in the form of pitch angle and pitch rate versus true anomaly are shown in Figures 5.42 and 5.43, respectively, for ten orbits. The grid lines of constant values of true anomaly occur for every $2\pi$ radians, allowing one to easily see both $\psi$ and $\psi'$ oscillate once every five orbits.

Figures 5.44, 5.45, 5.46, and 5.34 present a sequence of bifurcation diagrams

89
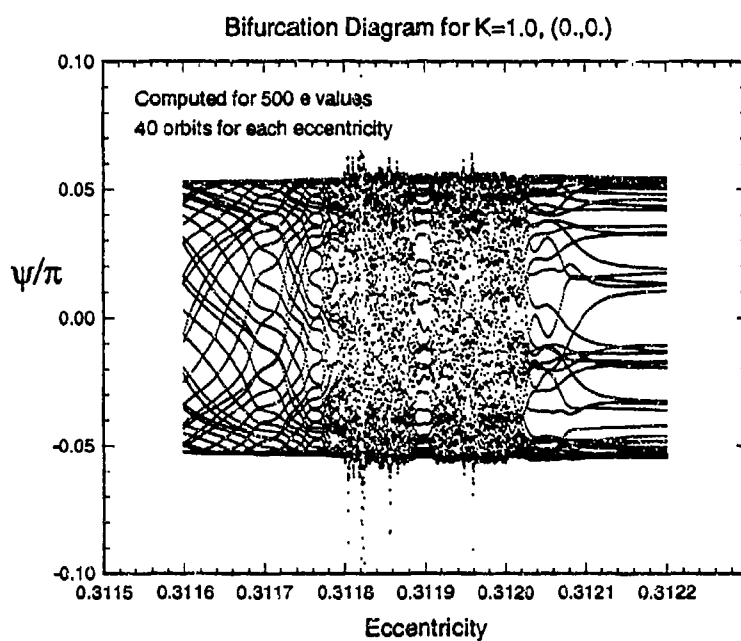
Figure 5.38: Pitch Angle Bifurcation Diagram near $e = 0.312$ for $K = 1.0$, $(0., 0.)$.
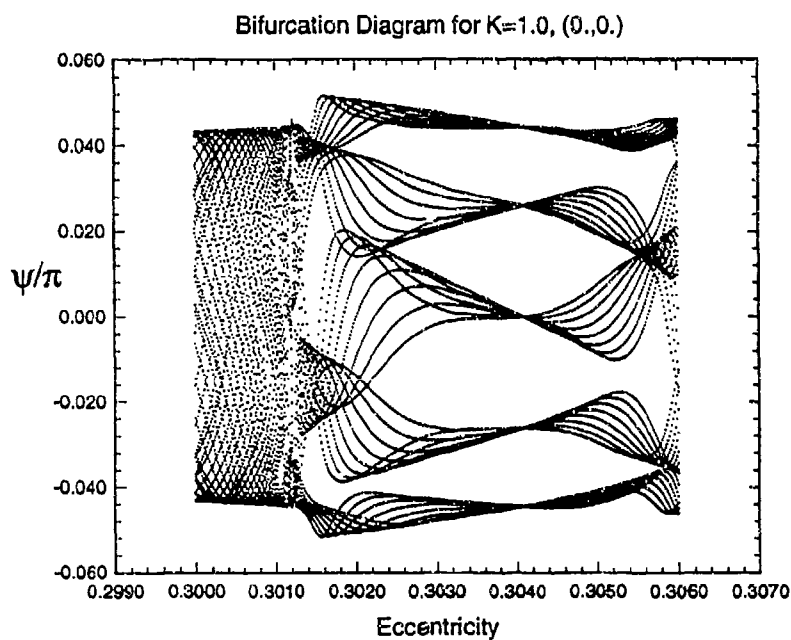


Figure 5.39: Pitch Angle Bifurcation Diagram near $e = 0.3040$ for $K = 1.0$, $(0., 0.)$.
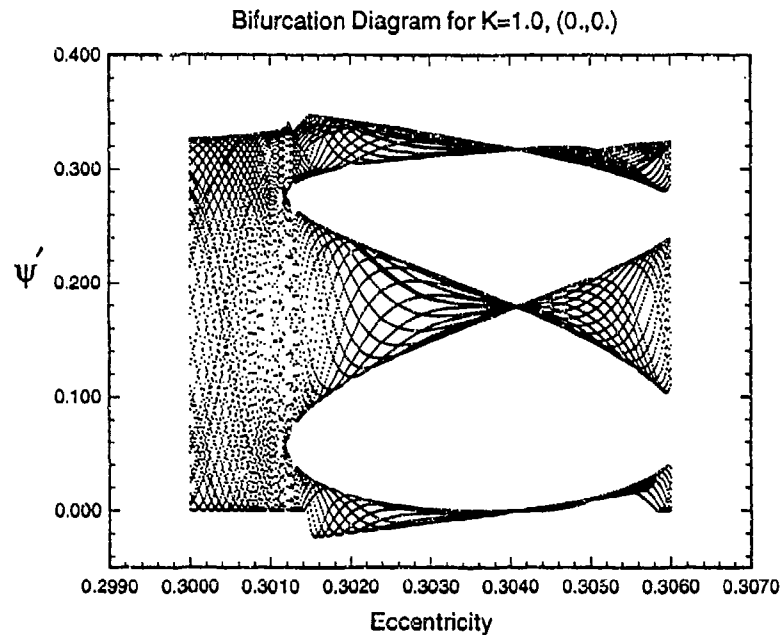
Figure 5.40: Pitch Rate Bifurcation Diagram near $e = 0.3040$ for $K = 1.0$, $(0.,0.)$.

for increasing values of $K$, ranging from $K = 0.1$ to $1.0$ for the initial state $(0.,0.)$. A somewhat rough trend may be discerned from this sequence; the chaotic region appears to shrink while the regular motion region expands for increasing values of $K$. In addition, the eccentricity value at which transition from regular to chaotic motion occurs increases for increasing inertia ratio. This trend appears to hold for a number of similar sequences for different values of $K$ on this scale.

Another example three-dimensional bifurcation diagram is presented in Figure 5.47 for small values of eccentricity. As in all of the other bifurcation digrams computed for an initial state of $(0.0, 0.0)$, a $P = 1/1$ solution occurs at $e = 0.0$ (circular orbit case.) The remainder of the trajectories displayed in this bifurcation diagram are revealed to be quasiperiodic solutions; chaos does not occur at these small values of eccentricity for this particular value of inertia ratio.

Although all of the previous bifurcation diagrams have utilized eccentricity as the bifurcation parameter, inertia ratio may also serve this function. Figures 5.48 - 5.51 present a sequence of bifurcation diagrams for increasing values of $e$, ranging from $e = 0.01$ to $e = 0.3$ for the initial state $(0.,0.)$. One can see chaotic motion does not occur for the full range of inertia ratio for the case of $e = .01$ (Figure 5.48); rather the motion is totally periodic and quasiperiodic libration. A band of chaotic motion occurs approximately for $0.35 \leq K \leq 0.48$, however, when eccentricity

91

## 3D Bifurcation Diagram for K=1.0, (0.,0.)
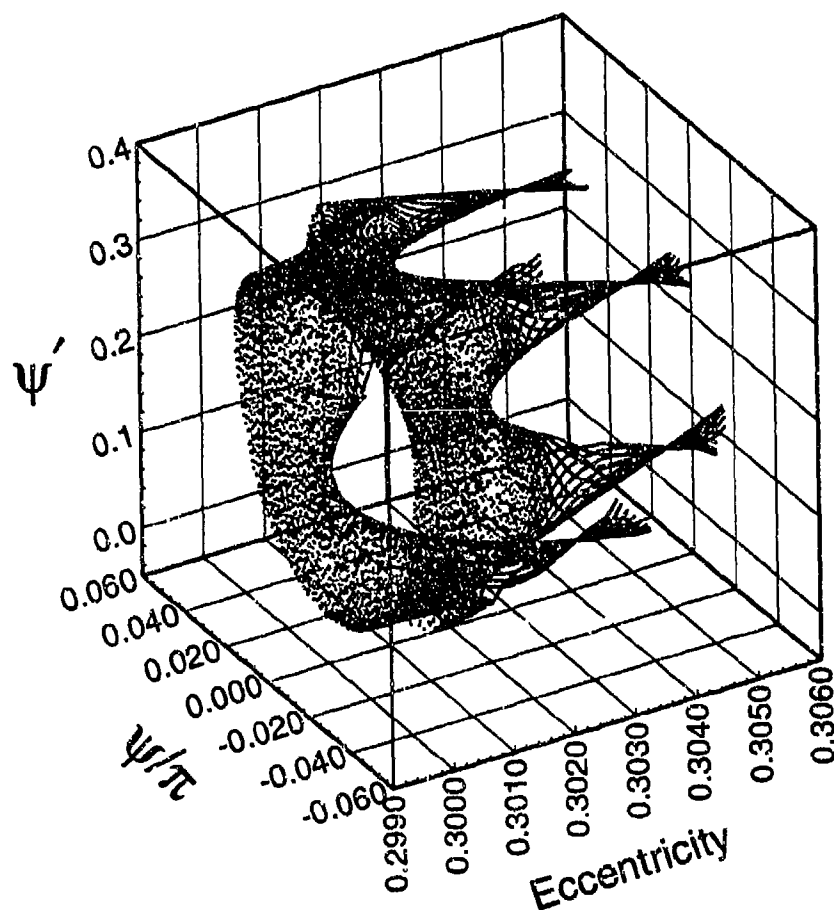


Figure 5.41: Three Dimensional Bifurcation Diagram near $e = 0.3040$ for $K = 1.0$, $(0., 0.)$.

Pitch Angle Rate Response for K=1.0, e=0.3041, and (0.,0.)
Orbits #1-10
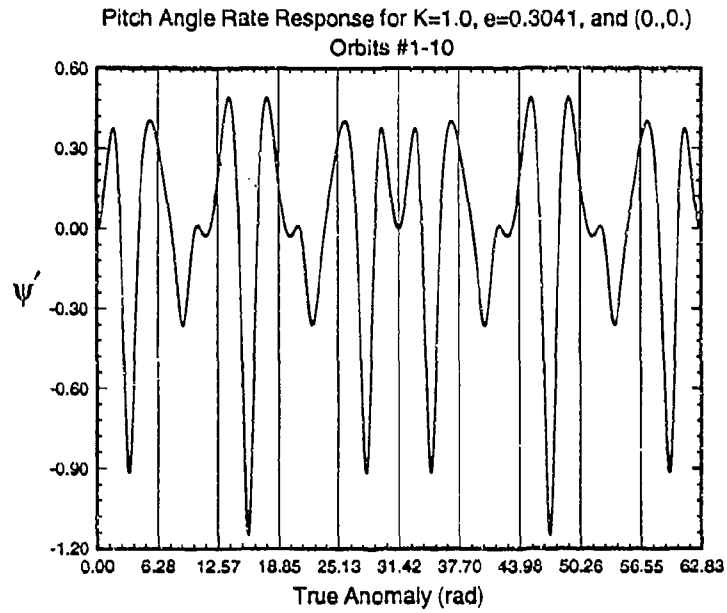


Figure 5.42:  Pitch Angle Response for $K = 1.0$ , $e = 0.3041$ and $(0., 0.)$   for Orbits #1-10.

Pitch Angle Response for K=1.0, e=0.3041, and (0.,0.)
Orbits #1-10
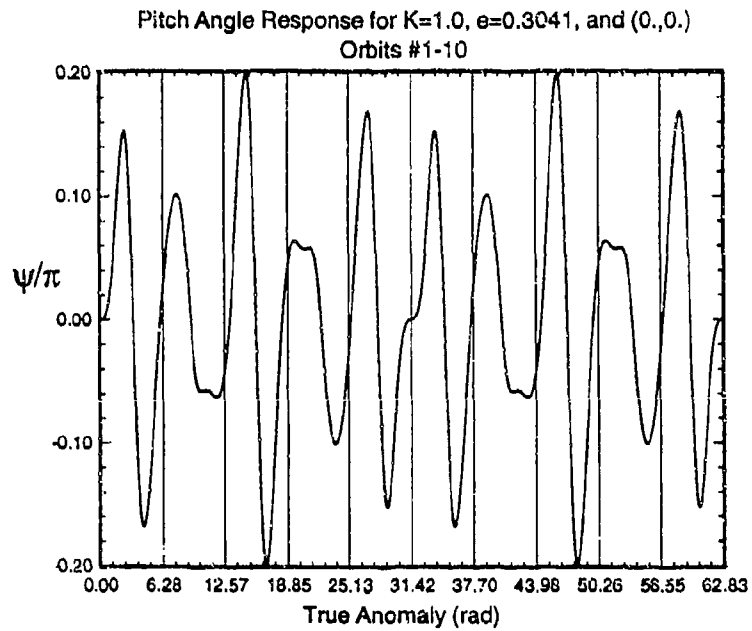


Figure 5.43:  Pitch Rate Response for $K = 1.0$, $e = 0.3041$ and $(0., 0.)$ for Orbits #1-10.

Bifurcation Diagram for K=0.1, (0.,0.)
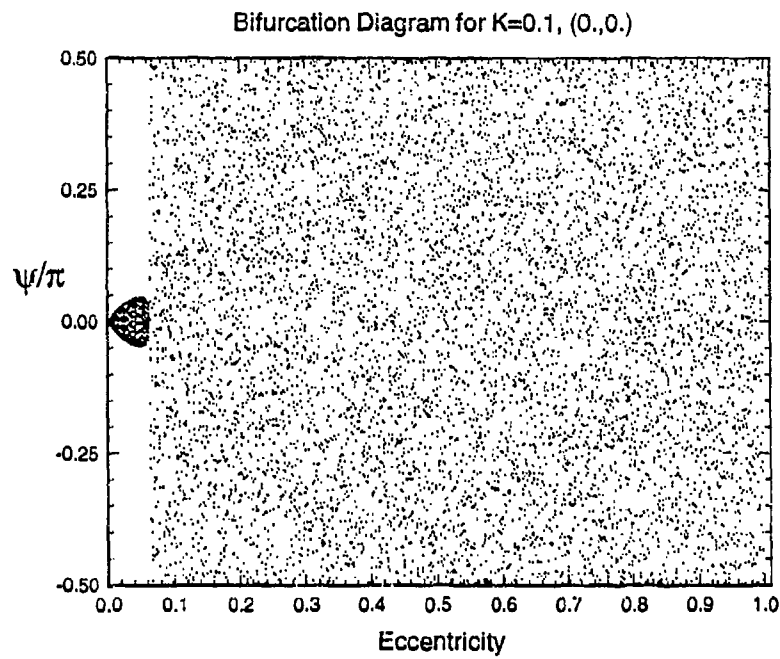
Figure 5.44: Pitch Angle Bifurcation Diagram for $K = 0.1, (0., 0.)$.



Bifurcation Diagram for K=0.5, (0.,0.)
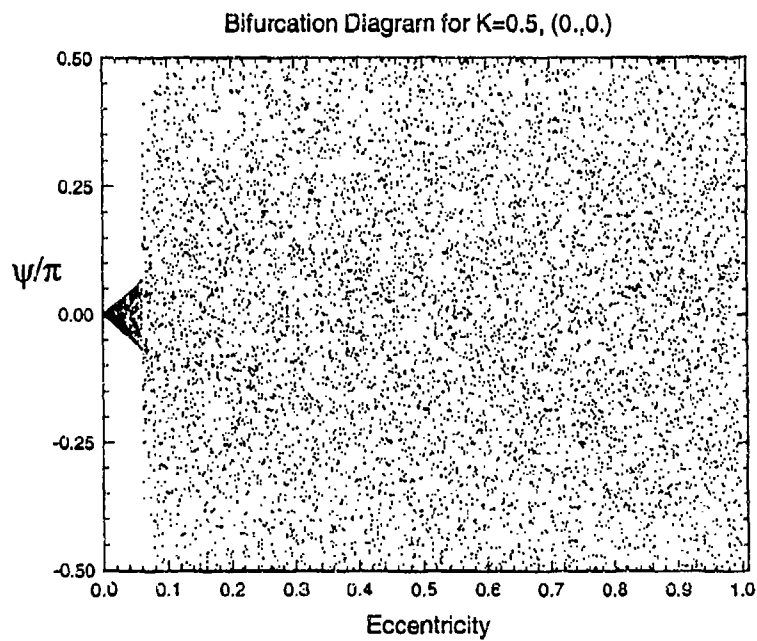
Figure 5.45: Pitch Angle Bifurcation Diagram for $K = 0.5, (0., 0.)$.
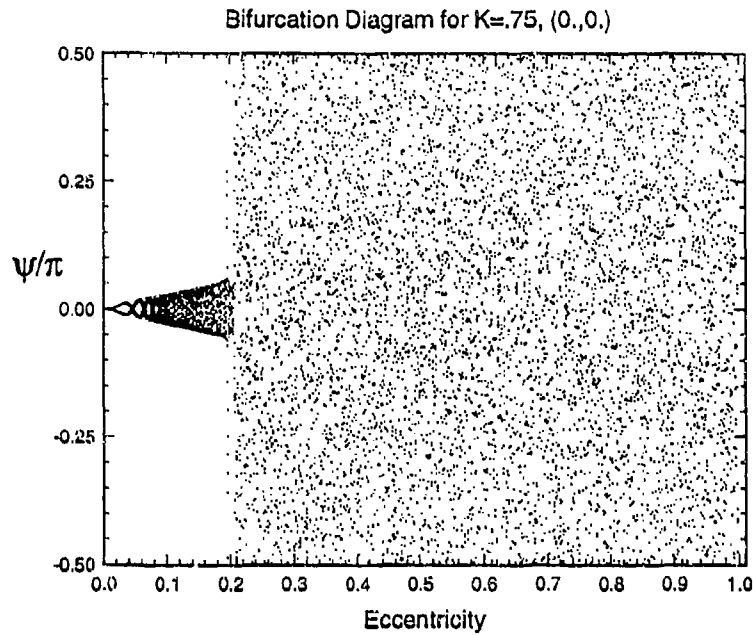
Figure 5.46: Pitch Angle Bifurcation Diagram for $K = 0.75, (0., 0.)$.

is increased to 0.05 (Figure 5.49.) Again the regular motion consists of periodic and quasiperiodic libration. Further increasing $e$ to a value of 0.10 (Figure 5.50) results in a significantly different bifurcation diagram. For very small values of $K$ in this plot the regular motion is rotation instead of libration. At slightly greater values of $K$ a second chaotic band appears to accompany the first, which itself has enlarged considerably. Between these chaotic regions exists regular librational motion. Increasing eccentricity to $e = 0.20$ and to $e = 0.30$ (Figures 5.2 and 5.51) one finds that regions of chaotic motion cover most of the range of inertia ratio. This trend continues as eccentricity is increased.

3D Bifurcation Diagram for K=1.0, (0.,0.)
Computed for 400 e values;  40 Orbits for each e value
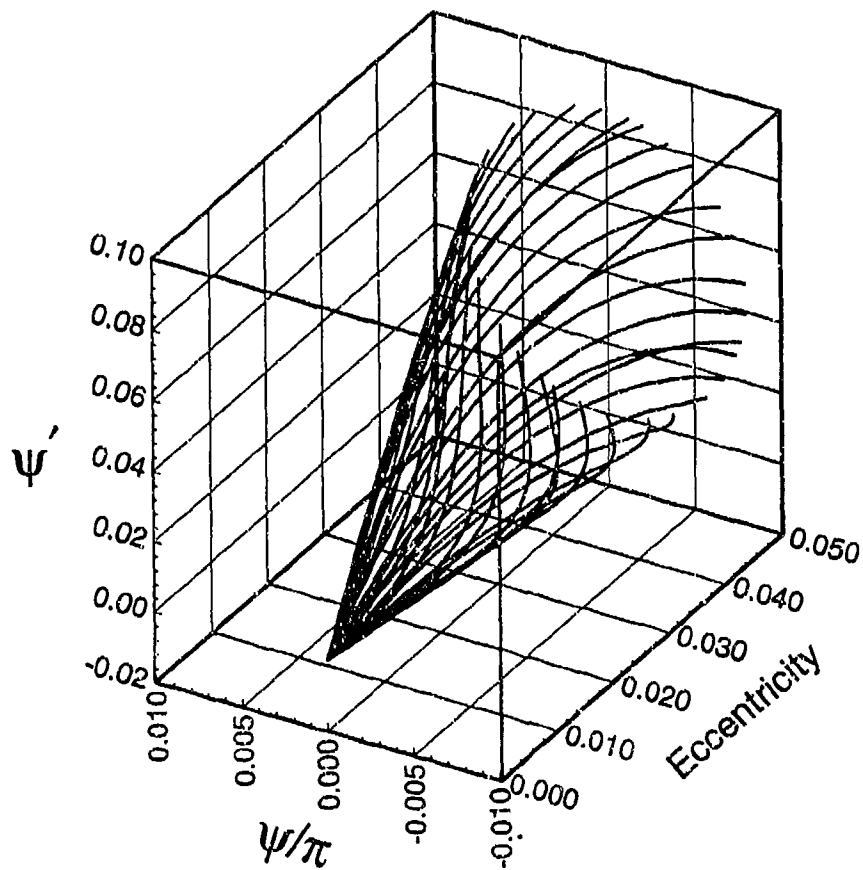
Figure 5.47:  Three Dimensional Bifurcation Diagram for $K = 1.0, (0., 0.)$.

Bifurcation Diagram for e=0.01, (0.,0.)
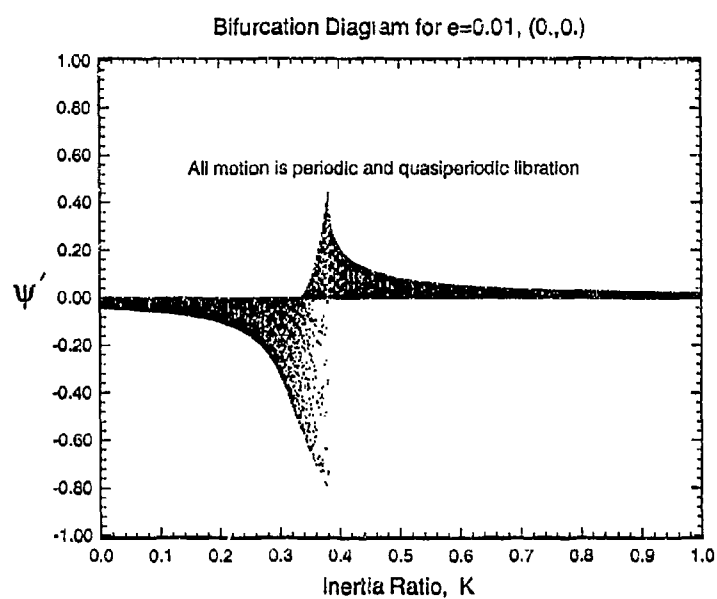


Figure 5.48: Pitch Rate Bifurcation Diagram for $e = 0.01, (0., 0.)$.

Bifurcation Diagram for e=0.05, (0.,0.)
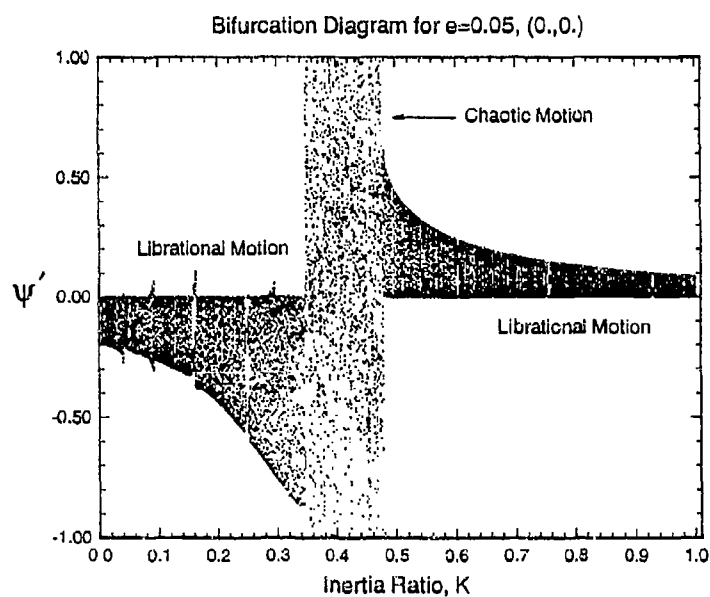


Figure 5.49: Bifurcation Diagram for $e = 0.05, (0., 0.)$.
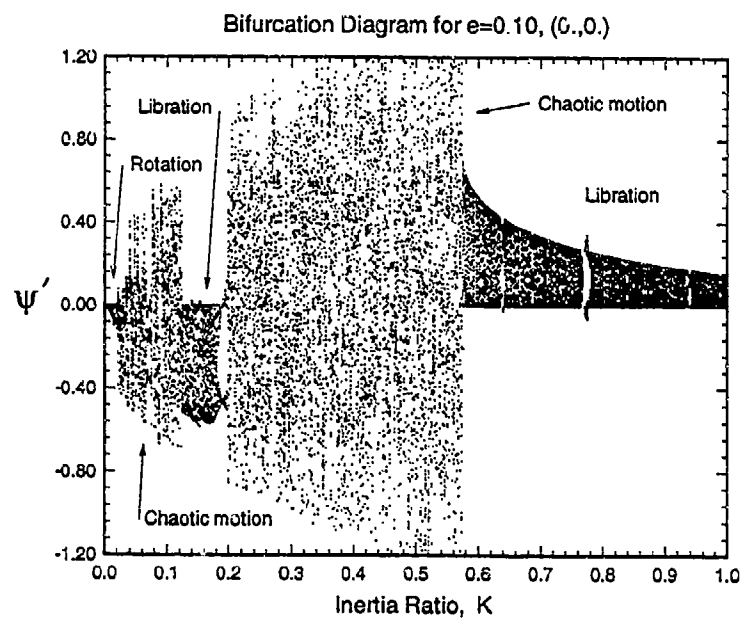
Figure 5.50: Bifurcation Diagram for $e = 0.10, (0., 0.)$.
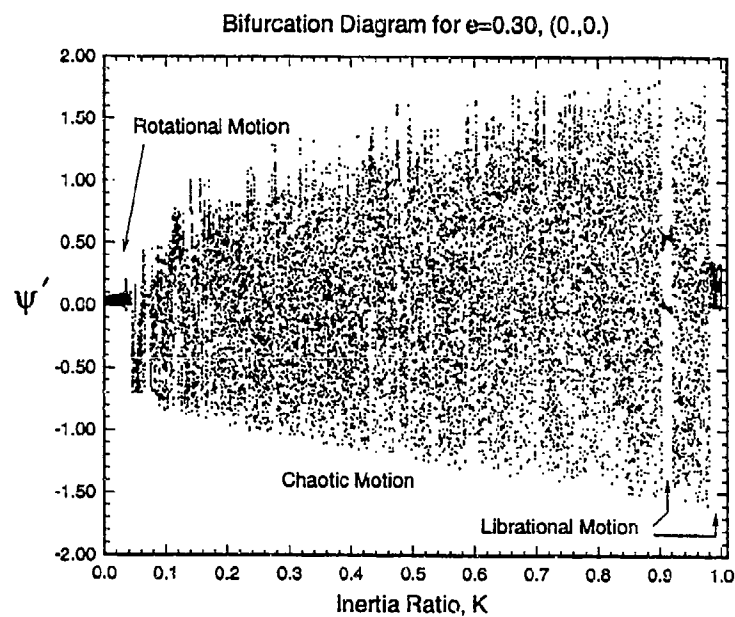


Figure 5.51: Bifurcation Diagram for $e = 0.30, (0., 0.)$.

## 5.4 Predicting the Onset of Chaos via Lyapunov Exponents and Chaos Diagrams

Chaos diagrams plot the magnitude of the first Lyapunov exponent as a function of the system parameters and thus indicate the occurrence and relative magnitude of chaotic motion for specified initial states. Color-scale chaos diagrams were created for a number of initial states. Because most interest in the gravity-gradient stabilization of artificial satellites lies in small librations about zero pitch angle, the examples shown here were all created for initial states in the vicinity of the origin.

Figure 5.52 shows a color-scale chaos diagram for the initial state (0.0, 0.0) and for $N=50$. White denotes regular motion and other colors indicate the motion is chaotic. The relative magnitude of the chaos in each trajectory is displayed in the color spectrum, ranging from blue (small $\sigma$), through green and yellow (intermediate $\sigma$), to red (large $\sigma$). On this scale of the entire ranges of the system parameters, increases in eccentricity can be seen to generally increase the magnitude of the chaos, or sensitivity to initial conditions, of the system. It is interesting to see how complex this chaotic sea is for such a simple system. Note the self-similar features of the chaotic "peninsulas" for small values of $K$, and the islands of regular motion surrounded by chaos. For very small values of $K$, the motion is regular – even for very large values of eccentricity. In fact, in the limit as $K \to 0$, the motion is regular for all $e$.[10] Similarly, in the limit as $e \to 0$, the motion is regular for all $K$.

Figure 5.53 presents an enlargement of a portion of Figure 5.52, showing the features of the chaos diagram for small values of eccentricity. The border between chaotic and regular motion is very complex and hints of a fractal form. The color spectrum indicating the relative magnitudes of the Lyapunov exponents has been rescaled from Figure 5.52. In fact, each of the following chaos diagrams was uniquely color-scaled to make their structure more easily seen.

To apply chaos diagrams as a first-order design tool to avoid chaotic pitching motion in gravity-gradient satellites would require knowledge of a variety of initial states of $(\psi_o, \psi'_o)$. A few additional example chaos diagrams for small variations about the origin are given in Figures 5.54 - 5.57. Figure 5.54 presents a chaos diagram for the initial state of (0.0, 0.5). The overall structure of this plot differs little from

---

[10]This cannot always be seen in these figures because the plotting package used in this study draws the axes such that they overlap a portion of the grid.

Figure 5.52 although some of the details (such as the size and shape of the chaotic peninsulas, for example) change somewhat. Chaos diagrams computed for the initial states $(0.0, -0.25)$ and $(0.0, -0.5)$ are given in Figures 5.55 and 5.56. Again, the basic structure of the diagrams seems to change little for this small variation in initial pitch rate. However, the islands of regular motion in the chaotic regions, barely discernible in some of the previous chaos diagrams, now appear to exhibit self-similarity. Figure 5.57 presents a chaos diagram for the initial state of $(5.0 \text{ deg}, 0.0)$. This plot varies little from Figure 5.52 except for the border between regular and chaotic motion at large values of the inertia ratio. Close-ups of the island chains depicted in Figures 5.52 and 5.56 are shown in Figures 5.58 and 5.59. These islands appear to be self-similar, with some twist or other distortion notwithstanding.
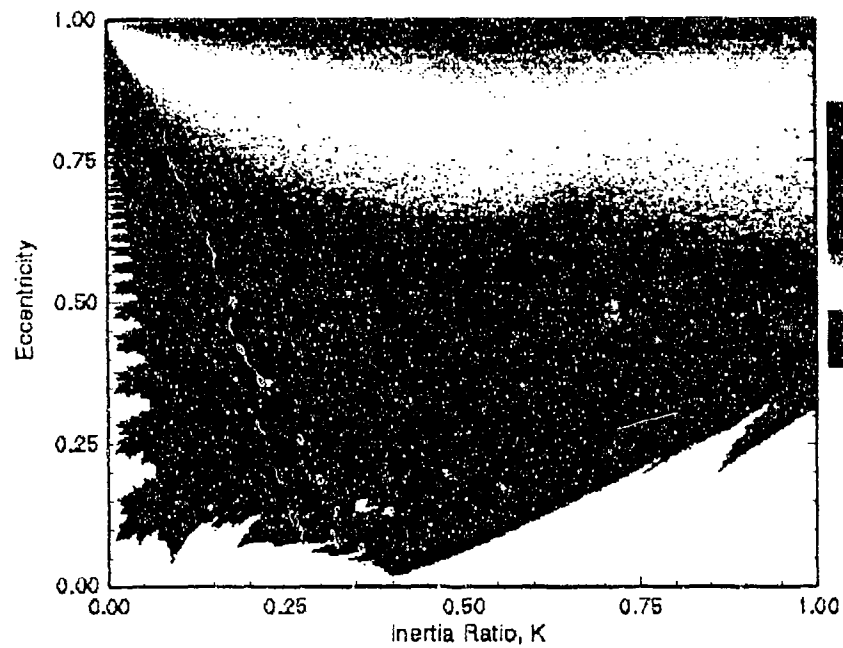
Figure 5.52: Chaos Diagram of Lyapunov Exponents for the Initial State (0., 0.). White denotes regular motion; other colors indicate chaos.
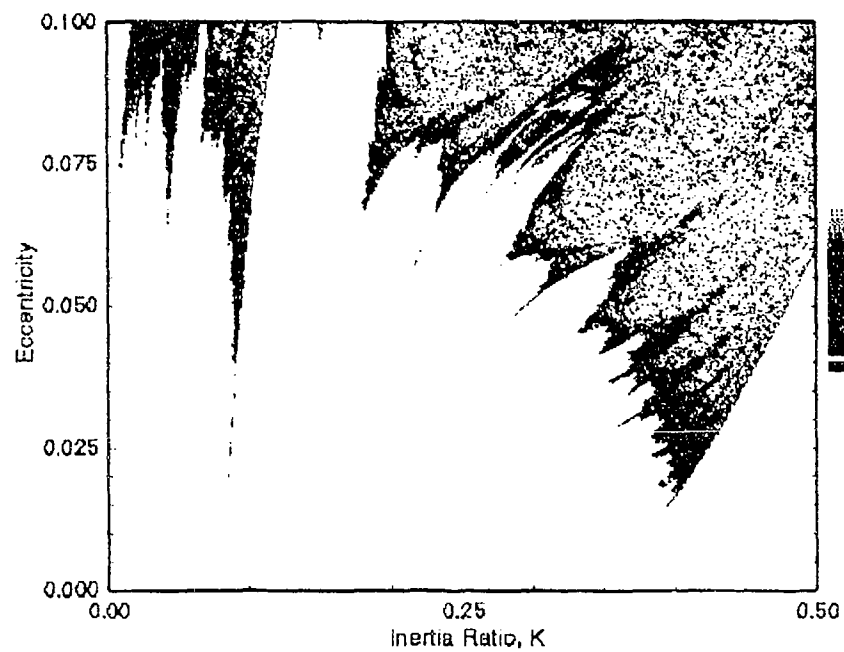


Figure 5.53: Chaos Diagram of Lyapunov Exponents for the Initial State (0., 0.) for Small Eccentricities.
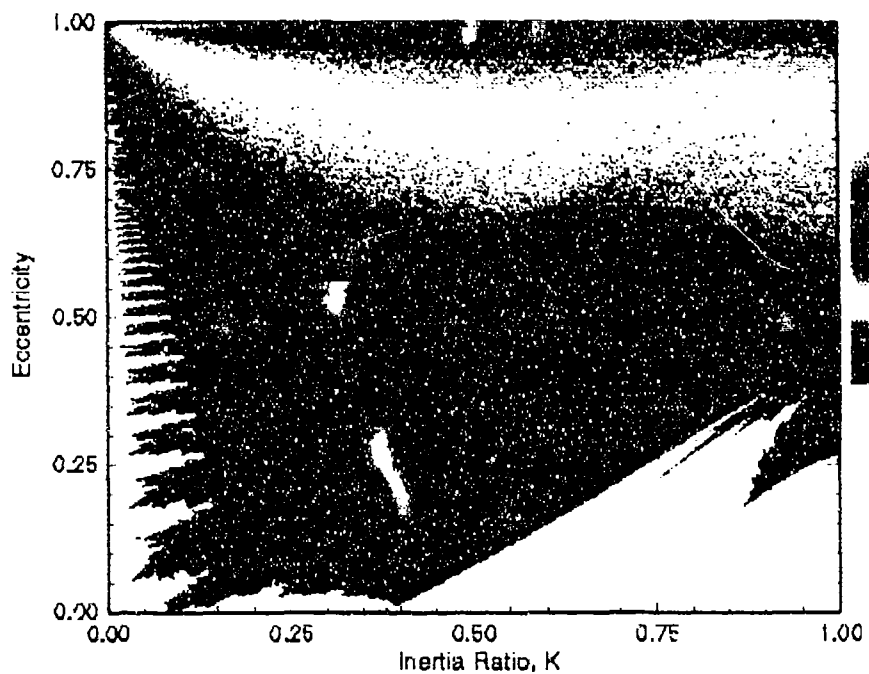
Figure 5.54: Chaos Diagram of Lyapunov Exponents for the Initial State (0., 0.5).
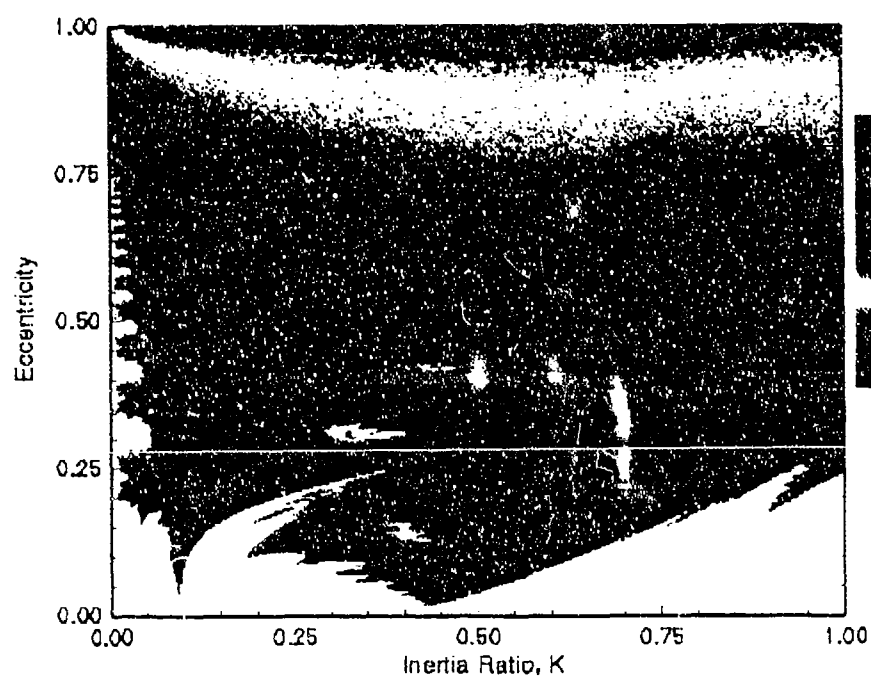


Figure 5.55: Chaos Diagram of Lyapunov Exponents for the Initial State (0., -0.25).
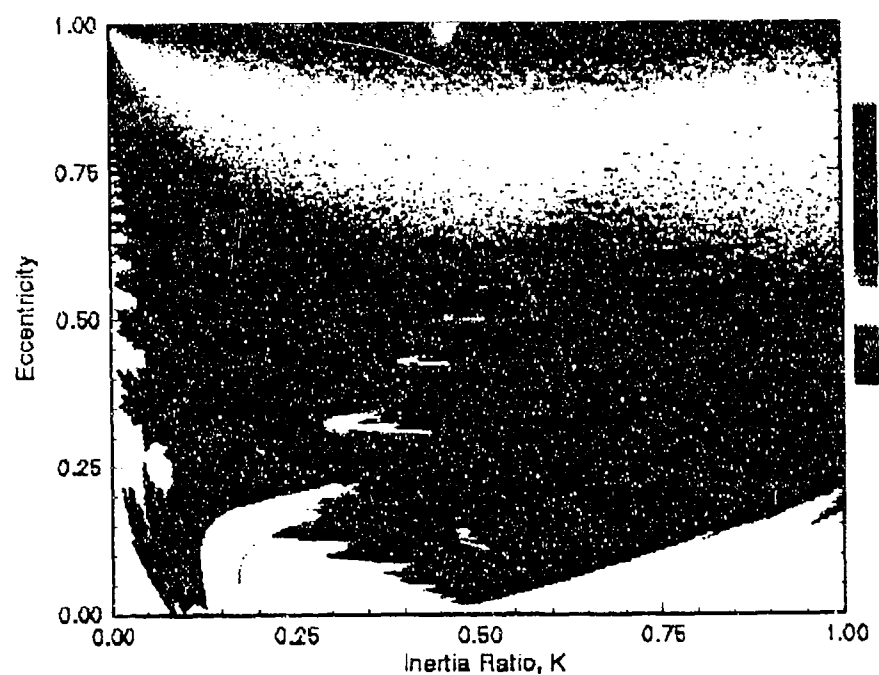
Figure 5.56: Chaos Diagram of Lyapunov Exponents for the Initial State (0., −0.5).
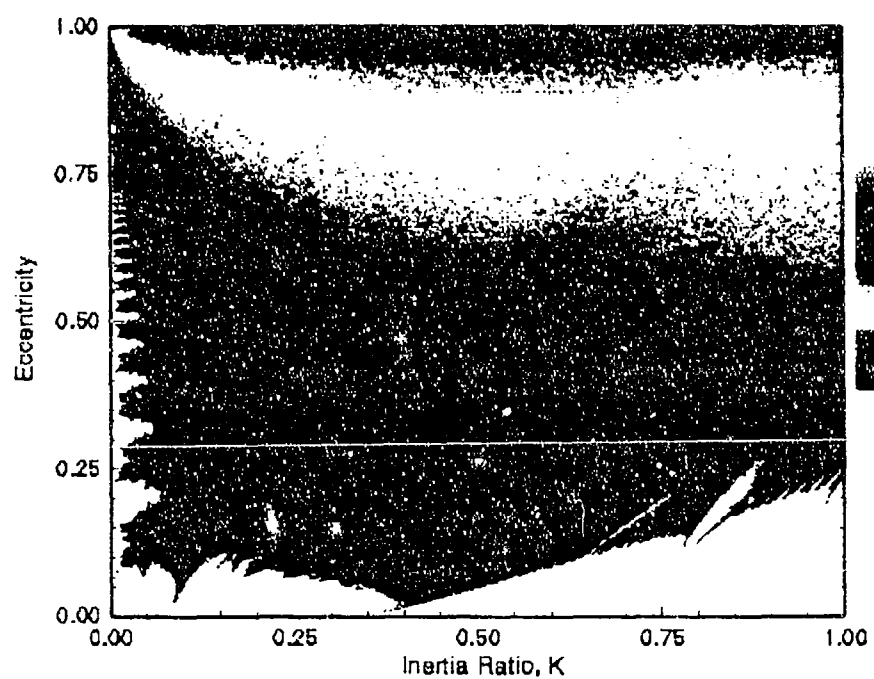


Figure 5.57: Chaos Diagram of Lyapunov Exponents for the Initial State (5.0 deg, 0.).
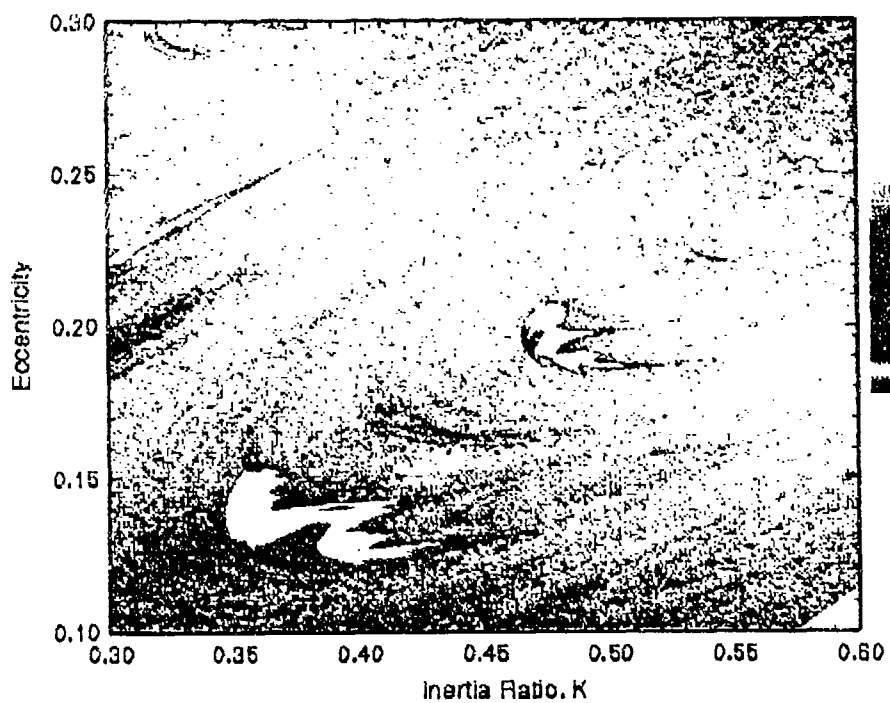
Figure 5.58: Close-up of Islands of Figure 5.52 for the Initial State (0., 0.).
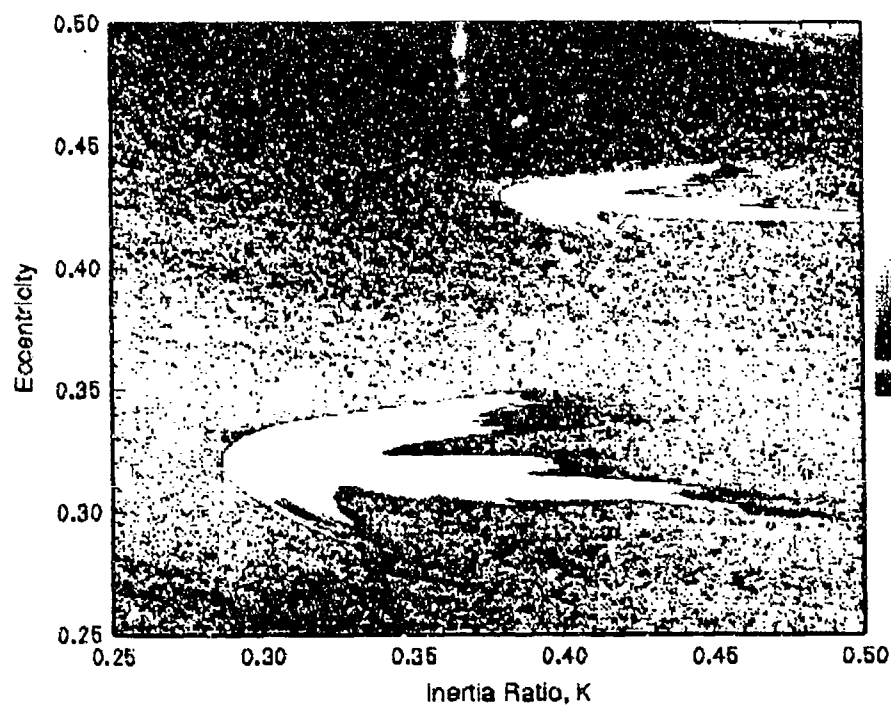


Figure 5.59: Close-up of Islands of Figure 5.56 for the Initial State (0., −.5).

## 5.5 Structure in the $\vec{\psi}_o = (0., 0.)$ Chaos Diagrams: Fractal Dimension and Periodic Solutions

### 5.5.1 Examination of the Fractal Border Between Chaotic and Regular Motion in Parameter Space

That at least a portion of the border between regular and chaotic motion is fractal is displayed in Figures 5.60 - 5.63 through two successive enlargements of a region of Figure 5.52. Figure 5.60 indicates the area of Figure 5.52 for the first enlargement, an area containing one of the peninsulas for small values of $K$. The first enlargement is presented in Figure 5.61 and the area for the second enlargement is shown in Figure 5.62. Figure 5.63 displays the second magnification. Comparison of Figures 5.61 and 5.63 shows the self-similarity between different scales, a characteristic of a fractal curve.

The concept that a continuous, Hamiltonian system may have a fractal transition curve between regular and chaotic motion is important. In general, "fractal" and "Hamiltonian" don't go together; fractal qualities such as fractal (strange) chaotic attractors appearing on Poincaré maps or fractal basin boundaries are phenomena usually associated with dissipative systems. Numerous transition prediction techniques produce smooth, nonfractal chaos boundaries and often, very simple criteria. To his knowledge, the author is unaware of the occurrence of this phenomena in any other Hamiltonian, numerical model. Fractal basin boundaries[11] are not uncommon (see References [44] and [45] for example) and the rarity of the appearance of the chaos diagram in the literature may explain why more fractal parameter space chaos boundaries have not been observed. This result is not completely unprecedented, however. In an experiment, Moon (see [46] and [47]) examined the dynamics of a buckled, steel, cantilevered beam placed between two permanent magnets with the entire system mounted upon an electromagnetic shaker. The experimental data for this system gave a fractal boundary between regular and chaotic motion in parameter space (in a chaos diagram), even though the one degree of freedom, nonautonomous equation

---

[11]Basin boundary diagrams are similar to chaos diagrams except that they fix the system parameters and plot the boundaries of various attractors for varying initial states. In contrast, the initial states are fixed in a chaos diagram and the system parameters are varied. In other words, basin boundary diagrams plot in initial condition space, whereas chaos diagrams plot in parameter space.

of motion used to model the system produced a smooth, nonfractal transition curve. This result raises serious questions to the accuracy of some of the analytical boundary prediction techniques that predict smooth and simple transition boundaries.
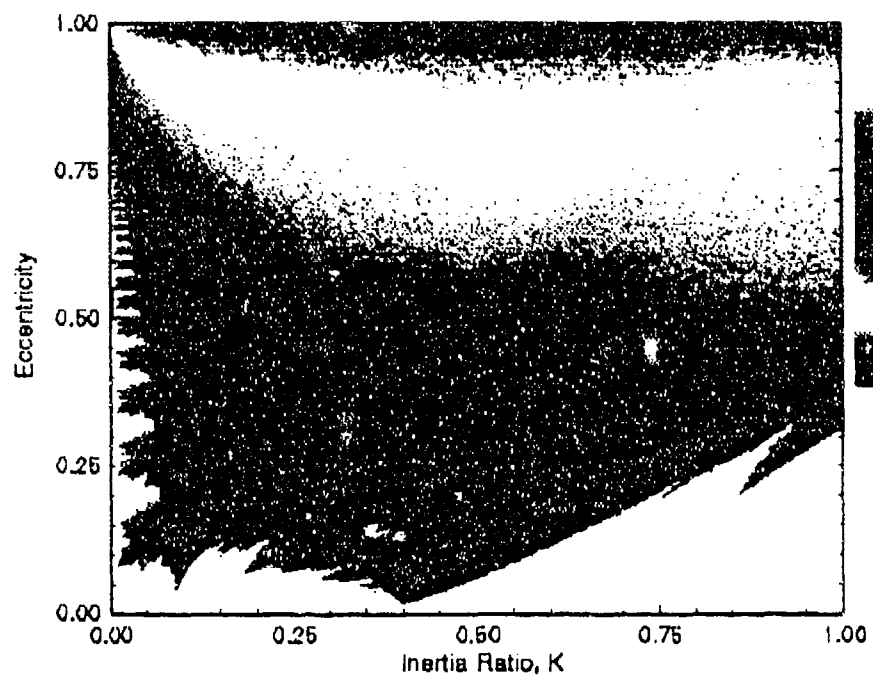
Figure 5.60: Area of Figure 5.52 to be Enlarged.
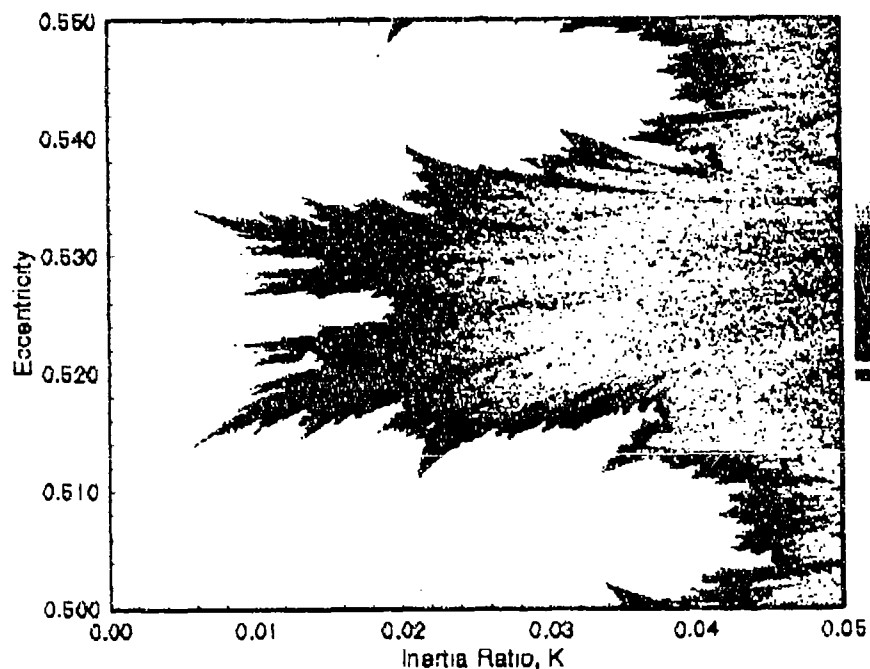


Figure 5.61: Enlargement of Chaotic Peninsula of Figure 5.52.

## 5.5.2 Computing the Fractal Dimension

The dimension of the boundary curve between chaotic and regular motion may be estimated using a simple graphical technique. This was accomplished for the border of the chaos diagram of Figure 5.63 in the same manner as carried out by Moon [47], and originally presented by Mandelbrot [48] (see also [49]).

Following [47], we approximate the length of the entire border of Figure 5.63 by a set of $n$ connected lines, each of length $l$. The length of the approximated border, $L$, is $L = nl$, and $n \to \infty$ as $l \to 0$. Thus, for a smooth, nonfractal curve $n \to dl^{-1}$ where $d$ is the length. The equivalent expression for a fractal curve is $n \to dl^{-D}$, where $D$ is the dimension of the curve, or

$$\log n = \log d + (-D) \log l \tag{5.2}$$

for small values of $l$. One therefore can plot $\log n$ versus $\log l$ and the slope of the least squares curve fit of the four data sets will give a value for $-D$. The dimension of a smooth curve would be an integer; a noninteger value of $D$ would verify that the border of Figure 5.63 is fractal. A set of drafter's dividers, fixed at a narrow setting, were used to estimate the total length of the boundary curve, $L$, in an enlarged copy of the chaos diagram. The width of the dividers, $l$, was then measured with a set of dial calipers. Four sets of data were obtained (Table 5.1) for four different divider widths. These results are plotted in Figure 5.64. The slope of the curve in this plot gives a fractal dimension of 1.30 for the chaos border of Figure 5.63.

## 5.5.3 Periodic Solutions in the Chaos Diagrams

As a rough check of the accuracy of these chaos diagrams, a bifurcation diagram for $\psi'$ was constructed by varying eccentricity while holding inertia ratio constant at $K = .0105$ for the initial state $(0.0, 0.0)$. This plot of the solutions of $\psi'$, periodically sampled in the same manner as for the Poincaré maps and collected for different values of eccentricity, was then compared with a gray-scale version of Figure 5.63. A combined plot, made by splitting the chaos diagram at $K = .0105$, and inserting the bifurcation diagram for the same range in eccentricity, is presented in Figure 5.65. The chaotic portions of the bifurcation diagram (computed with double precision and small integration step sizes) align with those of the $K = .0105$ slice of the chaos diagram, verifying the accuracy of the Lyapunov exponent calculations. Further,

| Data Set # | n | Dividers Width, l (1/1000 in) |
|---|---|---|
| 1 | 815 | 075. |
| 2 | 520 | 108. |
| 3 | 333 | 153. |
| 4 | 222 | 204. |

Table 5.1: Data Set for Estimating the Fractal Dimension.
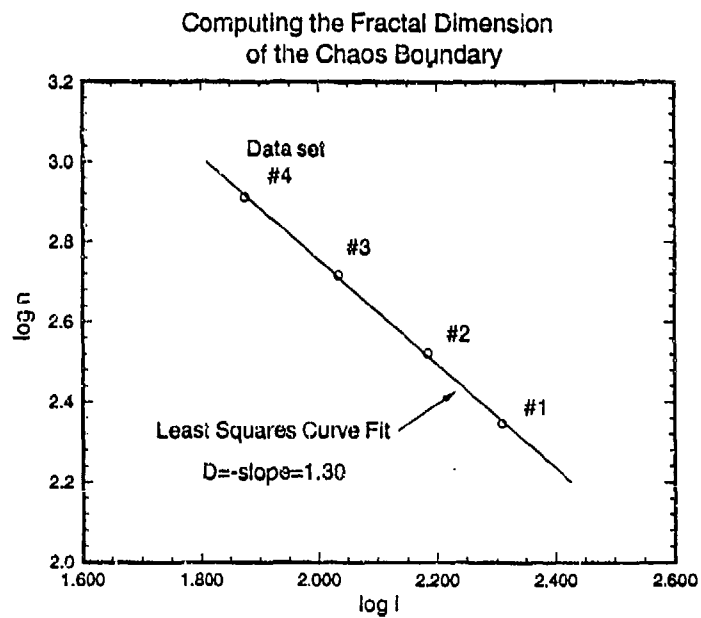


Figure 5.64: Computing the Fractal Dimension of the Chaos Boundary of Figure 5.63.

the portions of the bifurcation diagram of regular motion surrounded by bands of chaos display apparent periodic motion at their approximate centers. The center of each of the "bays" of regular motion, located between the chaotic peninsulas of the chaos diagram, appears to feature a periodic solution surrounded by quasiperiodic trajectories.

As another example of this phenomenon, bifurcation diagrams were created for $K = 0.04$ and the initial state $(0., 0.)$, dynamically equivalent to a vertical slice of Figure 5.52 a little to the left of the first tick mark from the left on the $K$ axis. Comparison of these bifurcation diagrams, Figures 5.66 (pitch angle versus eccentricity) and 5.67 (pitch rate versus eccentricity), with Figure 5.52 reveals that periodic trajectories occur in at least the first six[12] bays of regular motion on the lower left-hand side of Figure 5.52. Examination of the trajectories in these areas of regular motion proved to be interesting; the first bay of regular motion consisted of a stationary $(\psi(f) = \psi'(f) = 0)$ solution corresponding to the circular orbit case followed by regions of periodic and quasiperiodic librational motion for increasing values of eccentricity. A small band of librational motion also occurs after a brief band of chaos near $e = 0.09$. The second, third, and all other bays of regular motion have periodic tumbling solutions in their approximate centers, surrounded by regions of periodic and quasiperiodic tumbling motion. For example, $P = 1/2$ rotation occurs in the approximate center of the second bay near $e = 0.20$, $P = 1/1$ rotation in the third bay near $e = 0.32$, $P = 3/2$ rotation in the fourth bay near $e = 0.40$, and so forth. In summary, the frequency or winding number of the rotational (tumbling) motion near the center of each bay increases by $1/2$ in each bay as eccentricity increases in Figures 5.66 and 5.67. Not only are these bays self-similar, they also share common dynamical features – a rotational periodic solution near the center of each (except the first), with the frequency increasing with increasing eccentricity.

### 5.5.4    Analytical Periodic Solutions for an Axially Symmetric Satellite

Examination of a reduced version of the equation of motion sheds some light on this matter. Assuming very small values of inertia ratio (which in the limit as $K \rightarrow 0$ corresponds to an axially symmetric satellite) the equation of motion (5.1) reduces

---

[12]Indeed, there is no reason to believe that they don't occur for all of these bays, but successively finer bifurcation diagrams would have to be computed at successively smaller values of $K$ to examine this. The author leaves it an exercise for the reader.
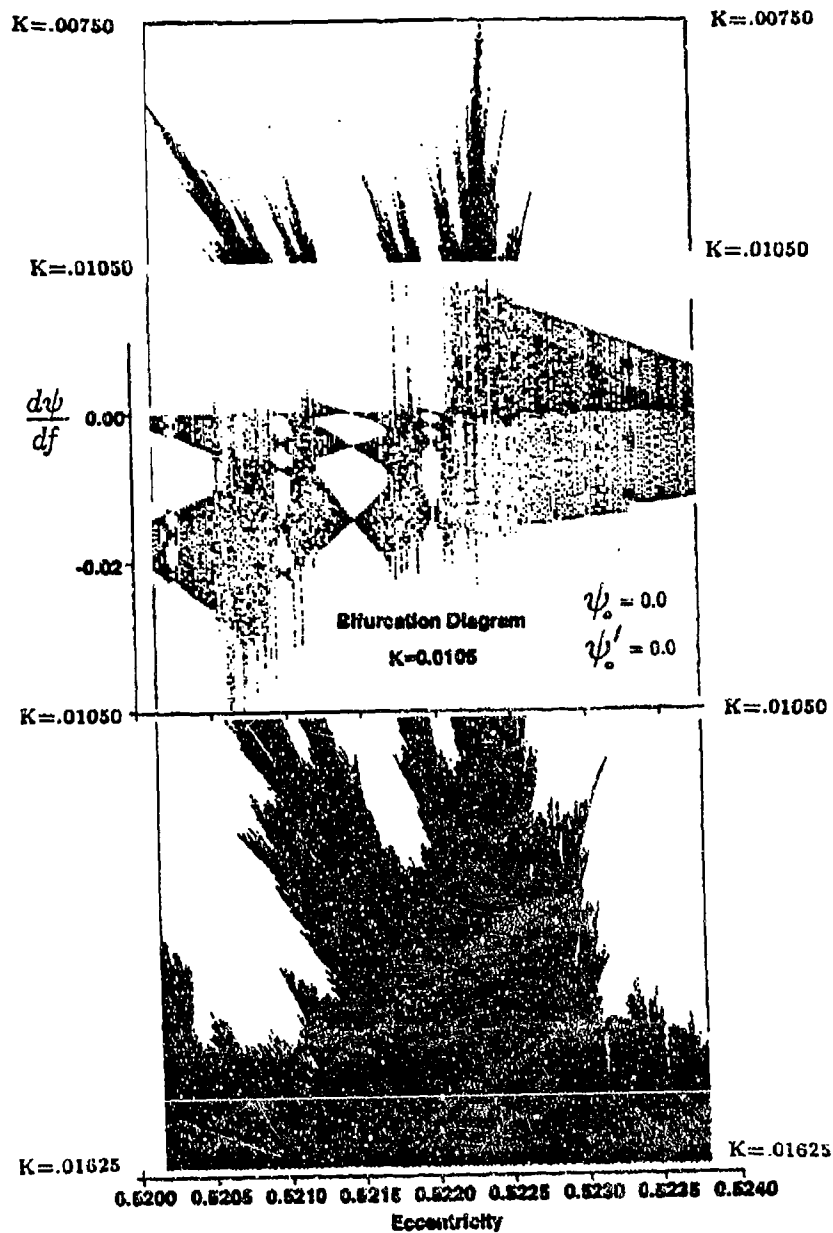
Figure 5.65: Combination of Figure 5.63 and of a Bifurcation Diagram for $.520 < e < .524$ and Initial State $(0., 0.)$.
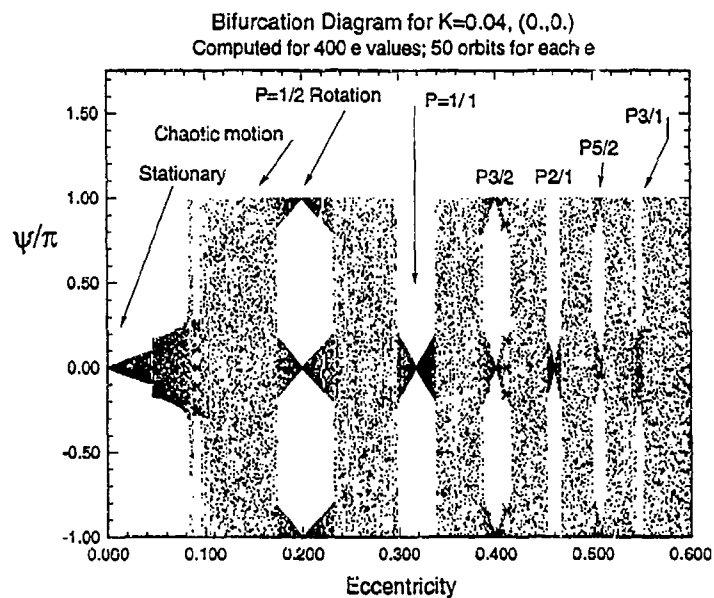
Figure 5.66: Bifurcation Diagram for $K = 0.04$ and $(0., 0.)$.
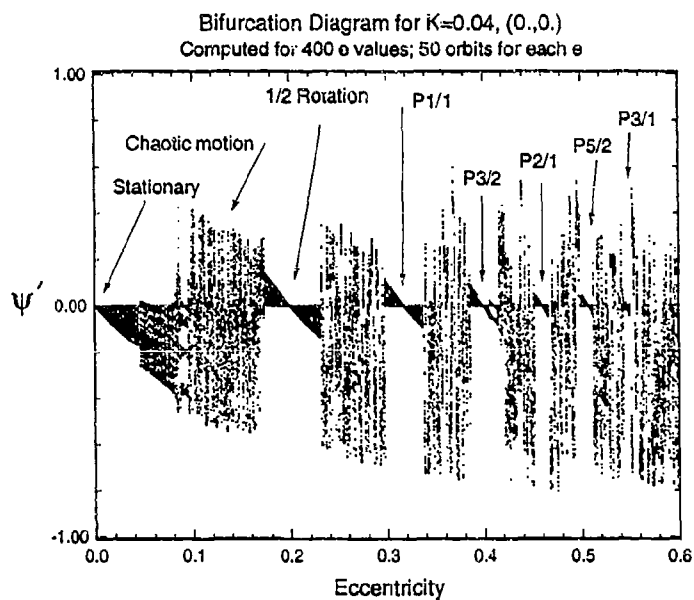


Figure 5.67: Bifurcation Diagram for $K = 0.04$ and $(0., 0.)$.

to

$$\frac{d^2\psi}{df^2}(1 + e\cos f) - 2e\left(\frac{d\psi}{df} + 1\right)\sin f \approx 0. \tag{5.3}$$

Substituting a dummy variable $\theta \equiv \psi' + 1$ reduces the equation of motion further into a form which may easily be analytically solved,

$$\frac{d\theta}{df}(1 + e\cos f) - 2e\theta\sin f \approx 0. \tag{5.4}$$

Equation 5.4 may be integrated, the appropriate substitutions made, and after a little work one obtains

$$\psi(f) = \frac{-C_1 e \sin f}{(1 - e^2)(1 + e\cos f)} - f + C_2 + \frac{2C_1}{(1 - e^2)^{3/2}}\arctan\left[\frac{\sqrt{1 - e^2}\tan(f/2)}{(1 + e)}\right], \tag{5.5}$$

and

$$\psi'(f) = \frac{C_1}{(1 + e\cos f)^2} - 1, \tag{5.6}$$

where the constants, $C_1$ and $C_2$, are given by the expressions

$$C_1 \equiv (\psi'_o + 1)(1 + e\cos f_o)^2 \tag{5.7}$$

$$C_2 \equiv \psi_o + f_o + \frac{e}{(1 - e^2)}\sin f_o(1 + \cos f_o)(\psi'_o + 1)$$

$$-2\frac{(1 + e\cos f_o)^2}{(1 - e^2)^{3/2}}(\psi'_o + 1)\arctan\left[\frac{\sqrt{1 - e^2}\tan(f_o/2)}{(1 + e)}\right]. \tag{5.8}$$

Equations 5.5 - 5.8 represent the general solutions for the zero inertia ratio case, which corresponds to an axially symmetric satellite. Of particular interest is the situation where $f_o = \psi_o = \psi'_o = 0$, as in the bifurcation and chaos diagrams above. For this special case $C_1 = (1 + e)^2$, $C_2 = 0$, and the solutions take the form

$$\psi(f) = \frac{-e(1 + e)^2\sin f}{(1 - e^2)(1 + e\cos f)} - f + \frac{2(1 + e)^2}{(1 - e^2)^{3/2}}\arctan\left[\frac{\sqrt{1 - e^2}\tan(f/2)}{(1 + e)}\right], \tag{5.9}$$

$$\psi'(f) = \frac{(1 + e)^2}{(1 + e\cos f)^2} - 1. \tag{5.10}$$

For rotational motion at the nth periapsis passage, Equation 5.10 indicates pitch rate is always zero,

$$\psi'(2\pi n) = 0, \tag{5.11}$$

and thus one expects to see zero values of $\psi'$ on all bifurcation diagrams at $K = 0$. In addition, $\arctan(0) = n\pi$, giving the expression

$$\psi(2\pi n) = -2\pi n + n\pi 2\frac{(1 + e)^2}{(1 - e^2)^{3/2}}. \tag{5.12}$$

120

After $n$ orbits the value of pitch angle is

$$\psi(2\pi n) = 2\pi m \tag{5.13}$$

or $m$ pitch rotations in $n$ orbits. Combining the latter two equations produces an equation relating the tumbling or rotational frequency (or winding number) with eccentricity,

$$P_{tumble} = \frac{m}{n} = \frac{(1+e)^2}{(1-e^2)^{3/2}} - 1. \tag{5.14}$$

This expression may be solved iteratively for $e$. As an example, one can easily calculate that a $P = 1/2$ rotation occurs at $e \approx 0.19$, a $P = 1/1$ rotation occurs at $e \approx 0.31$, and a $P = 3/2$ rotation occurs at $e \approx 0.395$. Comparison of these results with Figures 5.66 and 5.67 above shows that these estimates for eccentricity are good to within a few percent error, even for an inertia ratio as large as 0.04. The values for pitch rate at the periodic rotation points in Figure 5.67 are approximately zero, agreeing with the analytical theory above. Plotting Equation 5.14 results in the plots of Figure 5.68 (for the harmonics) and Figure 5.69 (for the subharmonics.) The frequency of rotation increases almost exponentially with increases of eccentricity, going to infinity very quickly for large values of $e$.

One can also examine the case for librational motion for a zero inertia ratio. From Equation 5.9

$$\psi(2\pi n) = 0 = -2\pi n + n\pi 2 \frac{(1+e)^2}{(1-e^2)^{3/2}}, \tag{5.15}$$

or

$$1 = \frac{(1+e)^2}{(1-e^2)^{3/2}}. \tag{5.16}$$

For $0 \leq e \leq 1.0$ only one real solution exists for Equation 5.16; $e = 0.0$. Thus, *libration cannot occur for* $K = 0.0$ *and* $\psi_o = \psi_o' = 0$ except for the trivial stationary solution where $\psi(f) = \psi'(f) = 0$ for all $f$. This result at first seems to be in conflict with the results presented in Figures 5.66 and 5.67. The first bay in these two bifurcation diagrams contained mostly librational motion and no rotational motion. These bifurcation diagrams were computed for $K = 0.04$, however, a small but non-zero inertia ratio. Re-examination of the structure of this first bay by computing bifurcation diagrams for smaller values of $K$ was carried out. Two of these new bifurcation plots are presented in Figures 5.70 and 5.71. One can see from comparing these two plots with Figure 5.66 that in the limit as $K \to 0.0$ the range of eccentricity for which librational motion occurs shrinks to zero.
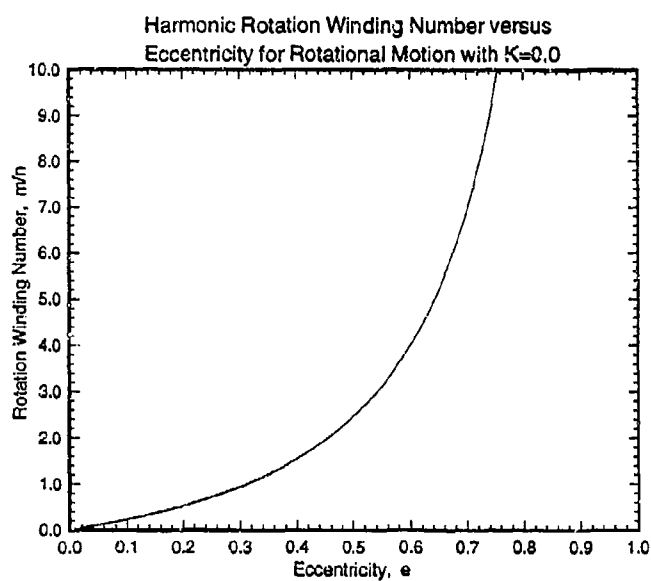
Figure 5.68: Harmonic Rotation Frequency versus Eccentricity for Rotational Motion with $K = 0.0$.
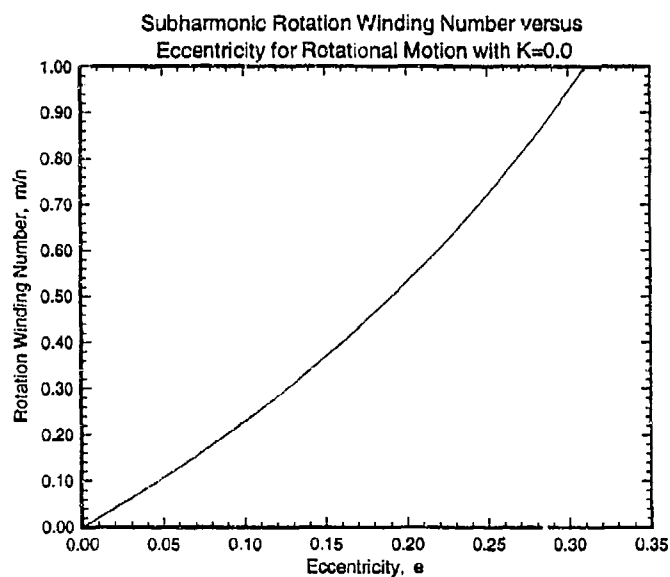


Figure 5.69: Subharmonic Rotation Frequency versus Eccentricity for Rotational Motion with $K = 0.0$.

122
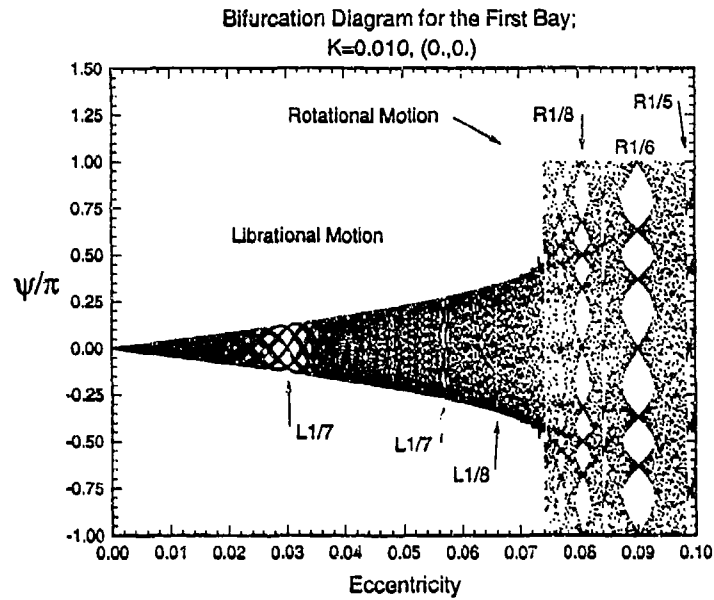
Figure 5.70: Bifurcation Diagram for the First Bay: $K = 0.010$, $(0., 0.)$.
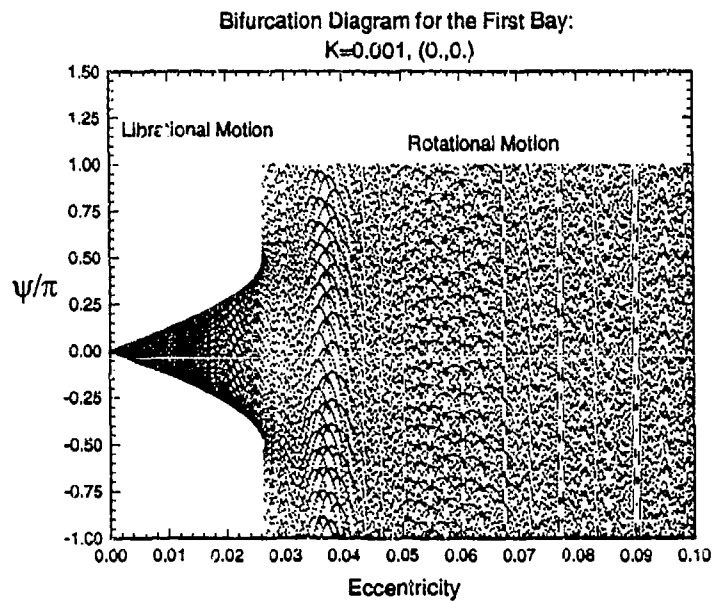


Figure 5.71: Bifurcation Diagram for the First Bay: $K = 0.0010$, $(0., 0.)$.
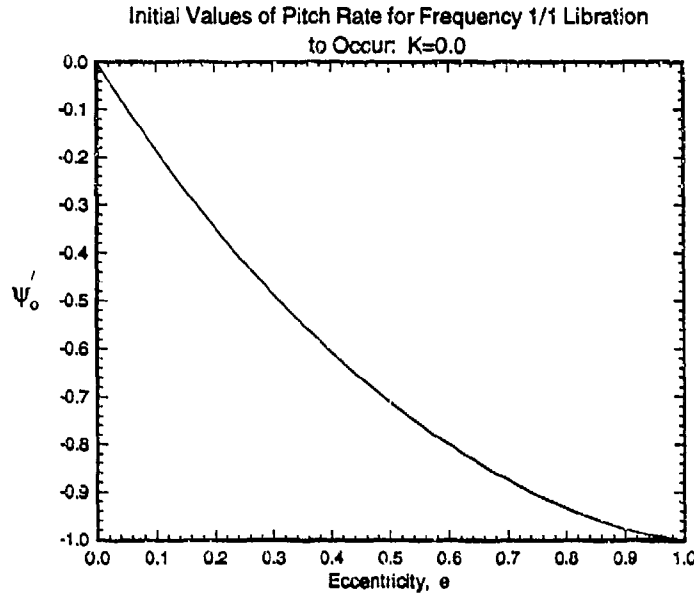
Figure 5.72: Initial Values of Pitch Rate for $P = 1/1$ Libration; $K = 0.0$.

Analytical periodic solutions for librational and rotational motion can also be found for the more general case where $\psi_o$ and $\psi'_o$ are not necessarily zero. Assuming the integration is still begun at periapsis, $f_o = 0$,

$$C_1 = (\psi'_o + 1)(1 + e)^2 \tag{5.17}$$

and

$$C_2 = \psi_o. \tag{5.18}$$

Substitution into Equation 5.5 gives

$$P = \frac{m}{n} = \frac{\psi_o}{2\pi n} - 1 + \frac{(\psi'_o + 1)(1 + e)^2}{(1 - e^2)^{3/2}} \tag{5.19}$$

for rotational motion, and

$$\psi'_o = \frac{(1 - e^2)^{3/2}}{(1 + e)^2} - 1 \tag{5.20}$$

for librational motion. This latter result shows that the initial value of pitch rate for libration is a function of eccentricity only. In fact, pitch rate ranges from $-1.0 \leq \psi' \leq 0.0$ as eccentricity ranges from $0.0 \leq e \leq 1.0$, as can be seen in Figure 5.72. For example, $\psi'_o = -0.019851$ for $e = 0.01$, and the trajectory is $P = 1/1$ libration for any initial pitch angle, $\psi_0$.

124
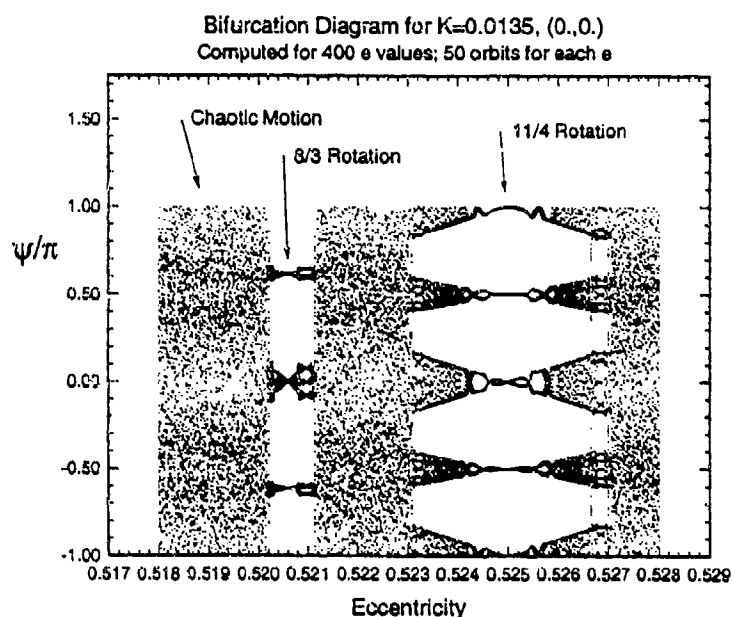
Figure 5.73: Bifurcation Diagram for $K = 0.0135$ and $(0., 0.)$.

## 5.5.5 Periodic Solutions in the Chaos Diagrams for Arbitrary $K$

The location of the periodic rotational trajectories for non-zero values of $K$ was explored further by computing numerous bifurcation diagrams for different values of $K$, recording the values of $e$ where a particular subharmonic occurred, and plotting these values on top of the chaos diagrams. A portion of one of these sequences of bifurcation diagram "slices" of a chaos diagram (in particular, Figures 5.61 and 5.63), computed for various inertia ratios, is presented in Figures 5.73 - 5.75. All of the periodic solutions displayed in these three plots are subharmonic tumbling trajectories. As $K$ decreases in these figures, the bifurcation diagrams show more order; more periodic trajectories become visible and the chaotic regions disappear. This is intuitive, for this sequence corresponds to a backing away from the chaotic region, moving from the right hand side of Figures 5.61 and 5.63 to the left.

The cumulation of the results of a number of similar sequences of harmonic and subharmonic periodic rotational solutions is presented by the plots of Figures 5.76 and 5.77. One can see from these two plots and the previous figures that periodic trajectories occur at the approximate centers of each bay and sub-bay of regular motion, extending from the left hand side of the chaos diagrams, where $K = 0$, to the

125
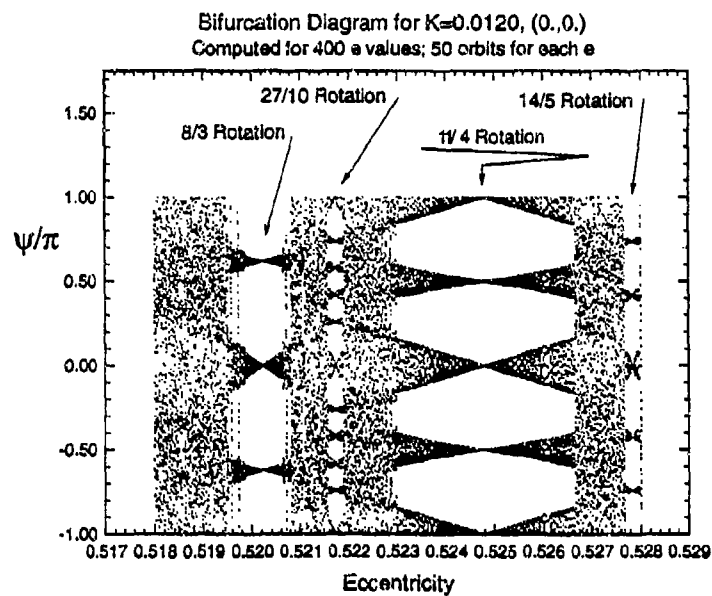
Figure 5.74: Bifurcation Diagram for $K = 0.0120$ and $(0., 0.)$.
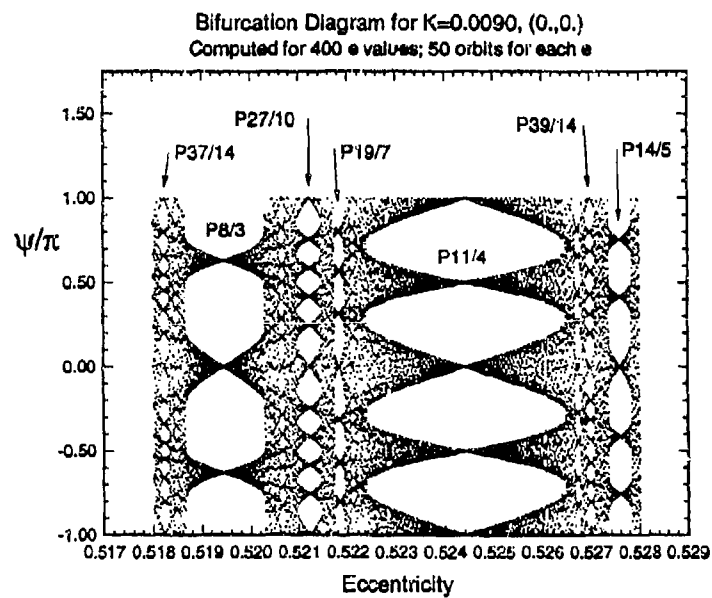


Figure 5.75: Bifurcation Diagram for $K = 0.0090$ and $(0., 0.)$.
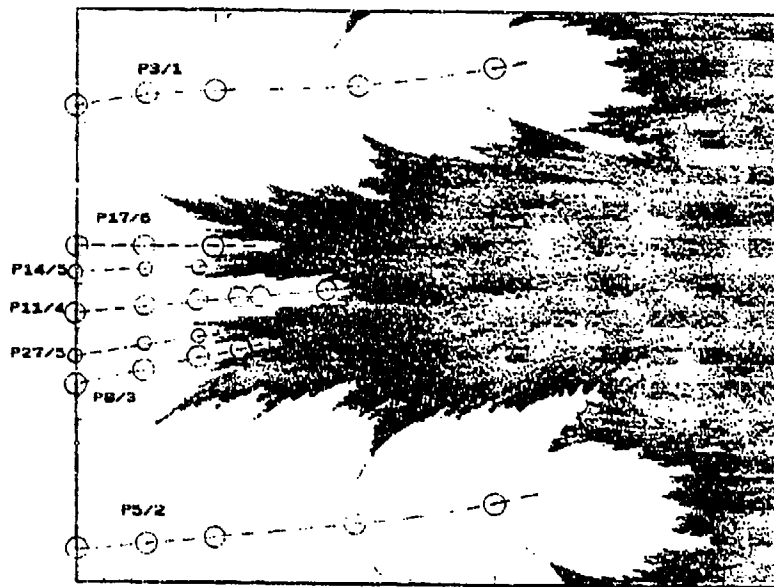
Figure 5.76: Mapping of Rotation Periodic Solutions on the Chaos Diagram of Figure 5.61.

right hand side until chaotic motion is reached. Further, at the center of the main, large bays (except for the first one) dwells periodic rotation trajectories of frequency $n/2$ where $n = 1, 2, 3, \ldots$ The next largest set of bays have at their centers solutions of frequency $(2n+1)/4$, such as the $P = 11/4$ set of solutions depicted in Figure 5.76. This appearance of periodic trajectories in the bays of regular motion on the chaos diagrams appears on multiple scales.

The structure of some of the subharmonic trajectories, shown in Figures 5.76 and 5.77, is repeated in other regular motion bays in the chaos diagram. This self-similarity can be seen in the comparison of Figures 5.78 (a bifurcation diagram for the second bay from the bottom of Figure 5.52) and 5.75 (a bifurcation diagram for the sixth bay). These two figures, in which only periodic and quasiperiodic pitch rotation occur, have the same pattern of harmonic solutions. The $P = 37/14$, $P = 8/3$, and $P = 11/4$ trajectories of Figure 5.75, for example, correspond to the $P = 9/14$, $P = 2/3$, and $P = 3/4$ solutions of Figure 5.78.
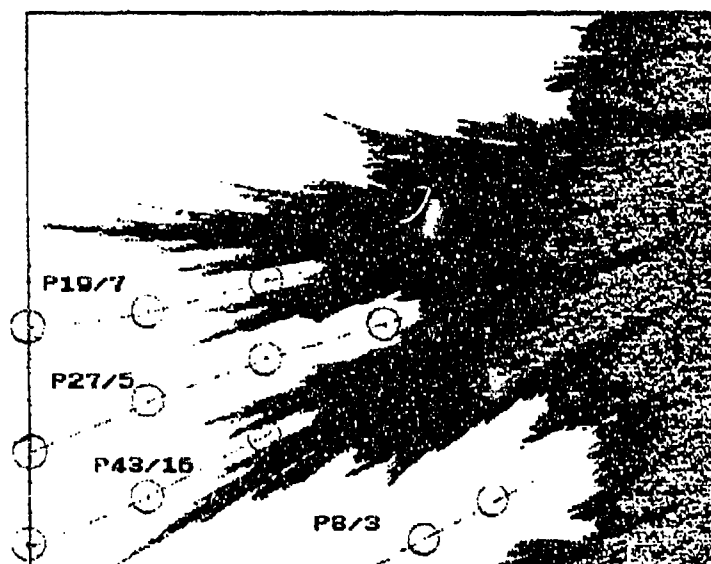
Figure 5.77: Mapping of Rotation Periodic Solutions on the Chaos Diagram of Figure 5.63.
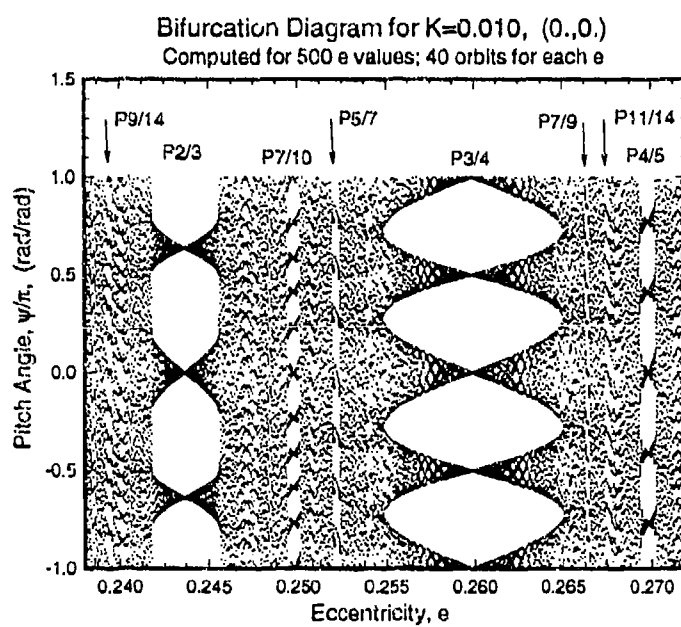


Figure 5.78: Bifurcation Diagram for $K = 0.010$ and $(0., 0.)$.

## 5.6  Summary

Many past studies of this problem have assumed that only eccentricity affects the nonlinearity of the system. This is wrong. The work presented here shows that both system parameters $e$ and $K$ affect the nonlinearity of the system, even for small values of inertia ratio. Whether or not a trajectory exhibits regular or chaotic motion is a function of the initial state, $(\psi_o, \psi'_o)$, $e$, and $K$. This fact was easily seen by examination of sequences of conventional nonlinear analysis numerically generated plots such as Poincaré maps and bifurcation diagrams, and also by examination of the chaos diagrams formed of grids of Lyapunov exponent values. The former two methods gave useful results but were restricted to a localized view of the relationships between the system parameters and the motion. In contrast, the chaos diagrams provide a global view of these relationships for the entire ranges of both system parameters.

It has been demonstrated in this report that chaos diagrams can be a very valuable tool. The use of chaos diagrams is very rare in the literature, and when they do appear, they are typically formed from a very coarse grid in which the border between chaotic and regular motion is approximated by only a few points, possibly far too few points for one to determine its true shape. The work presented here is unique in that the chaos diagrams are created for grids composed of hundreds of thousands of points and in color. This allowed enough detail of the border between regular and chaotic motion to be observed that its fractal form was easily discovered. The author could find only one other case in the literature of a fractal border in parameter space; in that case the fractal border was determined experimentally, not numerically. That the border was fractal in this section was verified by a simple calculation of fractal dimension using draftsman dividers and dial calipers to measure Figure 5.63. The chaos diagrams depicted a complex mix of regular and chaotic motion, with islands of regular motion appearing in a sea of chaos. This result raises serious questions to the accuracy of some of the analytical boundary prediction techniques that predict smooth and simple transition boundaries.

The above pages contribute significantly to our understanding of the motion for a gravity-gradient satellite in an eccentric orbit about a central body. Numerous Poincaré maps and phase space solutions were presented for a wide range of system parameters and initial conditions. Before this work, very few such plots existed in the literature. It is felt that the solutions presented here, especially the chaos diagrams, could prove to be of use in either orbit or satellite hardware design.

A number of bifurcation diagrams were presented in an attempt to obtain at least

a rudimentary knowledge of the structure of the chaos diagrams for the initial state $(0., 0.)$. These bifurcation diagrams represent dynamically equivalent vertical slices (constant $K$, variable $e$) and horizontal slices (constant $e$, variable $K$) of the chaos diagrams for the zero initial state. Figure 5.2 and other calculations showed that the islands of regular motion within the sea of chaos (Figure 5.58) portrayed rotational instead of librational motion. It was shown that, at least for the chaos diagrams for the $(0., 0.)$ initial state, most of the regular motion is libration, with rotation appearing generally for small values of $K$ and relatively larger values of $e$. Examination and comparison of these bifurcation diagram slices to the chaos diagrams revealed the existence of pitch angle tumbling periodic solutions centered roughly in the bays of regular motion in the chaos diagrams. These strings of periodic trajectories appeared on multiple scales in the chaos diagrams, with the winding number or frequency increasing with increasing eccentricity. To examine these trajectories further, an analytical solution was found for periodic tumbling motion for the limiting case of $K = 0$, which corresponds to the axially symmetric satellite. The analytical results agreed well with those found in the bifurcation diagrams and mapped in Figures 5.76 and 5.77, except for small values of eccentricity – apparently we need $e \gg K$ for these solutions to be useful.

Although numerous subharmonic librational trajectories were found in the study of the structure of the $(0., 0.)$ initial state chaos diagrams, no harmonic librational trajectories were observed. The circular orbit analytical theory allowed for a very limited range of periodic librational trajectories, and this range has probably been shifted even lower by the addition of eccentricity to the problem. In contrast, numerous examples of both harmonic and subharmonic rotational trajectories were found in the course of this study. The harmonics of the tumbling class of trajectories were unlimited; the $K = 0$ theory, similar to the circular orbit theory of the last section, showed that very high frequency rotations (approaching infinity) are possible.

# 6 Eccentric Orbit About an Oblate Central Body

## 6.1 Introduction

Because the effect of non-spherical gravitational torques is of the order $1/r_c{}^2$ smaller[1] than the gravitational torques produced by the inverse-square law terms, the oblate central-body terms are neglected in most studies. In fact, with the exception of Beletskii [12] and Koch and Bruhn [18], all of the research mentioned in the Introduction in Section 1 was based upon an inverse-square gravitational field. No matter how small the additional gravity-gradient torque due to a non-spherical central body, it is enough to produce perturbations in a satellite's orbit, leading to apsidal rotation, nodal regression, and variance in the orbit elements. A satellite's rotational and translational motions are therefore coupled, and its center of mass describes a non-Keplerian orbit. An extensive analytical examination of the resulting motion is provided by Beletskii [12].

This section presents a precursory look at the planar pitch angle dynamics for an uncontrolled gravity-gradient satellite in an elliptical polar orbit about an oblate central body. This study is restricted to polar orbits because of the simplifications that polar orbits introduce into the coupled equations. It is further assumed that roll and yaw remain zero for all time.[2] The analysis is mainly numerical. Nonlinear analysis techniques such as Poincaré maps and spectral analysis are utilized. The equations of motion include gravity-gradient perturbations in both the satellite's attitude and its orbit. This study builds upon the analytical work of Koch and Bruhn [18] by adding orbit perturbations due to oblateness and removing the restriction of small eccentricity. Periodic, quasiperiodic, and chaotic pitching motion are shown to exist.

---

[1] $r_c$ is the distance between the center of mass of the central body and the center of mass of the orbiting body.

[2] Although it can be shown that the pitch, roll, and yaw equations of motion are decoupled for a satellite in an eccentric orbit about a spherical (and homogeneous) central body, this is not the case for an oblate central body. Hughes [36, page 309] points out that if roll and yaw are initially small, they stay small for the spherical central body case. A study of the effects of this coupling for the oblate central body problem was initiated but not completed due to time constraints.

## 6.2 The Equations of Motion

The assumptions used in this section are the same as those discussed in Section 2 with the additional imposition here that the satellite is in a polar orbit about an oblate, axially-symmetric central body. The equations of motion derived below may be applied to any two-body system where the above assumptions are appropriate. In this investigation, the Earth is taken as the central body.

### 6.2.1 Pitch Equation of Motion

The potential due to a non-spherical central body can be represented by an expansion in terms of spherical harmonics which vary with latitude and longitude. In general, the most dominant contribution is the one obtained by modelling the central body as an ellipsoid of revolution. Figure 6.1 illustrates the geometry of this problem.

Here, $\psi$ is the the satellite pitch (or Earth pointing) angle measured with respect to the radial direction, $\omega$ is the argument of periapsis, and $f$ is the orbital true anomaly. A non-rotating, equatorial, Earth-centered coordinate system $(X, Y, Z)$ is used as the fundamental reference frame. The satellite principal-axis system is designated $(x, y, z)$. The orbit radial and transverse directions are denoted $\hat{e}_r$ and $\hat{e}_t$, respectively. For the case of an oblate central body, the gravitational potential of a differential satellite mass $dm$ at a distance $r$ from the center of mass of the Earth is expressed as,

$$d\mathcal{V} = \left[ -\frac{\mu}{r} + \frac{\mu J_2 R_e^2}{2r^3} \left( 3\sin^2\theta - 1 \right) \right] dm. \qquad (6.1)$$

$\mu$ is the Earth's gravitational constant, $R_e$ is the Earth's mean equatorial radius, $\theta$ is the satellite's argument of latitude, and $J_2$ is the dominant spherical harmonic coefficient ($J_2 \approx 1.08263 \times 10^{-3}$). Substitution for $\sin^2\theta$ in terms of $r$ allows this equation to be written as a function of $1/r^n$, $n = 1, 3, 5$. Since $\vec{r} \equiv \vec{r_c} + \vec{\rho}$ (Figure 6.2), one may carry out the integration of Equation (6.1) over the orbiting body's mass by expanding $r_c^n/r^n$ in terms of $\rho/r_c$ and $J_2$.[3] This yields the gravitational potential function[4]

$$\mathcal{V} = -\frac{\mu m}{r_c} \left[ 1 + \frac{1}{2} J_2 \frac{R_e^2}{r_c^2} \left( 1 - 3d_{13}^2 \right) \right]$$

---

[3] Note that $\rho/r_c$ for most satellites in low Earth orbit is the same order of magnitude as $(J_2)^2$.

[4] See the Appendix for a more detailed derivation of this equation.
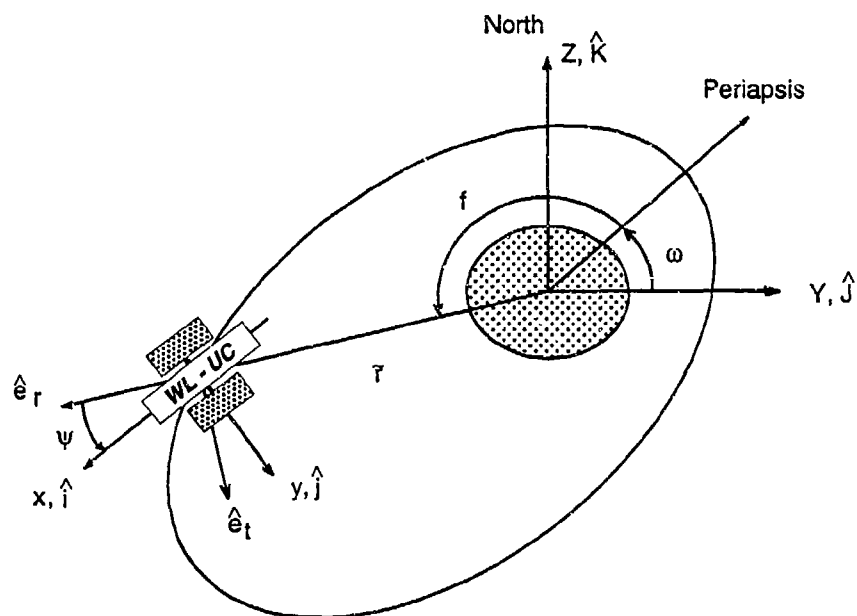
Figure 6.1: Orbit and Attitude Geometry in the Polar Orbit Plane.
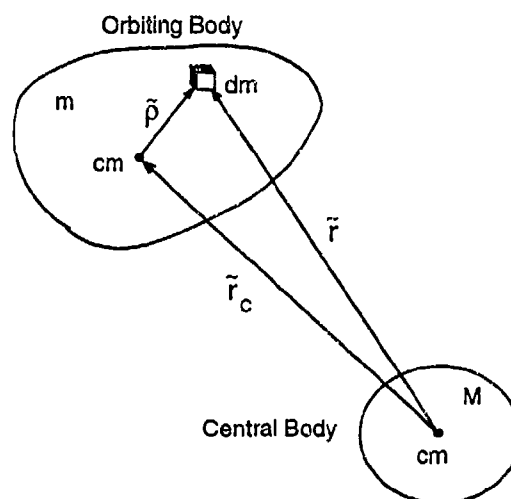


Figure 6.2: Definition of $\vec{\rho}$.

133

$$-\frac{\mu}{2r_c^3}\left(\Sigma_1 - 3\Sigma_2\right) - \frac{3J_2\mu R_e^2}{4r_c^2}\left[\left(1 - 5d_{13}^2\right)\Sigma_1\right.$$
$$\left. -5\left(1 - 7d_{13}^2\right)\Sigma_2 + 2\Sigma_3 - 20d_{13}\Sigma_4\right], \tag{6.2}$$

where

$$\begin{aligned}
\Sigma_1 &\equiv I_x + I_y + I_z,\\
\Sigma_2 &\equiv I_x c_{11}^2 + I_y c_{21}^2 + I_z c_{31}^2,\\
\Sigma_3 &\equiv I_x \alpha_1^2 + I_y \alpha_2^2 + I_z \alpha_3^2,\\
\Sigma_4 &\equiv I_x c_{13}\alpha_1 + I_y c_{23}\alpha_2 + I_z c_{33}\alpha_3,\\
\alpha_1 &\equiv c_{11}d_{13} + c_{12}d_{23} + c_{13}d_{33},\\
\alpha_2 &\equiv c_{21}d_{13} + c_{22}d_{23} + c_{23}d_{33},\\
\alpha_3 &\equiv c_{31}d_{13} + c_{32}d_{23} + c_{33}d_{33}.
\end{aligned} \tag{6.3}$$

The $I_i$ terms in Equations (6.3) are the satellite's principal moments of inertia, and the $c_{ij}$ terms are the direction cosines between the satellite's principal axes and the orbit radial, transverse, and normal directions. The Euler rotation matrix $\mathcal{C}$, which the $c_{ij}$ elements comprise, may be expressed as

$$\begin{bmatrix} \hat{i} \\ \hat{j} \\ \hat{k} \end{bmatrix} = \mathcal{C} \begin{bmatrix} \hat{e}_r \\ \hat{e}_t \\ \hat{e}_n \end{bmatrix}, \tag{6.4}$$

where

$$\begin{aligned}
c_{11} &= \cos\psi\cos\vartheta,\\
c_{12} &= \sin\phi\sin\vartheta\cos\psi + \sin\psi\cos\phi,\\
c_{13} &= \sin\phi\sin\psi - \cos\phi\sin\vartheta\cos\psi,\\
c_{21} &= -\sin\psi\cos\vartheta,\\
c_{22} &= \cos\psi\cos\phi - \sin\psi\sin\vartheta\sin\phi,\\
c_{23} &= \cos\psi\sin\phi + \cos\phi\sin\vartheta\sin\psi,\\
c_{31} &= \sin\vartheta,\\
c_{32} &= -\cos\vartheta\sin\psi,\\
c_{33} &= \cos\vartheta\cos\psi,
\end{aligned} \tag{6.5}$$

and where $\vartheta$ and $\phi$ are the roll and yaw angles of the satellite. The $d_{ij}$ are the direction cosines between the orbit radial, transverse, and normal directions and the reference frame axes $(X, Y, Z)$ (Figure 6.3).

The Euler rotation matrix $\mathcal{D}$ is

$$\begin{bmatrix} \hat{e}_r \\ \hat{e}_t \\ \hat{e}_n \end{bmatrix} = \mathcal{D} \begin{bmatrix} \hat{I} \\ \hat{J} \\ \hat{K} \end{bmatrix}, \tag{6.6}$$

134

Figure 6.3: System Coordinates and Axes.

with

$$d_{11} = \cos \Omega \cos \theta - \sin \Omega \sin \theta \cos I,$$
$$d_{12} = \sin \Omega \cos \theta + \cos \Omega \sin \theta \cos I,$$
$$d_{13} = \sin \theta \sin I,$$
$$d_{21} = - \cos \Omega \sin \theta - \sin \Omega \cos \theta \cos I,$$
$$d_{22} = - \sin \Omega \sin \theta + \cos \Omega \cos \theta \cos I, \qquad (6.7)$$
$$d_{23} = \cos \theta \sin I,$$
$$d_{31} = \sin \Omega \sin I,$$
$$d_{32} = - \cos \Omega \sin I,$$
$$d_{33} = \cos I,$$

and where $I$ is the orbital inclination and $\Omega$ is the longitude of the ascending node. These rotation matrices are considerably simplified with the planar, polar orbit assumption ($I = \pi/2$, $\Omega = 0$) and the assumption that the satellite does not roll or yaw.

Using the gravitational potential of Equation (6.2) and dropping the subscript "$c$" notation in $r_c$, the Lagrangian may be formed and the pitch equation of motion derived[5],

$$\ddot{\psi} + \ddot{f} + \frac{3\mu}{r^3} K \cos \psi \sin \psi$$

---

[5]See the Appendix for a more detailed derivation of this equation.

135

$$-\frac{3\mu J_2 K R_e^2}{8r^5}[16\cos 2\psi \sin 2\theta$$
$$+\sin 2\psi(5-19\cos 2\theta)]=0. \tag{6.8}$$

Again, $e$ is the orbital eccentricity and dots ($\dot{}$) represent differentiation with respect to time.

Note that this pitch equation of motion is derived to order $(J_2)^2$ which, for low-altitude satellites with a maximum dimension ($\rho$) on the order of five meters, is equivalent to order $(\rho/r)^3$. This equation is similar to that studied by Koch and Bruhn [18], but differs in that it preserves its explicit dependence upon the orbital distance.

## 6.2.2 Variation of the Orbital Elements

Gauss' form of the variational equations for the orbital elements $a$, $e$, and $\omega$ using the perturbative accelerations in the transverse, $a_t$, and radial, $a_r$, directions are [50]

$$\begin{aligned}
\frac{da}{dt} &= \frac{2a^2}{h}\left(e\sin f\, a_r + \frac{p}{r}a_t\right), \\
\frac{de}{dt} &= \frac{1}{h}\left(p\sin f\, a_r + [(p+r)\cos f + re]\, a_t\right), \\
\frac{d\omega}{dt} &= \frac{1}{he}\left[-p\cos f\, a_r + (p+r)\sin f a_t\right] - \dot{\Omega}\cos I.
\end{aligned} \tag{6.9}$$

The acceleration components are obtained from

$$\vec{\nabla}\mathcal{V}_{oblate} = -\frac{\partial \mathcal{V}_{oblate}}{\partial r}\hat{e}_r - \frac{\partial \mathcal{V}_{oblate}}{r\partial\theta}\hat{e}_t = a_r\hat{e}_r + a_t\hat{e}_t. \tag{6.10}$$

Accordingly,

$$\begin{aligned}
a_r &= -\frac{3\mu J_2 R_e^2}{2r^4}(1-3\sin^2\theta), \\
a_t &= -\frac{3\mu J_2 R_e^2}{r^4}\sin\theta\cos\theta.
\end{aligned} \tag{6.11}$$

From the definition of the argument of latitude $\theta$,

$$\dot{\theta} = \dot{\omega} + \dot{f}, \tag{6.12}$$

where in general,

$$\frac{df}{dt} = \frac{1}{he}\left[p\cos f\, a_r - (p+r)\sin f a_t\right] + \frac{n}{r^2}. \tag{6.13}$$

136

For the case of polar orbiters

$$\frac{d\Omega}{dt} = \frac{dI}{dt} = 0. \tag{6.14}$$

Consequently,

$$\dot{\theta} = \frac{h}{r^2}, \quad \text{(polar orbits only)}. \tag{6.15}$$

It is convenient to rewrite the pitch equation using the argument of latitude as the independent variable. For the case of polar orbiters, the relationship between time $t$ and $\theta$ is expressed in Equation (6.15) above. This transformation produces the following expressions for the variation of eccentricity and argument of periapsis:

$$\left.\begin{aligned}
\frac{de}{d\theta} &= \frac{r}{\mu} \left\{ \sin f a_r \left[ \frac{re}{p_* R_e} + \left( 1 + \frac{r}{p_* R_e} \right) \cos f \right] a_t \right\}, \\
\frac{d\omega}{d\theta} &= \frac{r}{\mu e} \left[ -\cos f a_r + \left( 1 + \frac{r}{p_* R_e} \right) \sin f a_t \right].
\end{aligned}\right\} \tag{6.16}$$

A scaled parameter has been introduced in these equations,

$$p_* \equiv h^2/(R_e \mu), \tag{6.17}$$

whose derivative with respect to $\theta$ is

$$\frac{dp_*}{d\theta} = \frac{2h}{R_e \mu} \frac{dh}{d\theta} = \frac{2r^3}{R_e \mu} a_t. \tag{6.18}$$

Making the indicated substitutions gives the following expressions for the $\theta$ variation of the pertinent Keplerian elements needed in the pitch equation:

$$\left.\begin{aligned}
\frac{dp_*}{d\theta} &= -\frac{3J_2}{p_*} [1 + e\cos(\theta - \omega)] \sin 2\theta, \\
\frac{de}{d\theta} &= -\frac{3J_2}{2p_*^2} [1 + e\cos(\theta - \omega)]^2 \left[ \sin(\theta - \omega)\left(1 - 3\sin^2\theta\right) \right. \\
&\quad \left. + \frac{e\sin 2\theta}{1 + e\cos(\theta - \omega)} + \sin 2\theta \cos(\theta - \omega) \cdot \left( 1 + \frac{1}{1 + e\cos(\theta - \omega)} \right) \right], \\
\frac{d\omega}{d\theta} &= -\frac{3J_2}{2ep_*^2} [1 + e\cos(\theta - \omega)]^2 \left[ \sin 2\theta \sin(\theta - \omega) \cdot \right. \\
&\quad \left. \left( 1 + \frac{1}{1 + e\cos(\theta - \omega)} \right) + \cos(\theta - \omega)\left( 3\sin^2\theta - 1 \right) \right].
\end{aligned}\right\} \tag{6.19}$$

After some algebra, the pitch equation can be rewritten in the form

$$\psi'' \left[1 + e \cos\left(\theta - \omega\right)\right] + \frac{3}{2} K \sin 2\psi - 2e \sin\left(\theta - \omega\right)\left(\psi' + 1\right)$$

$$= \frac{3K J_2}{8 p_*^2} \left[1 + e \cos\left(\theta - \omega\right)\right]^2 \cdot \left[16 \cos 2\psi \sin 2\theta + \sin 2\psi (5 - 19 \cos 2\theta)\right], \quad (6.20)$$

where primes ( $'$ ) now represent differentiations with respect to $\theta$ instead of $f$.

*Note that the $p_*$ and $e$ variational equations given above are the same order of magnitude as the $J_2$ terms in the pitch equation of motion,* Equation (6.20). In addition, the $\omega$ variational equation is of order $J_2/e$ and would be large for small eccentricity orbits. In the limit as $e \to 0$, however, this equation is singular and $\omega$ is undefined. These results indicate it is inconsistent to include terms of order $J_2$ in the pitch equation of motion without also accounting for variations in the orbital elements.[6]

# 6.3  Results

In the previous section the pitch equation of motion, Equation (6.20), was derived for a satellite in an eccentric, polar orbit about an oblate planet. This equation was numerically integrated using a fifth-order Runge-Kutta routine with an integration step size of $2\pi/1000$. The method of variation of parameters was applied to develop expressions for the deviation of the scaled parameter $p_*$, eccentricity, and argument of periapsis from their constant Keplerian values due to an oblate central body. These equations, Equations (6.19), were utilized to correct the orbital elements at each integration step of the pitch equation. The nonlinear properties of this system were numerically examined using Poincaré mappings and spectral analysis for an arbitrary example problem. This example problem used an inertia ratio of $K = 1.0$ for a satellite in a polar, 200 x 300 nautical mile (370 x 556 km) orbit about the Earth. Initial values of the orbital elements were $p_o = 2.2441053 \times 10^7$ feet (7440.3 km), $e_o = .013535$, $\omega_o = 10$ degrees, $f_o = 30$ degrees, and $\theta_o = 40$ degrees. Unless otherwise specified, all results were generated for the initial values of $(\psi_o, \psi'_o) = (0.0, 0.0)$. In the following sections, the terms "baseline model" and "Spherical Earth" refer to the evaluation of the pitch equation of motion without accounting for the $J_2$ and variational terms. The expressions "enhanced model" or "Oblate Earth + VOP"[7]

---

[6]The analytical work of [18] is missing these variations.

[7]The abbreviation VOP indicates the correction of the orbital elements at each time step with Equations (6.19), which were derived using the method of variation of parameters.
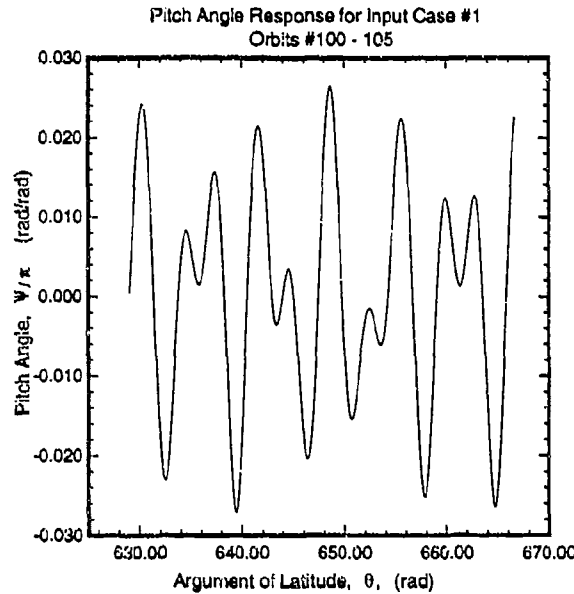
Figure 6.4: Pitch Angle Response Over Orbits 100-105.

refer to the evaluation of the pitch equation of motion with the $J_2$ and variation of orbital elements terms.

## 6.3.1 Response of System Parameters

The responses of $\psi$ and the rate $\psi'$ over six orbits is presented in Figures 6.4 and 6.5 after an integration of 100 orbits. The nature of the satellite's attitude motion (periodic, quasiperiodic, or chaotic) cannot be easily discerned from these plots. Although one can easily see that neither $\psi$ nor $\psi'$ is periodic over these six orbits, one cannot detect from these plots if the motion is chaotic or if it is periodic outside this six-orbit window. Figure 6.6 shows the variation of the argument of periapsis over these six orbits. The downward-tending slope of this plot reflects the secular terms of Equations (6.19) which has caused $\omega$ to decrease by approximately 27 degrees during the satellite's first 100 orbits.

Figures 6.7 and 6.8 display the variation in the eccentricity and the scaled parameter. Note that eccentricity varies on the order of 15% from its initial value of .013535.

139
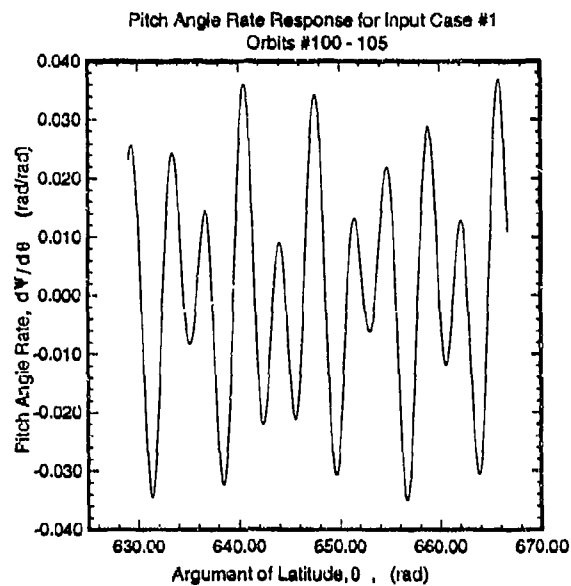
Figure 6.5: Pitch Angle Rate Response Over Orbits 100-105.
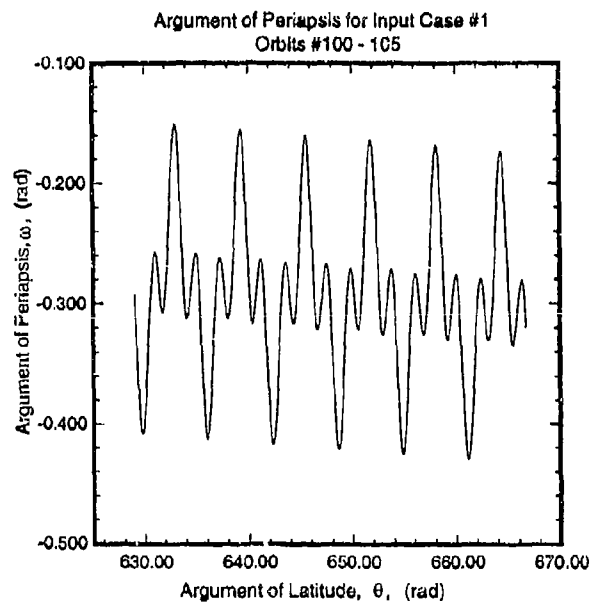


Figure 6.6: Variation in Argument of Periapsis Over Orbits 100-105.
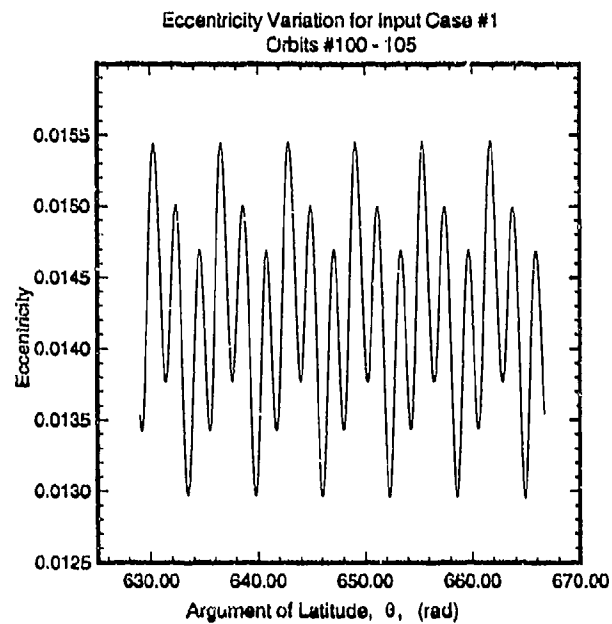
Figure 6.7: Variation in Eccentricity Over Orbits 100-105.
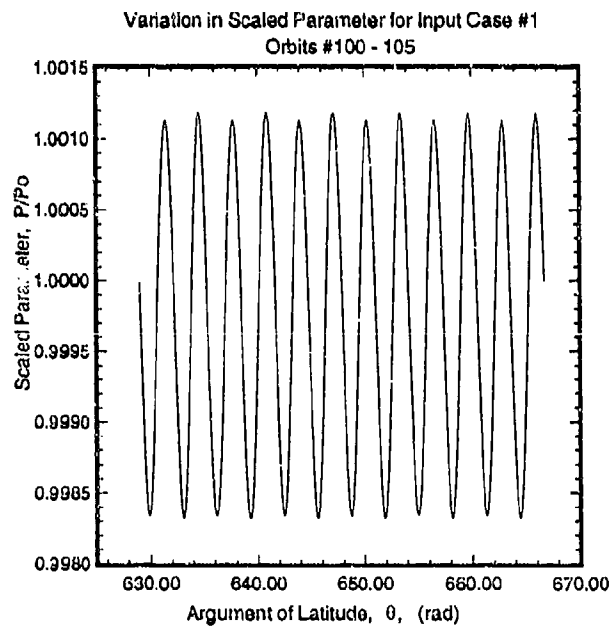


Figure 6.8: Variation in Scaled Parameter Over Orbits 100-105.

141
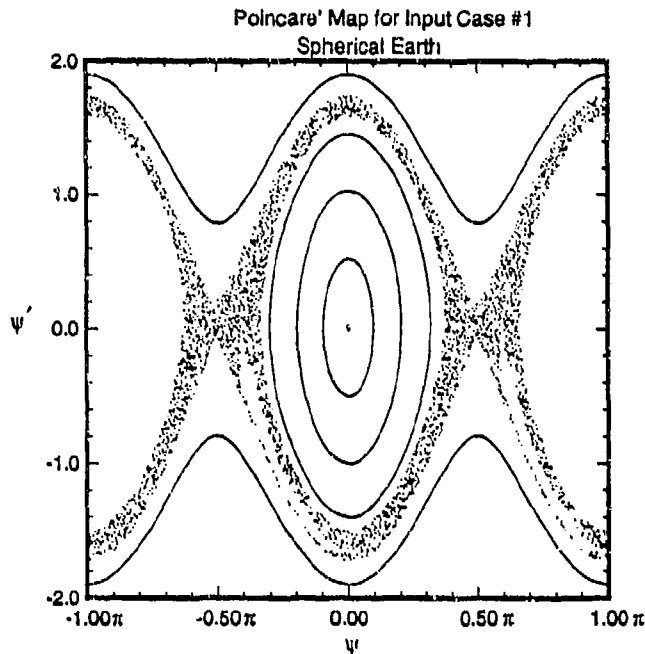
Figure 6.9: Poincaré Map for a Spherical Earth Model for Various Values of $\psi_o$ and $\psi_o'$.

## 6.3.2 Nonlinear Analysis

A Poincaré map for the baseline model (fixed $e$, $p_*$, and $\omega$, and $J_2 = 0$) of the example problem, generated from collecting values of $\psi$ and $\psi'$ each time the satellite passed through periapsis, is presented in Figure 6.9. This map is composed of multiple trajectories and required additional initial values of $\psi_o$ and $\psi_o'$. The resultant surface of section is very similar to that for a classical forced pendulum. Quasiperiodic pitching motion is depicted by the pitch-angle circulation, which occurs for large initial magnitudes of $\psi'$, and in the pitch-angle libration, which occurs on the centers of the Poincaré map. Chaotic pitching motion occurs for some initial values of $\psi$ and $\psi'$ and is represented by the scattering of points in the vicinity of the separatrices. Additional periodic and quasiperiodic solutions also would appear in a more detailed examination (and with the mapping of additional trajectories). For initial conditions near $(\psi_o, \psi_o') = (0.0, 0.0)$, however, the baseline model produces a period-one solution. The results of the previous section show that the pitching motion for the baseline model is dependent not only on the initial conditions of $\psi$ and $\psi'$, but also on the fixed values of $K$ and $e$. For the enhanced model, eccentricity is no longer constant and the problem becomes even more complicated.

142
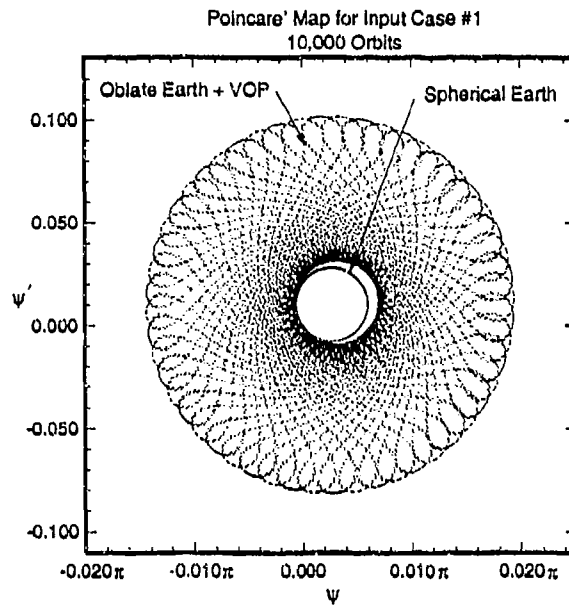
Figure 6.10: Comparison of Poincaré Maps for the Spherical Earth and Oblate Earth + VOP Models at $(\psi_o, \psi_o') = (0.0, 0.0)$.

A comparison of Poincaré maps (for single trajectories) for initial values of $(\psi_o, \psi_o') = (0.0, 0.0)$ for both the baseline and enhanced models is presented in Figure 6.10 for 10,000 orbits. The map for the baseline model is that of a simple center (quasiperiodic pitching motion) whereas the map of the enhanced model covers more of the phase space and displays more complexity. Because of the relatively large eccentricity variations depicted in Figure 6.7, and because the enhanced model incorporates additional terms, some variation between Poincaré maps for the two models was expected. The resultant symmetry of the enhanced model's Poincaré map was surprising, however. Figures 6.11 and 6.12 display the Poincaré map for the enhanced model plotted against eccentricity. One can conclude from Figures 6.10 - 6.12 that the initial conditions of $(\psi_o, \psi_o') = (0.0, 0.0)$ for the enhanced model case produces quasiperiodic pitching motion. This conclusion may be verified by spectral analysis of the data used in these Poincaré maps. Fast Fourier Transforms (FFT's) of the pitch angles generated by the baseline model and by the enhanced model are presented in Figures 6.13 and 6.14, respectively. Two fundamental frequencies appear in these nearly identical plots, demonstrating periodicity.

The importance of including the $J_2$ terms in the pitch equation of motion and of incorporating the variation of the orbital elements is exemplified by the results presented in Figure 6.15. This figure displays a comparison of Poincaré maps for the

143
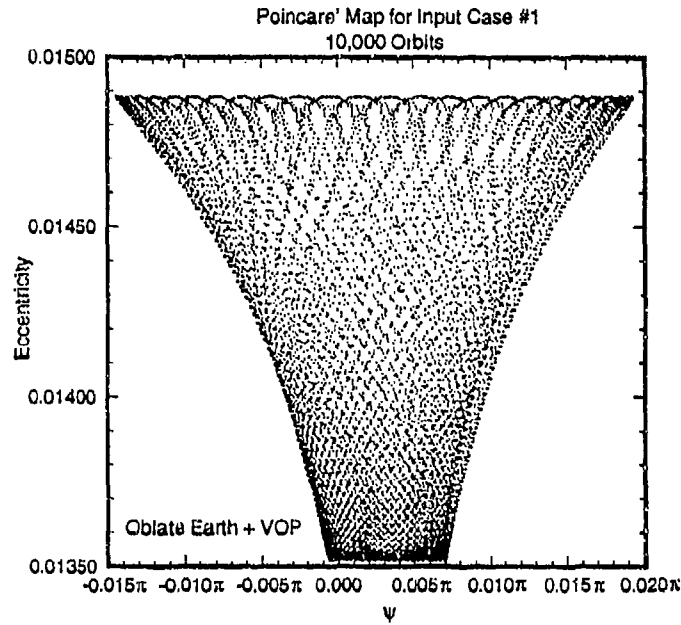
Figure 6.11: Poincaré Map with Eccentricity for the Oblate Earth + VOP Model at $(\psi_o, \psi_o') = (0.0, 0.0)$.
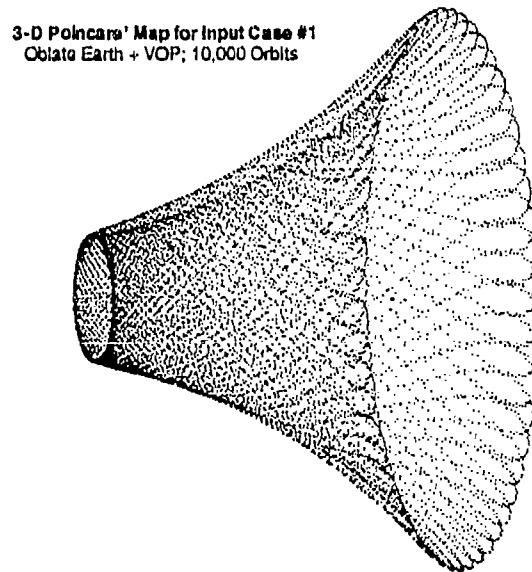


Figure 6.12: Three Dimensional Representation of a Poincaré Map for the Oblate Earth + VOP Model at $(\psi_o, \psi_o') = (.1013\pi, .2)$.

Fast Fourier Transform of Pitch Angle
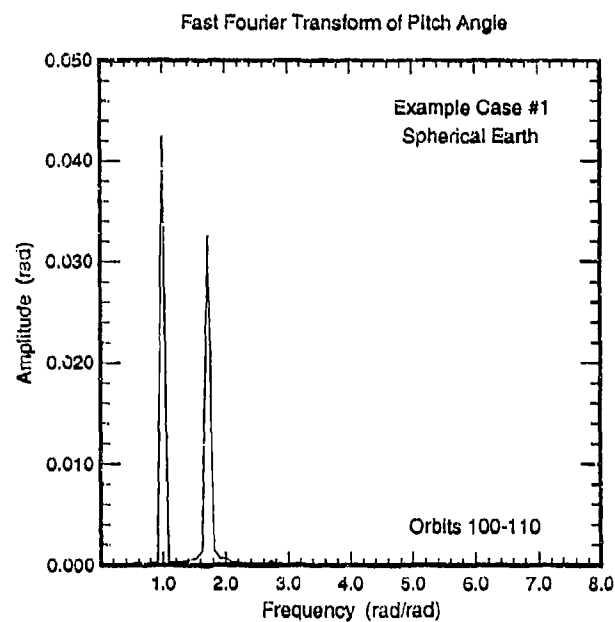


Figure 6.13: Fast Fourier Transform of Pitch Angle for the Spherical Earth Model at $(\psi_o, \psi'_o) = (0.0, 0.0)$.

Fast Fourier Transform of Pitch Angle
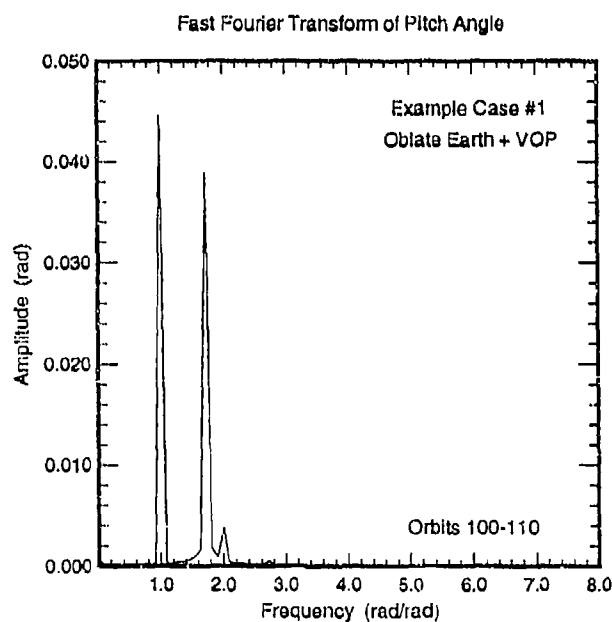


Figure 6.14: Fast Fourier Transform of Pitch Angle for the Oblate Earth + VOP Model at $(\psi_o, \psi'_o) = (0.0, 0.0)$.
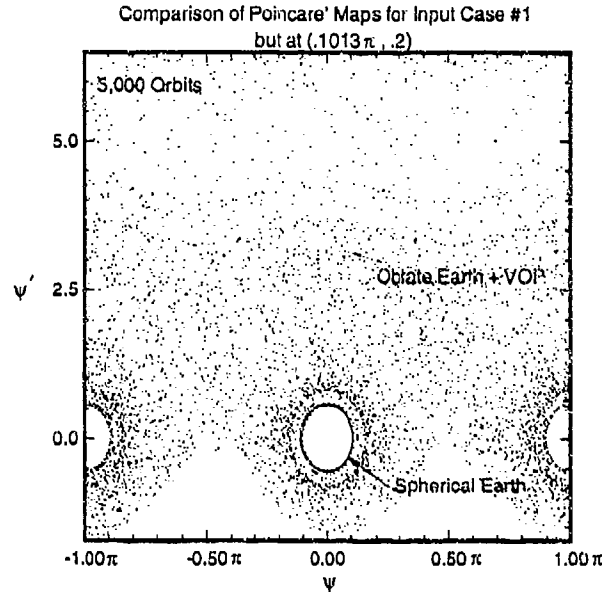
Figure 6.15: Comparison of Poincaré Maps for the Spherical Earth and the Oblate Earth + VOP Models at $(\psi_o, \psi_o') = (.1013\pi, .2)$.

two models for the initial values of $\psi_o$ and $\psi_o'$ of $(.1013\pi, 0.2)$. The surface of section for the baseline model is once again a simple center, indicating that the pitch angle's motion is not only regular, but it is predictable for all time and is restricted to a small portion of the phase space. In contrast, the surface of section for the enhanced model is chaotic. The pitch angle and its rate vary unpredictably and range over a large area of phase space. This result may be verified by spectral analysis of the data. Fast Fourier transforms of the pitch angles generated by the baseline model and by the enhanced model are presented in Figures 6.16 and 6.17, respectively. The former shows one or two fundamental frequencies (indicating periodicity) whereas the latter figure clearly demonstrates the aperiodicity feature of chaos.

## 6.4 Summary

A unique planar pitch equation of motion for a satellite in an eccentric, polar orbit about an oblate, axially symmetric planet was derived. In addition to the assumptions listed in Section 2, it was assumed that roll and yaw were zero for all time. The use of the osculating orbital elements was another unique feature of the nonlinear analysis of this problem. It was found that the variational equations for scaled parameter and eccentricity are the same order of magnitude as the $J_2$ terms in the pitch equation

146
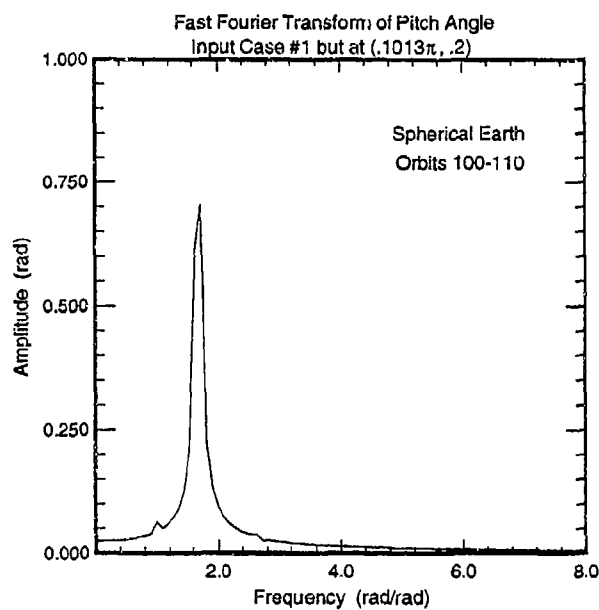
Figure 6.16: Fast Fourier Transform of Pitch Angle for the Spherical Earth Model at $(\psi_o, \psi_o') = (.1013\pi, .2)$.
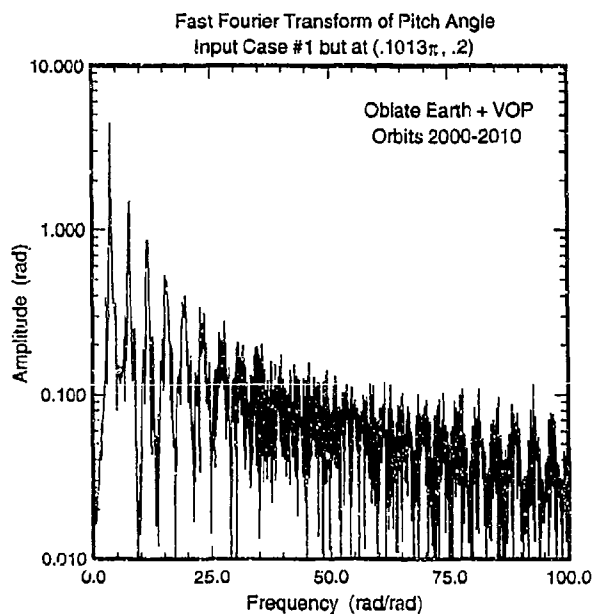


Figure 6.17: Fast Fourier Transform of Pitch Angle for the Oblate Earth + VOP Model at $(\psi_o, \psi_o') = (.1013\pi, .2)$.

of motion. This is an important finding as it indicates that it is inconsistent to include terms of order $J_2$ in the pitch equation of motion without also accounting for variations in the orbital elements.

The inclusion of the oblate terms and use of osculating orbital elements greatly affected the dynamics of the satellite pitching motion for a specific example problem. Eccentricity (assumed constant in previous nonlinear analyses of planar gravity-gradient pitch dynamics) was shown to vary almost 15%. A three-dimensional Poincaré mapping based on $(\psi(2\pi n), \psi'(2\pi n), e(2\pi n))$ where $n = 0, 1, 2, \ldots$ was created depicting quasiperiodic motion. With this more elaborate model, chaos was detected in areas of the phase space where the spherical, homogeneous central body model indicated the motion was regular.

# 7  Eccentric Orbit With Damping

## 7.1  Introduction

The main objective of this section is to provide an introduction to the pitching
dynamics for the gravity-gradient satellite problem with the addition of two separate
damping terms. The first term is simple linear damping and the second is nonlinear
damping that is a function of the square of the velocity. This section is meant to
serve as a supplement to the main emphasis of this study, the examination of gravity-
gradient pitch dynamics for eccentric orbits, discussed in Section 5.

The dynamics of a real satellite are not as simple as the model used in Section
5 may imply. A spacecraft is actually subjected to a variety of internal and external
torques that can contribute linear and nonlinear damping forces. The linear damping
case was (rather briefly) previously studied by Tong and Rimrott [22] and the work
presented here builds upon that foundation. To the author's knowledge, the nonlinear
damping case has not been studied except in the context of a transition study [19]
using the method of Melnikov.

A second objective of this section is to examine the validity of Melnikov's method
in the prediction of the border between chaos and regular motion. This method
has been applied a number of times in the past but with a minimum of emphasis
upon its accuracy. Many references present very impressive analytical derivations
of the Melnikov chaos criteria but make little, or in a few cases, no mention of the
accuracy of the prediction. Tortorelli and Vakakis [25] investigated the accuracy of
experimental and analytical chaos prediction techniques for a forced Duffing oscillator
and found the Melnikov criteria to have approximately an order of magnitude error.
The Melnikov chaos criteria for the nonlinear damping case was previously derived
by Seisl and Steindl [19], but the criteria for the linear damping case does not appear
in the literature.

## 7.2 Equations of Motion

The equation of motion for a gravity-gradient satellite in an elliptical orbit about a spherical central body with a generic damping term may be expressed as

$$\frac{d^2\psi}{dt^2} + \frac{d^2f}{dt^2} + \frac{3\mu}{2r^3}K\sin 2\psi = -C_D\dot{\psi}^p, \quad p = 1, 2, 3\ldots \tag{7.1}$$

where $C_D$ is the damping coefficient. The expressions for the motion of the center of mass of the satellite in a Keplerian orbit used in Section 2, Equations 2.2 and 2.3, are utilized to replace time with true anomaly as the independent variable in Equation 7.1. This results in the generic equation of motion,

$$\frac{d^2\psi}{df^2}(1 + e\cos f) - 2e\left(\frac{d\psi}{df} + 1\right)\sin f + \frac{3}{2}K\sin 2\psi$$
$$= -C_D\frac{h^{(6-3p)}\psi'^p}{\mu^{(4-2p)}(1 + e\cos f)^{(3-2p)}}. \tag{7.2}$$

In this section the linear damping case, p=1, and a nonlinear damping case where p=2 are examined.

Substitution into the above expression produces the equation of motion for p=1 damping,

$$\frac{d^2\psi}{df^2}(1 + e\cos f) - 2e\left(\frac{d\psi}{df} + 1\right)\sin f + \frac{3}{2}K\sin 2\psi = -C_{D_*}\frac{\psi'}{(1 + e\cos f)}. \tag{7.3}$$

where

$$C_{D_*} \equiv C_D\frac{h^3}{\mu^2}. \tag{7.4}$$

The equation of motion has now become a function of orbital angular momentum, $h$, and the Earth's gravitational constant, $\mu$. From Equation 7.2, the equation of motion for the nonlinear, p=2 damping case is

$$\frac{d^2\psi}{df^2}(1 + e\cos f) - 2e\left(\frac{d\psi}{df} + 1\right)\sin f + \frac{3}{2}K\sin 2\psi = -C_D\psi'^2(1 + e\cos f). \tag{7.5}$$

## 7.3 Pitching Motion for Linear (p=1) Damping

Tong and Rimrott presented in Reference [22] a brief but interesting look at this problem. They examined the case with $K = 0.50$ and $C_{D_*} = .05$, apparently for initial

150

states in the vicinity of $(-1. \leq \psi_o \leq 1.)$. Using phase diagrams, Tong and Rimrott portrayed two example period doubling sequences between $e = 0.10$ and $e = 0.182$ that lead to chaos. They also presented Poincaré maps for two chaotic attractors, and assumed that for $e > 0.182$ the motion remained chaotic. The following is a brief examination of some characteristics of the pitching motion for p=1 damping, including another look at the $K = 0.50$ and $C_{D_*} = .05$ case.

Figure 7.1 presents a bifurcation diagram for the $K = 0.50$ and $C_{D_*} = .05$ case with the initial state $(0., -1.0)$. This plot was made with 500 values of eccentricity (representing 500 separate trajectories) and because of the transient effects of damping, over 600 orbits were integrated for each trajectory before data was collected. A feature can be seen in this bifurcation diagram that did not appear in the undamped cases – the abrupt, discontinuous nature of the bifurcations and the appearance of scatterings of points that do not necessarily indicate the presence of chaotic motion. Note, for example, the region of the bifurcation diagram between $e = 0.0$ and $e = .1$. The $P = 1/1$ pitch rate solutions near zero eccentricity start at zero and increase with eccentricity before abruptly falling off close to $e = .03$ to a $P = 1/1$ branch of negative pitch rates. Continuing along this new branch, another abrupt change can be observed near $e = 0.11$. Here, over a range of eccentricity, one finds a scattering of points that represent periodic solutions. At a slightly greater value of $e$, however, the solutions jump back to the $P = 1/1$ branch briefly before beginning a period doubling sequence mentioned in Reference [22]. Also apparent in this figure are a number of alternating bands of regular and chaotic motion. Bifurcations within these gaps can barely be seen on this scale, and enlargements of these regions are necessary for their study.

Figure 7.2 is an enlargement of the two period doubling bifurcation sequences discussed by Tong and Rimrott. Branch discontinuities are evident in this plot, particularly in the $p = 1/1$ branch near $.10 \leq e \leq .12$. These points (and the ones in Figure 7.1 elaborated on above) likely represent solutions with transients that did not die out during the 600 preliminary integrated orbits, since a few disappeared from the bifurcation diagrams when the number of preliminary integrated orbits was raised from 600 to 2000.[1]

Figure 7.3 provides an additional magnification of the second period doubling sequence. Here a frequency 1/2 (period 2) branch of solutions bifurcates near $e = .1728$ into a period 4 branch, which in turn bifurcates into a period 8 branch close to $e = .1784$. This sequence continues until chaos is reached approximately at

---

[1]On the other hand, many still remained when over 10,000 preliminary orbits were integrated.
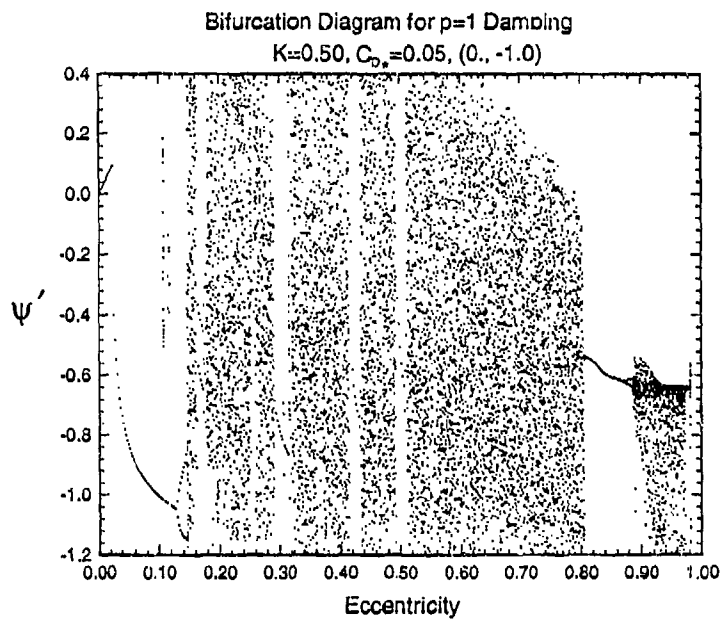
Figure 7.1: Bifurcation Diagram for Linear Damping: $K = 0.50$, $C_{D_*} = 0.05$, and $(0., -1.0)$.
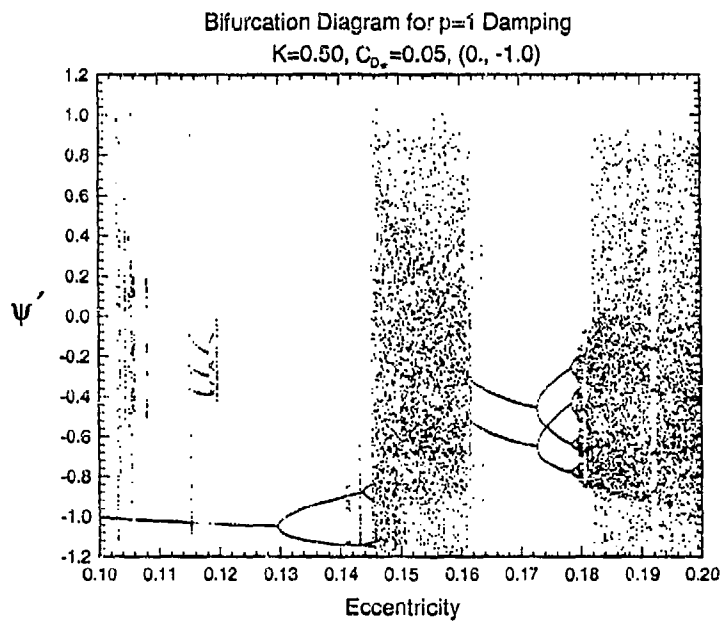


Figure 7.2: Bifurcation Diagram for Linear Damping: $K = 0.50$, $C_{D_*} = 0.05$, and $(0., -1.0)$.
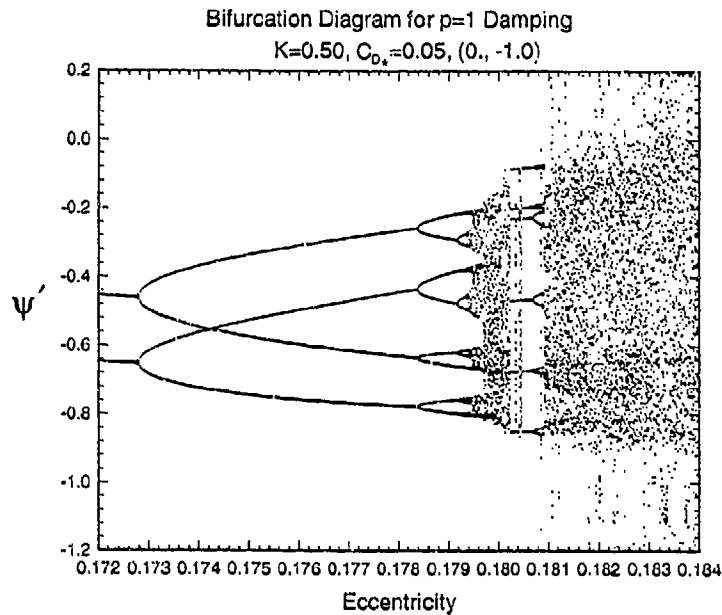
Figure 7.3: Bifurcation Diagram for Linear Damping: $K = 0.50$, $C_{D_*} = 0.05$, and $(0., -1.0)$.

$e = .180$. Another period doubling sequence is revealed in this figure,[2] emerging from this chaotic region but commencing with a period 6 branch close to $e = .1806$.

Further examination of the other gaps of regular motion in the bifurcation diagram of Figure 7.1 indicates that a number of other period doubling sequences exist, some for large eccentricities. The assumption in Reference [22] that motion for $e > .182$ remains chaotic is incorrect.

All of the bifurcations from periodic to chaotic motion that were examined occurred with period doubling. To observe this often required magnification of the branching points, such as for the period 1 branch near $e = 0.20$ of Figure 7.4 for $K = 0.2$, $C_{D_*} = 0.08$, and $(0., 0.7)$. A blow-up of the region $.50 \leq e \leq .55$ of this plot is presented in Figure 7.5. Two period doubling sequences of bifurcations appear – the one on the right for *increasing* values of $e$ and the one on the left for *decreasing* values of eccentricity. This latter finding demonstrates again that the routes to chaos for even basic problems are not necessarily simple. Convention would dictate that eccentricity is the nonlinear parameter and an increase in $e$ would cause the system to become more nonlinear. Yet here is an example of where a decrease in eccentricity causes an increase in system nonlinearity.

---

[2]Further magnifications would probably show even more sequences – look near $e = .192$ in Figure 7.2, for example.

153

Bifurcation Diagram for p=1 Damping: K=0.2, Cd=.08, (0.,0.7)
600 Orbits integrated before collecting data
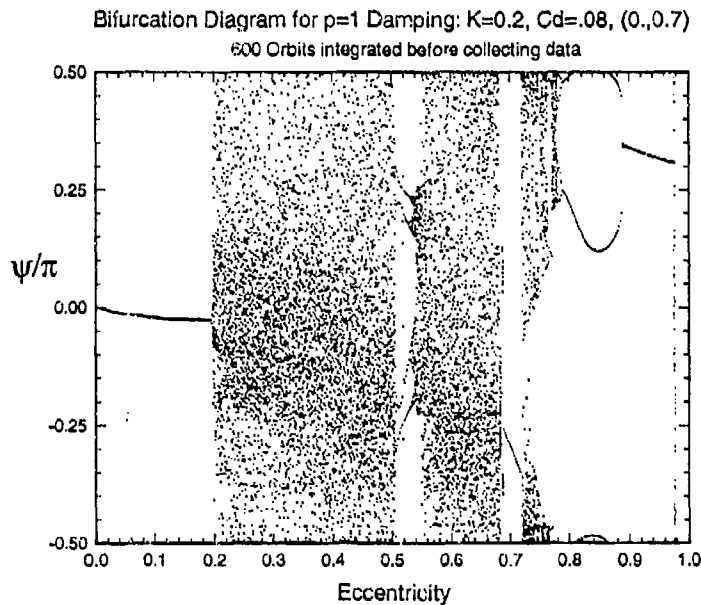


Figure 7.4: Bifurcation Diagram for Linear Damping: $K = 0.20$, $C_{D.} = 0.08$, and $(0., 0.70)$.

Interesting structure also appears in bifurcation diagrams employing inertia ratio as the bifurcation parameter in place of eccentricity (Figure 7.6 for example.) This was not explored further but it does hint that at least some routes to chaos may also depend on inertia ratio, as found for the undamped case, and not merely on eccentricity.

Figure 7.7 presents a bifurcation diagram for conditions identical to Figure 7.4, except for a smaller damping coefficient. It is interesting that the bifurcation diagram for this reduced damping case displayed fewer chaotic trajectories. The intuitive concept that increasing damping decreases chaos is not always correct.

Examples of Poincaré maps of trajectories from the two main bands of chaos in this bifurcation diagram are presented in Figure 7.8 for $c = 0.30$ and Figure 7.9 for $e = 0.66$. The differences between these two plots and example Poincaré maps for zero damping in Section 5 (Figures 5.23 - 5.33 for example) are startling but consistent with chaos theory. In the words of Moon [40 page 63],

> Chaotic orbits in conservative systems tend to visit all parts of a subspace of the phase space uniformly; that is, they exhibit a uniform probability density over restricted regions of the phase space.

154

Figure 7.5: Bifurcation Diagram for Linear Damping: $K = 0.20$, $C_{D_*} = 0.08$, and $(0., 0.7)$.
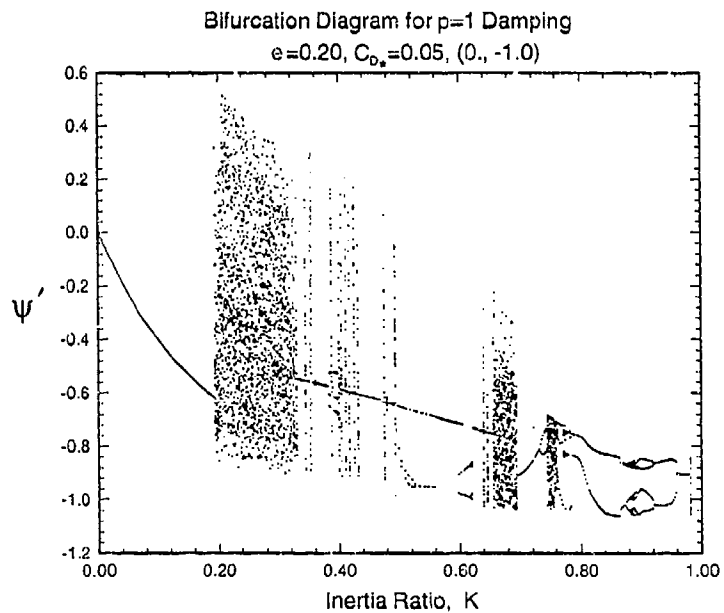


Figure 7.6: Bifurcation Diagram with Inertia Ratio for Linear Damping: $e = 0.20$, $C_{D_*} = 0.05$, and $(0., -1.0)$.

155
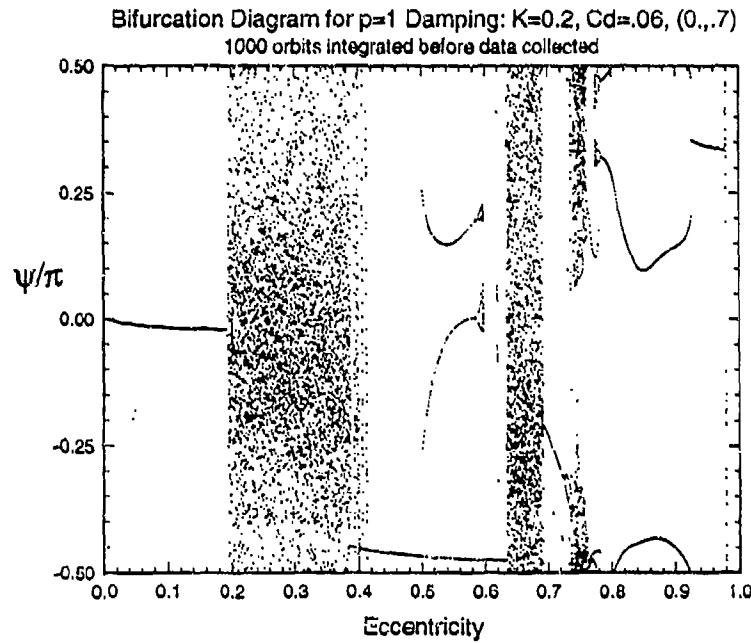
Figure 7.7: Bifurcation Diagram for Linear Damping: $K = 0.20$, $C_{D_*} = 0.06$, and $(0., 0.70)$.

This is the reason why if enough orbits were integrated, the chaotic regions of the Poincaré maps of Section 5 would be completely filled, forming a two-dimensional (integer) space. Areas of phase space for dissipative systems, however, are stretched and folded through elongations and contractions as may be measured by the Lyapunov exponents (Section 4). There is no conservation of phase space for a damped system, and thus if enough orbits are integrated, an initially close group of points becomes dispersed and mapped into a smaller, fractal area.

The dimension of a strange, or fractal, attractor may be calculated using the Lyapunov exponents [51]. For a two-dimensional map, the product of a two-degree-of-freedom autonomous system or of a one degree-of-freedom nonautonomous system, the "Lyapunov fractal dimension"[3], $d_L$, is simply

$$d_L \equiv 1 - \frac{\sigma_1}{\sigma_2}. \qquad (7.6)$$

The chaotic attractor of Figure 7.8 has a fractal dimension of about 1.72 based on the values of the first and second Lyapunov exponents of 0.257 and -0.357. Likewise, the attractor of Figure 7.9 has Lyapunov exponent values of 0.344 and -0.549 and a

---

[3]A number of other types of fractal dimensions also exist including capacity, correlation, information, and pointwise dimensions, and they usually give close results.
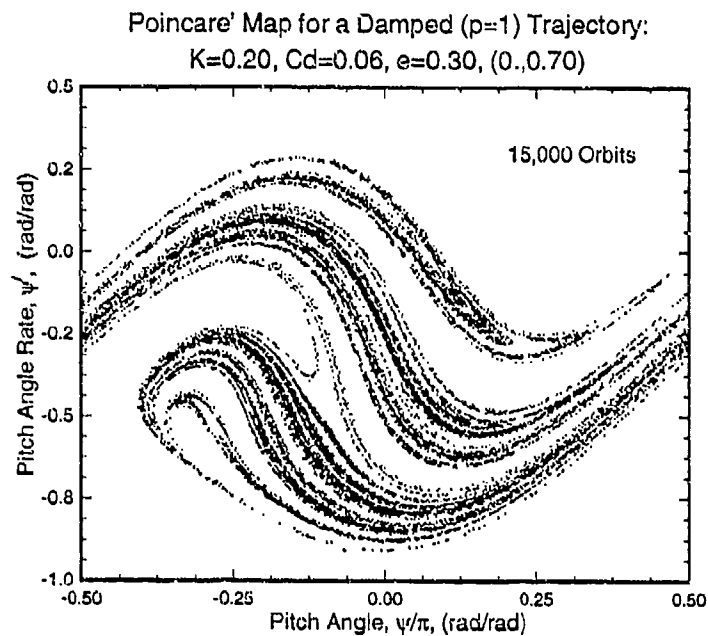
Figure 7.8: Poincaré Map for a Linearly Damped Trajectory: $K = 0.20$, $C_{D_*} = .06$, $e = .30$, and $(0., 0.70)$.
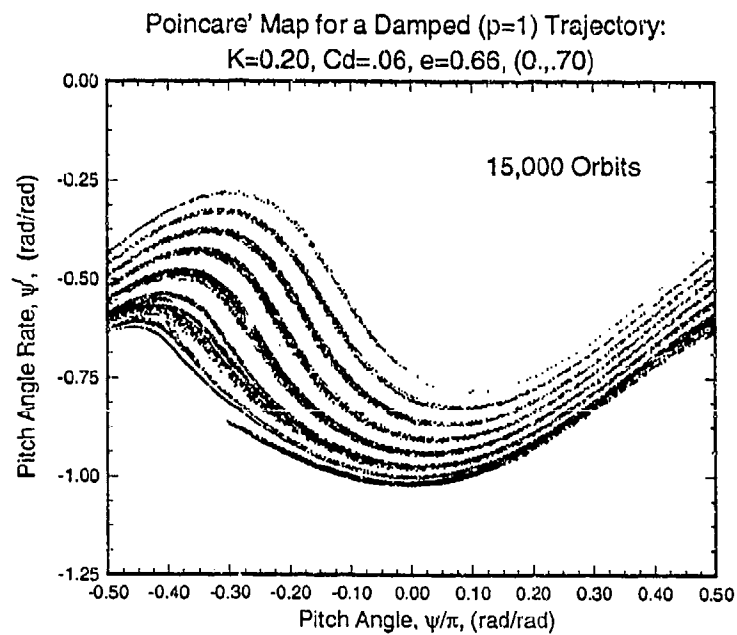


Figure 7.9: Poincaré Map for a Linearly Damped Trajectory: $K = 0.20$, $C_{D_*} = .06$, $e = .66$, and $(0., 0.70)$.
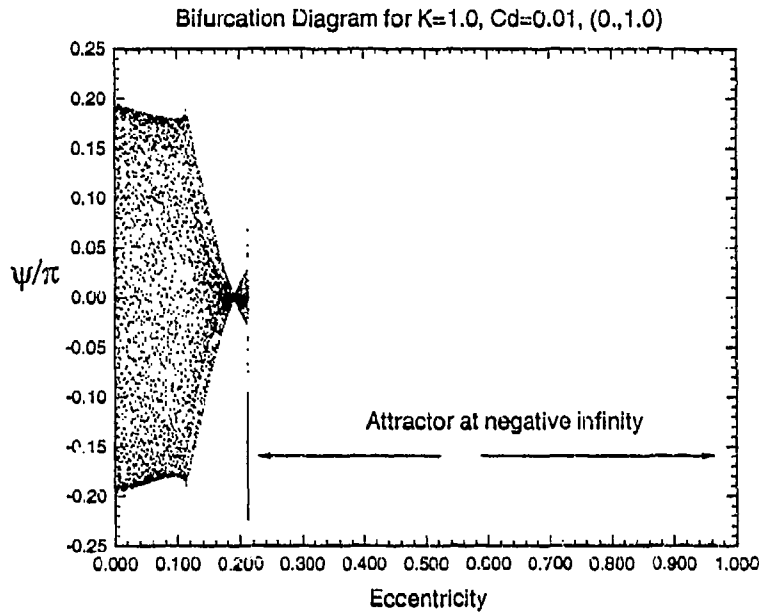
Figure 7.10: Bifurcation Diagram for Nonlinear (p=2) Damping: $K = 1.0, C_D = 0.01$, and $(0., 1.0)$.

fractal dimension of about 1.63. Because both chaotic attractors have a non-integer fractal dimension they are deemed "strange attractors".

## 7.4 Pitching Motion for Nonlinear (p=2) Damping

A typical bifurcation diagram for the nonlinear, p=2 damping case is found in Figure 7.10. All solutions for eccentricity values greater than approximately 0.2 go to a chaotic attractor at negative infinity, $(-\infty, -\infty)$. That this attractor is chaotic is not surprising when one compares this bifurcation diagram with its zero damping counterpart, Figure 7.11. In comparing these two plots, the region of chaos in the undamped case (eccentricity values of about 0.2 and greater) corresponds almost exactly to the region where all trajectories migrate towards an attractor at $(-\infty, -\infty)$ for the damped case. Also, the addition of the nonlinear damping term has caused the periodic solutions of the undamped case to become quasiperiodic solutions in the damped case.

Computing the first Lyapunov exponent for various eccentricities verifies that
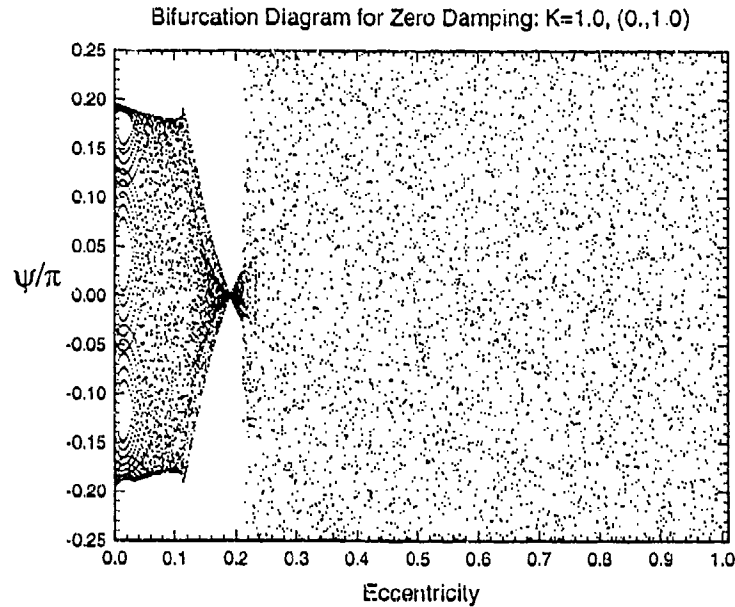
Figure 7.11: Bifurcation Diagram for Zero Damping: $K = 1.0$, $(0., 1.0)$.

the attractors at negative infinity are chaotic. Figure 7.12 shows $\sigma_1$ for $e = 0.10$, in the regular motion portion of the bifurcation diagram. After a number of trajectories the first Lyapunov exponent settles down to a nearly constant value of approximately -.013, affirming that the trajectory is regular. The first Lyapunov exponents for various values of $e$ that lie in region of the bifurcation diagram where the negative infinity attractors dwell, however, are all positive, and their values increase with increasing eccentricity (Figures 7.13 and 7.14.)

Variations in the damping coefficient appeared to have little effect on the basic structure of the bifurcation diagrams, but did have a significant effect on the existence and location of periodic and chaotic attractors for large values of eccentricity. Figures 7.15 - 7.17 demonstrate this finding. These three plots form a sequence of bifurcation diagrams for increasing damping coefficient. Figure 7.15, with $C_D = 0.01$, shows that quasiperiodic solutions exist for this problem for small eccentricities. For eccentricities above approximately $e = .08$, however, all trajectories eventually migrate towards the attractor at negative infinity, with the exception of a couple of periodic attractors indicated in the plot.

Increasing the damping coefficient from .01 to .05 produces a nearly identical bifurcation diagram (Figure 7.16) except for the appearance and disappearance of
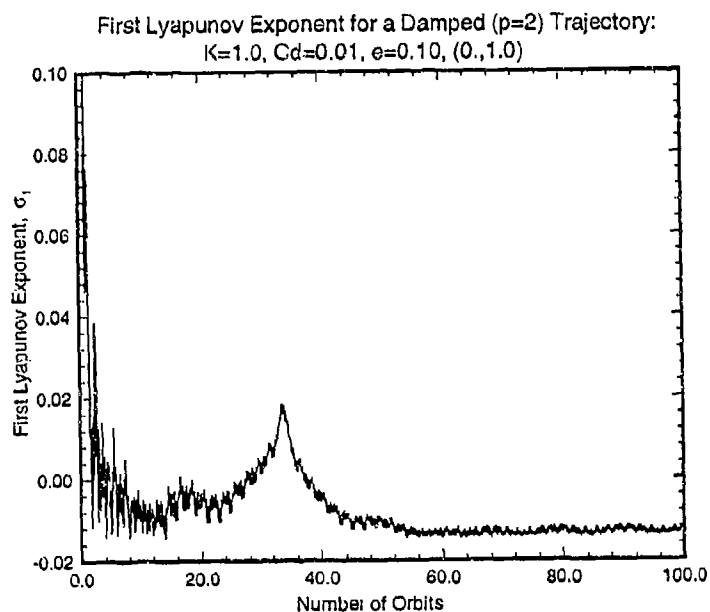
Figure 7.12: First Lyapunov Exponent for a Damped (p=2) Trajectory: $K = 1.0$, $C_D = 0.01$, $e = .10$, and $(0., 1.0)$.
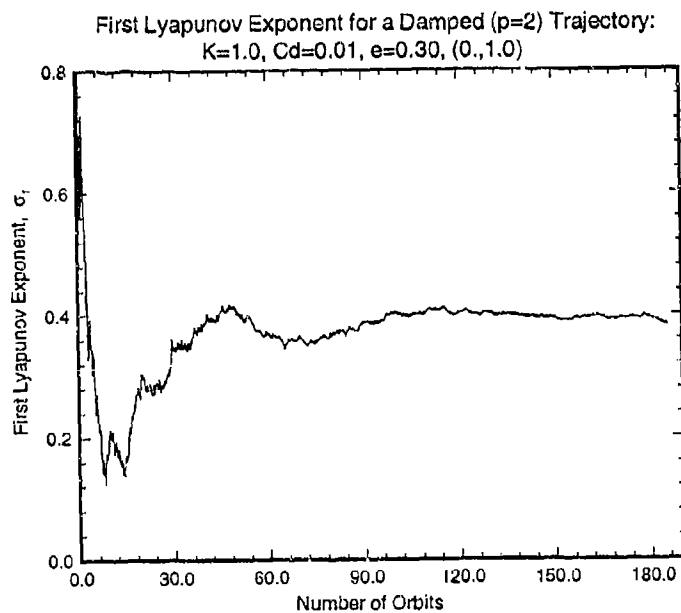


Figure 7.13: First Lyapunov Exponent for a Damped (p=2) Trajectory: $K = 1.0$, $C_D = 0.01$, $e = .30$, and $(0., 1.0)$.

First Lyapunov Exponent for a Damped (p=2) Trajectory:
K=1.0, Cd=0.01, e=0.80, (0.,1.0)
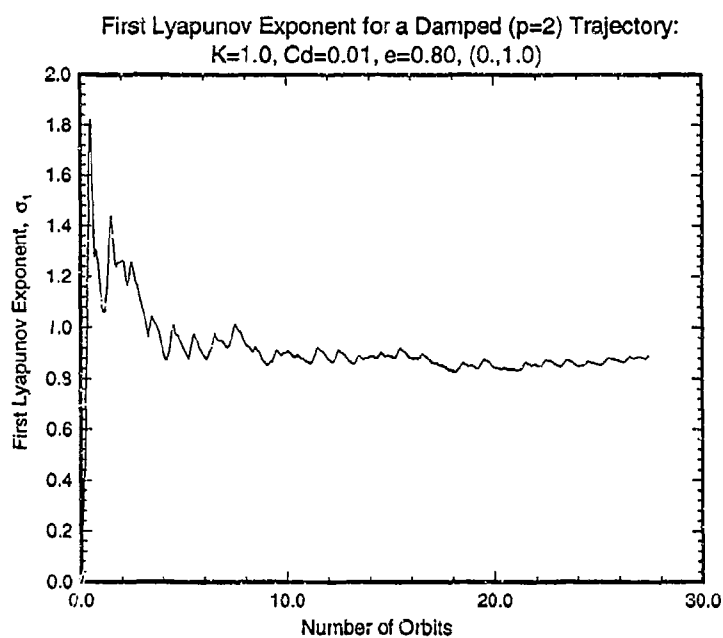


Figure 7.14: First Lyapunov Exponent for a Damped (p=2) Trajectory: $K = 1.0$, $C_D = 0.01$, $e = .80$, and $(0., 1.0)$.

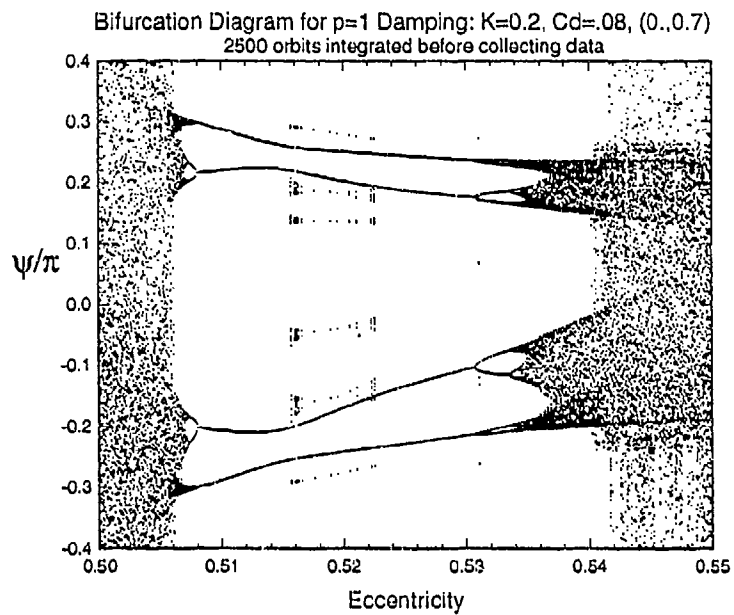Bifurcation Diagram for p=2 Damping:
K=0.50, Cd=0.01, (0.,0.5)
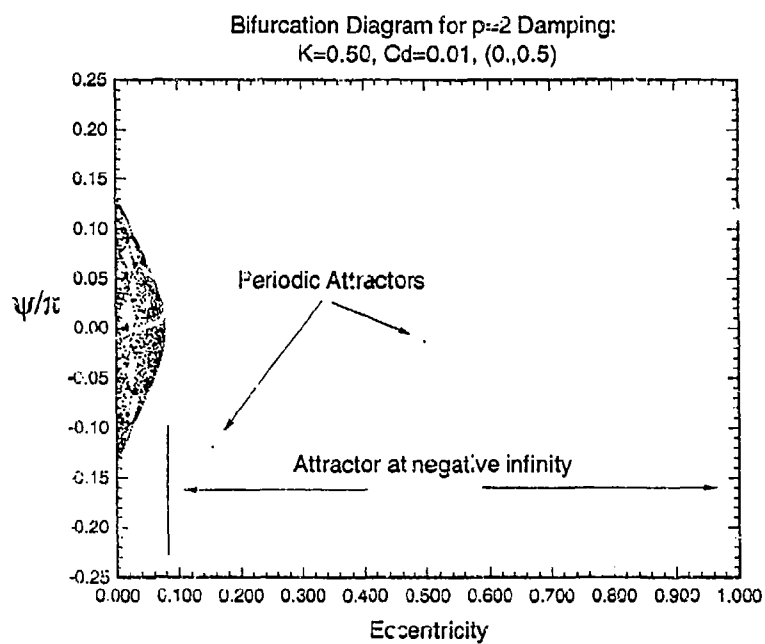


Figure 7.15: Bifurcation Diagram for Nonlinear (p=2) Damping: $K = 0.50$, $C_D = 0.01$, and $(0., 0.50)$.

161
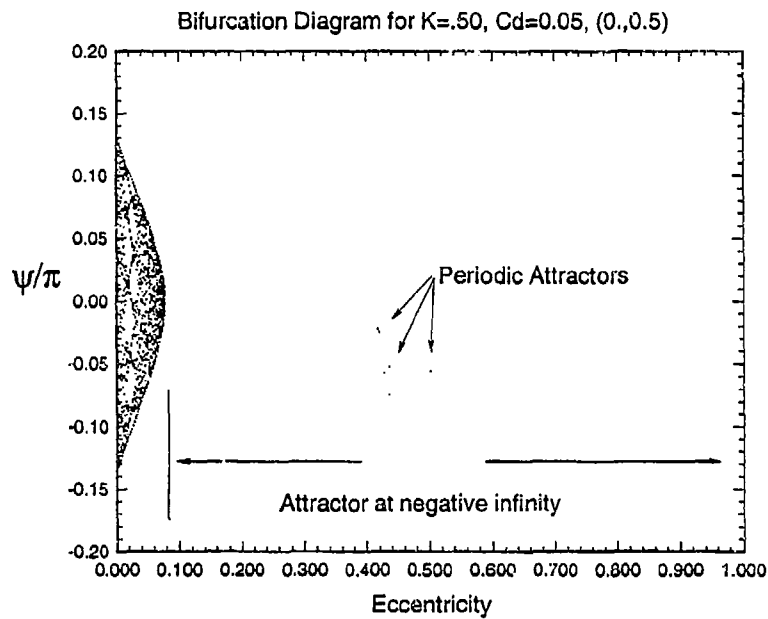
Figure 7.16: Bifurcation Diagram for Nonlinear (p=2) Damping: $K = 0.5, C_D = 0.05$, and $(0., 0.5)$.
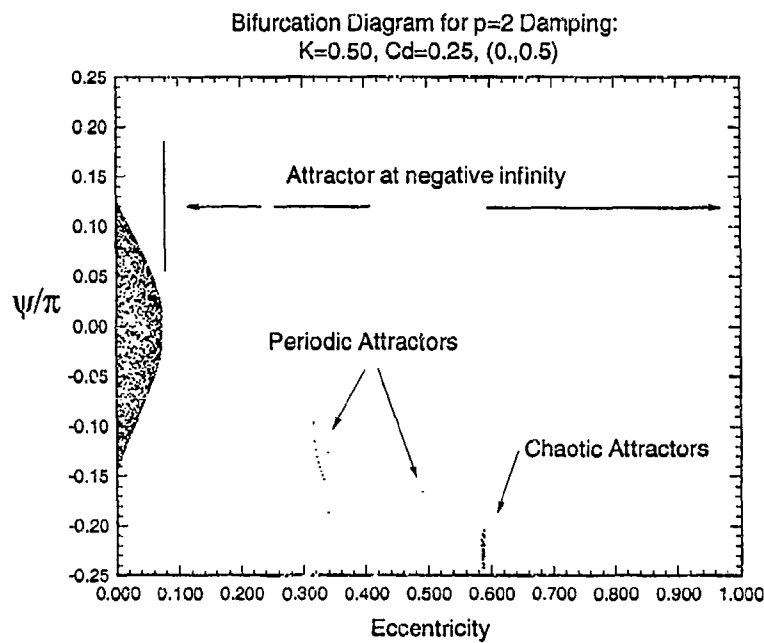


Figure 7.17: Bifur: ion Diagram for Nonlinear (p=2) Damping: $K = 0.5, C_D = 0.25$, and $(0., 0.5)$.

**Poincare' Map for a Damped (p=2) Trajectory:**
**K=0.50, Cd=.25, e=0.586, (0.,0.50)**

10,000 Orbits
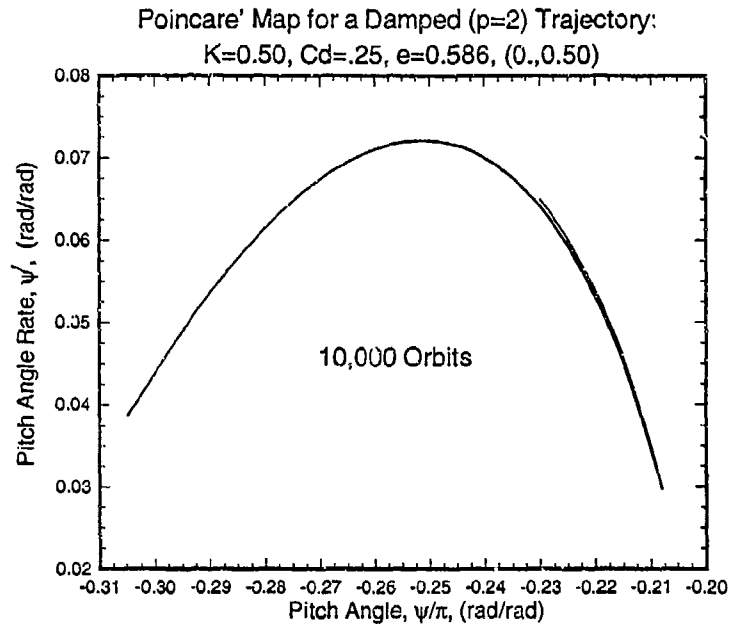
Figure 7.18: Poincaré Map for a Damped (p=2) Trajectory: $K = 0.5$, $C_D = 0.25$, $e = .586$, and $(0., 0.50)$.

some periodic attractors. Further increase of the damping coefficient to $C_D = 0.25$ gives the bifurcation diagram of Figure 7.17. A series of $P = 1/1$ trajectories appear near $e = 0.32$ and branch into $P = 1/2$ trajectories near $e = 0.34$. Another $P = 1/1$ trajectory appears near $e = 0.49$. The grouping of attractors near $e = 0.59$, however, are chaotic.

A Poincaré map of one of these attractors is displayed in Figure 7.18. This attractor looks more similar to a quasiperiodic attractor than to the chaotic attractors for the zero damping and linear damping cases, but an examination of its Lyapunov exponents (Figure 7.19) clearly shows it to be chaotic. It is also strange, with a fractal dimension of approximately 1.34.

Figure 7.20 gives the zero damping bifurcation diagram for $K = 0.5$ and for the initial state $(0., 0.5)$. Comparing this plot with Figures 7.15 - 7.17 once again shows that the main difference between the damped and undamped bifurcation diagrams is the location of the chaotic attractors. The chaotic attractors for the undamped case occur for each value of eccentricity for states close to those of the regular motion attractors instead of at $(-\infty, -\infty)$ for the damped cases.

The phase diagram of Figure 7.21 illustrates the manner in which many of the

163
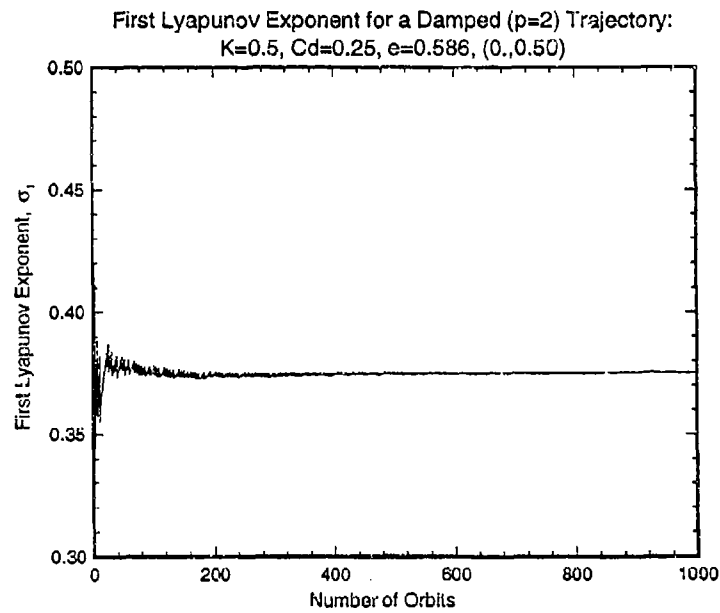
Figure 7.19: First Lyapunov Exponent for a Damped (p=2) Trajectory: $K = 0.5$, $C_D = 0.25$, $e = .586$, and $(0., 0.5)$.
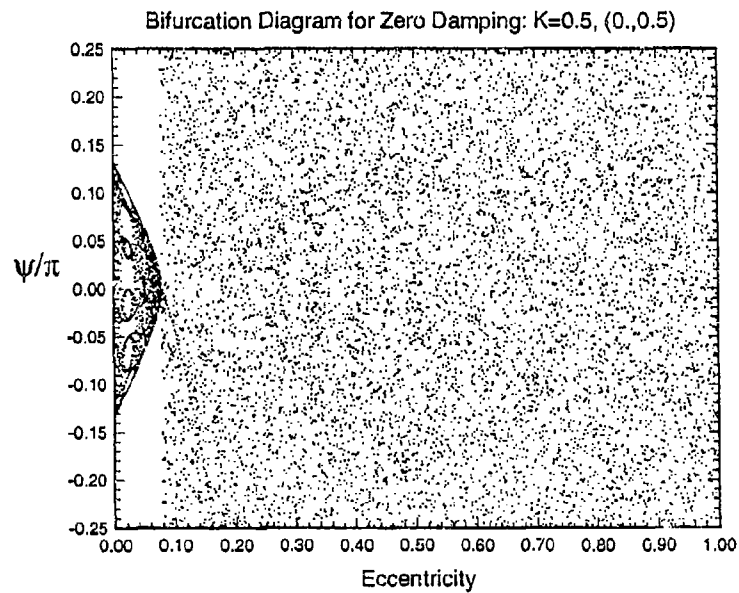


Figure 7.20: Bifurcation Diagram for Zero Damping: $K = 0.5$, $(0., 0.5)$.

164

Phase Diagram for a Damped (p=2) Trajectory:
K=1.0, Cd=0.001, e=0.01, (0.,1.70)
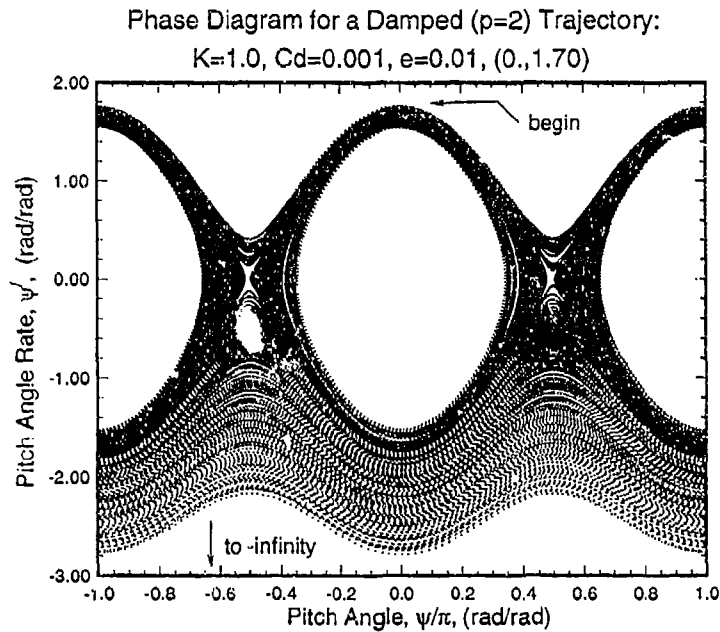


Figure 7.21: Phase Diagram for a Damped (p=2) Trajectory: $K = 1.0$, $C_D = 0.001$, $e = .01$, and $(0., 1.7)$.

p=2 damped trajectories move towards the attractor at negative infinity. In this particular case an initial condition of $(0., 1.70)$ produces chaotic motion and initial movement on the phase diagram from right to left. Hence, pitch angle increases for a number of trajectories until the damping term eventually causes $\psi'$ to first occasionally become, and later to remain, negative. Once the latter occurs, the movement on the phase diagram is from right to left in the lower portions of plot and both pitch angle (plotted here modulo $2\pi$) and pitch rate move to negative infinity. A plot of the first Lyapunov exponent indicates this trajectory is chaotic (Figure 7.22.) Other (p=2) damped trajectories, which go to attractors at negative infinity in either a regular or chaotic fashion, are shown in the next section.
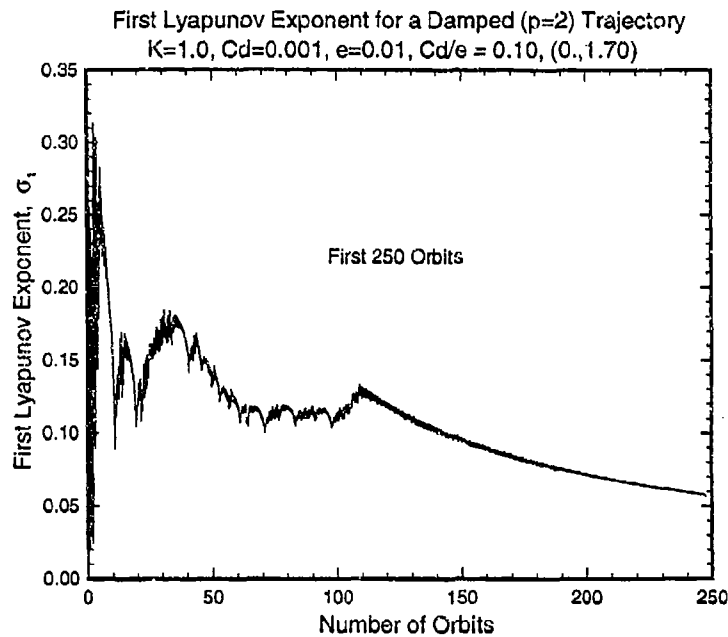
Figure 7.22: First Lyapunov Exponent for a Damped (p=2) Trajectory: $K = 1.0$, $C_D = 0.001$, $e = .01$, $C_D/e = 0.10$, and $(0., 1.7)$.

## 7.5 Transition Prediction Using the Method of Melnikov

### 7.5.1 Introduction

The formation of chaos for a Hamiltonian system undergoing a Hamiltonian perturbation was briefly discussed in Section 5. Of interest here is the formation of chaos for a Hamiltonian system undergoing a small Hamiltonian perturbation from the eccentricity terms and a small dissipative perturbation due to damping.

As for the purely Hamiltonian case, chaotic motion for damped pitch motion is caused by the breaking up of heteroclinic orbits of the unperturbed system due to the perturbations. When the heteroclinic orbits break up, the two manifolds inter ct transversely an infinite number of times leading to the formation of heteroclinic po its and a horseshoe-type mapping (or a baker's type of transformation). This action produces the stretching, contracting, and folding that causes chaos. Chaotic motion appears near the unperturbed heteroclinic orbits, the separatrices of the circular orbit case. For a dissipative perturbation, however, all KAM curves are destroyed. A trajectory in the vicinity of the unperturbed heteroclinic orbit may initially be

chaotic, but can roam far away in phase space before eventually becoming trapped in either a strange (chaotic) attractor, or a periodic (sink) attractor. This concept of "transient chaos" or "persistent chaos" is important. Is a trajectory truly chaotic if it initially appears to be so (with positive Lyapunov exponents), but quickly damps to a regular, periodic solution? This is an arguable point although most of the literature seems to judge such a trajectory to not be chaotic. Moon [46, page 62], for example, uses an experimental working definition for chaos which requires at least 4000 points of a fractal-like attractor to be computed in a Poincaré map to allow ample time for the transients to die out before calling the trajectory chaotic.

One can view the study of dynamics as a study of mappings – how an initial phase space is transformed or mapped by the equations of motion over time. The evolution of the initial conditions sphere for the case of chaotic motion is depicted in the mapping caricature of Figure 7.23. Here we see how an initial conditions volume is subjected to stretching, folding, and contraction in the phase space for each iteration of the mapping. As the number of iterations increases, the precision required to predict future states from a given initial condition also increases. After numerous iterations of the map the phase space becomes fractal, initially close trajectories exponentially diverge and predictability is impossible. This process of stretching, contracting, and folding is referred to in the literature as either a horseshoe mapping (from the shape), or a baker's transformation (from the stretching and folding in bread making.) One can see from this figure that initially close points on the initial conditions sphere can be quickly separated after only a few mapping iterations. The volume of the transformed initial conditions sphere remains constant under the mapping for a conservative system and it decreases as the number of mapping iterations increases for a dissipative system.

Melnikov's method [17] [4] provides an analytical criterion for chaotic motion in terms of the system parameters. It is a perturbation method used to measure the Melnikov function $M(t_o)$, which is the distance between the perturbed stable and unstable manifolds at some time $t_o$. For this particular problem we replace time with true anomaly and seek $M(f_o)$. When $M(f_o) \to 0$, transverse intersections of the manifolds exists and chaotic motion occurs. Due to symmetry, the Melnikov function needs to be calculated for only either the upper or lower heteroclinic orbit.

Melnikov's method assumes that the unperturbed system is integrable and has a known integrable solution to its heteroclinic orbits, $\vec{x}_h$. It is assumed that the system can take the form,

---

[4] Also see Guckenheimer and Holmes [41, pages 184-204] or Lichtenberg and Lieberman [42, pages 426-434] for a thorough discussion and a derivation of the Melnikov function.

Evolution of an Initial Conditions Sphere Under
a Horseshoe Mapping or Baker's Transformation



$$\Longrightarrow \quad \text{increasing number of mapping iterations} \quad \Longrightarrow$$
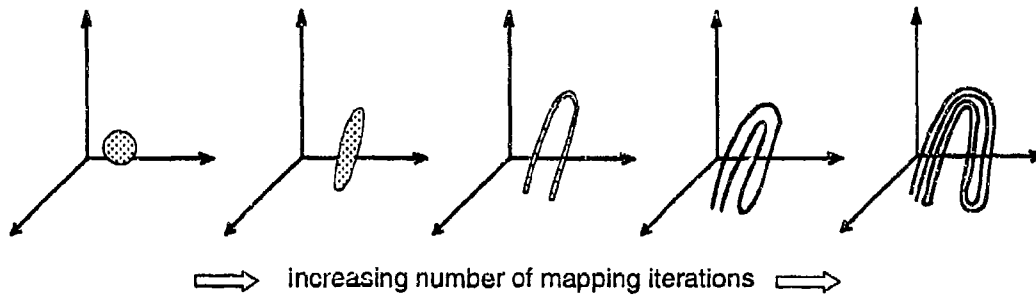
Figure 7.23: Evolution of an Initial Conditions Sphere Under a Horseshoe Mapping or Baker's Transformation.

$$\vec{x}' = \vec{g}(\vec{x}) + \epsilon\vec{h}(\vec{x}, f + f_o), \tag{7.7}$$

where

$$\vec{x}' \equiv \begin{bmatrix} x_1' \\ x_2' \end{bmatrix} = \begin{bmatrix} \psi' \\ \psi'' \end{bmatrix}, \tag{7.8}$$

$$\vec{g} \equiv \begin{bmatrix} g_1(\vec{x}) \\ g_2(\vec{x}) \end{bmatrix}, \tag{7.9}$$

and

$$\vec{h} \equiv \begin{bmatrix} h_1(\vec{x}, f + f_o) \\ h_2(\vec{x}, f + f_o) \end{bmatrix}. \tag{7.10}$$

The function $\vec{h}$ is assumed to be periodic in $f$ and $\epsilon\vec{h}(\vec{x}, f + f_o)$ is assumed to be a small perturbation which is not necessarily Hamiltonian. The method is noted to be a local, not global, criterion for chaos, valid only near the unperturbed heteroclinic orbits.

## 7.5.2 Melnikov Criteria for Linear (p=1) Damping

Referring to Equation 7.3, one finds $x_1' = x_2$ and

$$x_2' = \frac{2e \sin f}{(1 + e\cos f)}(x_2 + 1) - \frac{3}{2}K\frac{\sin 2x_1}{(1 + e\cos f)} - C_{D_*}\frac{x_2}{(1 + e\cos f)^2}. \tag{7.11}$$

In order to apply this method it must be assumed that both the eccentricity and the damping coefficient are small. Defining

$$e \equiv \epsilon e' \tag{7.12}$$

168

$$C_{D_*} \equiv \epsilon C'_{D_*},$$

and taking a Taylor's series expansion of the denominators of Equation 7.11 gives an expression for $x_2$ in the proper form,

$$x_2' = -\tfrac{3}{2}K\sin 2x_1 + \epsilon \left[ \tfrac{3}{2}K\sin 2x_1 e' \cos f \right. \tag{7.13}$$
$$\left. +2e'\sin f(x_2+1) - C'_{D_*}x_2 \right] + \mathcal{O}(\epsilon^2).$$

From Section 4, the solutions for the unperturbed, $e = 0, C_{D_*} = 0$, heteroclinic orbits which originate from the saddle points at $\pm\pi/2$ are

$$\vec{x}_h = \begin{bmatrix} x_{1h} \\ x_{2h} \end{bmatrix} = \begin{bmatrix} \arcsin\left[\tanh\left(\sqrt{3K}f\right)\right] \\ \sqrt{3K}\operatorname{sech}(\sqrt{3K}f) \end{bmatrix}. \tag{7.14}$$

The Melnikov integral is given by

$$M(f_o) = \int_{-\infty}^{\infty} \vec{g}\left(\vec{x}_h(f)\right) \wedge \vec{h}\left(\vec{x}_h(f), f+f_o\right) df. \tag{7.15}$$

where the symbol $\wedge$ indicates the cross product. With substitution, the Melnikov integral becomes

$$M(f_o) = \int_{-\infty}^{\infty} \sqrt{3K}\operatorname{sech}(\sqrt{3K}f)2e'\sin(f+f_o)df \tag{7.16}$$
$$+ \int_{-\infty}^{\infty} 3K\operatorname{sech}^2(\sqrt{3K}f)2e'\sin(f+f_o)df$$
$$+ \int_{-\infty}^{\infty} 3K\left[\cos\left(\arcsin\left\{\tanh\left(\sqrt{3K}f\right)\right\}\right)e'\cos(f+f_o)\right] \cdot$$
$$\left[\sqrt{3K}\operatorname{sech}(\sqrt{3K}f)\right]\tanh(\sqrt{3K}f)df$$
$$- \int_{-\infty}^{\infty} C'_{D_*}3K\operatorname{sech}^2(\sqrt{3K}f)df.$$

Defining $\gamma \equiv \sqrt{3K}$ and applying some trigonometric identities to simplify these integrals results in

$$M(f_o) = M_1(f_o) + M_2(f_o) + M_3(f_o) + M_4(f_o) \tag{7.17}$$

where

$$M_1(f_o) = 2\gamma e' \int_{-\infty}^{\infty} \operatorname{sech}(\gamma f)\sin(f+f_o)df \tag{7.18}$$
$$M_2(f_o) = 2\gamma^2 e' \int_{-\infty}^{\infty} \operatorname{sech}^2(\gamma f)\sin(f+f_o)df$$
$$M_3(f_o) = \gamma^3 e' \int_{-\infty}^{\infty} \cos(f+f_o)\operatorname{sech}^2(\gamma f)\tanh(\gamma f)df$$
$$M_4(f_o) = -\gamma^2 C'_{D_*} \int_{-\infty}^{\infty} \operatorname{sech}^2(\gamma f)df.$$
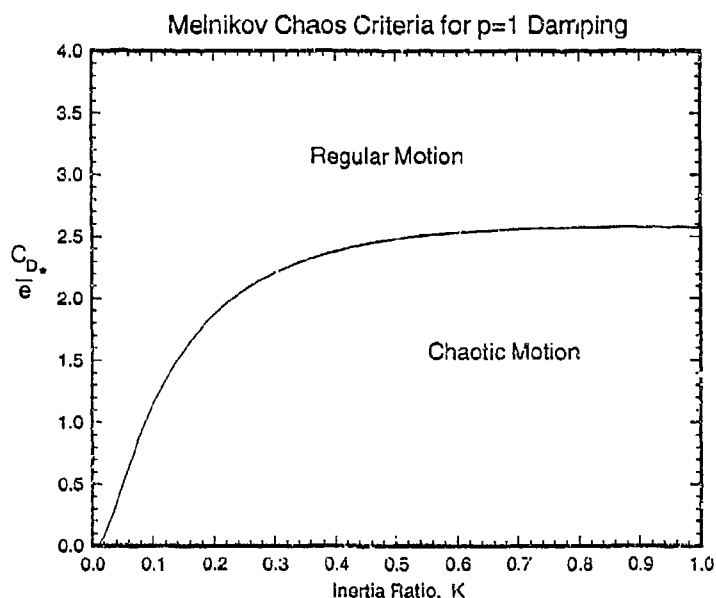
Figure 7.24: Melnikov Chaos Criteria for Linear Damping.

Finding some of these integrals is a long and tedious process involving contour integration. After considerable work with a symbolic manipulating mathematics package a solution to the Melnikov integral is found to be,[5]

$$M(f_o) = \frac{\pi e'}{2} \sin f_o \left[ 4\text{sech}\left(\frac{\pi}{2\gamma}\right) + 3\text{csch}\left(\frac{\pi}{2\gamma}\right) \right] - 2\gamma C'_{D_*}. \qquad (7.19)$$

Simple zeros for this expression other than the trivial solution $f_o = 0$ are sought, and the Melnikov chaos criteria is found to be a relatively simple function of inertia ratio and the ratio of the damping coefficient to eccentricity,

$$\frac{C_{D_*}}{e} < \frac{\pi}{2\sqrt{3K}} \left[ 2\text{sech}\left(\frac{\pi}{2\sqrt{3K}}\right) + \frac{3}{2}\text{csch}\left(\frac{\pi}{2\sqrt{3K}}\right) \right]. \qquad (7.20)$$

This criteria is plotted in Figure 7.24. The accuracy of this transition prediction method is evaluated by comparing these analytical results with numerical results. Consider the case where $K = 0.20$. Since the Melnikov method is applicable only in the vicinity of the stable and unstable manifolds, the chaos criteria displayed in Figure 7.24 is only good for the vicinity of the region about the heteroclinic orbits of the main 1/1 resonance depicted for the $K = 0.2$, $e = 0$ case of Figure 7.25 for small values of $e$ and $C_D$. For $K = 0.2$ the Melnikov criteria for chaos predicts that regular pitching motion will occur for $C_{D_*}/e > 1.87$, and chaotic pitching motion will occur

---

[5]See the Appendix for a more detailed derivation of these integrals.

170
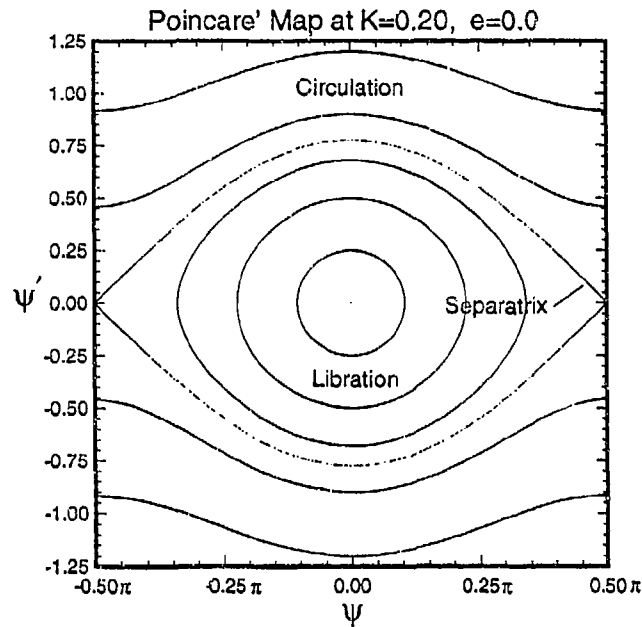
Figure 7.25: Poincaré Map for $K = 0.2$ and $e = 0.0$.

for $C_{D_*}/e < 1.87$. From the analytical examination of the circular orbit case in Section 4, the initial conditions which may be used to find the unperturbed heteroclinic orbits are $(0., \sqrt{3K})$. For this $K = 0.2$ example, the unperturbed heteroclinic orbit would occur for the initial state of $(0., 0.7745966...)$. The examination of neighboring trajectories is of interest here.

A number of trajectories for varying values of $e$ and $C_{D_*}$ were integrated and analyzed in this effort to determine the validity of the Melnikov transition criteria. Trajectory examples with $C_{D_*}/e$ values greater than the critical value all exhibited regular motion. Although chaotic motion was expected for the trajectories with $C_{D_*}/e$ less than the critical value, the actual results were surprising. A few representative cases are discussed below.

Figure 7.26 depicts the Poincaré Map for the case $K = 0.2$, $C_{D_*} = 0.001$, $e = 0.01$, and for an initial state that is just slightly greater than that of the heteroclinic orbit for the circular orbit case, $(0., 0.79)$. For small values of both eccentricity and damping coefficient, and for $C_{D_*}/e = 0.10$, the resulting motion is definitely regular (Figure 7.27. The trajectory is very quickly drawn into a sink, or point attractor, even though the ratio of damping coefficient to eccentricity is almost one twentieth of the critical value. The Melnikov prediction fails markedly for this example trajectory.

171
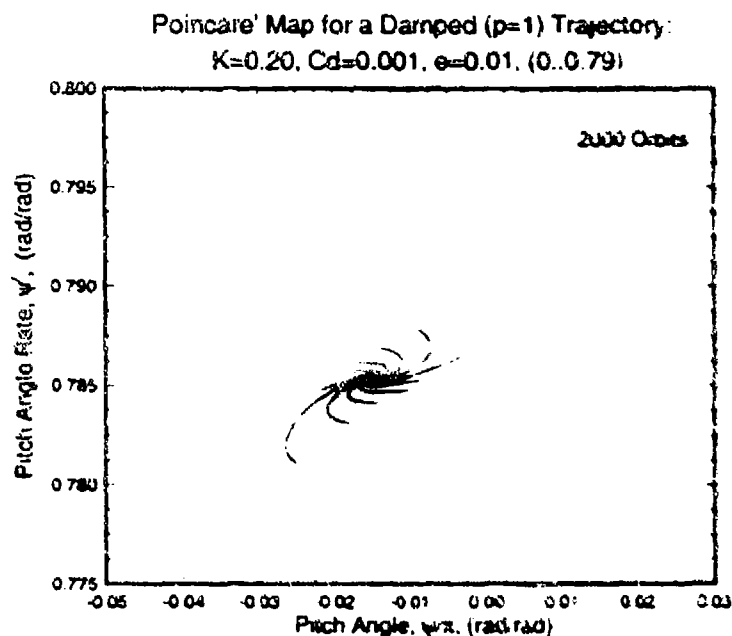
Figure 7.26: Poincaré Map for a Linearly Damped Trajectory: $K = 0.20$. $C_{D_\bullet} = 0.001$, $\epsilon = .01$, $C_{D_\bullet}/\epsilon = 0.10$, and $(0..0.79)$.
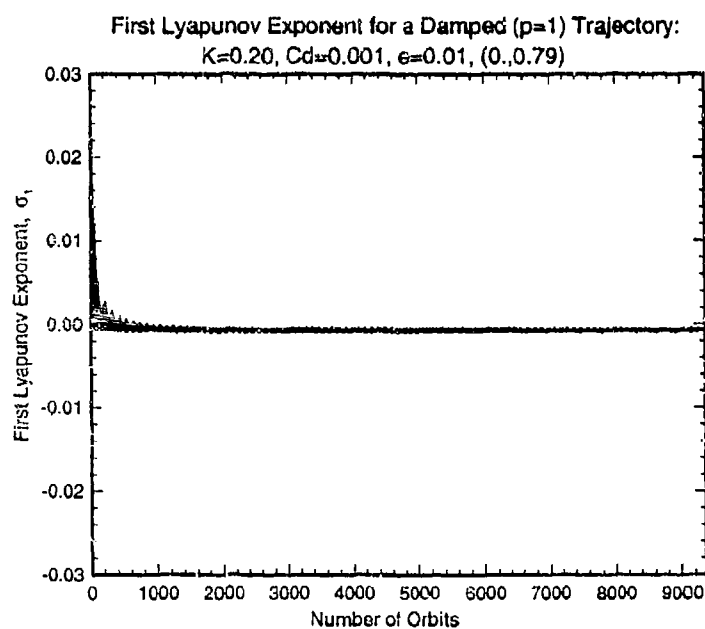


Figure 7.27: First Lyapunov Exponent for a Linearly Damped Trajectory: $K = 0.20$, $C_{D_\bullet} = 0.001$, $e = .01$, $C_{D_\bullet}/e = 0.1$, and $(0., 0.79)$.

Poincare' Map for a Damped (p=1) Trajectory:
K=0.20, Cd=0.001, e=0.01, (0.,0.75)
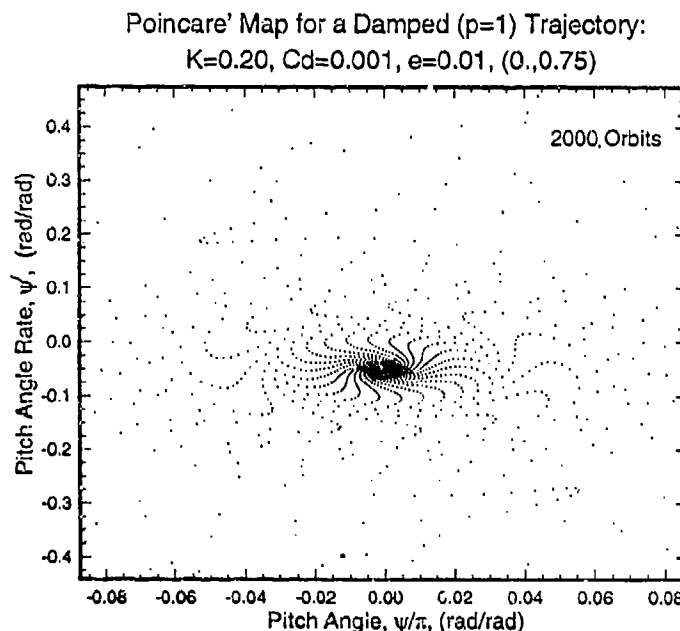
Figure 7.28: Poincaré Map for a Linearly Damped Trajectory: $K = 0.20$, $C_{D_*} = 0.001$, $e = .01$, $C_{D_*}/e = 0.10$, and $(0., 0.75)$.

Figure 7.28 displays the Poincaré map for a trajectory with identical initial conditions except for a slightly smaller initial state $(0., 0.75)$, which corresponds to an initially librating trajectory. Again the trajectory is quickly drawn to a point attractor, but this time to an attractor near the origin. Again the Melnikov prediction failed.

The next example is a trajectory with an initial state closer to that of the unperturbed heteroclinic orbit, $(0., 0.7746)$. The remainder of the initial conditions are the same as for the previous two examples. So are the results (Figure 7.29.) The trajectory is drawn into a point attractor near $(0., 0.785)$ and although it is initially chaotic, it becomes regular after only a few orbits.

A fourth example trajectory was run with the same parameters but for an initial state of $(0.37\pi, -.05)$ with similar results. Instead of chaotic motion, the Poincaré map for this trajectory (Figure 7.30), displays dual point attractors which produces $P = 1/2$ libration in the limit as the number of orbits goes to infinity.

A fifth example trajectory was integrated but for a reduced damping coefficient of only $C_{D_*} = .0001$, giving a damping-to-eccentricity ratio of about $1/187$ of the
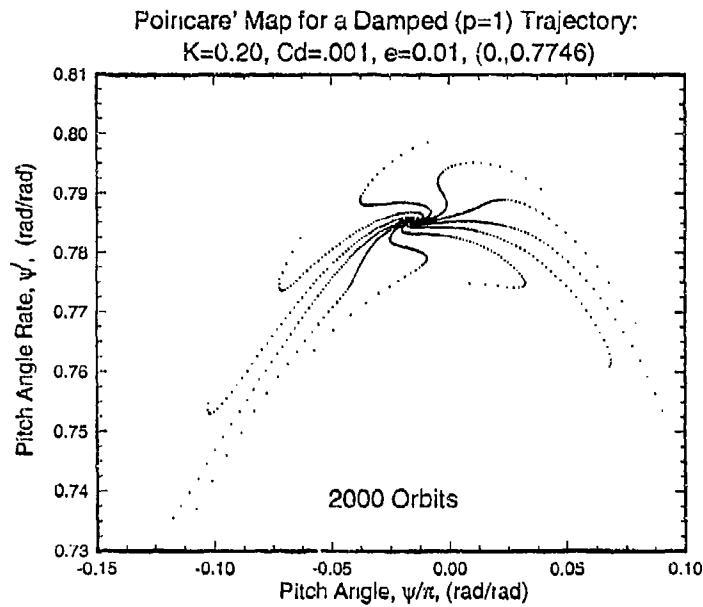
Figure 7.29: Poincaré Map for a Linearly Damped Trajectory: $K = 0.20$, $C_{D_*} = 0.001$, $e = .01$, $C_{D_*}/e = 0.10$, and $(0., 0.7746)$.
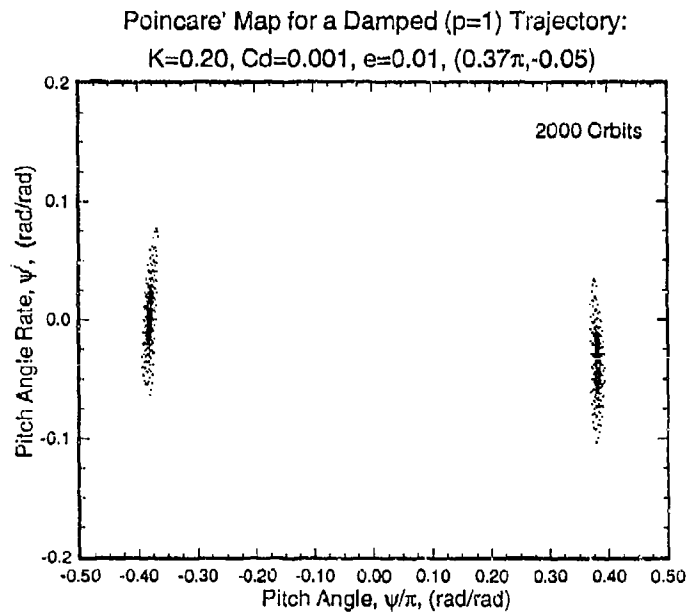


Figure 7.30: Poincaré Map for a Linearly Damped Trajectory: $K = 0.20$, $C_{D_*} = 0.001$, $e = .01$, $C_{D_*}/e = 0.10$, and $(0.37\pi, -0.05)$.

174
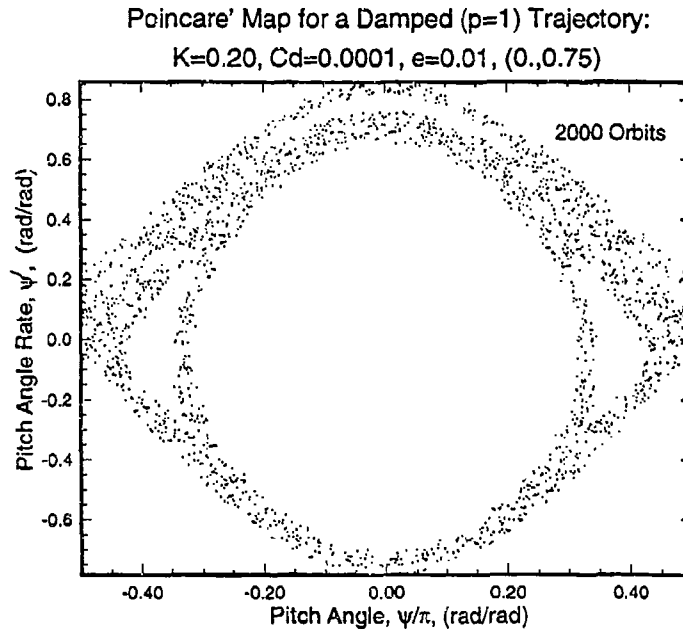
Figure 7.31: Poincaré Map for 2000 Orbits: $K = 0.20$, $C_{D_*} = 0.0001$, $e = .01$, $C_{D_*}/e = 0.01$, and $(0., 0.75)$.

critical value.[6] A 2000 orbit Poincaré map for this trajectory (Figure 7.31) appears to indicate chaotic motion, as does the plot of the first Lyapunov exponent computed for hundreds of orbits (Figure 7.32). If the integrations of the Poincaré data and the Lyapunov exponents are carried out to a greater number of orbits, however, one finds the chaotic motion to again be transient; although initially regular, the trajectory eventually becomes periodic. A plot of the Lyapunov exponent for 2000 orbits (Figure 7.33) verifies that the chaotic motion is being damped out[7] and a second Poincaré map for this trajectory (Figure 7.34), calculated for 15,000 orbits, also supports this. In fact, Lyapunov exponent plots of example trajectories calculated for even smaller damping ratio-eccentricity ratios all have negative slopes, indicating that they also follow this trend.

Similar example trajectories were also carried out for smaller values of eccentricity, for other values of inertia ratio, and for other initial states with the same results. The chaotic motion is transient and no long term or "true" chaotic motion[8] appeared

---

[6]Actually one of the fundamental assumptions of the Melnikov method is that $C_{D_*}$ and $e$ are both of order $\epsilon$. Hence, this example is extreme but does serve to illustrate chaos is transient.

[7]After 2000 orbits the first Lyapunov exponent for this case has a value of about 0.02. 8000 orbits later it has a value of about 0.0037 and is still decreasing.

[8]Many references don't consider the motion to be truly chaotic if it eventually damps out.
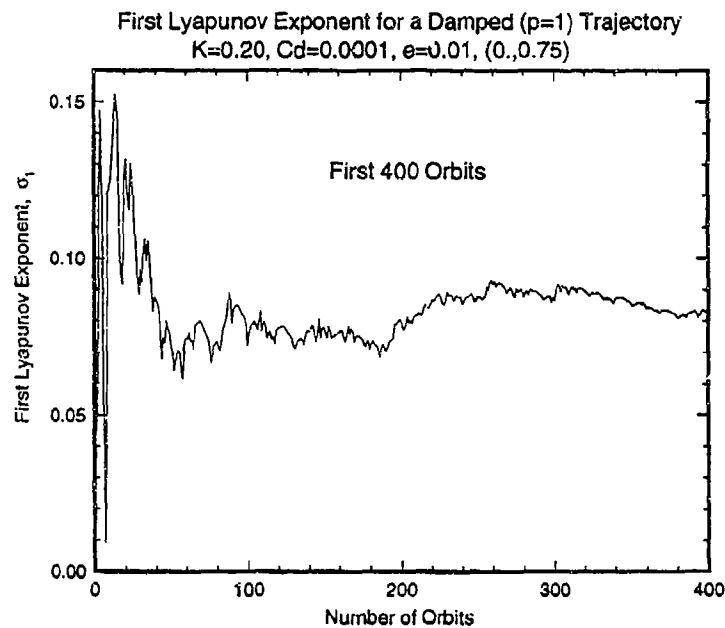
Figure 7.32: First Lyapunov Exponent for 400 Orbits: $K = 0.20$, $C_{D_*} = 0.0001$, $e = .01$, $C_{D_*}/e = 0.01$, and $(0., 0.75)$.
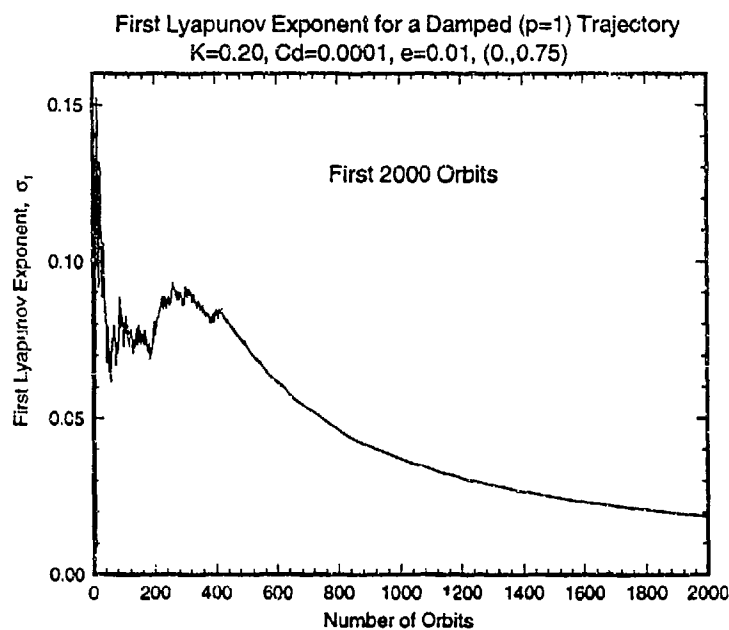


Figure 7.33: First Lyapunov Exponent for 2000 Orbits: $K = 0.20$, $C_{D_*} = 0.0001$, $e = .01$, $C_{D_*}/e = 0.01$, and $(0., 0.75)$.

Poincaré Map for a Damped (p=1) Trajectory:
K=0.20, Cd=0.0001, e=0.01, (0.,0.75)
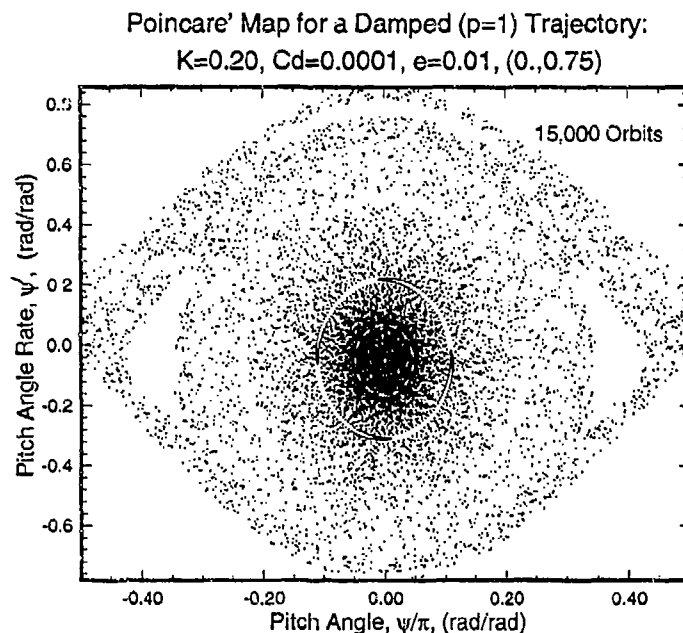


Figure 7.34: Poincaré Map for 15,000 Orbits: $K = 0.20$, $C_{D_*} = 0.0001$, $e = .01$, $C_{D_*}/e = 0.01$, and $(0., 0.75)$.

in the vicinity of the heteroclinic orbit. Only transitory chaotic motion appeared and even that only was seen for $C_{D_*}/e$ ratios two orders of magnitude less than that predicted using Melnikov's method. Intuitively, the greater the damping coefficient, the quicker (fewer orbits) the satellite reaches the $P = 1/1$ sink near the origin.

It is interesting to compare the above Poincaré Maps with their counterpart for zero damping, Figure 7.35. For small damping coefficients, such as in Figure 7.34, the transitory chaotic regions avoid many of the resonance areas or islands of the undamped case. These resonance areas become sinks for certain ranges of damping ratio with well described basins of attraction. With initial conditions lying within these resonance areas, the trajectory cannot escape and migrates to the middle of the sinks. Comparison of Figures 7.26 and 7.35 demonstrates this. The sink of Figure 7.26 is a $P = 1/1$ solution corresponding to its undamped counterpart in Figure 7.35, the island within the chaos region close to $(0., 0.78)$. Likewise, Figure 7.28 corresponds to the $P = 1/1$ solution near the origin and the $P = 1/2$ sinks of Figure 7.30 correspond to the regular motion areas close to $(\pm 0.37\pi, -0.05)$ in Figure 7.35.

The above examples raise an important consideration beyond that of criticizing the accuracy of the Melnikov criteria. In all of these example cases for small damping coefficients, the motion is *initially chaotic but always damps to a periodic solution*. Thus, true "steady-state" chaotic motion does not appear to exist for small damping

177
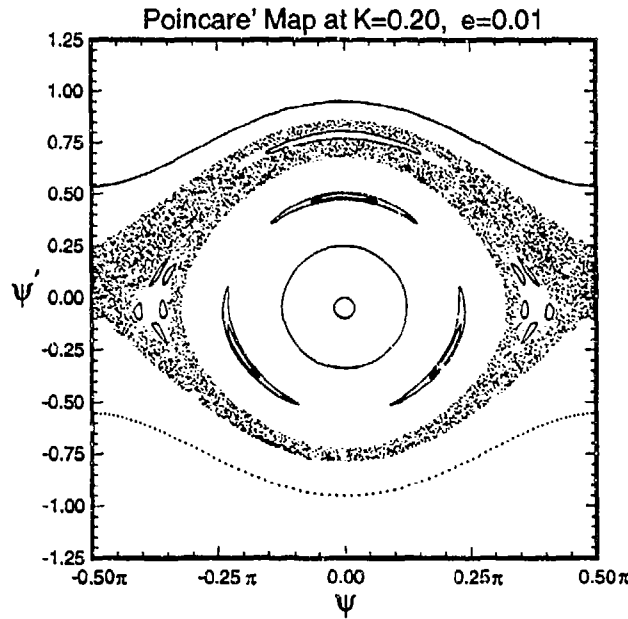
Figure 7.35: Poincaré Map for $K = 0.2$ and $e = .01$.

ratios despite the Melnikov prediction. The author could only find a few references to this curious phenomenon in the literature. Lichtenberg and Lieberman mention it [42, page 432], and Holmes [52] saw this type of transient behavior in a study of Duffing's equation. In a very interesting paper, Tsang and Lieberman [53] found that persistent chaotic motion does not exist for certain nearly integrable Hamiltonian systems perturbed by weak dissipation. They found that the motion for many such systems may be transiently chaotic over numerous orbits but eventually the trajectory is attracted to an island sink and the motion becomes periodic. Tsang and Lieberman demonstrated their findings with examples of two famous nonlinear dynamical systems, a weakly dissipative Fermi map and a modified Hénon map.

The linearly damped gravity-gradient satellite pitching problem is a nearly integrable Hamiltonian system perturbed by weak dissipation *if* eccentricity and damping coefficient are assumed to be small – the exact assumptions required to develop the Melnikov transition criteria. Hence, the Melnikov method fails for this problem and caution is emphasized in applying it to other near-integrable systems. There has been a considerable amount of work published containing impressive derivations of the Melnikov transition criteria for nearly integrable Hamiltonian systems but without validation of the solution. It would be prudent to view these criteria as suspect unless their accuracy is proven.

178
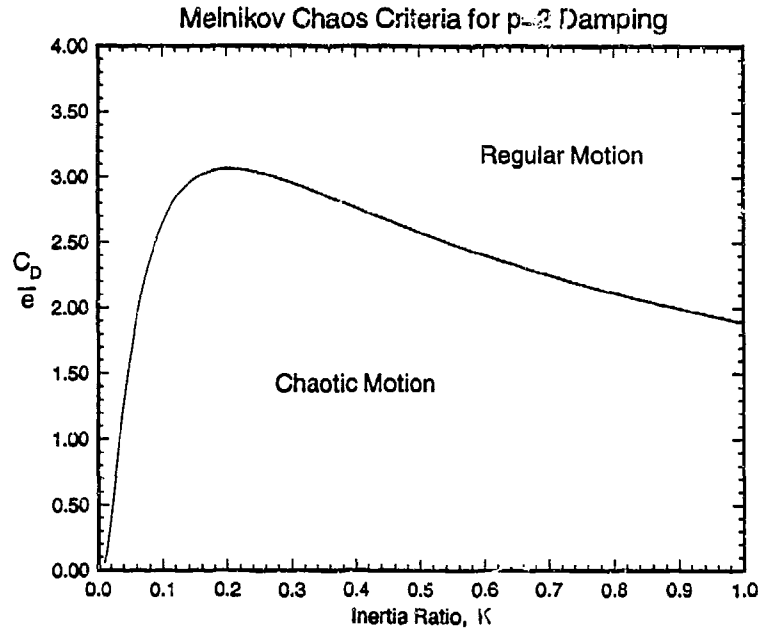
Figure 7.36: Melnikov Chaos Criteria for Nonlinear (p=2) Damping.

## 7.5.3 Melnikov Criteria for Nonlinear (p=2) Damping

The derivation of the Melnikov chaos criteria for the nonlinear damping case is nearly identical to the linear damping case presented above. The only term which is different, the $C_D$ term, may be directly integrated. Following the same procedure a similar solution to the Melnikov integral can be found,

$$M(f_o) = \frac{\pi e'}{2} \sin f_o \left[ 4 \operatorname{sech}\left(\frac{\pi}{2\gamma}\right) + 3\operatorname{csch}\left(\frac{\pi}{2\gamma}\right) \right] - \frac{\pi}{2}\gamma^2 C_D'. \tag{7.21}$$

This integral provides a Melnikov chaos criteria that differs from Equation 7.20 by a factor of $4/(\pi\gamma)$

$$\frac{C_D}{e} < \frac{4}{3K} \left[ \operatorname{sech}\left(\frac{\pi}{2\sqrt{3K}}\right) + \frac{3}{4}\operatorname{csch}\left(\frac{\pi}{2\sqrt{3K}}\right) \right]. \tag{7.22}$$

This criteria, which matches that derived by Seisl and Steindl [19], is plotted in Figure 7.36. As in the p=1 case discussed above, the validity of this chaos criteria is investigated by comparing the Melnikov prediction with numerical results. Begin by first examining the undamped case for an arbitrary inertia ratio and a small value of eccentricity and then comparing results for damped cases for various values of the damping coefficient-to-eccentricity ratio.
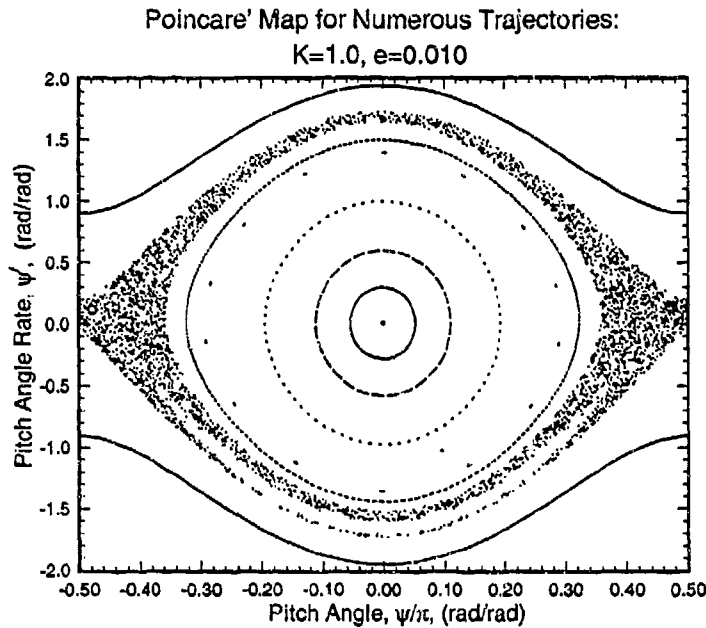
Figure 7.37: Poincaré Map for Various Undamped Trajectories: $K = 1.0$, $e = .01$.

Figure 7.37 presents a Poincaré map for a variety of undamped trajectories for $K = 1.0$ and $e = .01$. The area where the heteroclinic orbit resides for the $e = 0$ case is chaotic for this non-zero value of eccentricity. It is in the vicinity of this area that the Melnikov criteria applies. According to Figure 7.36, one should find regular motion in this region for all $C_D/e$ greater than approximately 1.9 for the chosen inertia ratio, and chaotic motion for $C_D/e$ ratios less than this value.

The initial state $(0., 1.5)$, an eccentricity of $.01$, and an inertia ratio of 1.0 produced the results shown in Figure 7.38. Poincaré maps for three damped trajectories are shown in this plot. All three trajectories display quasiperiodic motion, even for the $C_D = 0.002$ and $C_D = 0.01$ cases (with $C_D/e = 0.20$ and $C_D/e = 1.0$, respectively) which should be chaotic according to the Melnikov criteria. Figure 7.39 shows the first Lyapunov exponents for these two trajectories. The Melnikov criteria is very unaccurate for this case, although in all fairness, the initial state $(0., 1.5)$ may be stretching the Melnikov method assumption of being in the "vicinity" of the unperturbed heteroclinic orbit.

One possible set of initial conditions which produce the unperturbed heteroclinic orbit is $(0., 1.7320508...)$, an initial pitch rate value of about 15 percent greater than that used in the first example. Thus, an initial state of $(0., 1.732)$ is used for the second example instead of $(0., 1.50)$. The results are presented in Figure 7.40. For

180

**Poincare' Maps for 3 Damped (p=2) Trajectories:**
**K=1.0, e=0.01, (0.,1.50)**
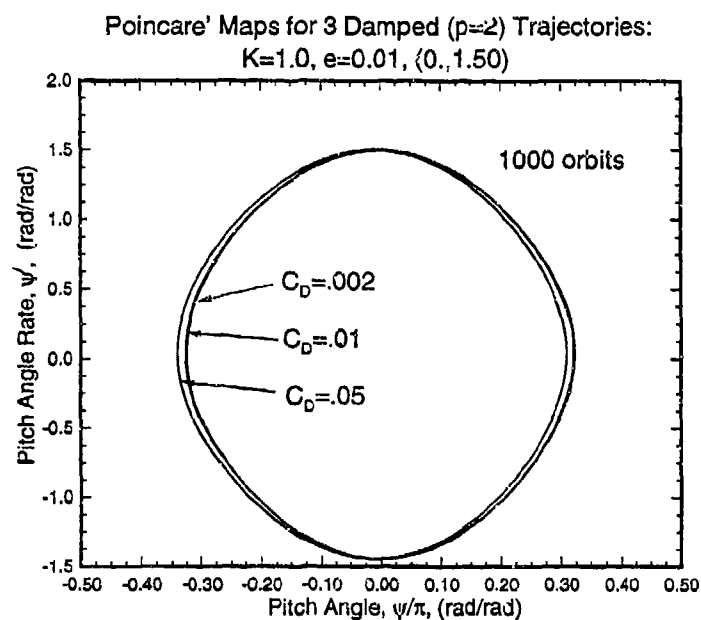
Figure 7.38: Poincaré Map for Three Damped (p=2) Trajectories: $K = 1.0$, $e = .01$, and $(0., 1.50)$.



**First Lyapunov Exponents for Two Damped (p=2) Trajectories:**
**K=1.0, e=0.01, (0.,1.50)**
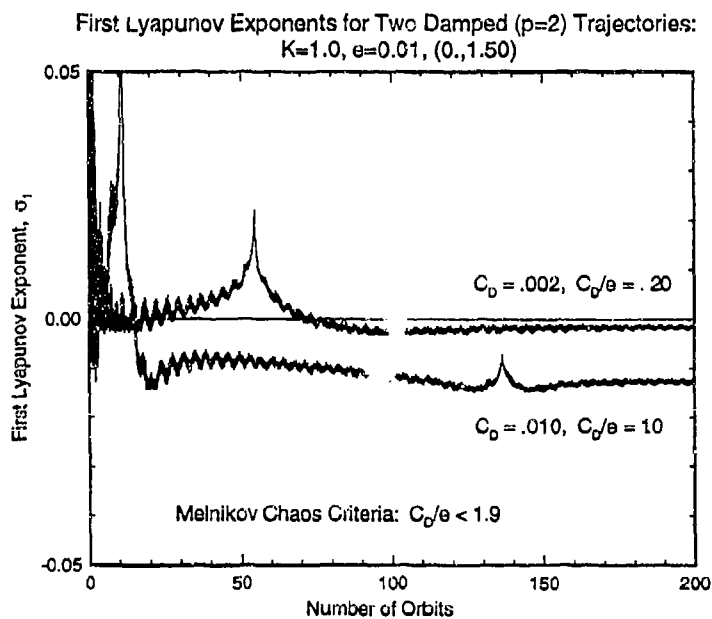
Figure 7.39: First Lyapunov Exponents for Two Damped (p=2) Trajectories: $K = 1.0$, $e = .01$, $(0., 1.5)$.

181

First Lyapunov Exponents for Two Damped (p=2) Trajectories:
K=1.0, e=0.01, (0.,1.732)
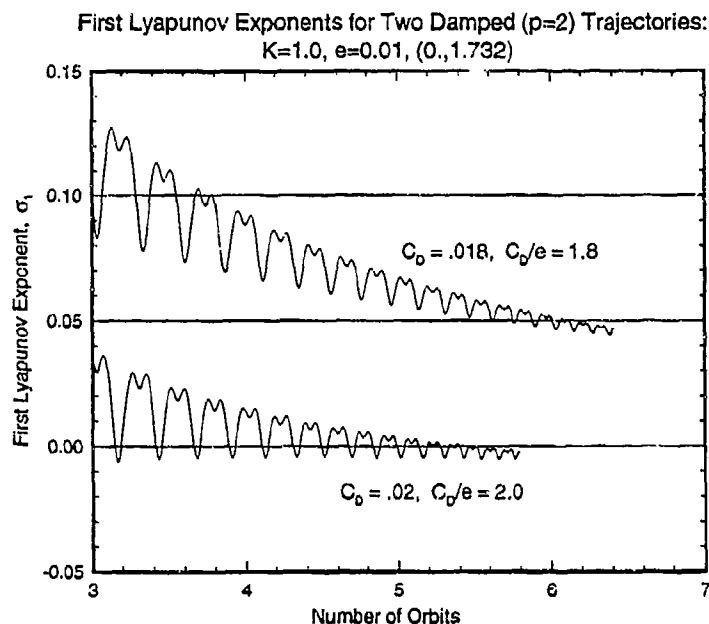


Figure 7.40: First Lyapunov Exponents for Two Damped (p=2) Trajectories: $K = 1.0$, $e = .01$, $(0., 1.732)$.

this case the Melnikov chaos prediction agrees very well with the numerical results. $C_D/e = 2.0$ gives a regular trajectory and $C_D/e = 1.8$ gives a chaotic trajectory, together bracketing the Melnikov critical value of approximately 1.9. [9] These results imply the Melnikov criteria is *accurate only very close to the heteroclinic orbits of the unperturbed system*.

As a third example take $K = 0.2$, $e = 0.01$, and an initial state very close to the unperturbed heteroclinic orbit, $(0., 0.7746)$. The results appear in Figure 7.41. The Melnikov predicts chaotic motion for $C_D/e < 3.06$ for this inertia ratio yet the actual border appears to be somewhere in the range $2.0 < C_D < 2.1$, giving about a 50% overprediction.

It has been shown that the Melnikov method may provide either excellent estimates or poor estimates of the border between regular and chaotic motion for the p=2 nonlinear damping problem, depending upon the value of inertia ratio. Apparently care must be taken to provide initial conditions very close to the heteroclinic orbits of the unperturbed system.

---

[9] Because of the speed in which the solution migrates towards the attractor at negative infinity, the integration routine and the Lyapunov exponent numerical routine fail after only a few orbits. Hence, there is some uncertainty in this determination, although the exponents appear to settle quickly.

First Lyapunov Exponent for Two Damped (p=2) Trajectories:
K=0.20, e=0.01, (0.,0.7746)
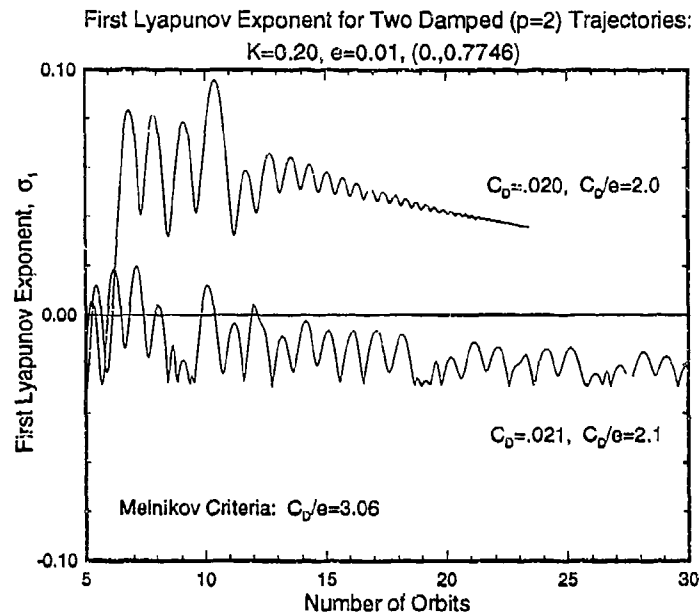


Figure 7.41: First Lyapunov Exponents for Two Damped (p=2) Trajectories: $K = 0.2$, $e = .01$, $(0., 0.7746.$

## 7.6 Summary

The pitching dynamics of a gravity-gradient satellite with linear damping was investigated in a precursory manner. As Tsang and Lieberman [53] found for a dissipative Fermi map and a modified Hénon map, persistent chaotic motion does not exist for this problem for small damping coefficients. Many trajectories are transiently chaotic over numerous orbits, but eventually are attracted to an island sink and the motion becomes periodic.

Bifurcation diagrams showed numerous period doubling sequences which lead to chaos. In fact, period doubling sequences appeared in each transition area of the bifurcation diagrams that was examined. Blowups of some of these areas displayed period doubling sequences for both increasing and decreasing values of eccentricity. Strange (fractal) chaotic attractors were found for this system for large values of $e$ and $C_{D_*}$.

The Melnikov method fails entirely for the linear damping problem and we emphasize caution in applying it to other near-integrable systems. There has been considerable work published containing impressive derivations of the Melnikov transition criteria for nearly integrable Hamiltonian systems but without validation of the solution. It would be prudent to view these criteria as suspect unless their

accuracy is proven.

The pitching dynamics of a gravity-gradient satellite with a nonlinear (p=2) damping term were also investigated in a precursory manner. The main effect of the damping term was to force the trajectories to an attractor at $(-\infty, -\infty)$. It appears from an examination of a number of bifurcation diagrams that almost all of the chaotic regions for the undamped case lie in the basin of attraction for the attractor at negative infinity. Only a few periodic and other chaotic solutions appeared – one of these was shown to be a strange chaotic attractor with a fractal dimension of about 1.34.

The Melnikov method has been shown to provide either excellent estimates or poor estimates of the border between regular and chaotic motion for the p=2 nonlinear damping problem, depending upon the value of inertia ratio, and the proximity of the trajectory to the unperturbed heteroclinic orbit.

# 8   Observations, Conclusions, and Future Considerations

## 8.1   Observations and Conclusions

The main objective of this research was to examine the nonlinear dynamics of the pitch equation of motion for a gravity-gradient satellite in an elliptical orbit about a central body. This was successfully carried out primarily with numerical nonlinear analysis tools, such as phase diagrams, Poincaré maps, bifurcation plots, spectral density plots, Lyapunov exponents, and chaos diagrams.

The circular orbit pitching problem is an important special case of the more general elliptical orbit problem, providing the form of the solutions in the limit as $e \rightarrow 0$. It was shown that the pitching motion for a gravity-gradient satellite in a circular orbit about a central body can either be tumbling or libration and either periodic or quasiperiodic. Analytical solutions were developed to describe each of these types of motion and example solutions were presented. Numerically obtained example trajectories were also presented for each type of motion. The contribution of this report for the circular orbit problem lies mainly in providing a more complete examination of this problem for arbitrary values of inertia ratio.

The addition of eccentricity brought chaos to the problem. The planar pitching motion of a gravity-gradient satellite in orbit about a spherical central body was shown to be either periodic, quasiperiodic, or chaotic, depending upon the initial state and the system parameters. Many past studies of this problem have wrongly assumed that only eccentricity affects the nonlinearity of the system. Instead, whether or not a trajectory exhibits regular or chaotic motion is a function of the initial state, $(\psi_o, \psi'_o)$, and both system parameters, $e$ and $K$. This fact can be easily seen by examination of sequences of nonlinear analysis numerical plots such as Poincaré maps and bifurcation diagrams, and also by examination of the chaos diagrams formed of grids of Lyapunov exponent values. The former two methods gave useful results but were restricted to a localized view of the relationships between the system parameters and the motion. In contrast, the chaos diagrams provided a global view of these relationships for the entire ranges of both system parameters.

185

This study demonstrated that chaos diagrams can be a very valuable tool in examining the relationship between the system parameters and the type of pitching motion. The structure of the chaos diagrams also proved to be very interesting. The chaos diagrams depicted a complex mix of regular and chaotic motion, with islands of regular motion appearing in a sea of chaos. The use of chaos diagrams is very rare in the literature, and when they do appear, they are made of a very coarse grid in which the border between chaotic and regular motion is approximated by only a few points (black for chaos and white for regular motion), probably far too few points for one to determine the true shape of the border. The work presented here is unique in that the chaos diagrams are created for grids composed of hundreds of thousands of points. This allowed enough detail of the border in parameter space between regular and chaotic motion to to be observed that its fractal form was easily discovered. These chaos diagrams are also unique in that they presented information about the relative magnitude of the chaos for each point in the plot. This was accomplished by introducing color scaling of the magnitude of each computed Lyapunov exponent – the greater the exponent, the faster the divergence.

The author could find only one other case in the literature of a fractal border in parameter space; in that case the fractal border was determined experimentally, not numerically. The border was verified to be fractal by a simple calculation of fractal dimension using draftsman dividers and dial calipers to measure Figure 5.63. This result raises serious questions to the accuracy of some of the analytical boundary prediction techniques that predict smooth and simple transition boundaries.

A number of bifurcation diagrams were presented in an attempt to obtain at least a rudimentary knowledge of the structure of the chaos diagrams for the initial state $(0., 0.)$. These bifurcation diagrams represent dynamically equivalent vertical slices (constant $K$, variable $e$) and horizontal slices (constant $e$, variable $K$) of the chaos diagrams for the zero initial conditions. Islands of regular motion within the sea of chaos were found to contain rotational instead of librational motion. At least for the chaos diagrams for the $(0., 0.)$ initial state, most of the regular motion is libration, with rotation appearing generally for small values of $K$ and relatively larger values of $e$. Examination and comparison of these bifurcation diagram slices to the chaos diagrams revealed the existence of pitch angle tumbling periodic solutions centered roughly in the bays of regular motion in the chaos diagrams. These strings of periodic solutions appeared on multiple scales in the chaos diagrams, with the winding number increasing with increasing eccentricity. To examine these solutions further, an analytical solution was found for periodic tumbling motion for the limiting case of $K = 0$, which corresponds to an axially symmetric satellite. The analytical results agreed well with the numerically obtained bifurcation diagrams except for

186

small values of eccentricity; apparently we need $e \gg K$ for these solutions to be useful.

Although numerous subharmonic librational trajectories were found in the study of the structure of the (0.,0.) initial state chaos diagrams, no harmonic librational trajectories were observed. The circular orbit analytical theory allowed for a very limited range of periodic librational trajectories, and this range has probably been reduced even more by the addition of eccentricity to the problem. In contrast, numerous examples of both harmonic and subharmonic rotational trajectories were found in the course of this study. The harmonics of the tumbling class of trajectories were unlimited; the $K = 0$ theory showed that very large period rotations (approaching infinity) are possible.

The dynamics of a real satellite are not as simple as the models employed in this study. An actual spacecraft is subjected to a variety of internal and external torques that may contribute linear and nonlinear damping forces. Thus, another objective of this work was to provide a precursory examination of the pitch dynamics of the basic system with a few modifications – the effect of an oblate central body for an eccentric, polar orbit, and the effect of the addition of two separate damping terms.

A unique planar pitch equation of motion for an uncontrolled satellite in an eccentric, polar orbit about an oblate, axially symmetric planet was derived using the osculating orbital elements. It was found that the variational equations for scaled parameter and eccentricity are the same order of magnitude as the $J_2$ terms in the pitch equation of motion. This is an important finding as it indicates that it is inconsistent to include terms of order $J_2$ in the pitch equation of motion without also accounting for variations in the orbital elements.

The inclusion of the oblate terms and use of osculating orbital elements greatly affected the dynamics of the satellite pitching motion for a specific example problem. Eccentricity, assumed constant in previous nonlinear analyses of planar gravity-gradient pitch dynamics, was shown to vary almost 15%. A three-dimensional Poincaré mapping was created depicting quasiperiodic motion. With this more detailed model, chaos was detected in areas of the phase space where only regular motion was previously found.

The first damping term investigated was simple linear damping, previously briefly studied by Tong and Rimrott [22]. The work presented in this report built upon that foundation and disproved one of their assumptions concerning the continuity of chaotic motion for large eccentricity by displaying bifurcation diagrams for the system. As Tsang and Lieberman [53] found for a dissipative Fermi map and a

modified Hénon map, persistent chaotic motion does not exist for this problem for small damping coefficients. Many trajectories are transiently chaotic over numerous orbits, but eventually are attracted to an island sink and the motion becomes periodic. Bifurcation diagrams showed numerous period doubling sequences that lead to chaos. In fact, period doubling sequences appeared in every transition area of the bifurcation diagrams that was examined. Blowups of some of these areas displayed period doubling sequences for both increasing and decreasing values of eccentricity. Strange (fractal) chaotic attractors were found for this system for large values of $e$ and $C_{D_*}$.

The second damping term investigated in this study was nonlinear damping proportional to the square of the velocity. To the author's knowledge, the nonlinear damping case has not been studied except for a study presenting the derivation of the Melnikov function by Seisl and Steindl [19]. The primary effect of this damping term was to force the trajectories to an attractor at $(-\infty, -\infty)$. It appears from an examination of a number of bifurcation diagrams that almost all of the chaotic regions for the undamped case lie in the basin of attraction for the attractor at negative infinity. Only a few periodic and other chaotic solutions appeared – one of these was shown to be a strange chaotic attractor with a fractal dimension of about 1.34.

The validity of Melnikov's method in the prediction of the border in parameter space between chaotic and regular motion was also investigated for the two damping cases. This method has been applied a number of times in the past but with a minimum of emphasis upon its accuracy. The Melnikov chaos criteria for the nonlinear damping case was previously derived (as noted above) but the criteria for the linear damping case does not appear in the literature.

The Melnikov method was shown to provide either excellent or poor estimates of the border between regular and chaotic motion for the nonlinear damping problem, depending upon the value of inertia ratio, and the proximity of the trajectory to the unperturbed heteroclinic orbit. The Melnikov chaos criteria fails entirely for the linear damping problem because the chaos is transient. This failure is not necessarily due to the Melnikov method itself since it may correctly predict the occurrence of transverse intersections of the stable and unstable manifolds, but rather to the assumption that these transverse intersections lead to anything more than very brief transient chaotic motion very close to the separatrices. Caution is advised in applying this transition prediction method to other near-integrable systems. There has been considerable work published containing impressive derivations of the Melnikov transition criteria for nearly integrable Hamiltonian systems but without validation of the solutions. It would be prudent to view these criteria as suspect unless their accuracy is proven.

## 8.2 Recommendations for Future Work

It appears that chaos diagrams may be constructed and utilized as an effective engineering tool for satellite orbit and hardware design, by allowing chaotic pitching motion to be avoided through careful selection of the orbit eccentricity and the satellite inertia ratio. It is recommended that chaos diagrams of the form developed in this research, i.e. having very dense grids and associating a color scale with the Lyapunov exponent magnitudes, be computed for other problems, especially for transition studies.

The only obvious route to chaos appearing in this study was the period doubling route for the linearly damped case, which appeared to depend only on eccentricity. The other study cases seemed to have complex transitions from regular to chaotic motion that were dependent on inertia ratio and the initial state and not merely on eccentricity. It should be emphasized that although some period doubling sequences leading to chaos were found, this phenomenon is a result of chaos, not the cause of it. In their study of the Duffing Equation, Reinhall et al. [33] points this out more succinctly, as well as showing how discretization itself can cause chaos (see also [31,32,34].) Thus, the actual mode of transition for these cases should be examined in detail using the results of the work presented here as a foundation, and the effects of discretization on the nonlinearity of each of the cases should be examined.

The oblate central body study produced surprising results. More in-depth numerical exploration of the nonlinear pitching motion of the polar-orbiter problem is warranted, as well as an investigation into the effects of orbit-attitude coupling among the roll, yaw, and pitch equations. Future work on this problem should involve discarding the restriction of a polar orbit and attempting an analysis for arbitrary-inclination orbits.

# References

[1] Yeh, Jiin-Po, and DiMaggio, Frank, "Chaotic Motion of Pendulum with Support in Circular Orbit," *Journal of Engineering Mechanics*, Vol. 117, No. 2, February 1991, pp. 329-347.

[2] Wisdom, J., "Chaotic Behavior in the Solar System," *Proc. R. Soc. Lond.* A 413, 1987, pp. 109-129.

[3] Ott, E., Grebogi, C., and Yorke, J. A., "Controlling Chaos," *Physical Review Letters*, Vol. 64, No. 11, 12 March 1990, pp. 1196-1199.

[4] Ditto, W.L., Rauseo, S.N., and Spano, M.L., "Experimental Control of Chaos," *Physical Review Letters*, Vol. 65, No. 26, 24 Dec 1990, pp. 3211-3214.

[5] Peterson, Ivars, "Ribbon of Chaos," *Science News*, Vol. 139, 26 January 1991, pp. 60-61.

[6] Langreth, Robert, "Engineering Dogma Gives way to Chaos," *Science*, Vol. 252, 10 May 1991, pp. 776-778.

[7] Pecora, L.M., and Caroll T.L., "Synchronization in Chaotic Systems," *Physical Review Letters*, Vol. 64, No. 8, 19 February 1990, pp. 821-824.

[8] Pecora, Louis M., and Caroll Thomas L., "Driving Systems with Chaotic Signals," *Physical Review A*, Vol. 44, No. 4, 15 August 1991, pp. 2374-2383.

[9] Langreth, Robert, "Flying High With Chaos Control," *Science*, Vol. 252, 10 May 1991, pp. 777.

[10] Hauenstein, A.J. et al., "Chaotic and Nonlinear Dynamic Response of Aerosurfaces with Structural Nonlinearities," AIAA-92-2547-CP, 1992.

[11] Zlatoustov, V.A. et al., "The Oscillations of an Artificial Satellite in the Plane of an Elliptical Orbit," *Cosmic Research* (Translated from Russian) Vol. 2, No. 5, September-October, 1964.

[12] Beletskii, V.V., *"Motion of an Artificial Satellite About its Center of Mass,"* (Translated from Russian) NASA TT F-429, 1966.

[13] Modi, V.J. and Brereton, R.C., "Periodic Solutions Associated with the Gravity-Gradient-Oriented System, Part I. Analytical and Numerical Determination," *AIAA Journal*, No. 7, July 1969, pp. 1217-1225.

[14] Modi, V.J. and Brereton, R.C., "Periodic Solutions Associated with the Gravity-Gradient-Oriented System, Part II. Stability Analysis," *AIAA Journal*, No. 8, August 1969, pp. 1465-1468.

[15] Anand, D.K., et al., "Gravity-Gradient Capture and Stability in an Eccentric Orbit," *Journal of Spacecraft*, Vol. 6, No. 12, September 1969, pp. 1456-1459.

[16] Anand, D.K., Yuhasz, R.S., and Whisnant, J.M., "Attitude Motion in an Eccentric Orbit," *Journal of Spacecraft*, Vol. 8, No. 8, August 1971, pp. 903-905.

[17] Melnikov, V.K., "On the Stability of the Center for Time Perturbation," *Transactions of the Moscow Mathematical Society*, Vol 12, pp. 1-57, 1963.

[18] Koch, B.P. and Bruhn, B., "Chaotic and Periodic Motions of Satellites in Elliptic Orbits," *Z. Naturforsch*, 44a., pp. 1155-1162, 1989.

[19] Seisl, M. and Steindl, A., "Chaotische Schwingungen von Satelliten," *Z. fuer Angewandte Mathematik und Mechanik*, Vol. 69, No. 5, pp. 352-354, 1989.

[20] Tong, X. and Rimrott F.P.J., "Numerical Studies on Chaotic Planar Motion of Satellites in an Elliptic Orbit," *Chaos, Solitons & Fractals*, Vol. 1, No. 2, pp. 179-186, 1991.

[21] Gulyaev V.I., Zubritskaya, A.L., and Koshkin, V.L., "Universal Sequence of Bifurcations of Doubling of the Oscillation Period for a Satellite in an Elliptical Orbit," *Izv. AN SSSR. Mekhanika Tverdogo Tela*, Vol. 24, No. 3, pp. 3-8, 1989, translation, 1989 Allerton Press.

[22] Tong, X. and Rimrott F.P.J., "Some Observations of Chaotic Motion of Satellites with Damping in an Elliptic Orbit," *Proceedings of the Thirteenth Canadian Congress of Applied Mechanics*, pp. 750-751, May, 1991.

[23] Cole, J.W., and Calico, R.A., "Nonlinear Oscillations of a Controlled Periodic System," *Journal of Guidance, Control, and Dynamics*, Vol. 15, No. 3, May-June 1992.

[24] Gray, G.L., and Stabb, M.C., "Chaos in Controlled, Gravity-Gradient Satellite Pitch Dynamics via the Method of Melnikov, Part I - Center Stabilization," AAS-93-132, Presented at the AAS/AIAA Spaceflight Mechanics Meeting, Pasedena, California, February, 1993.

[25] Tortorelli, D.A., and Vakakis, A.F., "The Prediction of the Onset of Chaos with Sensitivity Analysis," AIAA-92-2550-CP, 1992.

[26] Karasopoulos, H., and Richardson, D.L., "Chaos in the Pitch Equation of Motion for the Gravity-Gradient Satellite," AIAA-92-4369, Presented at the 1992 AIAA/AAS Astrodynamics Conference, Hilton Head, South Carolina, August, 1992.

[27] Karasopoulos, H.A., and Richardson, D.L., "Numerical Investigation of Chaos in the Attitude Motion of a Gravity-Gradient Satellite," AAS-93-581, Presented at the 1993 AAS/AIAA Astrodynamics Specialist Conference, Victoria, B.C., Canada, August, 1993.

[28] Karasopoulos, H.A., and Richardson, D.L., "Investigation of Chaotic Motions for a Gravity-Gradient Satellite in Orbit About an Oblate Central Body," IAF-93-A.3.19, 44th Congress of the International Astronautical

[29] Wolf, A., Swift, J.B., Swinney, H.L., and Vastano, J.A., "Determining Lyapunov Exponents from a Time Series," *Physica 16D*, 1985, pp. 285-317.

[30] Parker, T. and Chau, L., *Practical Numerical Algorithms for Chaotic Systems*, Springer-Velag, New York, 1989, pp. 83-114.

[31] Sweby, P.K., Yee, H.C., and Griffiths, D.F., "On Spurious Steady-State Solutions of Explicit Runge-Kutta Schemes," NASA TM 102819, April 1990.

[32] Yee, H.C., Sweby, P.K., and Griffiths, D.F., "A Study of Spurious Asymptotic Numerical Solutions of Nonlinear Differential Equations by the Nonlinear Dynamics Approach," Lecture Notes in Physics #371, 12th International Conference on Numerical Methods in Fluid Dynamics, 1991.

[33] Reinhall, P.G., Caughey, T.K., and Storti, D.W., "Order and Chaos in a Discrete Duffing Oscillator: Implications on Numerical Integration," *Journal of Applied Mechanics,* Vol. 56, pp. 162-167, March 1989.

[34] Lorenz, Edward N., "Computational Chaos - A Prelude to Computational Instability", *Physica D* 35 (1989), pp. 299-317.

[35] Moran, John P., "Effects of Plane Librations on the Orbital Motion of a Dumbbell Satellite," *ARS Journal*, 31, 1961, pp. 1089-1096.

[36] Hughes, P.C., *Spacecraft Attitude Dynamics*, John Wiley & Sons, Inc., New York, 1986.

[37] Elrod, B.D., "A Quasi-Inertial Attitude Mode for Orbiting Spacecraft," *Journal of Spacecraft*, Vol. 9, No. 12, December 1972.

[38] Percival, I.C., F.R.S., "Chaos in Hamiltonian Systems", *Proc. R. Soc. Lond.*, A 413, 1987, pp. 131-144.

[39] Chernikov, A.A., Sagdeev, R.Z., and Zaslavsky, G.M., "Chaos: How Regular Can it Be?", *Physics Today*, November 1988, pp. 27-35.

[40] Tabor, M., *Chaos and Integrability in Nonlinear Dynamics*, John Wiley & Sons, Inc., New York, 1989.

[41] Guckenheimer, J., and Holmes, P., *Nonlinear Oscillations, Dynamical Systems, and Bifurcations of Vector Fields*, Springer-Verlag, New York, 1983.

[42] Lichtenberg, A.J., and Lieberman, M.A., *Regular and Stochastic Motion*, Springer-Verlag, New York, 1983.

[43] Chirikov, B.V., "A Universal Instability of Many Dimensional Oscillator Systems," *Physics Reports*, Vol. 52, pp. 265.

[44] Gwinn, E.G., and Westervelt, R.M., "Intermittent Chaos and Low-Frequency Noise in the Driven Damped Pendulum," *Physical Review Letters* Vol 54, No. 15, pp. 1613-1616, 15 April 1985.

[45] Moon, F.C., and Li, G.X., "Fractal Basin Boundaries and Homoclinic Orbits for Periodic Motion in a Two-Well Potential," *Physical Review Letters* Vol 55, No. 14, pp. 1439-1442, 30 September 1985.

[46] Moon, Francis C., *Chaotic Vibrations: An Introduction for Applied Scientists and Engineers*, John Wiley & Sons, Inc., New York, 1987.

[47] Moon, F.C., "Fractal Boundary for Chaos in a Two State Mechanical Oscillator," *Physical Review Letters* Vol 53, No. 10, pp. 962-964, 3 September 1984.

[48] Mandelbrot, B., *Fractals*, W. H. Freeman and Co., San Francisco, 1977.

[49] Mandelbrot, B.B., *The Fractal Geometry of Nature*, W. H. Freeman and Co., New York, 1983.

[50] Battin, R.H., *An Introduction to the Mathematics and Methods of Astrodynamics*, American Institute of Aeronautics and Astronautics, Inc., New York, 1987.

[51] Farmer, J.D., Ott, E., and Yorke, J.A., "The Dimension of Chaotic Attractors," *Physi a 7D*, 1983, pp. 153-180.

[52] Holmes, P. "A Nonlinear Oscillator With a Strange Attractor," *Philosophical Transactions of the Royal society of London,* Vol. 292, pp. 419-448.

[53] Tsang, K.Y., and Lieberman,M.A., "Transient Chaotic Distributions in Dissipative Systems," *Physica 21D*, 1986, pp. 401-414.

# 9  Appendix: Mathematical Derivations

## 9.1  Derivation of Equation 6.2: the Gravitational Potential Function for a Satellite in an Eccentric Polar Orbit About an Oblate Central Body

The potential due to a non-spherical central body can be represented by an expansion in terms of spherical harmonics that vary with latitude and longitude. In general, the most dominant contribution is the one obtained by modelling the central body as an ellipsoid of revolution, the $J_2$ term. The derivation of Equation 6.2, the gravitational potential function for a satellite in an eccentric polar orbit about an oblate central body, was briefly discussed in Section 6. The following is a more detailed derivation.

The derivation is begun in the same manner as in Section 6, by noting that the gravitational potential of a differential satellite mass $dm$ at a distance from the center of the Earth is given by the expression

$$dV = \left[ -\frac{\mu}{r} + \frac{\mu J_2 R_e{}^2}{2r^3} \left( 3 \sin^2 I \sin^2 \theta - 1 \right) \right] dm. \tag{9.1}$$

$\mu$ is the Earth's gravitational constant, $R_e$ is the Earth's mean equatorial radius, $\theta$ is the satellite's argument of latitude, $I$ is the orbit inclination, and $J_2$ is the dominant spherical harmonic coefficient ($J_2 \approx 1.08263 \times 10^{-3}$) in this equation. A non-rotating, equatorial, Earth-centered coordinate system $(X, Y, Z)$ is used as the fundamental reference frame, the satellite principal-axis system is designated $(x, y, z)$, and the orbit radial and transverse directions are denoted $\hat{e}_r$ and $\hat{e}_t$, respectively. Figure 6.3 displays these coordinate systems. $\omega$ is the argument of periapsis, and $\Omega$ is the the longitude of the ascending node in this figure. Using spherical trigonometry, latitude $\delta$ may be written as

$$\sin \delta = \sin I \sin \theta \tag{9.2}$$

and since

$$Z = \vec{r} \cdot \hat{K} = r \sin \delta, \tag{9.3}$$

195

one can express the differential gravitational potential per unit mass as

$$\frac{d\mathcal{V}}{dm} = -\frac{\mu}{r} + \frac{\beta\mu}{r^3}\left(\frac{3Z^2}{r^2} - 1\right) \tag{9.4}$$

where the constant $\beta$ has been defined for convenience to be

$$\beta \equiv \frac{J_2 R_e^{\,2}}{2}. \tag{9.5}$$

The gravitational potential is a function of $1/r^n$, $n = 1, 3, 5$. Since $\vec{r} \equiv \vec{r_c} + \vec{\rho}$ (Figure 6.2), Equation (9.4) can be integrated over the orbiting body's mass by expanding $r_c^n/r^n$ in terms of $\rho/r_c$ and $J_2$. Specifically,

$$r^2 = \vec{r} \cdot \vec{r} = (\vec{r_c} + \vec{\rho}) \cdot (\vec{r_c} + \vec{\rho}) = r_c^{\,2} + \rho^2 + 2\vec{r_c} \cdot \vec{\rho} \tag{9.6}$$

or

$$r^2 = r_c^{\,2}\left[1 + \left(\frac{\rho}{r_c}\right)^2 + 2\frac{\vec{\rho} \cdot \vec{r_c}}{r_c^{\,2}}\right]. \tag{9.7}$$

Taking the second and third terms within the brackets of this equation as a small parameter $\epsilon$,

$$\epsilon \equiv \left(\frac{\rho}{r_c}\right)^2 + 2\frac{\vec{\rho} \cdot \vec{r_c}}{r_c^{\,2}}, \tag{9.8}$$

a Taylor's Series expansion for small values of $\epsilon$ gives

$$\frac{r_c^{\,2}}{r^2} = 1 - \epsilon + \frac{\epsilon^2}{2} + \mathcal{O}(\epsilon^3). \tag{9.9}$$

In general,

$$\frac{r_c^{\,n}}{r^n} = 1 - \frac{n}{2}\epsilon + \frac{n}{4}\left(\frac{n}{2} + 1\right)\epsilon^2 + \mathcal{O}(\epsilon^3). \tag{9.10}$$

or

$$\frac{r_c^{\,n}}{r^n} = 1 - \frac{n}{2}\left(\frac{\rho^2}{r_c^{\,2}} + 2\frac{\vec{\rho} \cdot \vec{r_c}}{r_c^{\,2}}\right) + n\left(\frac{n}{2} + 1\right)\left(\frac{\vec{\rho} \cdot \vec{r_c}}{r_c^{\,2}}\right)^2 + \mathcal{O}(\epsilon^3). \tag{9.11}$$

Taking $R_e \approx 6.378x10^6$ m, $J_2 \approx 1.083x10^{-3}$, and assuming the satellite's largest dimension is of the order $\rho \approx 1$ m, $\frac{\rho}{r_c} \approx 1.57x10^{-7} \approx \frac{1}{7}J_2$. Hence, for a typical artificial Earth satellite, $\frac{\rho}{r_c} = \mathcal{O}(J_2^{\,2}) \equiv \mathcal{O}(2)$.

Note that $\rho/r_c$ for most satellites in low Earth orbit is the same order of magnitude as $(J_2)^2$, giving a truncation error for the expansions of Equation 9.10 of

$$\mathcal{O}(J_2^{\,3}) = \mathcal{O}\left(\frac{\rho}{r_c}\right)^3 = \mathcal{O}(6). \tag{9.12}$$

196

Equation 9.1 may be integrated over the orbiting body's mass, assuming that the distance from the center of mass of the satellite to its differential mass, dm, is $\vec{\rho} \equiv x\hat{i} + y\hat{j} + z\hat{k}$, using the principal axes:

$$\int_B \frac{dm}{r^n} = \frac{1}{r_c{}^n} \int_B \left[ 1 - \frac{n}{2}\left(\frac{\rho^2}{r_c{}^2} + 2\frac{\vec{\rho}\cdot\vec{r_c}}{r_c{}^3}\right) + n\left(\frac{n}{2}+1\right)\left(\frac{\vec{\rho}\cdot\vec{r_c}}{r_c{}^2}\right)^2 + \mathcal{O}\left(\frac{\rho^3}{r_c{}^3}\right) \right] dm, \tag{9.13}$$

and writing $Z$ (from Equation 9.2) in the form

$$\frac{Z^2}{r_c{}^2} = \frac{\left(\vec{r_c}\cdot\hat{K}\right)^2}{r_c{}^2} + \frac{2(\vec{r_c}\cdot\hat{K})(\vec{\rho}\cdot\hat{K})}{r_c{}^2} + \frac{\left(\vec{\rho}\cdot\hat{K}\right)^2}{r_c{}^2}. \tag{9.14}$$

This integration is

$$\int_B d\mathcal{V} = -\mu \int_B \frac{dm}{r} - \int_B \beta\mu \int_B \frac{dm}{r^3} + 3\beta\mu \int_B \frac{Z^2 dm}{r^5}, \tag{9.15}$$

or

$$\begin{aligned}
\mathcal{V} = &-\frac{\mu}{r_c}\left[ \int_B dm - \frac{1}{2}\int_B \frac{\rho^2}{r_c{}^2}dm + \frac{3}{2}\int_B \left(\frac{\vec{\rho}\cdot\vec{r_c}}{r_c{}^2}\right)^2 dm \right] \\
&-\frac{\beta\mu}{r_c{}^3}\left[ \int_B dm - \frac{3}{2}\int_B \frac{\rho^2}{r_c{}^2}dm + \frac{15}{2}\int_B \left(\frac{\vec{\rho}\cdot\vec{r_c}}{r_c{}^2}\right)^2 dm \right] \\
&\frac{3\beta\mu}{r_c{}^3}\left[ \int_B \frac{(\vec{r_c}\cdot\hat{K})^2}{r_c{}^2}dm + \frac{2(\vec{r_c}\cdot\hat{K})}{r_c}\int_B \frac{(\vec{\rho}\cdot\hat{K})}{r_c}dm + \int_B \frac{(\vec{\rho}\cdot\hat{K})^2}{r_c{}^2}dm \right. \\
&\left. -\frac{5}{2}\frac{(\vec{r_c}\cdot\hat{K})^2}{r_c}\int_B \frac{\rho^2}{r_c{}^2}dm - \frac{5}{2}\frac{(\vec{r_c}\cdot\hat{K})^2}{r_c}\int_B \frac{2(\vec{\rho}\cdot\vec{r_c})}{r_c{}^2}dm \right. \\
&\left. +\frac{35}{2}\frac{(\vec{r_c}\cdot\hat{K})^2}{r_c{}^2}\int_B \left(\frac{\vec{\rho}\cdot\vec{r_c}}{r_c{}^2}\right)^2 dm - 10\frac{(\vec{r_c}\cdot\hat{K})}{r_c}\int_B \frac{(\vec{\rho}\cdot\vec{r_c})(\vec{\rho}\cdot\hat{K})}{r_c{}^3}dm + \mathcal{O}(6) \right] \tag{9.16}
\end{aligned}$$

where the subscript "B" on the integrals indicates integration over the spacecraft body. By definition of the center of mass,

$$\int_B \rho\, dm = 0, \tag{9.17}$$

which causes two of the terms in Equation 9.16 to equal zero. At this point in the derivation, take time out to briefly examine some coordinate system transformations needed to evaluate these integrals. Applying a 1-2-3 (yaw-roll-pitch) Euler sequence of rotations (Figure 9.1). gives us the direction cosines, $c_{ij}$, between the satellite's

197

Figure 9.1: Euler Rotations Between the $(\hat{i}\hat{j}\hat{k})$ and $(\hat{e}_r\hat{e}_t\hat{e}_n)$ Directions

principal axes and the orbit radial, transverse, and normal directions. The Euler rotation matrix $\mathcal{C}$, which the $c_{ij}$ terms comprise, may be expressed as

$$
\begin{bmatrix} \hat{i} \\ \hat{j} \\ \hat{k} \end{bmatrix} = \mathcal{C} \begin{bmatrix} \hat{e}_r \\ \hat{e}_t \\ \hat{e}_n \end{bmatrix},
\tag{9.18}
$$

where

$$
\begin{aligned}
c_{11} &= \cos\psi\cos\vartheta, \\
c_{12} &= \sin\phi\sin\vartheta\cos\psi + \sin\psi\cos\phi, \\
c_{13} &= \sin\phi\sin\psi - \cos\phi\sin\vartheta\cos\psi, \\
c_{21} &= -\sin\psi\cos\vartheta, \\
c_{22} &= \cos\psi\cos\phi - \sin\psi\sin\vartheta\sin\phi, \\
c_{23} &= \cos\psi\sin\phi + \cos\phi\sin\vartheta\sin\psi, \\
c_{31} &= \sin\vartheta, \\
c_{32} &= -\cos\vartheta\sin\psi, \\
c_{33} &= \cos\vartheta\cos\psi,
\end{aligned}
\tag{9.19}
$$

and where $\psi$, $\vartheta$ and $\phi$ are the pitch, roll and yaw angles of the satellite.

Likewise, one can use the standard relationships between the central body coordinate system $(\hat{I}, \hat{J}, \hat{K})$ and the orbit radial, transverse, and normal directions $(\hat{e}_r, \hat{e}_t, \hat{e}_n)$ with the 3-1-3 (longitude of the ascending node-inclination-argument of latitude) Euler sequential rotations (Figure 9.2).
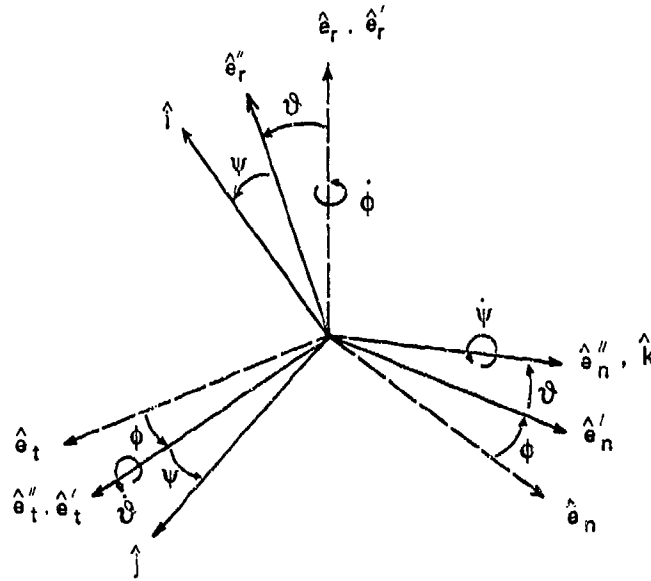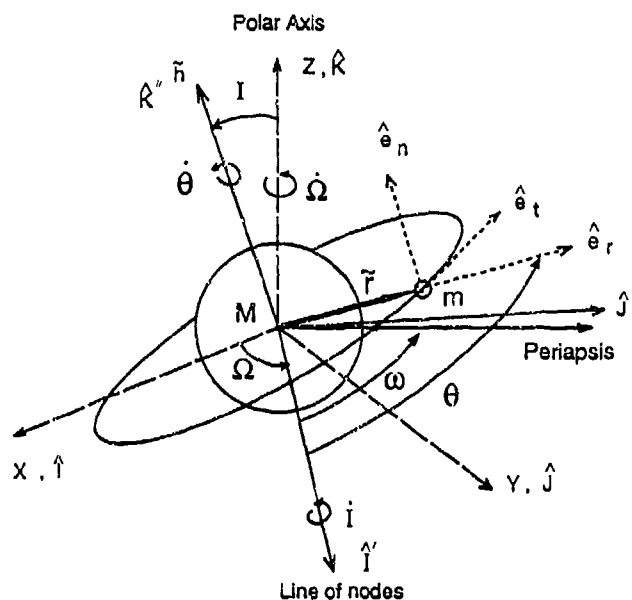
Figure 9.2: Euler Rotations Between the $(\hat{I}\hat{J}\hat{K})$ and $(\hat{e}_r\hat{e}_t\hat{e}_n)$ Directions

The Euler rotation matrix $\mathcal{D}$ is

$$
\begin{bmatrix} \hat{e}_r \\ \hat{e}_t \\ \hat{e}_n \end{bmatrix} = \mathcal{D} \begin{bmatrix} \hat{I} \\ \hat{J} \\ \hat{K} \end{bmatrix},
\tag{9.20}
$$

with

$$
\begin{aligned}
d_{11} &= \cos\Omega\cos\theta - \sin\Omega\sin\theta\cos I, \\
d_{12} &= \sin\Omega\cos\theta + \cos\Omega\sin\theta\cos I, \\
d_{13} &= \sin\theta\sin I, \\
d_{21} &= -\cos\Omega\sin\theta - \sin\Omega\cos\theta\cos I, \\
d_{22} &= -\sin\Omega\sin\theta + \cos\Omega\cos\theta\cos I, \\
d_{23} &= \cos\theta\sin I, \\
d_{31} &= \sin\Omega\sin I, \\
d_{32} &= -\cos\Omega\sin I, \\
d_{33} &= \cos I,
\end{aligned}
\tag{9.21}
$$

and where $I$ is the orbital inclination and $\Omega$ is the longitude of the ascending node. These rotation matrices are considerably simplified with the planar, polar orbit assumption ($I = \pi/2$, $\Omega = 0$) and the assumption that the satellite does not roll or yaw.

Note that

$$
\vec{r_c} = r_c\hat{e}_r = r_c c_{11}\hat{i} + r_c c_{21}\hat{j} + r_c c_{31}\hat{k},
\tag{9.22}
$$

$$\vec{\rho} = x\hat{i} + y\hat{j} + z\hat{k}, \tag{9.23}$$

$$\left(\frac{\vec{r_c} \cdot \vec{\rho}}{r_c}\right) = c_{11}x + c_{21}y + c_{31}z, \tag{9.24}$$

and

$$\left(\frac{\vec{r_c} \cdot \vec{\rho}}{r_c}\right)^2 = c_{11}{}^2 x^2 + c_{21}{}^2 y^2 + c_{31}{}^2 z^2 + \text{ mixed terms}, \tag{9.25}$$

where the "mixed terms" of Equation 9.25 are ignorable because the integral of these terms over the body mass using the body's principal axes produces products of inertia that are zero.

Continuing,

$$\left(\vec{\rho} \cdot \hat{K}\right) = \left(x\hat{i} + y\hat{j} + z\hat{k}\right) \cdot (d_{13}\hat{e}_r + d_{23}\hat{e}_t d_{33}\hat{e}_n) = x\alpha_1 + y\alpha_2 + z\alpha_3 \tag{9.26}$$

where the $\alpha_i$ are defined as

$$\begin{aligned}
\alpha_1 &\equiv d_{13}c_{11} + d_{23}c_{12} + d_{33}c_{13} \\
\alpha_2 &\equiv d_{13}c_{21} + d_{23}c_{22} + d_{33}c_{23} \\
\alpha_3 &\equiv d_{13}c_{31} + d_{23}c_{32} + d_{33}c_{33},
\end{aligned} \tag{9.27}$$

$$\vec{r_c} \cdot \hat{K} = r_c d_{13}, \tag{9.28}$$

and

$$\left(\vec{\rho} \cdot \hat{K}\right)^2 = x^2 \alpha_1{}^2 + y^2 \alpha_2{}^2 + z^2 \alpha_3{}^2 + \text{ mixed terms}, \tag{9.29}$$

where these mixed terms again produce products of inertia and therefore may be ignored.

With the above expressions, one can finally begin evaluating some of the integrals of Equation 9.16. By definition,

$$\int_B \rho^2 dm = \frac{1}{2}(I_x + I_y + I_z). \tag{9.30}$$

Since,

$$\begin{aligned}
x^2 &= \rho^2 - (y^2 + z^2) \\
y^2 &= \rho^2 - (x^2 + z^2) \\
z^2 &= \rho^2 - (x^2 + y^2),
\end{aligned} \tag{9.31}$$

$$\int_B \left(\frac{\vec{r_c} \cdot \vec{\rho}}{r_c}\right)^2 dm = \frac{1}{2}(I_x + I_y + I_z) - I_x c_{11}{}^2 - I_y c_{21}{}^2 - I_z c_{31}{}^2. \tag{9.32}$$

Using the results of Equation 9.29,

$$\int_B \left(\vec{\rho} \cdot \hat{K}\right)^2 dm = (\alpha_1{}^2 + \alpha_2{}^2 + \alpha_3{}^2) \int_B \rho^2 dm - I_x \alpha_1{}^2 - I_y \alpha_2{}^2 - I_z \alpha_3{}^2). \tag{9.33}$$

200

Expanding the terms $(\alpha_1{}^2 + \alpha_2{}^2 + \alpha_3{}^2)$ gives a great number of terms that can be substantially reduced by noting the orthonormal qualities of the direction cosine matrices and factoring appropriate expressions. For example, column orthogonality allows us to factor out expressions like $(c_{11}c_{12} + c_{21}c_{22} + c_{31}c_{32})$ and equate it to zero, and row normality allows us to factor out and equate to one expressions like $(c_{11}{}^2 + c_{21}{}^2 + c_{31}{}^2)$. Eventually one finds

$$(\alpha_1{}^2 + \alpha_2{}^2 + \alpha_3{}^2) = 1 \tag{9.34}$$

and

$$\int_B \left(\vec{\rho} \cdot \hat{K}\right)^2 dm = -I_x\alpha_1{}^2 - I_y\alpha_2{}^2 - I_z\alpha_3{}^2 + \frac{1}{2}(I_x + I_y + I_z). \tag{9.35}$$

Deriving an expression for the last integral in Equation 9.16 again utilizes the orthonormality of the cosine rotation matrices and produces

$$\int_B \frac{(\vec{\rho} \cdot \vec{r_c})(\vec{\rho} \cdot \hat{K})}{r_c} dm = -I_x\alpha_1 c_{11} - I_y\alpha_2 c_{21} - I_z\alpha_3 c_{31} + \frac{d_{13}}{2}(I_x + I_y + I_z). \tag{9.36}$$

Combining all of the above results gives the gravitational potential function of Equation 6.2

$$\begin{aligned}
\mathcal{V} = {}&{} -\frac{\mu m}{r_c}\left[1 + \frac{1}{2}J_2\frac{R_e{}^2}{r_c^2}\left(1 - 3d_{13}{}^2\right)\right] \\
&{} -\frac{\mu}{2r_c^3}\left(\Sigma_1 - 3\Sigma_2\right) - \frac{3J_2\mu R_e{}^2}{4r_c^2}\left[\left(1 - 5d_{13}{}^2\right)\Sigma_1 \right. \\
&{} \left. -5\left(1 - 7d_{13}{}^2\right)\Sigma_2 + 2\Sigma_3 - 20d_{13}\Sigma_4\right] + \mathcal{O}(6),
\end{aligned} \tag{9.37}$$

where

$$\begin{aligned}
\Sigma_1 &\equiv I_x + I_y + I_z, \\
\Sigma_2 &\equiv I_x c_{11}{}^2 + I_y c_{21}{}^2 + I_z c_{31}{}^2, \\
\Sigma_3 &\equiv I_x \alpha_1{}^2 + I_y \alpha_2{}^2 + I_z \alpha_3{}^2, \\
\Sigma_4 &\equiv I_x c_{13}\alpha_1 + I_y c_{23}\alpha_2 + I_z c_{33}\alpha_3, \\
\alpha_1 &\equiv c_{11}d_{13} + c_{12}d_{23} + c_{13}d_{33}, \\
\alpha_2 &\equiv c_{21}d_{13} + c_{22}d_{23} + c_{23}d_{33}, \\
\alpha_3 &\equiv c_{31}d_{13} + c_{32}d_{23} + c_{33}d_{33}.
\end{aligned} \tag{9.38}$$

## 9.2   Derivation of Equation 6.8: the Pitch Equation of Motion for a Satellite in an Eccentric Polar Orbit About an Oblate Central Body

The derivation of Equation 6.8, the pitch equation of motion for a satellite in an eccentric polar orbit about an oblate central body, was briefly discussed in Section 6. The following is a more detailed derivation.

This derivation is carried out by first forming an effective Lagrangian from the potential energy function derived above and an effective kinetic energy function. Translational kinetic energy is not considered for the effective kinetic energy function since it is not a function of the roll, pitch, or yaw angles.

The rotational kinetic energy, $T$, is given by

$$T = \frac{1}{2}\mathbf{I}\vec{\omega} \cdot \vec{\omega} = \frac{1}{2}\left(I_x\omega_x{}^2 + I_y\omega_y{}^2 + I_z\omega_z{}^2\right) \tag{9.39}$$

where $\mathbf{I}$ is the moment of inertia tensor and $\vec{\omega}$ is the angular velocity vector in body frame relative coordinates,

$$\vec{\omega} = \vec{\omega_x}\hat{i} + \vec{\omega_y}\hat{j} + \vec{\omega_z}\hat{k} \tag{9.40}$$

From Figures 9.1 and 9.2,

$$\vec{\omega} = \dot{\phi}\hat{e}_r + \dot{\vartheta}\hat{e}_t{}'' + \dot{\psi}\hat{k} + \dot{I}\hat{I}' + \dot{\theta}\hat{K}'' + \dot{\Omega}\hat{K} \tag{9.41}$$

or, using the coordinate system relationships which formulate the Euler rotation matrices, $\mathcal{C}$ and $\mathcal{D}$,

$$\begin{aligned}
\vec{\omega} = \ & \left(\dot{\phi} + \dot{I}\cos\theta + \dot{\Omega}\sin\theta\sin I\right)\hat{e}_r \\
& + \left(\dot{\Omega}\cos\theta\sin I - \dot{I}\sin\theta\right)\hat{e}_t \\
& + \left(\dot{\theta} + \dot{\Omega}\cos I\right)\hat{e}_n + \dot{\vartheta}\hat{e}_t{}'' + \dot{\psi}\hat{k} \\
\equiv \ & \omega_r\hat{e}_r + \omega_t\hat{e}_t + \omega_n\hat{e}_n + \dot{\vartheta}\hat{e}_t{}'' + \dot{\psi}\hat{k}.
\end{aligned} \tag{9.42}$$

After transforming to the satellite's principal axes directions,

$$\begin{aligned}
\omega_x &= \ \omega_r c_{11} + \omega_t c_{12} + \omega_n c_{13} + \dot{\vartheta}\sin\psi \\
\omega_y &= \ \omega_r c_{21} + \omega_t c_{22} + \omega_n c_{23} + \dot{\vartheta}\cos\psi \\
\omega_z &= \ \dot{\psi} + \omega_n c_{33}.
\end{aligned} \tag{9.43}$$

202

The Lagrangian, $\mathcal{L} = \mathcal{T} + \mathcal{V}$, may be now formed from Equations 9.37, 9.39, and 9.43 and the equations of motion may be derived from the well known expression

$$\frac{d}{dt}\left(\frac{\partial \mathcal{L}}{\partial \dot{\psi}}\right) - \frac{\partial \mathcal{L}}{\partial \psi} = 0. \tag{9.44}$$

To evaluate this equation requires first finding the partials of components of both $\mathcal{V}$ and $\mathcal{T}$. Begin by noting that the partials of the direction cosine matrices, $\mathcal{C}$ and $\mathcal{D}$ are

$$\frac{\partial \mathcal{C}}{\partial \psi} = \begin{bmatrix} c21 & c22 & c23 \\ -c11 & -c12 & -c13 \\ 0 & 0 & 0 \end{bmatrix}, \tag{9.45}$$

and

$$\frac{\partial \mathcal{D}}{\partial \psi} = [0]. \tag{9.46}$$

With this information, the partials of the other components (Equations 9.38 and 9.43) can be found. After simplification,

$$\frac{\partial \alpha_1}{\partial \psi} = \alpha_2, \quad \frac{\partial \alpha_2}{\partial \psi} = -\alpha_1, \quad \frac{\partial \alpha_3}{\partial \psi} = 0$$

$$\frac{\partial \Sigma_1}{\partial \psi} = 0, \qquad \frac{\partial \Sigma_2}{\partial \psi} = 2c_{11}c_{21}(I_x - I_y),$$

$$\frac{\partial \Sigma_3}{\partial \psi} = 2\alpha_1\alpha_2(I_x - I_y), \quad \frac{\partial \Sigma_4}{\partial \psi} = 2\alpha_1 c_{21}(I_x - I_y) + 2\alpha_2 c_{11}(I_x - I_y),$$

and

$$\frac{\partial \omega_x}{\partial \psi} = \omega_y, \quad \frac{\partial \omega_y}{\partial \psi} = -\omega_x, \quad \frac{\partial \omega_z}{\partial \psi} = 0,$$

$$\frac{\partial \omega_x}{\partial \dot{\psi}} = 0, \quad \frac{\partial \omega_y}{\partial \dot{\psi}} = 0, \quad \frac{\partial \omega_z}{\partial \dot{\psi}} = 1,$$

$$\frac{\partial V}{\partial \dot{\psi}} = 0.$$

With this information, Equation 9.44, and the simplifications of the planar, polar orbit assumption ($I = \pi/2, \Omega = 0$) and the assumption that the satellite does not roll or yaw ($\vartheta = \dot{\vartheta} = \phi = \dot{\phi} = 0$), one finds the pitch equation of motion for a satellite in an eccentric polar orbit about an oblate central body to be

$$\ddot{\psi} + \ddot{f} + \frac{3\mu}{r^3}K\cos\psi\sin\psi$$
$$- \frac{3\mu J_2 K R_e^2}{8r^5}[16\cos 2\psi \sin 2\theta$$
$$+ \sin 2\psi(5 - 19\cos 2\theta)] = 0, \tag{9.47}$$

203

where "c" subscript has been dropped from "$r_c$". Note that this equation reduces to the equation of motion for a satellite in an eccentric orbit about a spherical (homogeneous) central body, Equation 2.1, when $J_2$ is set to zero.

## 9.3 Derivation of Equation 7.19: the Melnikov Integral for the Linear Damping Case

The Melnikov integral from Section 7 was,

$$M(f_c) = M_1(f_o) + M_2(f_o) + M_3(f_o) + M_4(f_o) \tag{9.48}$$

where

$$
\begin{aligned}
M_1(f_o) &= 2\gamma e' \int_{-\infty}^{\infty} \text{sech}(\gamma f)\sin(f+f_o)df \tag{9.49}\\
M_2(f_o) &= 2\gamma^2 e' \int_{-\infty}^{\infty} \text{sech}^2(\gamma f)\sin(f+f_o)df \\
M_3(f_o) &= \gamma^3 e' \int_{-\infty}^{\infty} \cos(f+f_o)\text{sech}^2(\gamma f)\tanh(\gamma f)df \\
M_4(f_o) &= -\gamma^2 C'_{D_*} \int_{-\infty}^{\infty} \text{sech}^2(\gamma f)df.
\end{aligned}
$$

Since $\sin(f+f_o) = \sin f \cos f_o + \cos f \sin f_o$, $M_1(f_o)$ may be written

$$
\begin{aligned}
M_1(f_o) &= 2\gamma e' \cos f_o \int_{-\infty}^{\infty} \frac{\sin f}{\cosh(\gamma f)}df \\
&+ 2\gamma e' \sin f_o \int_{-\infty}^{\infty} \frac{\cos f}{\cosh(\gamma f)}df.
\end{aligned}
$$

The first integral is over a function which is a product of an even and an odd function and thus is zero. The second integral is found through simple contour integration and application of the method of residues to be

$$M_1(f_o) = 2e'\pi \sin f_o \text{sech}(\frac{\pi}{2\gamma}). \tag{9.50}$$

The $M_2$ integral may also be expanded,

$$
\begin{aligned}
M_2(f_o) &= 2\gamma^2 e' \cos f_o \int_{-\infty}^{\infty} \frac{\sin f}{\cosh^2(\gamma f)}df \\
&+ 2\gamma^2 e' \sin f_o \int_{-\infty}^{\infty} \frac{\cos f}{\cosh^2(\gamma f)}df.
\end{aligned}
$$

204

Again the first integral is over a function which is a product of an even and an odd function and must be zero. To obtain the solution to the second integral requires the calculation of the residue of a function $g(z)$ at a double pole using the formula

$$\text{Res}[g(z)] = \lim_{z \to z_p} \left\{ \frac{d}{dz} \left[ (z - z_p)^2 g(z) \right] \right\}, \tag{9.51}$$

where for this application and for the chosen contour in the imaginary plane,

$$g(z) = \frac{e^{iz/\gamma}}{\cosh^2 z} \tag{9.52}$$

and $z_p = \pi i/2$ . The evaluation of this rather innocent appearing residue actually required considerable use of a symbolic manipulator computer program. Three successive applications of L'Hopital's rule were necessary to evaluate the limit, and the third differential of the numerator still had 26 terms after factoring. This residue was found to be $-ie^{-\pi/(2\gamma)}/\gamma$ and the solution to the Melnikov $M_2$ integral is

$$M_2(f_o) = 2e'\pi \sin f_o \, \text{cosech}(\frac{\pi}{2\gamma}). \tag{9.53}$$

Through integration by parts, $M_3$ may be evaluated as a function of $M_2$. Using the familiar formula

$$\int_{-\infty}^{\infty} u \, dv = \int_{-\infty}^{\infty} uv - \int_{-\infty}^{\infty} v \, du \tag{9.54}$$

where $u = \cos(f + f_o)$ and $dv = \text{sech}^2(\gamma f) \tanh(\gamma f)$ leads to the solution

$$M_3(f_o) = -\frac{1}{2\gamma} M_2(f_o) = -\frac{e'\pi}{2} \sin f_o \, \text{cosech}(\frac{\pi}{2\gamma}). \tag{9.55}$$

$M_4(f_o)$ can be found from simple integration:

$$M_4(f_o) = -\gamma C'_{D_*} \left[ \tanh(\gamma f) \right]_{-\infty}^{\infty} = -2\gamma C'_{D_*} \tag{9.56}$$

Summing the integrals derived above results in the Melnikov integral for the linear damping case.

$$M(f_o) = \frac{\pi e'}{2} \sin f_o \left[ 4\text{sech}\left(\frac{\pi}{2\gamma}\right) + 3\text{csch}\left(\frac{\pi}{2\gamma}\right) \right] - 2\gamma C'_{D_*}. \tag{9.57}$$

205